

# Mineralogy, composition, and alteration of Mars Pathfinder rocks and soils: Evidence from multispectral, elemental, and magnetic data on terrestrial analogue, SNC meteorite, and Pathfinder samples

Richard V. Morris,<sup>1</sup> D. C. Golden,<sup>2</sup> James F. Bell III,<sup>3</sup> Tad D. Shelfer,<sup>2</sup> Andreas C. Scheinost,<sup>4</sup> Nancy W. Hinman,<sup>5</sup> George Furniss,<sup>5</sup> Stanley A. Mertzman,<sup>6</sup> Janice L. Bishop,<sup>7</sup> Douglas W. Ming,<sup>1</sup> Carlton C. Allen,<sup>2</sup> and Daniel T. Britt<sup>8</sup>

**Abstract.** Major element, multispectral, and magnetic properties data were obtained at Ares Vallis during the Mars Pathfinder mission. To understand the compositional, mineralogical, and process implications of these data, we obtained major element, mineralogical, and magnetic data for well-crystalline and nanophase ferric minerals, terrestrial analogue samples with known geologic context, and SNC meteorites. Analogue samples include unaltered, palagonitic, and sulfatetic tephra from Mauna Kea Volcano (hydrolytic and acid-sulfate alteration), steam vent material from Kilauea Volcano (hydrolytic alteration), and impactites from Meteor Crater (relithification). Salient results for Mars Pathfinder include: (1) Band depths BD530b and BD600 and the reflectivity ratio R800/R750 are consistent with the dominant ferric mineral being nanophase ferric oxide associated with an unknown amount of H<sub>2</sub>O and occurring in composite particles along with subordinate amounts of other ferric minerals. Hematite and hematite plus nanophase goethite are most consistent with the data, but maghemite, akaganéite, schwertmannite, and nanophase lepidocrocite are also possible interpretations. Ferric oxides that are consistently not favored by the data as sole alteration products are jarosites and well-crystalline goethite and lepidocrocite. (2) The strength of the ferric adsorption edge (R750/R445) implies the Fe<sup>3+</sup>/Fe<sup>2+</sup> values for Pathfinder rock and soil are within the ranges 0.7–3 and 3–20, respectively. (3) Ferrous silicates are indicated for subsets of Pathfinder rocks and soils. One subset has a band minimum near 930 nm that can be attributed to low-Ca pyroxene. Alternatively, the band could be a second manifestation of certain ferric oxides, including nanophase goethite, maghemite, akaganéite, and schwertmannite. Another subset has a negative spectral slope from ~800 to 1005 nm which could result from the high-energy wing of a high-Ca pyroxene and/or olivine band, a mixture of bright and dark materials, and, for rocks, thin coatings of bright dust on dark rocks. (4) Chemical data on Pathfinder rocks and soils are consistent with two-component mixtures between an “andesitic” rock with low MgO and SO<sub>3</sub> concentrations (soil-free rock) and a global, basaltic soil with high MgO and SO<sub>3</sub> concentrations (rock-free soil). Pathfinder rock-free soil can be modeled as a chemical mixture of SNC meteorites and the Pathfinder soil-free rock. (5) Pathfinder soil cannot be obtained by chemical alteration of Pathfinder rocks by any of the hydrolytic and acid-sulfate alteration processes we studied. Presumably, global mixing has obscured and possibly erased the elemental signatures of chemical alteration. (6) The strongly magnetic phase in palagonitic and sulfatetic tephra is titanomagnetite and possibly its oxidation product titanomaghemite (Fe-Ti spinels). The saturation magnetization of the tephra samples (0.5–2.0 Am<sup>2</sup>/kg) is at or below the low end of the range inferred for Martian dust (4±2 Am<sup>2</sup>/kg), implying that lithogenic Fe-Ti spinels are a possible candidate for the Martian strongly magnetic phase. (7) The predominantly palagonitic spectral signature and magnetic nature of Martian soil and dust are consistent with glassy precursors with imbedded Fe-Ti spinel particles. Comparison with lunar glass production rates suggests that production of sufficient quantities of glassy materials on Mars by volcanic and impact processes is sufficient to account for these observations.

<sup>1</sup>NASA Johnson Space Center, Houston, Texas.

<sup>2</sup>Lockheed Martin Space Operations Co., Houston, Texas.

<sup>3</sup>Department of Astronomy, Cornell University, Ithaca, New York.

<sup>4</sup>Department of Plant and Soil Science, University of Delaware, Newark.

<sup>5</sup>Department of Geology, University of Montana, Missoula.

<sup>6</sup>Department of Geosciences, Franklin and Marshall College, Lancaster, Pennsylvania.

<sup>7</sup>NASA Ames Research Center, Moffett Field, California.

<sup>8</sup>Lunar and Planetary Laboratory, University of Arizona, Tucson.

## 1. Introduction

The Mars Pathfinder mission returned elemental and multispectral data for soil and rock and magnetic data for airborne dust at the Ares Vallis landing site. First results and interpretations were reported in a recent series of papers [Hviid *et al.*, 1997; Rieder *et al.*, 1997; Smith *et al.*, 1997a]. The purpose of this paper is to provide equivalent elemental, spectral, and magnetic data on Martian analogue and meteorite samples that provide constraints on the mineralogy and chemical state of rocks and soils at the Pathfinder landing site and insights into those alteration processes that brought the Martian surface to its present state. Our focus is primarily on ferric oxides, oxy-hydroxides,

and oxyhydroxysulfates because they are important indicators of formation pathways in the terrestrial alteration environment [e.g., *Cornell and Schwertmann*, 1996]. We report laboratory data for five categories of samples: (1) synthetic and naturally occurring ferric minerals that are possible Martian alteration products; (2) volcanic tephra and samples from active steam vents from the island of Hawaii whose alteration products imply hydrolytic, sulfuric, and hydrochloric alteration processes; (3) Meteor Crater impactites that contain phases whose elements came from both target and impactor; (4) SNC meteorites, which contain ferrous minerals that are likely present on the Martian surface; and (5) basaltic rocks with alteration rinds and freshly broken surfaces. We analyzed many samples that have the same ferric mineralogy in order to determine the natural variations in characterizing physicochemical parameters, because uniqueness in mineral identification (the real challenge for natural samples with complex assemblages) is a function of both the average parameter value and its standard deviation [e.g., *Scheinost et al.*, 1998]. Similarly, we analyzed many tephra samples from nominally the same alteration regime in order to characterize the natural variation in elemental, spectral, and magnetic data that result from different degrees of alteration and/or from the formation of different alteration products as environmental conditions change (e.g., temperature and pH). The diversity of elemental and, especially, spectral data for rocks and soils at the Pathfinder site is well documented [*Smith et al.*, 1997a; *Rieder et al.*, 1997; *McSween et al.*, 1999; *Bell et al.*, this issue], and comparing this diversity to that of known terrestrial alteration regimes provides additional clues for the nature of alteration processes on Mars.

The ferric minerals we studied are oxides (hematite  $\alpha\text{-Fe}_2\text{O}_3$  and maghemite  $\gamma\text{-Fe}_2\text{O}_3$ ), oxyhydroxides (goethite  $\alpha\text{-FeOOH}$ , lepidocrocite  $\gamma\text{-FeOOH}$ , akaganéite  $\beta\text{-FeOOH}$ , and ferrihydrite  $\sim\text{Fe}_2\text{O}_3 \cdot 9/5\text{H}_2\text{O}$ ), and oxyhydroxysulfates (jarosite  $(\text{K},\text{Na},\text{H}_3\text{O})\text{Fe}_3(\text{SO}_4)_2(\text{OH})_6$  and schwertmannite  $(\text{Fe}_{16}\text{O}_{16}(\text{OH})_y(\text{SO}_4)_z \cdot n\text{H}_2\text{O})$ ) that form as terrestrial alteration products and have been suggested as possible alteration products on Mars [e.g., *Gibson*, 1970; *Hargraves et al.*, 1979; *Burns*, 1986, 1988; *Morris et al.*, 1989, 1996, 1997; *Coe et al.*, 1990; *Banin et al.*, 1993; *Murchie et al.*, 1993; *Bishop et al.*, 1993; *Bishop and Murad*, 1996; *Morris and Golden*, 1998; *Madsen et al.*, 1999]. For convenience, we will use the term "ferric oxide" to refer to the aggregate of these minerals. Various lines of evidence, including the width of X-ray diffraction lines and the temperature dependence of Mössbauer spectra, show that all these ferric oxides (except ferrihydrite and schwertmannite) occur in natural environments as discrete particles or as components of composite particles in both poorly crystalline and well-crystalline forms. Ferrihydrite and schwertmannite occur as discrete particles and as components of composite particles in only poorly crystalline forms [e.g., *Cornell and Schwertmann*, 1996]. Our sample suite, which includes both synthetic and natural samples, was chosen to represent the possible range in crystallinity appropriate for each mineral. Spectral data for ferric phases are important primarily for fixing the position of mineralogically diagnostic spectral features (e.g., reflectivity minima and maxima) and thus for identification of specific minerals from Pathfinder multispectral data. Less mineralogically specific, but also important, is recognition of Pathfinder wavelengths where there are large differences in reflectivity for certain combinations of phases. Magnetic data for ferric phases also constrain mineralogy because Martian soil is known to contain a magnetic component [e.g., *Madsen et al.*, 1999].

Tephra samples from Mauna Kea Volcano (Hawaii) consist of unaltered basaltic (hawaiitic) tephra and altered tephra derived from the volcano by hydrolytic (breaking of bonds and adding the elements of water) and sulfuric (breaking of bonds and adding sulfate,  $\text{SO}_4^{2-}$ ) alteration processes. Our sample set includes palagonitic tephra (from hydrolytic alteration) from this locale that are well-documented spectral analogues of Martian bright regions [e.g., *Singer*, 1982; *Morris et al.*, 1990, 1993, 1997]. We analyzed tephra altered by sulfuric activity on Mauna Kea because the high abundance of sulfur in Martian soil ( $\sim 6\text{--}8\%$  as  $\text{SO}_3$  [*Clark et al.*, 1982; *Rieder et al.*, 1997]) suggests that sulfuric alteration processes might be prevalent on the Martian surface [e.g., *Burns*, 1988; *Burns and Fischer*, 1990a,b; *Bishop and Murad*, 1996; *Morris et al.*, 1996; *Banin et al.*, 1997]. We also have samples of highly altered basaltic material from active steam vents (hydrothermal hydrolytic alteration) at Sulfur Bank and Mauna Ulu, Kilauea Volcano (Hawaii). The sample from a now quiescent steam vent at Mauna Ulu is the only one we have of basaltic material that has undergone hydrochloric (breaking of bonds and adding the elements of HCl) alteration processes. Multispectral, magnetic, and elemental data from these altered volcanic samples are important for understanding the nature and diversity of ferric alteration products that are possible from hydrolytic, sulfuric, and hydrochloric alteration processes on Mars.

In contrast to the usual situation where igneous mineral assemblages are precursors to secondary mineral assemblages, Meteor Crater impactites are examples of igneous-like assemblages (basaltic glass, pyroxene, and olivine) that formed from sedimentary target materials (sandstone and dolomitic limestone) and projectile material. Multispectral, magnetic, and elemental data from these impactites are important for understanding the nature of igneous-like assemblages that can be derived from sedimentary material by this impact-driven "relithification" process.

SNC meteorites are igneous rocks that are generally considered to have crystallized from molten lava on Mars [e.g., *McSween*, 1985, 1994, and references therein] and are not altered Martian surface material. We report spectral data for each compositional class of SNC meteorites except dunite (lherzolite, basalt, clinopyroxenite, and orthopyroxenite). The data are used primarily as indicators of which spectral features in Pathfinder multispectral data might be associated with ferrous minerals, especially low-Ca and high-Ca pyroxenes. Elemental data are reported by *Lodders* [1998].

Analyses of rocks with alteration rinds provide data on the proportion of material within rinds that is actually altered and the fraction of probing radiation that is returned to spectral and elemental analyzers from the rinds themselves and from the underlying rock. If rinds are present and are chemically and mineralogically different from underlying rock, it is possible that Mars Pathfinder multispectral and elemental data for rocks are decoupled in the sense that they represent analyses of different materials. The magnitude of decoupling depends on rind thickness and the sampling (penetration) depths of exciting radiations. Conceivably, a rind that is optically thick could be relatively thin with respect to transmission of X rays. We report spectral and Mössbauer (backscatter) data for unaltered (freshly broken) and altered surfaces of two rocks, a basalt and a basaltic komatiite.

Our laboratory spectral, magnetic, and elemental data were made as equivalent as possible to corresponding Pathfinder data [e.g., *Hviid et al.*, 1997; *Rieder et al.*, 1997; *Smith et al.*, 1997a;

*Madsen et al.*, 1999; *McSween et al.*, 1999; *Bell et al.*, this issue]. Spectral data, which we obtained at high spectral resolution in the laboratory, were convolved to Pathfinder multispectral data using the filter positions and band passes compiled by *Smith et al.* [1997b]. Pathfinder magnetic data are multispectral images of the Magnet Arrays (MAs). The saturation magnetization and low-field magnetic susceptibility of adhering dust is inferred from the number of magnets with adhering dust and the geometric patterns the dust makes. We report the same magnetic parameters for our samples. Our elemental data, which were obtained on samples that were homogenized by grinding to fine powders before analysis by X-ray fluorescence, are bulk chemical compositions. Pathfinder elemental data, which were obtained by Alpha Proton X-ray Spectrometer (APXS) analyses of exposed soil and rock surfaces [*Rieder et al.*, 1997], represent chemical compositions of near-surface regions of rocks and soils. These analyses are likely equivalent to the bulk chemical composition of fine-grained, homogenized Martian soil but arguably may not be representative of the bulk chemical compositions of rocks when dust coatings and/or alteration rinds are present. *Rieder et al.* [1997] recognized this possibility and corrected their rock analyses for soil coatings by assuming that all rocks had the same chemical composition and all sulfur in rock analyses was from the soil coating. However, these corrected compositions may still represent the composition of an alteration rind and not primary rock material. In addition to spectral, magnetic, and elemental data, we obtained X-ray diffraction and Mössbauer data on most samples to identify minerals and/or to determine their degree of crystallinity.

Our paper is organized into 12 sections, including the introduction (section 1). In section 2 we give an overview of pre-Pathfinder evidence for specific ferric-bearing phases on the Martian surface, primarily from the perspective of spectral (visible and near-IR) and magnetic data. Section 3 on methods is a description of the analytical instruments and procedures we used to obtain physicochemical properties. The next six sections describe the samples and the multispectral, magnetic, and/or elemental data we obtained on monomineralic or nearly monomineralic ferric oxides (section 4), palagonitic and sulfatetic tephra from Mauna Kea (section 5), hydrothermally altered volcanic material from Kilauea steam vents (section 6), impactites from Meteor Crater (section 7), basaltic rocks with alteration rinds (section 8), and SNC meteorites (section 9). The next two sections are a synthesis of the results from analogue and meteorite samples (section 10) and an application of that synthesis to the mineralogy, composition, and alteration of rocks and soils at the Pathfinder landing site (section 11). Section 12 is our summary of important conclusions. Additional detailed discussions of Pathfinder rocks and soils that follow the initial mission reports are given by *McSween et al.* [1999], *Madsen et al.* [1999], and *Bell et al.* [this issue].

## 2. Ferric Mineralogy of Pre-Pathfinder Mars

### 2.1. Evidence for Nanophase Ferric Oxides

Spectral data at visible and near-IR wavelengths for typical Martian bright regions like Olympus Mons and Amazonis Planitia are characterized by a general shape consisting of a ferric absorption edge extending from ~400 to ~750 nm and relatively constant reflectivity extending from ~750 nm to beyond 2000 nm [e.g., *Singer et al.*, 1979; *Mustard and Bell*, 1994; *Erard and Calvin*, 1997]. The best spectral analogues for this general shape

among terrestrial geologic materials are certain palagonitic tephra from Hawaii [*Evans and Adams*, 1979; *Singer*, 1982; *Adams et al.*, 1986; *Morris et al.*, 1990, 1993, 1997; *Bell et al.*, 1993; *Bishop et al.*, 1998a]. On the basis of transmission electron microscope (TEM), Mössbauer, reflectivity, and selective dissolution data, the ferric pigment in these palagonites is poorly crystalline, nanometer-sized particles which are dispersed through an aluminosilicate matrix [*Morris et al.*, 1993]. It is possible to associate these ferric particles and (by implication) the pigmenting particles on Mars with ferrihydrite ( $\sim\text{Fe}_2\text{O}_3 \cdot 9/5\text{H}_2\text{O}$ ), a poorly crystalline phase whose properties are discussed extensively in the literature [e.g., *Carlson and Schwertmann*, 1981; *Eggleton and Fitzpatrick*, 1988; *Cornell and Schwertmann*, 1996]. However, we prefer not to assign this mineral because (1) we do not know the hydration state of the nanophase particles in palagonitic tephra and (2) there is evidence (developed below) from synthetic samples that the anhydrous equivalent of ferrihydrite can satisfy spectral constraints for palagonites and for Mars. We use the phrase "nanophase ferric oxide" as a generic name for poorly crystalline and nanometer-sized particles of ferric iron that are associated with unknown amounts of  $\text{H}_2\text{O}$ , OH, and other species. Nanophase ferric oxide particles can be discrete particles or, as in palagonitic tephra, components of composite particles.

*Morris et al.* [1989] and *Morris and Lauer* [1990] prepared a series of synthetic powders that contained nanophase ferric oxide (np-Ox) particles by calcination (in air at  $\sim 550^\circ\text{C}$ ) of silica and alumina gels that were impregnated with ferric nitrate solutions. The particle number density was controlled by the concentration of the impregnating ferric nitrate solutions and the number of impregnation-calcination cycles. Particle size was largely controlled by gel pore size. Martian bright region spectra were reproduced with mixtures that contained these nanophase ferric oxide particles as components. As was the case for palagonites, we do not actually know the hydration state of the nanophase ferric oxide particles, but the high temperatures used in calcination favor anhydrous forms (nanophase hematite). It is possible that the difference in reflectivity spectra between ferrihydrite and the nanophase ferric oxide particles associated with the gels is evidence for the anhydrous nature of the latter. Reflectivity spectra for synthetic ferrihydrite published by *Bishop and Murad* [1996] are characterized by reflectivity maxima and minima near 800 and 910 nm, respectively. The reflectivity spectra of the most ferric-rich gels (Type D samples of *Morris et al.* [1989]) are characterized by a plateau centered near 850 nm and do not have definable maxima and minima equivalent to those for ferrihydrite.

A complicating factor for inferring the hydration state of nanophase ferric oxides is that X-ray diffraction (XRD) spectra are apparently insensitive to the degree of hydration. Synthetic, 2-XRD-line ferrihydrite and many naturally occurring ferrihydrites have two broad XRD lines near 0.25 and 0.15 nm [e.g., *Cornell and Schwertmann*, 1996]. Slow thermal decomposition (in air) of trinuclear acetato hydroxy-iron(III) nitrate ( $\text{Fe}_3(\text{OCOCH}_3)_7\text{OHNO}_3 \cdot 2\text{H}_2\text{O}$ ) with a final temperature of  $\sim 220^\circ\text{C}$  yields a powder with the same two XRD lines, an oxalate solubility ( $\text{Fe}_o/\text{Fe}_t \sim 0.4$ ) that is significantly lower than that for ferrihydrite ( $\text{Fe}_o/\text{Fe}_t \sim 1.0$ ), and a reflectivity spectrum equivalent to the one just discussed for silica gels calcined at  $550^\circ\text{C}$  [*Morris et al.*, 1991]. All three observations suggest a lower hydration state for this nanophase product as compared to ferrihydrite. Thermal decomposition of iron pentacarbonyl ( $\text{Fe}(\text{CO})_5$ ) under controlled conditions in an oxidizing atmosphere also yields a

powder with the same broad XRD lines at 0.25 and 0.15 nm. *Cornell and Schwertmann* [1996] call this material ferrihydrite, although no evidence is presented to show that it contains any  $H_2O$  (none is implied by the carbonyl precursor). The name "ferrihydrite" is therefore being used for poorly crystalline ferric material that is characterized by the two broad XRD lines near 0.25 and 0.15 nm, irrespective of  $H_2O$  content.

We suggest that there exists a continuous series of poorly ordered nanometer-sized materials whose chemical compositions range from  $Fe_2O_3$  to  $Fe_2O_3 \cdot 9/5H_2O$  and whose XRD powder diffraction patterns are two broad lines near 0.25 and 0.15 nm. According to *Fleisher et al.* [1975], the mineral name ferrihydrite is reserved for the hydrous endmember. The anhydrous endmember has no approved name, but we have previously referred to it as nanophase hematite because its properties are reasonably an extension of those of hematite to nanoscale dimensions [e.g., *Morris et al.*, 1989]. We suggest that nanophase hematite was present but not detected in experiments involving dry heating [*Stanjek and Weidler*, 1992] and differential thermal analyses [e.g., *Carlson and Schwertmann*, 1981] of 2-XRD-line ferrihydrite because the ferrihydrite to nanophase hematite transition is not detectable in XRD data. We will use the generic name "nanophase ferric oxide" in situations (like palagonites) where we want to imply the presence of poorly crystalline ferric oxide particles without any implications for water content. The distinction between ferrihydrite and nanophase ferric oxides as names is important in the planetary context because the name "ferrihydrite" implies the presence of  $H_2O$  and the name "nanophase ferric oxide" leaves the issue of the presence or absence of  $H_2O$  open. Thus we attribute the general shape of the reflectivity of Martian bright regions to nanophase ferric oxides.

In summary, it is reasonable to associate (by analogy with palagonitic tephra) the general shape of reflectivity spectra for Martian bright regions with silicate material pigmented by nanophase ferric oxide particles that are associated with an unknown amount of  $H_2O$ . The general correspondence in spectral properties of palagonitic tephra and Martian bright regions does not necessarily imply that palagonitization (alteration of basaltic glass) is an important hydrolytic alteration process on Mars. It does imply that operative processes on Mars produce the optical equivalent of palagonitic tephra. Note that this constraint permits the nanophase ferric oxides in terrestrial palagonites and on the Martian surface to have different amounts of  $H_2O$  associated with them. It is possible, for example, for nanophase ferric oxides in terrestrial palagonites and on the Martian surface to be relatively hydrous and relatively anhydrous, respectively.

## 2.2. Evidence for Well-Crystalline Ferric Oxides

Weak spectral features present in the Martian ferric absorption edge suggest the presence of moderately to well-crystalline ferric-bearing minerals in addition to nanophase ferric oxides. For the Olympus-Amazons region, these weak features are near 600 nm (a shoulder), 750 nm (a reflectivity maximum), and 860 nm (a reflectivity minimum) [e.g., *Bell et al.*, 1990; *Mustard and Bell*, 1994; *Merenyi et al.*, 1996]. These weak features have been associated with subordinate amounts (<5%) of red (i.e., well-crystalline and pigmentary) hematite, as summarized by *Morris et al.* [1997]. *Morris and Golden* [1998] showed that hematitic Martian spectral data permit the presence of some goethite, because the characteristic goethite spectral features (e.g., the minimum near 900 nm) are overwhelmed by those for hematite and thus are not observed. A similar situation permits the

presence of maghemite under the spectral constraints of hematite [*Morris et al.*, 1998a]. Presumably, similar results apply to other ferric-bearing phases, but this has not yet been demonstrated. In addition to hematitic regions, there are other, areally more restricted Martian bright regions that have weak minima near 900 nm [*Geissler et al.* 1993; *Murchie et al.*, 1993]. The 900-nm phase could be any combination of a number of ferric-bearing minerals, and maghemite, goethite, jarosite, schwertmannite, and nontronite have been proposed [*Murchie et al.*, 1993; *Bishop and Murad*, 1996; *Morris et al.*, 1996]. In summary, the spectral evidence is that there are at least two crystalline and ferric-bearing minerals in the optical surface of Mars in addition to nanophase ferric oxide. One of them is most likely hematite, and the other is one or more of several possible phases.

The magnetic mineralogy of Martian soil was investigated by the Viking Landers in 1976. The results of the Viking magnetic properties experiment indicated the presence of 1-7 wt % of a highly magnetic phase that is most probably present as a minor component of composite particles rather than as discrete magnetic grains [*Hargraves et al.*, 1977, 1979; *Moskowitz and Hargraves*, 1982; *Posey-Dowty et al.*, 1986]. The preferred interpretation of Hargraves and coworkers is that the strongly magnetic phase is maghemite ( $\gamma\text{-Fe}_2O_3$ ). *Moskowitz and Hargraves* [1982] note that if either magnetite or maghemite is the strongly magnetic phase, the saturation magnetization for Martian soil approaches 1-7 Am<sup>2</sup>/kg. Other ferric-bearing phases that have been proposed for the magnetic mineral include Fe-Ti spinels (titanomagnetite and titanomaghemite) [*Coe et al.*, 1990; *Morris et al.*, 1990] and nanophase hematite [*Morris et al.*, 1989].

## 3. Methods

High-resolution diffuse reflectivity spectra (350-2100 nm) were obtained at room temperature (~293 K) with a Cary-14 spectrophotometer configured with a 23-cm-diameter integrating sphere. The instrument is a double-beam double monochromator with a resolving power of 0.1-0.3 nm and a wavelength accuracy of ~0.4 nm. Sample and reference ports are located in the bottom of the sphere so that samples are measured in a horizontal orientation flush with port openings. Beam size (monochromatic light) at sample and reference ports was ~1.0 x 2.0 cm; sample depths were 4-5 mm. Halon is used as the reflectivity standard and as the coating for the integrating sphere; reflectivity measurements were converted to absolute reflectivity using literature data for the absolute reflectivity of Halon [*Weidner and Hsia*, 1981]. The compartment of the Cary-14 that contains the integrating sphere and samples was flushed with dry  $N_2$  gas (derived from liquid  $N_2$ ) for at least 1 hour prior to obtaining reflectivity spectra. Laboratory spectra were convolved to equivalent Imager for Mars Pathfinder (IMP) multispectral data using Gaussian line shapes and the band passes published by *Smith et al.* [1997b]. The wavelengths for IMP multispectral data are nominally (rounded to the nearest 5 nm) 445, 480, 530, 600, 670, 750, 800, 860, 900, 930, 965, and 1005 nm. By convention, we will use the notation R445, R480, ..., R1005 to refer to the magnitude of reflectivity for either Martian IMP spectra or laboratory spectra convolved to IMP band passes.

A Scintag XDS 2000 X-ray diffractometer using  $CuK\alpha$  radiation and a step size of  $0.02^\circ 2\theta$  was employed to obtain X-ray diffraction powder patterns (~293 K) on powdered samples (<150  $\mu m$ ). We prepared fine powders from rocks or coarse-grained particulate samples by pulverization in an alumina mortar and



pestle until the powdered material easily passed through a 150- $\mu$ m sieve. Magnetization curves for 10–40 mg of sample were recorded at room temperature in fields up to 2.1 T using a Princeton Applied Research Model 155 Vibrating Sample Magnetometer. Saturation magnetizations  $J_s$  were calculated from a linear least squares fit of the magnetization data between 1.3 and 2.1 T. Typical uncertainties are the greater of  $\pm 20\%$  or  $\pm 0.008$  Am<sup>2</sup>/kg for  $0 < J_s < 0.1$  Am<sup>2</sup>/kg;  $\pm 8\%$  for  $0.1 < J_s < 1.0$  Am<sup>2</sup>/kg;  $\pm 5\%$  for  $1.0 < J_s < 10$  Am<sup>2</sup>/kg; and  $\pm 2\%$  for  $J_s > 10$  Am<sup>2</sup>/kg. Mass-specific susceptibilities  $\chi_{lf}$  were obtained for sample volumes of  $\sim 10^{-6}$  m<sup>3</sup> at  $\sim 293$  K with a Bartington Model MS2 magnetic susceptibility meter with MS2B sensor; typical uncertainties are  $\pm 15\%$ .

Transmission and backscatter Mössbauer spectra were obtained at room temperature ( $\sim 293$  K) on Ranger Scientific spectrometers [Morris *et al.*, 1985, 1989] and an instrument developed at the Johnson Space Center (JSC), respectively, using <sup>57</sup>Co(Rh) sources at intensities of  $\sim 25$  mCi. Mirror-image spectra were obtained using a triangular waveform and a 1024-channel analyzer. Velocity calibration was done with laser interferometers (Ranger instruments) and metallic iron foil (JSC instrument). Absorbers for transmission experiments were made by dispersing powdered samples ( $< 150$   $\mu$ m) in epoxy to a density

of 50–100 kg/m<sup>3</sup> of natural Fe. Backscatter experiments were done with no sample preparation and only on rock surfaces. Mössbauer parameters, derived by fitting folded spectra to theoretical line shapes using an in-house computer program (JSCFIT), are the isomer shift (IS) relative to the midpoint of the spectrum of metallic iron foil at 293 K, quadrupole shift (QS), hyperfine field strength  $B_{hf}$ , and full widths at half maximum intensity ( $W$ ). Typical uncertainties are  $\pm 0.01$  mm/s for IS and QS, 0.1 T for  $B_{hf}$ , and 0.02 mm/s for  $W$ .

Major element chemistry was determined by X-ray fluorescence (XRF) using a 9:1 Li<sub>2</sub>B<sub>4</sub>O<sub>7</sub>-sample flux-fusion procedure to prepare glass disks and a Philips 2404 XRF spectrometer equipped with a 4 kW Rh X-ray tube [see Boyd and Mertzman, 1987]. Loss on ignition (LOI) was ascertained by heating an exact aliquot of sample powder at 950°C in air for a minimum of 1 hour. Because major element analyses were done on the residue of LOI measurements, total iron is reported as Fe<sub>2</sub>O<sub>3</sub>T. The amount of Fe<sup>2+</sup> was measured on unheated samples using a modified Reichen and Fahey [1962] procedure. Approximately 2.5 g of sample was used for measurement of major element, LOI, and Fe<sup>2+</sup> concentrations. Total sulfur measurements (reported as SO<sub>3</sub>) were made on unheated samples using a LECO IR-32 total sulfur analyzer.

**Table 1.** Listing of Ferric Oxides, Their Origins, and Selected References to Previous Work

Phase	Sample	Origin and Reference
Akg	AKS1	Synthetic; per Schwertmann and Cornell [1991]
Akg	SAK1	Synthetic; Murad [1979]
Feh	6Y, 27B	Natural; Carlson and Schwertmann [1981]
Feh	H3, H4, J1, J2, J3, I.1, S4, S5, S8	Natural; Carlson and Schwertmann [1987]
Feh	N162, N163	Natural; 0.1–0.2 $\mu$ m; Schwertmann and Fischer [1973]
Feh	19E, FE047, FE152, FE258, PJ5a, S3, S7a, SA144b	Natural; U. Schwertmann collection
Feh	FH2S1 and FH6S1	Synthetic 2-XRD-line and 6-XRD-line; per Schwertmann and Cornell [1991]
Feh	FE518-1	Synthetic; A. Scheinost collection
Gt	4D-1, 6D-1, 6D-2, 6D-3	Natural; ferricrete; Daisy Creek (New World Mining District), Montana; Furniss <i>et al.</i> [1999]
Gt	4FG-9, 4FG-10, 6F-1, 6F-2, 6F-3	Natural; ferricrete; Fisher Creek (New World Mining District), Montana; Furniss <i>et al.</i> [1999]
Gt	6SB-1	Natural; ferricrete; Soda Butte Creek (New World Mining District), Montana; Furniss <i>et al.</i> [1999]
Gt	6SC-E2	Natural; ferricrete; Stevens Creek (Heddeleston Mining District), Montana
Gt	7PM10-42, 7PM10-46, 7PM10-48	Natural; ferricrete; Paymaster Creek (Heddeleston Mining District), Montana
Gt	GTS2, GTS3, GTS5	Synthetic; commercial products; Morris <i>et al.</i> [1985]
Hm	HMN3	Natural; commercial product
Hm	HMS2, HMS3, HMS10, HMS12, HMS13, HMS14, HMS15	Synthetic; commercial products; Morris <i>et al.</i> [1985]
Jar-H <sub>2</sub> O	JARHS3	Synthetic; modified Brophy and Sheridan [1965]
Jar-Na	LNVIJAR1	Natural; Luning, Nevada; Morris <i>et al.</i> [1996]
Jar-K	JARKS1	Synthetic; per Brophy and Sheridan [1965]
Lp	LPS2	Synthetic; commercial product; Morris <i>et al.</i> [1985]
Lp	LPS3	Synthetic; per Schwertmann and Cornell [1991]
Mh	LPS2-3-265	Synthetic; Morris <i>et al.</i> [1998b]
Mh	MHS3, MHS4, MHS6	Synthetic; commercial products; Morris <i>et al.</i> [1985]
Mt	MTS4, MTS5	Synthetic; commercial products; Morris <i>et al.</i> [1985]
Mt	MTCCU1	Natural; Cedar City, Utah
Mt	MTISH1	Natural; Ishpeming, Michigan
Sch	BT-4	Natural; Belmont Co., Ohio; Bigham <i>et al.</i> [1990]
Sch>>Gt	5F-108	Natural; ferricrete; Fisher Creek (New World Mining District), Montana; Furniss <i>et al.</i> [1999]
Sch>>Gt	6PM-0	Natural; ferricrete; Paymaster Creek (Heddeleston Mining District), Montana

For simplicity, ferric oxides, oxyhydroxides, and oxyhydroxysulfates are referred to as ferric oxides. All samples are powders (none coarser than 90  $\mu$ m). JARHS1 synthesis procedure was modified by excluding the alkali metals from the starting solution and by reducing the temperature of reaction to 95°C. Phases: Akg, akaganéite; Feh, ferrihydrite; Gt, goethite; Hm, hematite; Jar, jarosite; Lp, lepidocrocite; Mh, maghemite; Mt, magnetite; Sch, schwertmannite.

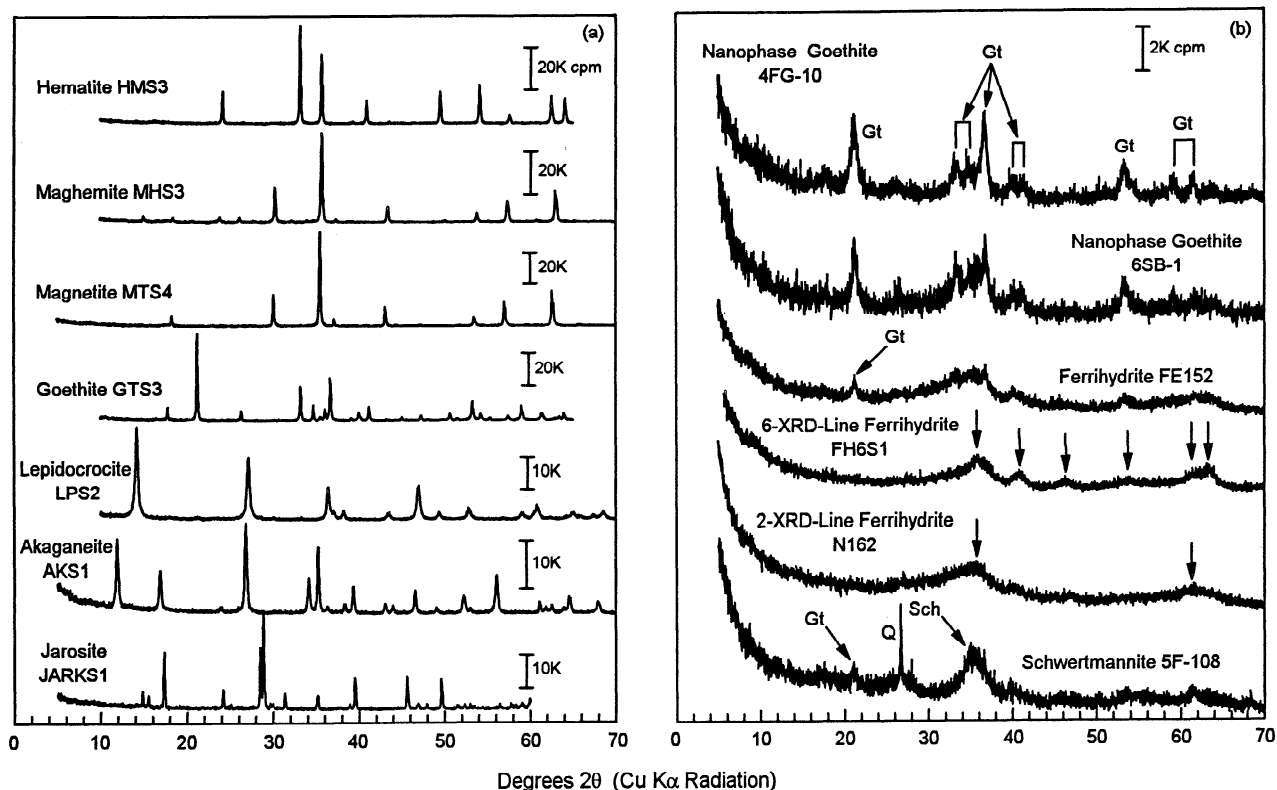


**Figure 1.** Representative X-ray diffraction (XRD) powder patterns (293 K) for (a) well-crystalline hematite (HMS3), maghemite (MHS3), magnetite (MTS4), goethite (GTS3), lepidocrocite (LPS2), akaganéite (AKS1), and jarosite (JARKS1) and (b) nanophase goethites (4FG-10 and 6SB-1), ferrihydrites (FE152, FH6S1, and N162), and schwertmannite (5F-108). Note that XRD lines for well-crystalline phases are narrow and intense and those for the poorly crystalline phases are weak and broad. Ferrihydrite N152 has a goethite (Gt) and quartz (Q) impurities.

## 4. Ferric Minerals

### 4.1. Samples

Samples representing nine different ferric minerals (hematite, maghemite, magnetite, goethite, lepidocrocite, akaganéite, ferrihydrite, schwertmannite, and K-, Na-, and H<sub>3</sub>O-jarosite) are listed in Table 1, together with references to previous studies. All minerals, except lepidocrocite and akaganéite, are represented by both synthetic and naturally occurring samples. Jarosites (JARKS1 and JARHS1), akaganéite (AKS1), lepidocrocite (LPS3), and ferrihydrites (FH2S1 and FH6S1) were synthesized as a part of this study using recipes from *Brophy and Sheridan* [1965] and *Schwertmann and Cornell* [1991]. Samples from deposits of ferricrete (stratified iron oxyhydroxide or clastic sediment cemented iron oxyhydroxide), which contain goethite and/or schwertmannite, are from the New World and Heddleston mining districts (Montana) and were collected between 1994 and 1997 (N. Hinman and G. Furniss) as friable to moderately coherent rocks [Furniss et al., 1999]. A poorly crystalline maghemite (LPS2-3-265) was made by dehydroxylation of lepidocrocite LPS2 [Morris and Lauer, 1981]. Naturally occurring ferrihydrite samples were obtained from the collection of U. Schwertmann. Synthetic akaganéite SAK1 and natural schwertmannite BT-4 were provided by E. Murad and J. Bigham. All other samples were obtained from sample collections at the NASA Johnson Space Center. All samples except the ferricretes and the natural magnetites were obtained or synthesized as fine

powders. The ferricretes and magnetites were ground to fine powders (<150 μm) using an alumina mortar and pestle.

### 4.2. Properties

The synthetic hematites (HMS2 through HMS15), goethites (GTS2, GTS3, and GTS5), maghemites (MHS3 through MHS6), lepidocrocites (LPS2 and LPS3), akaganéites (SAK1 and AKS1), magnetites (MTS4 and MTS5), and jarosites (JARHS1 and JARKS1) and the natural hematite (HMN3), Na-jarosite (LNVJAR1), and magnetite (MTCCU1 and MTISH1) are all well-crystalline materials based on narrow XRD lines as reported in previous studies (Table 1) or as obtained from XRD data as a part of this study. Representative XRD powder patterns of well-crystalline ferric minerals are shown in Figure 1a.

Schwertmannite and ferrihydrite are both inherently poorly crystalline materials and have no well-crystalline counterparts. XRD powder patterns for schwertmannite 5F-108 and ferrihydrites FE152, FH6S1, and N162 are shown in Figure 1b. Peaks from minor goethite, which is a common aqueous alteration product of both minerals, can be seen in the XRD patterns of 5F-108 and FE152. Ferrihydrite is generally characterized by either two or six broad XRD lines (Figure 1b), although ferrihydrites with an intermediate number of lines have been reported [Cornell and Schwertmann, 1996]. Ferrihydrites with two broad XRD lines near 0.25 and 0.15 nm (35.9° and 61.8° 2θ, respectively, for CuKα radiation) are apparently the most common natural product, and they seem to occur always in association

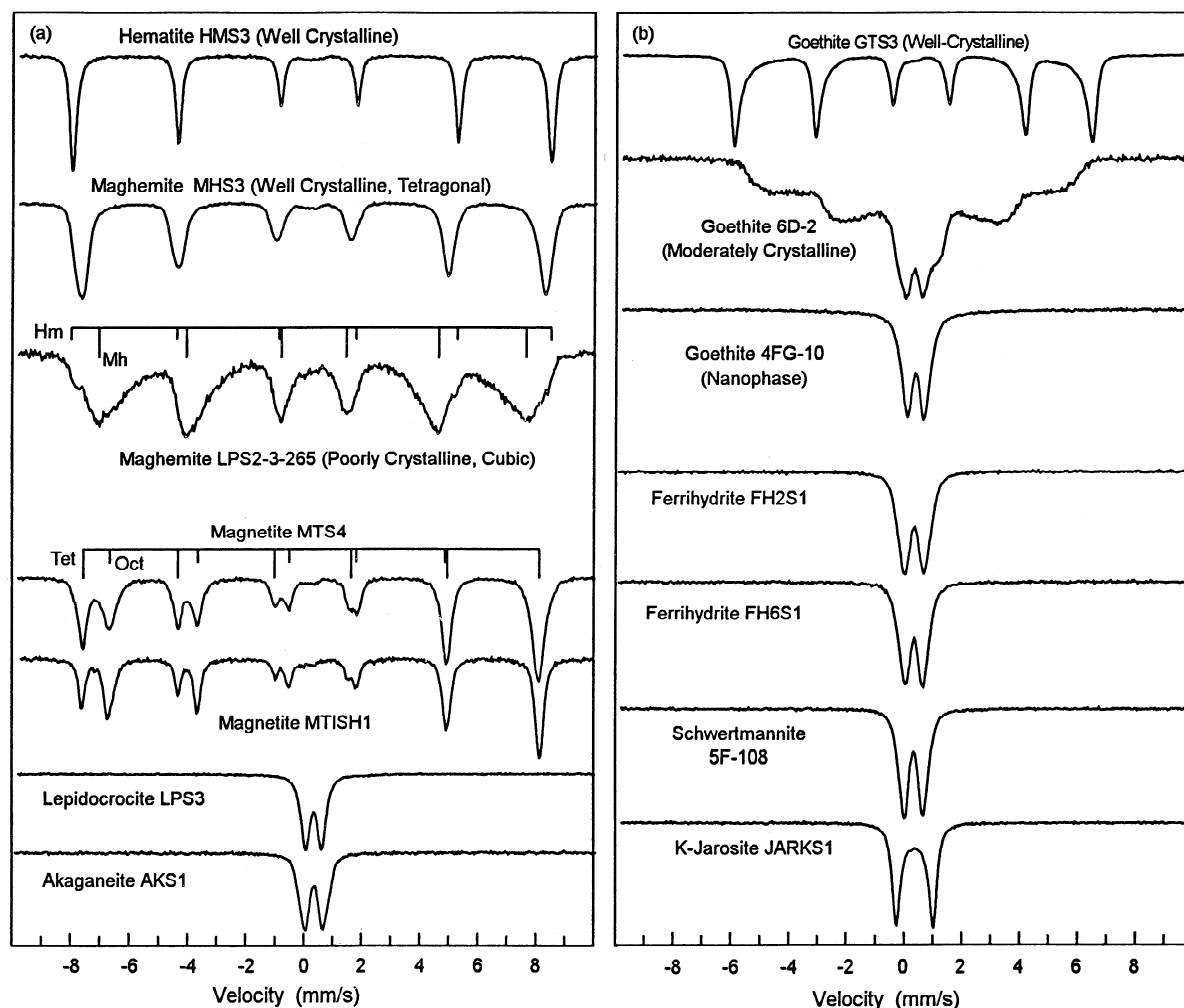


**Figure 2.** Representative Mössbauer spectra (293 K) for (a) hematite (HMS3), maghemites (MHS3 and LPS2-3-265), magnetites (MTS4 and MTISH1), lepidocrocite (LPS3), and akaganéite (AKS1) and (b) goethites (GTS3, 6D-2, and 4FG-10), ferrihydrites (FH2S1 and FH6S1), schwertmannite (5F-108), and jarosite (JARKS1). Maghemite LPS2-3-265, derived by heating lepidocrocite, has a minor hematite impurity. The three goethite samples represent a sequence from well-crystalline (magnetic sextet GTS3) to nanophase (superparamagnetic doublet 4FG-10) behavior.

with  $\text{SiO}_2$ . Except for two schwertmannite-bearing samples (5F-108 and 6PM-0), XRD data for Montana ferricretes indicate the presence of goethite having a range of crystallinities. Powder patterns for two ferricretes (4FG-10 and 6SB-1) with poorly crystalline (nanophase) goethite are shown in Figure 1b.

Representative Mössbauer spectra (293 K) for each ferric mineral are shown in Figure 2, and derived Mössbauer parameters are compiled in Table 2. Also included in Table 2 are Mössbauer parameters for nanophase hematite [from Morris *et al.*, 1989], np-Ox in palagonite (section 5.3.2), and ferrous and ferric iron in glass (sections 5.3.1 and 5.3.3). Spectra and derived parameters are consistent with literature data [e.g., Burns and Solberg, 1990; McCammon, 1995; Murad, 1996; Cornell and Schwertmann, 1996; Herbert, 1997; Stevens *et al.*, 1998]. Sextet spectra for well-crystalline hematite, maghemite, goethite, and magnetite are sufficiently distinct to serve as a basis for mineralogical identification. Note that maghemite LPS2-3-265 appears to have a minor hematite impurity. The magnetites have octahedral iron ( $\text{Fe}^{2+}$  and  $\text{Fe}^{3+}$ ) to tetrahedral iron ( $\text{Fe}^{3+}$  only) ratios (1.06 to 1.88) that are less than the stoichiometric value

(2.0), indicating some oxidation. In agreement with the results of Johnston and Norrish [1981] and Schwertmann *et al.* [1985], the progressive collapse of the goethite sextet to a superparamagnetic doublet for samples GTS3, 6D-2, and 4FG-10 is a result of decreasing particle size and decreasing crystallinity as observed in XRD data.

The Mössbauer spectra (293 K) of jarosite, lepidocrocite, akaganéite, ferrihydrite, schwertmannite, nanophase goethite and hematite, and np-Ox (palagonite) are doublets associated with octahedrally coordinated ferric iron. The Mössbauer parameters of jarosite ( $\text{IS}=0.36\pm0.01$  mm/s and  $\text{QS}=1.14\pm0.08$  mm/s) are distinct from those for the other seven phases and are thus diagnostic. The Mössbauer parameters for lepidocrocite, akaganéite, ferrihydrite, schwertmannite, np-goethite, np-hematite, and np-Ox (palagonite) are sufficiently similar ( $\text{IS}=0.33\text{--}0.36$  mm/s and  $\text{QS}=0.57\text{--}0.75$  mm/s) that it is likely impossible to use only room-temperature Mössbauer data to identify one of these phases to the exclusion of the others in a natural sample. That is, a Mössbauer doublet at  $\sim 293$  K having  $\text{IS}\sim 0.34$  mm/s and  $\text{QS}\sim 0.6\text{--}0.8$  mm/s reasonably results from

**Table 2.** Average Values and Standard Deviations (One Sigma) of Mössbauer Parameters (293 K) for Iron-Bearing Phases

Phase	IS, mm/s	QS, mm/s	$B_{hf}$ , T	$W$ , mm/s	Line Shape	N	Samples Used for Average
<i>Ferric doublets</i>							
Jarosite (wc)	0.36±0.01	1.14±0.08	--	0.34±0.04	L+G	6	JARKS1, JARHS1, LNVJAR1, and <5 µm of HWMK24, HWMK504, and HWMK515
np-Ox (palagonite)	0.34±0.02	0.75±0.03	--	0.55±0.03	L+G	5	<2 µm of HWHP301, HWMK530, HWMK600, JSC Mars-1, and PN-9
Ferrihydrite (np)	0.34±0.01	0.73±0.07	--	0.52±0.04	L+G	2	FH2S1 and FH6S1
Hematite (np)	0.33±0.01	0.63±0.08	--	0.63±0.07	V	33	Supported on silica gel; <i>Morris et al.</i> [1989]
Goethite (np)	0.35±0.01	0.63±0.02	--	0.42±0.02	L+G	5	4FG-10, 6F-1, 6F-2, 6F-3, 6SB-1
Schwertmannite (np)	0.34±0.01	0.69±0.01	--	0.42±0.01	L+G	2	6PM-0 and 5F-108
Akaganéite (wc)	0.36±0.01	0.67±0.01	--	0.44±0.01	L+G	2	AKS1 and SAK1
Lepidocrocite (wc)	0.36±0.01	0.57±0.01	--	0.32±0.04	L+G	2	LPS2 and LPS3
Glass, Tet-Fe <sup>3+</sup>	0.32±0.01	1.04±0.01	--	0.72±0.03	L+G	1	<1 mm of HWMK20
Glass, Oct-Fe <sup>3+</sup>	0.45±0.02	0.86±0.03	--	0.80±0.02	L+G	2	HWMK513 (nonmagnetic) and PH-13
<i>Ferrous doublets</i>							
Glass, Oct-Fe <sup>2+</sup>	1.00±0.07	2.18±0.03	--	0.80±0.02 0.90±0.01	L+G	2	HWMK513 (nonmagnetic) and PH-13
Olivine, Fe <sup>2+</sup>	1.14±0.01	2.89±0.01	--	0.33±0.03	L	3	PN-9, HWMK12, and HWMK530
<i>Sextets</i>							
Hematite (wc)							
Symmetric lines	0.37±0.01	-0.20±0.01	51.1±0.1	0.30±0.03	L	4	HMN3, HMS3, HMS12, and HMS14, <1 mm of HWSB531 and <5 µm of HWMK20
Asymmetric lines	0.39±0.02	-0.17±0.02	50.6±0.3	0.56±0.11	Skew-L	3	and HWMK504
Goethite (wc)	0.37±0.01	-0.24±0.01	38.7±0.1	0.46±0.06	Skew-L	2	GTS2 and GTS3
Maghemite (wc)	0.32±0.01	0.02±0.01	49.7±0.1	0.66±0.11	L+G	2	MCIS1 and MHS3
Magnetite (wc)							
Octahedral	0.68±0.01	0.02±0.01	45.8±0.2	0.47±0.11	L	3	MTCCU1 (1.35), MTISH1 (1.88), and
Tetrahedral	0.29±0.02	0.02±0.02	48.9±0.2	0.33±0.07	L	3	MTS4 (1.06)

Only samples that are monomineralic or highly enriched in the indicated phases were used to calculate average values. IS is calculated relative to the midpoint of metallic iron foil at 293 K. Doublet line widths are the average of lines 1 and 2 (except Oct-Fe<sup>2+</sup> in glass); sextet line widths are the average of lines 1 and 6. Line shapes: L, Lorentzian; L+G, Lorentzian and Gaussian linear combination; Skew-L, skewed Lorentzian; V, Voigt. N is the number of samples used to calculate averages. Initials: wc, well crystalline; np, nanophas. Number in parentheses for magnetites is the area ratio of octahedral to tetrahedral sites.

octahedrally coordinated ferric iron but is otherwise not mineralogically specific. Although we did not obtain low-temperature Mössbauer spectra as a part of this study, magnetic splitting (i.e., sextets) at low temperatures can be used as mineralogical constraints of these ferric phases [e.g., *Murad*, 1990, 1996; *Cornell and Schwertmann*, 1996].

The Mössbauer doublet parameters for ferric and ferrous iron in the glass phases of our samples are distinct from those for the octahedrally coordinated ferric oxides (Table 2). Tetrahedrally coordinated Fe<sup>3+</sup>, which is characterized by relatively low (0.32 mm/s) and high (1.04 mm/s) values of IS and QS, is especially distinctive. Octahedrally coordinated Fe<sup>3+</sup> in our glasses is distinguished by its relatively high value of IS (~0.45 mm/s). Octahedrally coordinated Fe<sup>2+</sup> in glass, relative to ferric iron and as is typical for crystalline ferrous silicates [e.g., *Burns and Solberg*, 1990], has large values of both IS (~1.0 mm/s) and QS (~2.2 mm/s).

IMP-equivalent multispectral data, magnetic properties, and chemical compositions for samples with a single ferric mineral are compiled in Tables 3 and 4. Magnetic data are generally in agreement with literature values for the same mineral [e.g., *Nagata*, 1961; *Carmichael*, 1982; *Morris et al.*, 1985]. Except for spinel minerals (maghemite and magnetite), all samples are weakly magnetic or nonmagnetic on the basis of their low values of saturation magnetization (generally <1 Am<sup>2</sup>/kg) and low-field susceptibility (generally <5×10<sup>-6</sup> m<sup>3</sup>/kg). In comparison, the strongly magnetic spinels have high saturation magnetizations

(~50-92 Am<sup>2</sup>/kg) and high low-field susceptibilities (~300×10<sup>-6</sup> - 550×10<sup>-6</sup> m<sup>3</sup>/kg). High-resolution spectral data for each ferric mineral are consistent with published spectra [e.g., *Sherman et al.*, 1982; *Morris et al.*, 1985, 1996; *Clark et al.*, 1990; *Nagano et al.*, 1992; *Bishop and Murad*, 1996]. Representative reflectivity spectra are shown for each mineral in Figure 3. Even at the low spectral resolution of IMP multispectral data (~30 nm), significant mineralogical information can be obtained, as discussed next.

The positions of reflectivity maxima (M1) and minima (T1) for ferric minerals occur between 650 and 1005 nm in IMP-equivalent spectral data, as shown by the histograms in Figure 4. For cases where maximum or minimum reflectivity is the same at adjacent IMP wavelengths, values of M1 and T1 were taken as the average position. In a monomineralic ferric oxide, T1 is the position of the reflectivity minimum of the ferric <sup>6</sup>A<sub>1</sub>→<sup>4</sup>T<sub>2g</sub> electronic transition, and M1 is the reflectivity maximum between that transition and the adjacent <sup>6</sup>A<sub>1</sub>→<sup>4</sup>T<sub>1g</sub> transition [e.g., *Morris et al.*, 1985; *Sherman and Waite*, 1985; *Burns*, 1993]. In an assemblage of multiple ferric minerals, M1 and T1 correspond to the maximum and minimum of the envelope formed by the individual ferric minerals. The eight different ferric minerals divide into five groups that have unique values of M1 and/or T1. The values of T1 for hematite (860 nm) and lepidocrocite (970-985 nm) and the M1 value for jarosite (670-710 nm) are unique and would, by themselves, provide evidence for these minerals in a complex sample. These three minerals comprise single-member



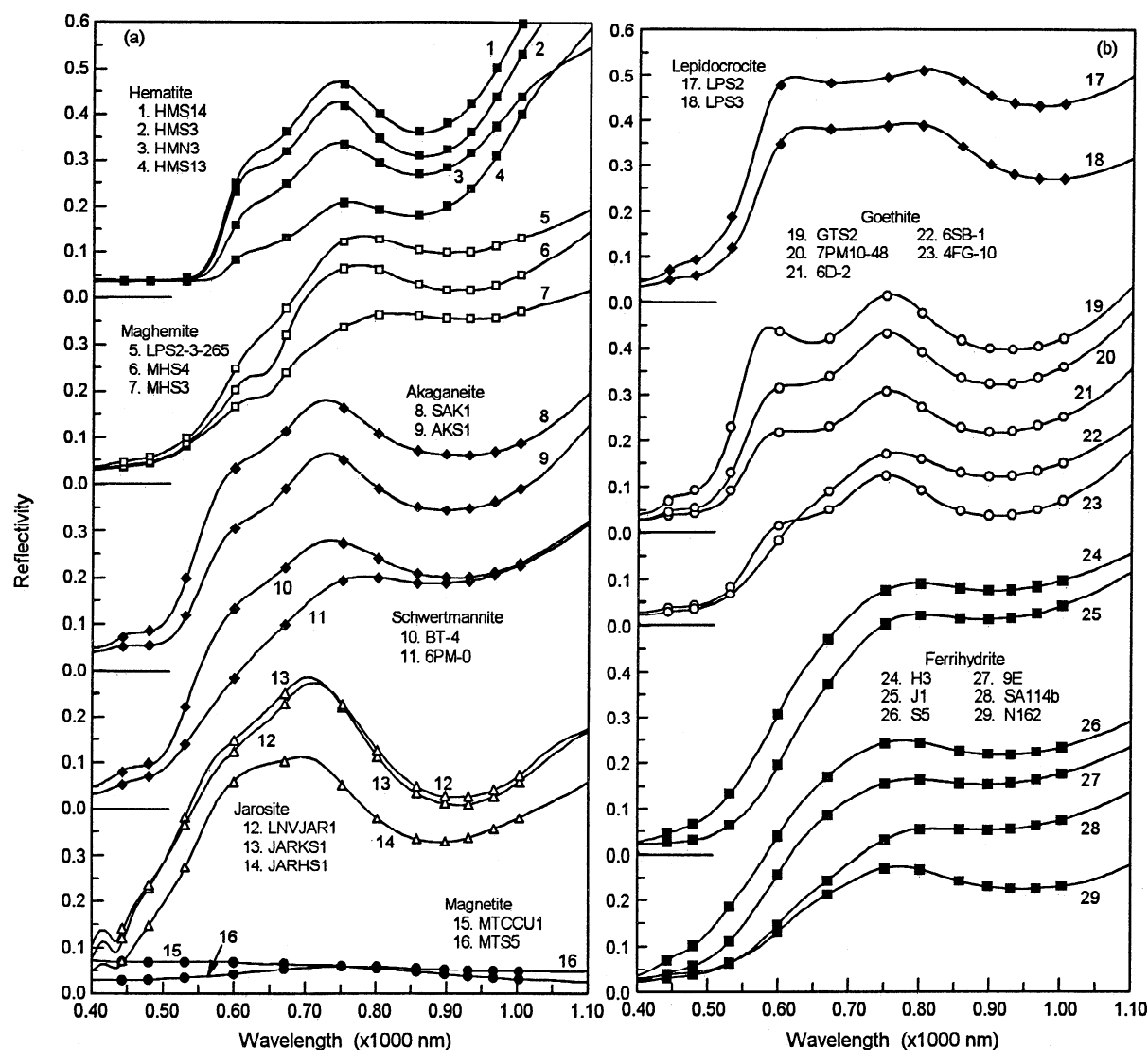


Table 4. Multispectral, Magnetic, and Chemical Data for Ferric Mineral Powders

Phase Type	Sample															
	HMN3	4D-1	6D-1	6D-2	6D-3	6F-1	6F-2	6F-3	4FG-10	7PM10-42	7PM10-46	7PM10-48	6SC-E2	6PM-0	MTCCU1	MTISH1
	Hm Nat.	Gt Nat.	Gt Nat.	Gt Nat.	Gt Nat.	Gt Nat.	Gt Nat.	Gt Nat.	Gt Nat.	Gt Nat.	Gt Nat.	Gt Nat.	Gt Nat.	Sch>Gt Nat.	Mt Nat.	Mt Nat.
Wavelength <sup>a</sup> , nm																
445	0.035	0.056	0.049	0.038	0.040	0.034	0.040	0.041	0.037	0.035	0.027	0.046	0.038	0.054	0.069	0.054
480	0.035	0.066	0.059	0.044	0.046	0.040	0.047	0.047	0.043	0.042	0.031	0.055	0.042	0.071	0.068	0.052
530	0.040	0.140	0.130	0.091	0.094	0.086	0.094	0.095	0.084	0.105	0.079	0.130	0.078	0.139	0.068	0.051
600	0.160	0.314	0.296	0.218	0.225	0.227	0.227	0.227	0.215	0.270	0.231	0.314	0.181	0.284	0.067	0.051
670	0.246	0.331	0.310	0.230	0.235	0.297	0.297	0.277	0.250	0.295	0.261	0.339	0.189	0.399	0.064	0.049
750	0.334	0.412	0.393	0.307	0.310	0.368	0.380	0.342	0.323	0.385	0.349	0.431	0.253	0.493	0.059	0.045
800	0.294	0.377	0.358	0.272	0.277	0.339	0.352	0.315	0.291	0.348	0.314	0.391	0.224	0.498	0.058	0.043
860	0.268	0.328	0.306	0.229	0.234	0.311	0.312	0.282	0.248	0.297	0.263	0.336	0.188	0.488	0.054	0.041
900	0.283	0.317	0.294	0.219	0.224	0.305	0.303	0.274	0.238	0.283	0.251	0.323	0.180	0.488	0.051	0.039
930	0.315	0.317	0.295	0.220	0.226	0.307	0.304	0.274	0.239	0.283	0.253	0.323	0.180	0.492	0.049	0.040
970	0.373	0.332	0.307	0.233	0.236	0.320	0.317	0.288	0.251	0.296	0.266	0.336	0.190	0.506	0.049	0.039
1005	0.437	0.352	0.328	0.251	0.254	0.342	0.339	0.310	0.270	0.318	0.288	0.360	0.205	0.525	0.047	0.036
Magnetic Properties																
J <sub>s</sub> , Am <sup>2</sup> /kg	1.72	0.392	0.036	0.016	0.029	0.036	0.000	0.061	0.022	0.012	0.020	0.008	0.035	0.000	63.0	82.6
χ <sub>16</sub> , 10 <sup>-6</sup> m <sup>3</sup> /kg	15.9	2.28	0.50	0.36	0.41	0.62	0.33	0.64	0.40	0.40	0.36	0.35	0.36	0.35	432	494
Chemical Composition, %																
SiO <sub>2</sub>	1.96	45.84	22.62	2.18	3.98	14.52	5.74	12.26	2.24	3.32	3.50	3.82	3.66	3.30	0.99	0.11
TiO <sub>2</sub>	0.18	0.14	0.22	0.04	0.08	0.18	0.08	0.09	0.04	0.06	0.06	0.06	0.08	0.06	0.11	0.05
Al <sub>2</sub> O <sub>3</sub>	0.96	7.88	2.4	0.6	0.7	0.8	1.1	1.1	0.5	0.8	0.9	0.7	1.5	1.2	0.51	0.46
Fe <sub>2</sub> O <sub>3</sub> ·T	95.55	42.89	71.64	95.11	92.46	81.43	90.83	82.66	92.58	94.71	94.25	94.85	91.40	93.47	95.22	98.46
MnO	0.10	0.02	0.02	0.00	0.00	0.02	0.00	0.00	0.00	0.00	0.00	0.00	0.00	0.00	0.74	0.04
MgO	0.12	0.38	0.36	0.28	0.36	0.36	0.28	0.29	0.12	0.14	0.14	0.14	0.32	0.16	1.38	0.08
CaO	0.14	0.18	0.18	0.16	0.28	0.46	0.16	0.25	0.10	0.10	0.10	0.10	0.20	0.12	0.47	0.13
Na <sub>2</sub> O	0.05	0.22	0.12	0.08	0.16	0.40	0.08	0.13	0.08	0.08	0.08	0.06	0.08	0.06	0.11	0.06
K <sub>2</sub> O	0.04	2.42	1.40	0.04	0.12	0.46	0.04	0.09	0.04	0.04	0.04	0.06	0.08	0.06	0.05	0.03
P <sub>2</sub> O <sub>5</sub>	0.15	0.06	0.08	0.08	0.20	0.08	0.08	0.09	3.81	0.02	0.02	0.04	0.56	0.18	0.08	0.06
V, μg/g	20	10	26	88	100	16	0	20	162	16	8	6	120	12	166	10
Cr, μg/g	254	34	134	64	152	82	12	44	124	64	84	184	80	78	20	10
Total	99.27	99.99	99.04	98.57	98.34	98.71	98.39	96.96	99.51	99.27	99.09	99.83	97.88	98.61	99.64	99.47
LOI	1.51	10.68	16.93	22.22	19.73	29.65	28.48	25.64	21.93	25.95	26.61	23.86	19.77	48.07	0.42	0.49
SO <sub>3</sub>	--	--	--	--	--	--	--	--	--	--	--	--	--	--	--	--
FeO	0.19	0.30	0.42	0.38	0.30	1.04	1.55	0.80	0.37	1.46	1.12	1.33	0.24	4.44	25.75	34.86
Fe <sub>2</sub> O <sub>3</sub>	95.34	42.56	71.17	94.69	92.13	80.27	89.11	81.77	92.17	93.09	93.01	93.37	91.13	88.54	66.61	59.72
Fe <sup>3+</sup> /Fe <sup>2+</sup>	452	128	152	224	276	69	52	92	224	57	75	63	342	89	2.33	1.54

<sup>a</sup>Values given for each wavelength are the reflectivity (equivalent IMP multispectral data).





**Figure 3.** Representative high-resolution and Imager for Mars Pathfinder (IMP)-equivalent spectral data (293 K) for ferric minerals. All minerals except magnetite have ferric absorption edges in the visible region (~445-750 nm) that are responsible for their color.

in 1996 when sample HWMK620 was taken as a surface sample from the same location.

All tephra samples discussed in this study are the <1-mm-size fraction or subsplits thereof. The <1-mm size fractions were obtained by dry sieving either during sample collection in the field or subsequently in the laboratory. The <150- $\mu$ m and the 150-1000- $\mu$ m size fractions of sample HWMK530 and <150- $\mu$ m size fraction of JSC Mars-1 were obtained by wet sieving in ethanol with rhodium-plated nickel sieves. The <149- $\mu$ m magnetic and nonmagnetic fractions were obtained by dry sieving with a stainless-steel sieve and using a hand magnet to divide the size separate into magnetic and nonmagnetic fractions. All size fractions reported as 500-1000, 53-500, 5-53, 2-5, <5, and <2  $\mu$ m were obtained by ultrasonication and sedimentation in water using procedures outlined by M. L. Jackson (Soil Chemical Analysis: Advanced Course, 895 pp., 1985; published by the author). Typically, the amount of <1-mm tephra that is <5  $\mu$ m is ~5%. For tephra HWMK600, size fractions between 1000 and 2  $\mu$ m and <2  $\mu$ m (A) were obtained using normal ultrasonication

procedures; size fraction <2  $\mu$ m (B) was obtained using aggressive ultrasonication to obtain sufficient material to do major element analyses.

## 5.2. Alteration Processes

Multispectral, magnetic, and elemental data for the Mauna Kea tephra samples are compiled in Tables 6-8. On the basis of chemical data, the tephra samples are classified into three groups according to the type of alteration process. Figure 5a is a plot of LOI (weight loss on ignition at ~950°C) versus  $\text{SO}_3$  concentration for <1-mm size fraction of tephra. LOI in air at 950°C would include loss of adsorbed  $\text{H}_2\text{O}$  and volatile loss from decomposition of hydrous (e.g., phyllosilicates and oxyhydroxides), carbon-bearing (e.g., carbonates), and sulfur-bearing (e.g., sulfates) phases. The dashed lines refer to different LOI/ $\text{SO}_3$  ratios, with a value of 1.0 corresponding to the case where  $\text{SO}_3$  is the only volatile species. The tephra samples fall into three distinct groups. The first group (six samples) is volatile

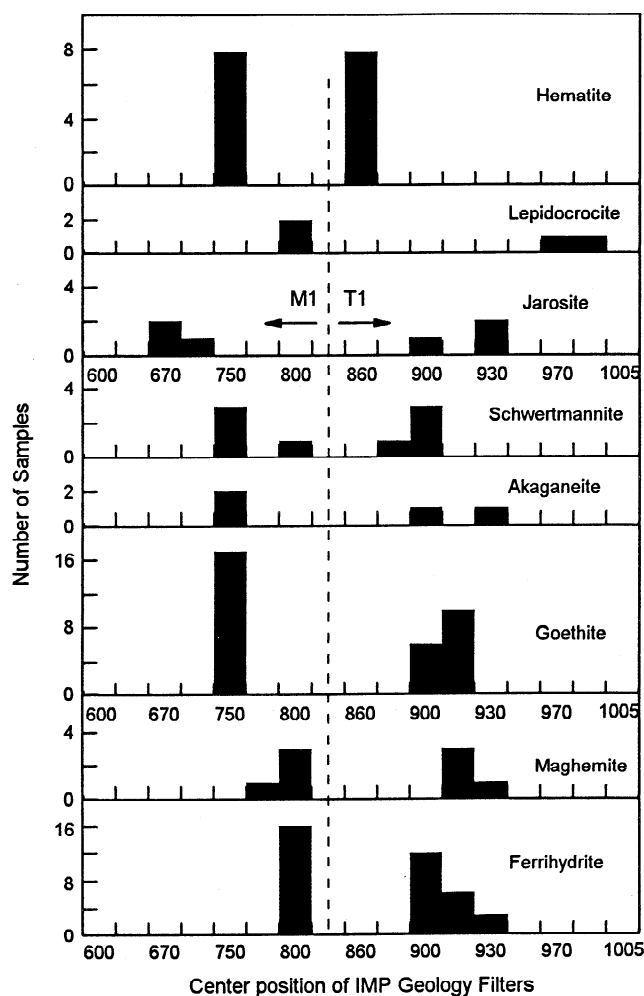


**Figure 4.** Histograms showing positions of the M1 (reflectivity maximum) and T1 (reflectivity minimum) spectral features derived from IMP-equivalent spectra for ferric minerals. The T1 values of hematite (860 nm) and lepidocrocite (970-985 nm) and the M1 value of jarosite (670-710 nm) are specific for those minerals. The other oxides divide into two groups on the basis of M1-T1 values. One is schwertmannite, akaganéite, and goethite with M1 and T1 values of 750 nm (one exception) and 880-930 nm, respectively. The other is maghemite and ferrihydrite with M1 and T1 values of 775-800 nm (one exception) and 900-930 nm.

poor ( $\text{LOI} < 3\%$  and  $\text{SO}_3 < 0.15\%$ ), which implies either little or no alteration by uptake of volatiles or alteration by dry heating (calcination) to induce oxidation and/or devolatilization. The former is the case for our six samples, as shown by low values of  $\text{LOI}$  and  $\text{Fe}^{3+}/\text{Fe}^{2+}$  (Figures 5b and 5c).

The second group has high concentrations of  $\text{SO}_3$  ( $\text{SO}_3 > 0.6\%$  and  $1 < (\text{LOI}/\text{SO}_3) < 6$ ), which implies sulfuric (or acid sulfate) alteration process. The most  $\text{SO}_3$ -rich sample (HWMK24) is described by Morris *et al.* [1996] as a product of acid-sulfate alteration with K-rich jarosite  $((\text{K}, \text{Na}, \text{H}_3\text{O})\text{Fe}_3(\text{SO}_4)_2(\text{OH})_6)$  as the primary iron-bearing alteration product. This conclusion is supported by the chemical data. The observed value of  $\text{LOI}/\text{SO}_3$  for this sample (1.6) is slightly larger than the value calculated (1.4) assuming K-jarosite is the only volatile bearing phase. The high  $\text{SO}_3$  concentrations for this group imply that they all contain products of sulfuric alteration, with the concentration of  $\text{SO}_3$

varying in proportion with the extent of alteration. By analogy with HWMK24, sulfuric alteration probably occurred when solutions rich in sulfuric acid ( $\text{H}_2\text{SO}_4$ ) percolated through unaltered tephra. Because there are no known sulfide deposits on Mauna Kea, the only viable source of the acid is  $\text{SO}_2$ -rich volcanic gas, which dissolves in  $\text{H}_2\text{O}$  to form the  $\text{H}_2\text{SO}_3$  that subsequently undergoes oxidation to sulfuric acid.

The third group has low concentrations of  $\text{SO}_3$  and high concentrations of  $\text{H}_2\text{O}$  ( $\text{SO}_3 < 0.4\%$  and  $\text{LOI}/\text{SO}_3 > 40$ ), which implies that hydrolytic alteration dominates. This group includes PN-9 and HWMK530, which are described [Morris *et al.*, 1993, 1997] as palagonitic tephra. Palagonite is the (hydrolytic) alteration product of basaltic glass and corresponds to the yellow isotropic glass-like phase observed in thin section (for HWMK1 see Morris *et al.* [1990]) and, at a smaller scale, the nanophase ferric oxide particles imbedded in a noncrystalline aluminosilicate matrix as observed in TEM analyses (for PN-9, see Morris *et al.* [1993]).

Because we do not have  $\text{SO}_3$  abundances for all samples, we are unable to classify all our samples according to Figure 5a. We found, however, that the  $\text{K}_2\text{O}/\text{MgO}$  ratio could be used instead, as shown in Figure 5b. None of the samples cross groups between Figures 5a and 5b, and all samples plot in one of the three groups. We also include in Figure 5b all size fractions that include material finer than  $53 \mu\text{m}$ . Because alteration processes tend to produce finer-grained material, these smaller size fractions tend to emphasize alteration products and thus confirm our alteration classification. As will be discussed in more detail later, the ratio  $\text{K}_2\text{O}/\text{MgO}$  works as an indicator of alteration process because alkalis are preferentially lost during hydrolytic alteration because of their high solubility but are retained in sulfuric alteration because of formation of insoluble sulfates (jarosite). The converse is true for  $\text{MgO}$ , which forms highly soluble sulfates. Figure 5c is a plot of the  $\text{Fe}^{3+}/\text{Fe}^{2+}$  ratio versus the  $\text{K}_2\text{O}/\text{MgO}$  ratio. As expected for oxidative alteration, unaltered tephra have low values of  $\text{Fe}^{3+}/\text{Fe}^{2+}$  (0.5-1.0), and palagonitic and sulfatetic tephra have high values (1.0-20).

In the above discussion, Mauna Kea tephra were classified according to alteration processes using chemical data for bulk ( $< 1\text{-mm}$ ) samples. It would be possible for a tephra to appear heavily altered with respect to a surface-sensitive technique like reflectance spectroscopy, but be unaltered with respect to bulk chemical analyses, if the alteration were confined to the skin of the tephra particles. Similarly, tephra heavily altered by one process subsequently could acquire a skin of alteration products from a different process. It will be evident in the discussions that follow that, in general, the classification developed from bulk chemical analyses is invariant with respect to analytical technique.

### 5.3. Chemistry and Mineralogy

In the field, unaltered tephra and palagonitic (hydrolytic) samples are recognized by their black and yellow-brown color, respectively. Sulfatetic tephra comes in a variety of colors, including white, green, yellow, orange, and red. The colors correspond to differences in the iron mineralogy of the tephra, as discussed next.

**5.3.1. Unaltered tephra.** The compositional parameters for the six chemically unaltered tephra (HWMK12, HWMK22, HWMK506, HWMK513, IWMK514, and PH-13) are listed in Table 6. As shown in Figure 6a, their compositional parameters are relatively constant. This figure is a semilogarithmic plot of

**Table 5.** Listing of Volcanic Tephra, Steam Vent, and Rock Samples, Their Origin, and Previous Work

Sample Name	Collection Site and References
<i>Volcanic Tephra</i>	
HWHP301	Mauna Kea; gully north of Visitor's Center (2830 m); unit laf
HWMK1	Mauna Kea; gully near Visitor's Center (2830 m); unit laf; <i>Morris et al.</i> [1990]
HWMK11 and HWMK12	Mauna Kea; switchback to summit telescopes (4080 m); unit loc; <i>Golden et al.</i> [1993]
HWMK20 through HWMK24	Mauna Kea; summit near Subaru telescope (4100 m); unit loc; <i>Morris et al.</i> [1996]
HWMK501 through HWMK517 and HWMK620	Mauna Kea; summit near Gemini telescope (4190 m); unit loc
HWMK530	Mauna Kea; Puu Kilohana cinder cone (WNW of Visitor's Center), north flank (2890 m); unit loc; <i>Morris et al.</i> [1997]
HWMK600 through HWMK605 and HWMK612	Mauna Kea; south side of VLBA road, near telescope (3730 m); unit lmt
HWMK606	Mauna Kea; north side of VLBA road, near telescope (3730 m); unit lmt
JSC Mars-1	Mauna Kea; Puu Nene cinder cone (2010 m); unit loc; <i>Allen et al.</i> [1998a,b]
PH-13	Mauna Kea; Puu Huluhulu cinder cone (2010 m); unit loc
PN-9	Mauna Kea; Puu Nene cinder cone (2010 m); unit loc; <i>Morris et al.</i> [1993]
<i>Steam Vent</i>	
HWSB501 and HWSB531 through HWSB536	Kilauea; Sulfur Bank steam vents (1200 m)
HWMU387	Kilauea, Mauna Ulu steam vent (980 m)
<i>Rocks</i>	
M1497	Basaltic komatiite, Munroe Township, Canada
WD232	Basalt, Meridan, Connecticut; obtained from Wards Scientific

Elevation of collection sites is given in parenthesis. Subaru, Japan National Subaru Telescope; Gemini, Gemini Telescope; VLBA, Very Long Baseline Array Telescope. Mauna Kea geologic map units (all Laupahoehoe Volcanics) are from *Wolfe et al.* [1997] as follows: laf, air-fall deposits; lmt, glacial till; loc, cinder cones.

the ratio of the value for a compositional parameter (e.g., SiO<sub>2</sub> concentration) to its average value for all seven unaltered tephra samples (average unaltered hawaiitic tephra (AUHT)) for each compositional parameter. The compositional parameters are all constant to within factors of 0.90 to 1.13, except for LOI and Fe<sup>3+</sup>/Fe<sup>2+</sup> whose sample/AUHT ratios vary from 0.76 to 1.57. The average chemical composition of the unaltered tephra samples is very similar to the major element chemistry of hawaiitic basalt HAW-16 [*Basaltic Volcanism Study Project*, 1981] and high-Fe hawaiitic lava [*West et al.*, 1988].

As shown by the Mössbauer spectra for HWMK12 and PH-13 in Figure 7, iron is associated with glass and the crystalline phases olivine and Fe-Ti spinel. The glass contains both Fe<sup>3+</sup> and Fe<sup>2+</sup> in octahedral coordination. The relative proportion of iron in glassy and crystalline phases is different in HWMK12 and PH-13 (e.g., the olivine doublet is relatively more intense in the former), suggesting that the ratio of glassy to crystalline phases deposited during ash eruptions is variable. In support of this view are petrographic observations of palagonitic tephra HWMK1 [*Morris et al.*, 1990], which show that the tephra is composed of two basic types of composite particles (black and orange in color) that differ principally in the degree of crystallinity of the mesostasis component. Black particles are vesicular fragments of tachylite (nearly opaque, microcrystalline basalt) with abundant microphenocrysts of plagioclase, minor olivine, and trace pyroxene. Tachylite particles are black because the unaltered mesostasis contains abundant Fe-Ti oxides as disseminated grains <20 µm in size. TEM observations of similar Hawaiian palagonitic tephra [*Morris et al.*, 1993; *Golden et al.*, 1998] indicate that particle diameters of disseminated Fe-Ti oxides extend down to ~5-30 nm. Orange particles consist of highly palagonitized sideromelane (clear, brown, basaltic glass) with the same microphenocryst population as the tachylite particles. Unlike tachylite particles, palagonitized sideromelane particles do not contain appreciable disseminated Fe-Ti oxides; some

contain one or more large (50-150 µm) Fe-Ti oxide grains. Tachylite and sideromelane particles apparently coevolve through ash eruptions where conditions favor formation of both crystalline and glassy particles in different proportions from magma that has already crystallized plagioclase, olivine, and the larger iron oxide particles. The disseminated Fe-Ti oxide grains probably formed during cooling of tachylite particles (quench crystals). A similar origin is proposed for the small Fe-Ti oxide particles reported in volcanic ash samples from other locations and in the glassy parts of mid-ocean ridge basalts [e.g., *Heidner et al.*, 1993; *Pick and Tauxe*, 1994]. Variations in the amount of alteration products within tephra deposits that are aqueously altered at low temperatures are likely controlled by local values of the sideromelane to tachylite ratio, because sideromelane-rich particles are more susceptible to aqueous alteration than the largely crystalline tachylite particles.

Electron microprobe analyses of HWMK1, HWMK12, and PN-9 and literature data for hawaiitic lava show that Fe-Ti spinel particles generally have Ti/Fe weight ratios between 0.18 and 0.32 and also contain minor Mg and Al as impurities [*Morris et al.*, 1993], although oxide grains with compositions approaching ulvöspinel and ilmenite are also present [*Morris et al.*, 1990]. XRD data (Figure 8a) show that plagioclase feldspar is the dominant crystalline phase in unaltered tephra.

IMP-equivalent multispectral data for unaltered tephra are shown in Figure 9. The reflectivity is always <0.08 and, except for HWMK506 and HWMK514, nearly constant. The weak ferric absorption edges for HWMK506 and HWMK514 and absence of chemical alteration (including low Fe<sup>3+</sup>/Fe<sup>2+</sup> ratios) imply minor oxidation at particle surfaces for these two tephra. The low and uniform reflectivity of nonmagnetic (sideromelane-rich) and magnetic (tachylite-rich) fractions of HWMK513 shows that the sideromelane to tachylite ratio does not have significant influence on the spectral properties of unaltered tephra.

**5.3.2. Palagonitic tephra.** The compositional parameters for

**Table 6.** Multispectral, Magnetic, and Chemical Data for Chemically Unaltered Tephra from Mauna Kea Volcano

	Sample							PH-13 <1 mm Puu Hulululu	Average Unaltered Hawaiitic Tephra
	HWMK12	HWMK22	HWMK506	HWMK513	HWMK513, Gemini		HWMK514		
	Switchback <1 mm	Subaru <1 mm	Gemini <1 mm	Gemini <1 mm	<1mm magnetic	<1mm nonmagnetic	Gemini <1 mm		
Wavelength <sup>a</sup> , nm									
445	0.082	0.042	0.031	0.032	0.027	0.032	0.036	0.034	--
480	0.082	0.042	0.031	0.030	0.027	0.032	0.036	0.034	--
530	0.082	0.045	0.032	0.030	0.027	0.033	0.038	0.034	--
600	0.082	0.050	0.057	0.030	0.027	0.033	0.056	0.033	--
670	0.077	0.048	0.067	0.032	0.028	0.035	0.073	0.032	--
750	0.073	0.048	0.068	0.031	0.028	0.036	0.074	0.036	--
800	0.073	0.045	0.063	0.029	0.026	0.035	0.072	0.033	--
860	0.072	0.045	0.061	0.029	0.024	0.035	0.069	0.030	--
900	0.069	0.043	0.060	0.027	0.025	0.035	0.069	0.030	--
930	0.064	0.042	0.063	0.028	0.026	0.036	0.069	0.027	--
970	0.064	0.043	0.060	0.027	0.024	0.034	0.070	0.030	--
1005	0.065	0.042	0.059	0.028	0.024	0.035	0.073	0.029	--
Magnetic Properties									
$J_s$ , Am <sup>2</sup> /kg	1.29	0.76	1.30	0.85	4.33	0.16	0.71	0.64	0.92
$\chi_{lf}$ , 10 <sup>-6</sup> m <sup>3</sup> /kg	11.3	6.5	11.7	11.9	74.5	1.40	11.1	6.4	9.8
Chemical Composition, %									
SiO <sub>2</sub>	49.25	49.99	49.69	49.44	44.80	50.48	49.47	50.57	49.74
TiO <sub>2</sub>	2.94	2.72	2.82	2.81	4.27	2.57	2.81	2.54	2.77
Al <sub>2</sub> O <sub>3</sub>	17.25	17.50	17.40	17.30	15.61	17.84	17.36	17.31	17.35
Fe <sub>2</sub> O <sub>3</sub> T	12.15	12.16	12.28	11.89	17.92	10.59	12.26	11.43	12.03
MnO	0.20	0.21	0.21	0.21	0.24	0.20	0.21	0.22	0.21
MgO	4.45	3.71	3.82	4.23	4.65	3.79	3.53	3.83	3.93
CaO	6.84	6.53	6.26	6.66	5.89	6.98	6.69	6.59	6.60
Na <sub>2</sub> O	4.17	4.34	4.51	4.43	3.67	4.29	4.19	4.34	4.33
K <sub>2</sub> O	1.78	1.90	1.94	1.91	1.71	1.83	1.88	1.91	1.90
P <sub>2</sub> O <sub>5</sub>	0.79	0.87	0.84	0.84	0.78	0.82	0.86	0.91	0.85
V, µg/g	140	119	132	135	240	101	118	110	126
Cr, µg/g	20	15	15	17	<10	<10	55	13	23
Total	99.82	99.93	99.77	99.72	99.54	99.38	99.26	99.73	99.71
LOI	2.50	1.77	1.37	1.20	0.97	1.31	1.45	1.29	1.60
SO <sub>3</sub>	0.088	0.103	0.103	0.090			0.090	0.092	0.094
FeO	5.84	6.12	5.86	6.59	9.86	5.94	6.46	5.26	6.02
Fe <sub>2</sub> O <sub>3</sub>	5.66	5.36	5.77	4.57	6.96	3.99	5.08	5.58	5.34
Fe <sup>3+</sup> /Fe <sup>2+</sup>	0.872	0.788	0.886	0.624	0.635	0.604	0.708	0.955	0.797

<sup>a</sup>Values given for each wavelength are the reflectivity (equivalent IMP multispectral data).

palagonitic tephra are given in Table 7 and their variations relative to average unaltered hawaiitic tephra (AUHT) for all samples (<1-mm size fractions) are shown in Figure 6b. Relative to AUHT, palagonitic tephra are oxidized and rich in water. They are also systematically depleted (relative to volatile-free compositions) in SiO<sub>2</sub>, CaO, and the alkali metals (K<sub>2</sub>O and Na<sub>2</sub>O) and enriched in TiO<sub>2</sub>, Al<sub>2</sub>O<sub>3</sub>, Fe<sub>2</sub>O<sub>3</sub>T, and MnO. MgO and P<sub>2</sub>O<sub>5</sub> are enriched in some samples and depleted in others. The relatively high dispersion for MgO compared to other major elements suggests variability in the MgO concentration of the precursor materials. The chemical fractionation trends that occur during formation of palagonitic tephra by hydrolytic alteration are more evident in Figure 6c, where the average of the four samples (<1 mm) with the lowest SiO<sub>2</sub> and K<sub>2</sub>O concentrations is plotted.

Chemical fractionation is usually observed in palagonitic materials [e.g., Jakobsson, 1972; Ailin-Pyzik and Sommer, 1981; Staudigel and Hart, 1983; Eggleton et al., 1987; Jercinovic et al., 1990; Thorseth et al., 1991; Morris et al., 1993]. SiO<sub>2</sub> and alkali loss to aqueous solutions (leaching) usually results where meteoric water is involved. In marine environments, alkali loss is reduced, and enrichments (e.g., K<sub>2</sub>O and MgO) are sometimes observed, presumably in response to the higher alkali content in

seawater relative to meteoric water. Al<sub>2</sub>O<sub>3</sub> is apparently enriched or depleted depending on acidity. According to Thorseth et al [1991], oxidizing environments and pH >3 are required for retention (precipitation) of Al<sub>2</sub>O<sub>3</sub>, TiO<sub>2</sub>, and Fe<sub>2</sub>O<sub>3</sub>T. Our samples probably represent the relatively simple case where leaching by meteoric water (from rain and snow) under oxidizing conditions (high Fe<sup>3+</sup>/Fe<sup>2+</sup> in palagonitic tephra) preferentially removes soluble SiO<sub>2</sub>, MgO, CaO, and alkalis and leaves behind (passive enrichment) insoluble phases containing TiO<sub>2</sub>, Al<sub>2</sub>O<sub>3</sub>, Fe<sub>2</sub>O<sub>3</sub>T, MnO, and P<sub>2</sub>O<sub>5</sub>.

Also shown in Figure 6c are data for the <2-µm size fraction of palagonitic tephra HWP301 and HWMK600. Except for MgO and P<sub>2</sub>O<sub>5</sub>, the major elements are fractionated to a greater extreme, but in the same direction, as for the <1-mm size fraction. MgO is highly depleted and P<sub>2</sub>O<sub>5</sub> is highly enriched in the <2-µm size fraction. Because the <2-µm size fraction is dominated by fine-grained alteration products, we attribute differences in behavior between the <1-mm and <2-µm size fractions to high MgO solubility but slow dissolution kinetics of MgO-rich phases. Slow dissolution kinetics relative to SiO<sub>2</sub> and the other depleted elements in the <1-mm size fraction produce the observed passive enrichment of MgO in that size fraction.

Table 7. Multispectral, Magnetic, and Chemical Data for Palagonitic Tephra from Mauna Kea Volcano

Wavelength <sup>a</sup> , nm	HWP301				HWMK1				HWMK530 Puu Kihohana				HWMK600 VLBA				HWMK- 602				HWMK- 604			
	Gully N. of Visitor's Center				Visit. Ctr.				150-				53-				VLBA				VLBA			
	<1 mm	5-53 $\mu$ m	<2 $\mu$ m	<1 mm	<1 mm	<1 mm	<1 mm	<1 mm	<1 mm	1000 $\mu$ m	<150 $\mu$ m	<5 $\mu$ m	<1 mm	500- 1000 $\mu$ m	53- 500 $\mu$ m	5-53 $\mu$ m	2-5 $\mu$ m	<2 $\mu$ m (A)	<2 $\mu$ m (B)	<1 mm	<1 mm	<1 mm	<1 mm	<1 mm
445	0.066	0.064	0.096	0.055	0.057	0.051	0.066	0.071	0.070	0.064	0.048	0.048	0.079	0.111	0.096	0.042	0.056							
480	0.082	0.079	0.121	0.067	0.071	0.056	0.084	0.093	0.085	0.072	0.051	0.051	0.107	0.144	0.128	0.046	0.063							
530	0.126	0.121	0.174	0.099	0.103	0.069	0.127	0.153	0.123	0.089	0.060	0.060	0.184	0.221	0.202	0.057	0.083							
600	0.196	0.197	0.241	0.144	0.161	0.096	0.207	0.266	0.192	0.119	0.082	0.082	0.330	0.353	0.324	0.082	0.120							
670	0.248	0.256	0.286	0.174	0.203	0.115	0.258	0.347	0.230	0.134	0.093	0.093	0.423	0.434	0.396	0.097	0.142							
750	0.276	0.292	0.308	0.186	0.225	0.126	0.292	0.403	0.252	0.144	0.105	0.105	0.478	0.481	0.432	0.102	0.157							
800	0.280	0.299	0.309	0.183	0.227	0.124	0.299	0.413	0.254	0.145	0.106	0.106	0.489	0.492	0.435	0.100	0.157							
860	0.276	0.299	0.304	0.177	0.226	0.121	0.299	0.419	0.250	0.141	0.105	0.105	0.494	0.493	0.431	0.098	0.155							
900	0.273	0.297	0.298	0.174	0.227	0.121	0.298	0.423	0.250	0.138	0.103	0.103	0.494	0.494	0.430	0.095	0.153							
930	0.272	0.296	0.294	0.170	0.225	0.119	0.297	0.425	0.251	0.137	0.104	0.104	0.494	0.494	0.429	0.095	0.153							
970	0.270	0.292	0.289	0.170	0.228	0.123	0.300	0.428	0.249	0.137	0.106	0.106	0.498	0.494	0.427	0.092	0.154							
1005	0.270	0.294	0.282	0.168	0.228	0.121	0.300	0.430	0.250	0.138	0.108	0.108	0.502	0.497	0.425	0.094	0.156							
Magnetic Properties																								
$J_s$ , Am <sup>2</sup> /kg	0.99	0.74	0.68	1.02	1.24	1.25	1.05	0.57	1.16	1.23	1.56	1.56	0.42	0.37	0.65	1.14	1.22							
$\chi_{10^{-6}}$ m <sup>3</sup> /kg	13.6	14.0	15.5	14.0	10.8	10.3	10.8	8.5	12.1	9.7	13.4	13.4	7.5	5.0	9.0	12.0	10.5							
Chemical Composition, %																								
SiO <sub>2</sub>	39.66	38.82	30.19	41.16	45.73	46.80	44.54	--	46.60	47.76	46.88	46.88	41.24	--	31.44	48.22	47.42							
TiO <sub>2</sub>	3.99	3.87	5.30	4.13	2.82	2.60	3.23	--	3.00	2.80	2.98	2.98	3.62	--	5.58	2.81	2.94							
Al <sub>2</sub> O <sub>3</sub>	23.41	26.21	36.90	22.85	18.22	16.68	21.21	--	20.01	19.41	18.11	18.11	25.00	--	33.28	19.15	19.74							
Fe <sub>2</sub> O <sub>3</sub> T	17.29	17.10	20.01	16.91	13.98	13.46	14.73	--	13.58	12.59	13.94	13.94	15.66	--	20.48	12.67	13.47							
MnO	0.31	0.31	0.54	0.28	0.23	0.22	0.25	--	0.25	0.24	0.24	0.24	0.29	--	0.36	0.23	0.24							
MgO	5.98	5.25	1.67	4.98	7.23	8.21	4.62	--	4.32	4.07	5.09	5.09	3.52	--	1.62	3.85	4.07							
CaO	5.47	5.04	1.70	5.41	6.41	6.67	5.89	--	5.94	6.18	6.16	6.16	5.11	--	2.58	6.11	5.9							
Na <sub>2</sub> O	2.29	1.93	0.80	2.52	3.33	3.19	3.24	--	3.95	4.38	4.07	4.07	2.74	--	1.54	4.16	3.84							
K <sub>2</sub> O	0.52	0.32	0.22	0.56	1.03	1.07	0.92	--	1.38	1.51	1.43	1.43	0.67	--	0.45	1.64	1.42							
P <sub>2</sub> O <sub>5</sub>	0.87	1.02	2.53	0.81	0.85	0.75	1.04	--	0.97	0.92	0.80	0.80	1.34	--	2.57	0.94	0.98							
V, $\mu$ g/g	232	194	200	177	148	127	157	--	129	128	153	153	165	--	281	124	127							
Cr, $\mu$ g/g	167	175	70	86	296	372	138	--	67	38	84	84	103	--	50	43	55							
Total	99.79	99.87	99.86	99.61	99.83	99.65	99.67	--	100.00	99.86	99.70	99.70	99.19	--	99.90	99.78	100.02							
LOI	15.57	18.03	30.77	13.19	5.40	3.40	9.06	--	5.28	3.27	2.65	2.65	13.89	--	22.71	3.75	4.81							
SO <sub>3</sub>	--	--	--	--	0.118	--	--	0.224	0.109	--	--	--	--	--	--	--	--							
FeO	6.71	5.22	2.57	5.57	5.36	5.72	5.01	--	4.17	3.98	5.28	5.28	2.77	--	4.54	4.90	4.31							
Fe <sub>2</sub> O <sub>3</sub>	9.82	11.30	17.15	10.72	8.02	7.10	9.16	--	8.95	8.17	8.07	8.07	12.58	--	15.43	7.22	8.68							
Fe <sup>3+</sup> /Fe <sup>2+</sup>	1.32	1.95	6.67	1.73	1.35	1.12	1.64	--	1.93	1.85	1.38	1.38	4.09	--	3.06	1.33	1.81							

Table 7. (continued)

Wavelength <sup>a</sup> , nm	HWMK-605 VLBA		HWMK-606 VLBA		HWMK612 VLBA		JSC Mars-1 Puu Nene						PN-9 Puu Nene			
	<1 mm	5-53 μm	<1 mm	5-53 μm	<2 μm	500-1000 μm			53-500 μm	5-53 μm	2-5 μm	<2 μm	<149 μm		<1 mm	<2 μm
						<1 mm	53-500 μm	5-53 μm					magnetic	nonmagnetic		
445	0.055	0.068	0.070	0.054	0.087	0.048	0.043	0.043	0.042	0.055	0.074	0.042	0.044	0.048	0.037	0.081
480	0.065	0.091	0.083	0.069	0.112	0.059	0.052	0.053	0.055	0.077	0.103	0.052	0.052	0.060	0.047	0.111
530	0.093	0.153	0.118	0.112	0.166	0.096	0.082	0.085	0.098	0.145	0.184	0.088	0.076	0.101	0.088	0.194
600	0.147	0.270	0.173	0.194	0.234	0.161	0.135	0.143	0.185	0.261	0.306	0.153	0.110	0.177	0.161	0.313
670	0.179	0.348	0.209	0.253	0.277	0.219	0.179	0.194	0.274	0.364	0.408	0.214	0.130	0.251	0.223	0.402
750	0.195	0.389	0.227	0.286	0.301	0.262	0.208	0.228	0.358	0.454	0.492	0.263	0.143	0.317	0.271	0.471
800	0.198	0.399	0.227	0.290	0.302	0.268	0.213	0.235	0.388	0.488	0.522	0.275	0.142	0.336	0.282	0.487
860	0.196	0.399	0.224	0.288	0.295	0.268	0.211	0.231	0.402	0.507	0.537	0.279	0.138	0.343	0.281	0.496
900	0.194	0.400	0.221	0.286	0.291	0.268	0.208	0.229	0.410	0.517	0.544	0.280	0.134	0.346	0.280	0.499
930	0.194	0.400	0.219	0.285	0.285	0.267	0.206	0.228	0.416	0.523	0.550	0.282	0.133	0.350	0.281	0.502
970	0.194	0.401	0.217	0.284	0.283	0.268	0.208	0.230	0.424	0.534	0.557	0.284	0.130	0.356	0.284	0.505
1005	0.196	0.404	0.216	0.284	0.278	0.272	0.210	0.232	0.432	0.542	0.565	0.289	0.129	0.363	0.287	0.509
Magnetic Properties																
$J_s$ , Am <sup>2</sup> /kg	1.11	1.00	1.06	0.74	0.67	0.65	0.57	0.66	0.23	0.30	0.19	0.47	1.72	0.099	0.85	0.30
$\chi_{ir}$ , 10 <sup>-6</sup> m <sup>3</sup> /kg	10.8	9.1	13.4	13.9	13.4	7.5	8.7	8.2	3.5	3.8	3.4	5.9	19.1	1.46	8.5	4.3
Chemical Composition, %																
SiO <sub>2</sub>	47.08	44.07	41.53	39.00	--	43.75	44.75	43.42	38.72	--	--	42.21	45.66	43.52	43.48	--
TiO <sub>2</sub>	2.98	3.32	3.92	4.24	--	3.66	3.75	3.64	3.66	--	--	3.56	3.50	3.24	3.61	--
Al <sub>2</sub> O <sub>3</sub>	19.83	23.11	22.69	25.96	--	22.72	21.88	22.35	28.01	--	--	24.29	18.53	24.54	21.59	--
Fe <sub>2</sub> O <sub>3</sub> T	13.63	14.76	16.74	17.72	--	16.18	15.43	16.02	19.24	--	--	16.71	16.30	16.20	16.08	--
MnO	0.24	0.29	0.28	0.28	--	0.27	0.24	0.27	0.45	--	--	0.32	0.28	0.35	0.25	--
MgO	4.01	3.49	5.00	4.62	--	3.69	3.51	3.88	1.73	--	--	3.36	4.85	3.38	4.78	--
CaO	5.84	5.06	5.60	4.78	--	5.97	5.89	6.03	5.32	--	--	5.86	6.21	5.37	6.17	--
Na <sub>2</sub> O	3.75	3.36	2.55	1.97	--	2.31	2.75	2.34	1.06	--	--	1.92	2.76	1.37	2.39	--
K <sub>2</sub> O	1.41	1.11	0.59	0.29	--	0.73	0.82	0.61	0.29	--	--	0.54	0.88	0.49	0.68	--
P <sub>2</sub> O <sub>5</sub>	1.01	1.11	0.81	0.96	--	0.79	0.74	0.76	1.38	--	--	0.93	0.71	0.93	0.78	--
V, μg/g	128	130	180	--	--	180	158	189	190	--	--	188	179	148	165	--
Cr, μg/g	71	101	97	--	--	138	92	153	128	--	--	136	310	246	206	--
Total	99.78	99.68	99.71	99.82	--	100.07	99.76	99.32	99.86	--	--	99.70	99.68	99.39	99.81	--
LOI	5.17	10.61	13.14	16.97	--	18.08	13.38	15.75	29.81	--	--	22.71	9.66	24.89	16.63	--
SO <sub>3</sub>	--	--	--	--	--	--	--	--	--	--	--	--	--	--	0.315	--
FeO	4.18	2.60	5.66	4.73	--	3.57	3.28	3.42	1.98	--	--	2.40	5.58	2.29	4.02	--
Fe <sub>2</sub> O <sub>3</sub>	8.98	11.87	10.45	12.46	--	12.21	11.78	12.22	17.04	--	--	14.04	10.10	13.66	11.61	--
Fe <sup>3+</sup> /Fe <sup>2+</sup>	1.93	4.11	1.66	2.37	--	3.08	3.23	3.22	7.74	--	--	5.26	1.63	5.37	2.60	--

<sup>a</sup>Values given for each wavelength are the reflectivity (equivalent IMP multispectral data).

Table 8. Multispectral, Magnetic, and Chemical Data for Sulfate-rich Tephra from Mauna Kea Volcano

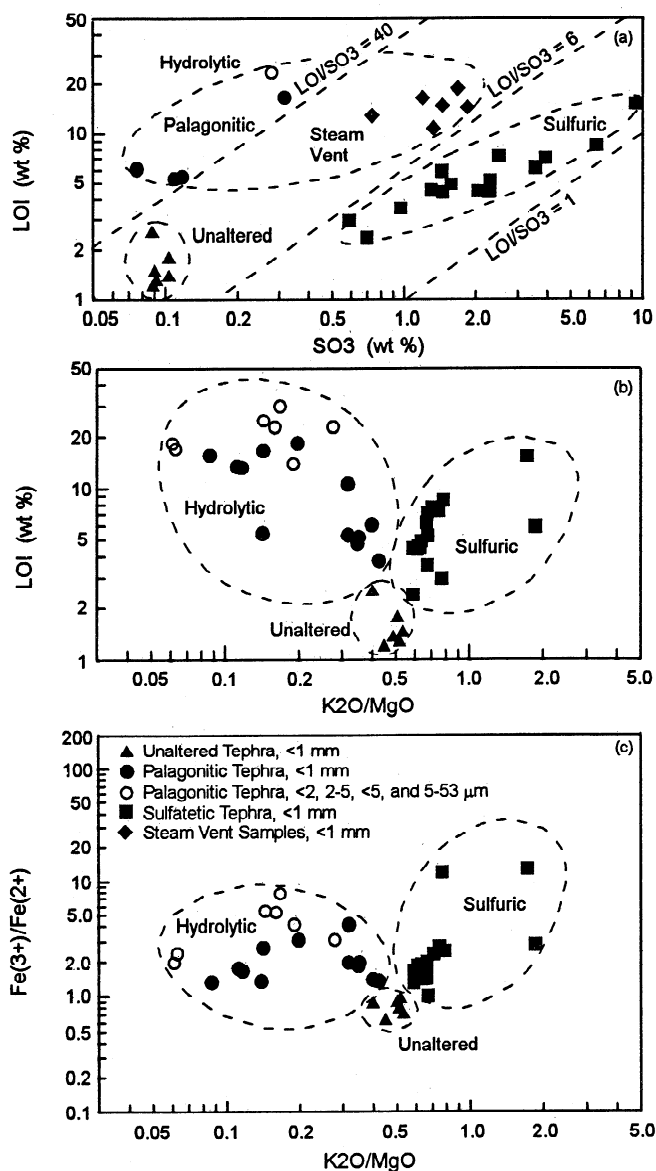
Wavelength <sup>a</sup> , nm	HWMK20		HWMK24		HWMK26		HWMK-501		HWMK-502		HWMK-503		HWMK-504		HWMK-505		HWMK-507	
	Subaru	<1 mm	Subaru	<5 µm	Gemini	<1 mm	Gemini	<1 mm	Gemini	<1 mm	Gemini	<1 mm	Gemini	<1 mm	Gemini	<1 mm	Gemini	<5 µm
0.443	0.039	0.038	0.079	0.105	0.087	0.065	0.047	0.039	0.074	0.054	0.091	0.081	0.081	0.081	0.081	0.081	0.179	
0.480	0.041	0.043	0.123	0.182	0.105	0.085	0.058	0.045	0.100	0.057	0.110	0.098	0.098	0.098	0.098	0.107	0.267	
0.531	0.052	0.056	0.172	0.282	0.125	0.104	0.077	0.058	0.140	0.062	0.129	0.115	0.115	0.115	0.115	0.132	0.367	
0.600	0.152	0.206	0.242	0.439	0.142	0.118	0.106	0.099	0.260	0.092	0.241	0.125	0.125	0.125	0.125	0.153	0.496	
0.671	0.230	0.353	0.275	0.527	0.146	0.121	0.116	0.122	0.347	0.120	0.363	0.128	0.128	0.128	0.128	0.161	0.559	
0.752	0.274	0.458	0.284	0.552	0.144	0.120	0.117	0.129	0.394	0.132	0.429	0.124	0.124	0.124	0.124	0.161	0.588	
0.802	0.260	0.427	0.253	0.490	0.138	0.116	0.111	0.120	0.369	0.122	0.396	0.118	0.118	0.118	0.118	0.155	0.566	
0.858	0.246	0.398	0.233	0.440	0.135	0.111	0.105	0.112	0.340	0.117	0.376	0.113	0.113	0.113	0.113	0.148	0.538	
0.898	0.251	0.411	0.225	0.429	0.131	0.109	0.102	0.111	0.339	0.117	0.383	0.110	0.110	0.110	0.110	0.145	0.528	
0.931	0.263	0.439	0.225	0.435	0.127	0.106	0.102	0.112	0.346	0.121	0.399	0.110	0.110	0.110	0.110	0.145	0.529	
0.967	0.284	0.485	0.232	0.455	0.126	0.108	0.102	0.115	0.362	0.126	0.426	0.108	0.108	0.108	0.108	0.145	0.540	
1.003	0.301	0.530	0.240	0.486	0.123	0.108	0.103	0.119	0.381	0.131	0.455	0.107	0.107	0.107	0.107	0.146	0.556	
Magnetic Properties																		
$J_s$ , Am <sup>2</sup> /kg	0.49	0.25	0.92	0.089	0.49	0.69	0.81	0.68	0.25	0.73	0.88	1.09	1.09	1.09	1.09	0.81	0.17	
$\chi_{if}$ , 10 <sup>-6</sup> m <sup>3</sup> /kg	6.3	3.7	7.6	1.3	4.7	8.1	9.8	9.1	0.37	8.2	--	12.9	12.9	12.9	12.9	10.4	0.68	
Chemical Composition, %																		
SiO <sub>2</sub>	52.22	--	43.89	--	54.18	49.07	49.15	49.49	--	48.08	--	50.03	50.03	50.03	50.03	49.45	--	
TiO <sub>2</sub>	2.66	--	2.40	--	3.45	2.77	2.90	2.89	--	2.75	--	2.92	2.92	2.92	2.92	2.76	--	
Al <sub>2</sub> O <sub>3</sub>	18.68	--	15.09	--	18.24	16.83	17.68	17.42	--	17.17	--	17.55	17.55	17.55	17.55	17.21	--	
Fe <sub>2</sub> O <sub>3</sub> T	11.67	--	24.34	--	9.72	14.46	13.56	14.16	--	14.88	--	12.39	12.39	12.39	12.39	13.48	--	
MnO	0.16	--	0.12	--	0.11	0.17	0.18	0.18	--	0.19	--	0.18	0.18	0.18	0.18	0.19	--	
MgO	2.25	--	1.66	--	1.20	2.87	2.96	2.88	--	3.07	--	2.91	2.91	2.91	2.91	3.30	--	
CaO	5.66	--	5.03	--	5.27	5.92	5.97	5.92	--	5.94	--	6.19	6.19	6.19	6.19	6.10	--	
Na <sub>2</sub> O	3.58	--	3.74	--	4.45	4.57	4.50	4.13	--	4.53	--	4.42	4.42	4.42	4.42	4.52	--	
K <sub>2</sub> O	1.74	--	2.86	--	2.23	1.93	1.82	1.76	--	1.94	--	1.95	1.95	1.95	1.95	1.94	--	
P <sub>2</sub> O <sub>5</sub>	0.94	--	0.84	--	0.87	0.83	0.85	0.88	--	0.83	--	0.87	0.87	0.87	0.87	0.85	--	
V, µg/g	117	--	82	--	84	135	134	121	--	150	--	112	112	112	112	119	--	
Cr, µg/g	15	--	26	--	52	16	13	13	--	9	--	179	179	179	21	21	--	
Total	99.56	--	99.97	--	99.72	99.42	99.57	99.71	--	99.38	--	99.68	99.68	99.68	99.68	99.80	--	
LOI	2.96	--	15.28	--	5.94	5.21	4.42	4.53	--	4.51	--	3.51	3.51	3.51	3.51	4.44	--	
SO <sub>3</sub>	0.593	2.39	9.28	27.2	1.44	2.32	1.46	1.30	15.1	2.04	--	0.96	0.96	0.96	0.96	2.30	24.7	
FeO	0.80	--	1.59	--	2.32	4.39	4.52	4.48	--	4.65	--	4.61	4.61	4.61	4.61	4.58	--	
Fe <sub>2</sub> O <sub>3</sub>	10.78	--	22.57	--	7.14	9.58	8.54	9.18	--	9.71	--	7.27	7.27	7.27	7.27	8.39	--	
Fe <sup>3+</sup> /Fe <sup>2+</sup>	12.1	--	12.8	--	2.77	1.96	1.70	1.84	--	1.88	--	1.42	1.42	1.42	1.42	1.65	--	



Table 8. (continued)

Wavelength <sup>a</sup> , nm	HWMK508		HWMK-509		HWMK-510		HWMK511		HWMK512		HWMK515		HWMK517		HWMK-620	
	Gemini	<1 mm	Gemini	<1 mm	Gemini	<1 mm	Gemini	<1 mm	Gemini	<1 mm	Gemini	<1 mm	Gemini	<1 mm	Gemini	<1 mm
445	0.222	0.340	0.042	0.131	0.060	0.103	0.056	0.091	0.120	0.233	0.062	0.113	0.098	0.098	0.113	0.098
480	0.230	0.382	0.047	0.167	0.078	0.150	0.067	0.119	0.157	0.347	0.076	0.157	0.120	0.120	0.157	0.120
530	0.241	0.439	0.063	0.193	0.114	0.246	0.109	0.197	0.183	0.448	0.108	0.252	0.155	0.155	0.252	0.155
600	0.251	0.519	0.085	0.207	0.155	0.390	0.195	0.321	0.195	0.528	0.159	0.436	0.199	0.199	0.436	0.199
670	0.253	0.554	0.088	0.209	0.165	0.448	0.237	0.377	0.199	0.559	0.170	0.490	0.213	0.213	0.490	0.213
750	0.252	0.575	0.089	0.203	0.165	0.474	0.258	0.403	0.194	0.560	0.176	0.538	0.216	0.216	0.538	0.216
800	0.246	0.576	0.084	0.197	0.158	0.454	0.247	0.398	0.186	0.537	0.166	0.511	0.209	0.209	0.511	0.209
860	0.241	0.571	0.080	0.187	0.148	0.427	0.234	0.387	0.177	0.510	0.157	0.475	0.201	0.201	0.475	0.201
900	0.239	0.567	0.077	0.184	0.146	0.420	0.228	0.380	0.173	0.496	0.153	0.469	0.196	0.196	0.469	0.196
930	0.236	0.566	0.077	0.181	0.143	0.420	0.228	0.376	0.168	0.491	0.152	0.469	0.195	0.195	0.469	0.195
970	0.234	0.566	0.077	0.181	0.142	0.426	0.230	0.378	0.169	0.496	0.152	0.481	0.192	0.192	0.481	0.192
1005	0.231	0.567	0.076	0.181	0.145	0.437	0.233	0.379	0.170	0.505	0.151	0.497	0.192	0.192	0.497	0.192
Magnetic Properties																
$J_s$ , Am <sup>2</sup> /kg	0.49	0.11	1.45	0.52	0.87	0.16	0.47	0.25	0.38	0.06	0.65	0.11	0.49	0.49	0.11	0.49
$\chi_{16}$ , 10 <sup>-6</sup> m <sup>3</sup> /kg	6.2	1.2	13.4	5.4	8.5	1.78	8.6	2.6	3.0	0.86	13.6	1.59	5.8	5.8	1.59	5.8
Chemical Composition, %																
SiO <sub>2</sub>	49.01	--	49.42	49.00	48.21	--	--	--	48.49	--	49.76	--	49.57	49.57	--	49.57
TiO <sub>2</sub>	2.90	--	2.87	2.89	3.22	--	--	--	2.75	--	3.01	--	3.00	3.00	--	3.00
Al <sub>2</sub> O <sub>3</sub>	20.65	--	17.21	16.68	18.25	--	--	--	16.54	--	17.52	--	18.79	18.79	--	18.79
Fe <sub>2</sub> O <sub>3</sub> T	9.84	--	13.48	14.30	14.48	--	--	--	15.57	--	13.92	--	13.18	13.18	--	13.18
MnO	0.16	--	0.20	0.18	0.15	--	--	--	0.16	--	0.17	--	0.17	0.17	--	0.17
MgO	2.81	--	3.22	3.00	2.18	--	--	--	2.54	--	2.70	--	2.38	2.38	--	2.38
CaO	6.17	--	6.34	6.39	6.00	--	--	--	5.59	--	6.37	--	5.72	5.72	--	5.72
Na <sub>2</sub> O	4.87	--	4.07	4.63	4.31	--	--	--	4.78	--	3.75	--	4.01	4.01	--	4.01
K <sub>2</sub> O	1.90	--	1.90	2.01	1.64	--	--	--	1.99	--	1.72	--	1.69	1.69	--	1.69
P <sub>2</sub> O <sub>5</sub>	1.03	--	0.89	0.91	0.99	--	--	--	0.84	--	0.86	--	0.87	0.87	--	0.87
V, µg/g	137	--	133	110	151	--	--	--	112	--	135	--	134	134	--	134
Cr, µg/g	14	--	399	286	12	--	--	--	10	--	9	--	15	15	--	15
Total	99.34	--	99.60	99.99	99.43	--	--	--	99.25	--	99.78	--	99.38	99.38	--	99.38
LOI	7.10	--	2.36	6.23	7.30	--	--	--	8.50	--	4.91	--	7.69	7.69	--	7.69
SO <sub>3</sub>	3.90	--	0.70	3.58	2.51	13.9	1.64	--	6.46	28.6	1.58	14.2	--	--	1.58	--
FeO	4.41	--	5.24	4.61	3.57	--	--	--	4.02	--	5.22	--	3.59	3.59	--	3.59
Fe <sub>2</sub> O <sub>3</sub>	4.94	--	7.66	9.18	10.51	--	--	--	11.10	--	8.12	--	9.19	9.19	--	9.19
Fe <sup>3+</sup> /Fe <sup>2+</sup>	1.01	--	1.32	1.79	2.65	--	--	--	2.48	--	1.40	--	2.30	2.30	--	2.30

<sup>a</sup>Values given for each wavelength are the reflectivity (equivalent IMP multispectral data).



**Figure 5.** Classification of Mauna Kea tephra according to hydrolytic or sulfuric type of alteration: (a) Loss on ignition (LOI) versus  $\text{SO}_3$  concentration for palagonitic and sulfuric tephra and steam vent samples; (b) LOI versus  $\text{K}_2\text{O}/\text{MgO}$  ratio for palagonitic and sulfuric tephra; and (c)  $\text{Fe}^{3+}/\text{Fe}^{2+}$  versus  $\text{K}_2\text{O}/\text{MgO}$  ratio for palagonitic and sulfuric tephra. Hydrolytic alteration (palagonitic tephra and steam vent samples) has  $\text{LOI}/\text{SO}_3 > 6$  and, for palagonitic tephra,  $\text{K}_2\text{O}/\text{MgO} < 0.5$ . Steam vent samples are not included in Figure 5b and 5c because analyses of unaltered precursor materials were not available. Compared to unaltered tephra, altered tephra are volatile rich and oxidized.

Once dissolved, however, MgO has a high solubility and is leached away and not deposited in the  $<2\text{-}\mu\text{m}$  size fraction. A similar situation likely exists for  $\text{P}_2\text{O}_5$ , except that, once dissolved, it forms insoluble compounds and/or complexes with the ferric np-Ox particles that are abundant and have a high surface area in the  $<2\text{-}\mu\text{m}$  size fraction. Phosphate sorption by ferric oxides is a well-known phenomenon in terrestrial soils and is considered to occur by formation of binuclear bridging complexes with ferric iron atoms [e.g., Parfitt, 1978; Borggaard,

1983; Pena and Torrent, 1984; Schwertmann and Taylor, 1989; Cornell and Schwertmann, 1996].

The iron mineralogy of palagonitic tephra is very different from that for unaltered tephra because the ferrous and ferric iron in glass (sideromelane) is replaced by nanophase ferric oxides as a result of hydrolytic alteration. This replacement is readily apparent in the Mössbauer spectra in Figure 7. Instead of ferrous and ferric iron in glass (the PH-13 spectrum), palagonitic tephra, including JSC Mars-1, HWMK530, and HWMK600 ( $<1\text{-mm}$  size fractions), are characterized by a doublet whose Mössbauer parameters ( $\text{IS} \sim 0.34 \text{ mm/s}$  and  $\text{QS} \sim 0.73 \text{ mm/s}$  at 293 K) imply octahedrally coordinated ferric iron. As discussed previously by Morris *et al.* [1993], the ferric doublet and the brown color result from np-Ox particles that are imbedded within a hydrated aluminosilicate matrix. The particles are associated with an

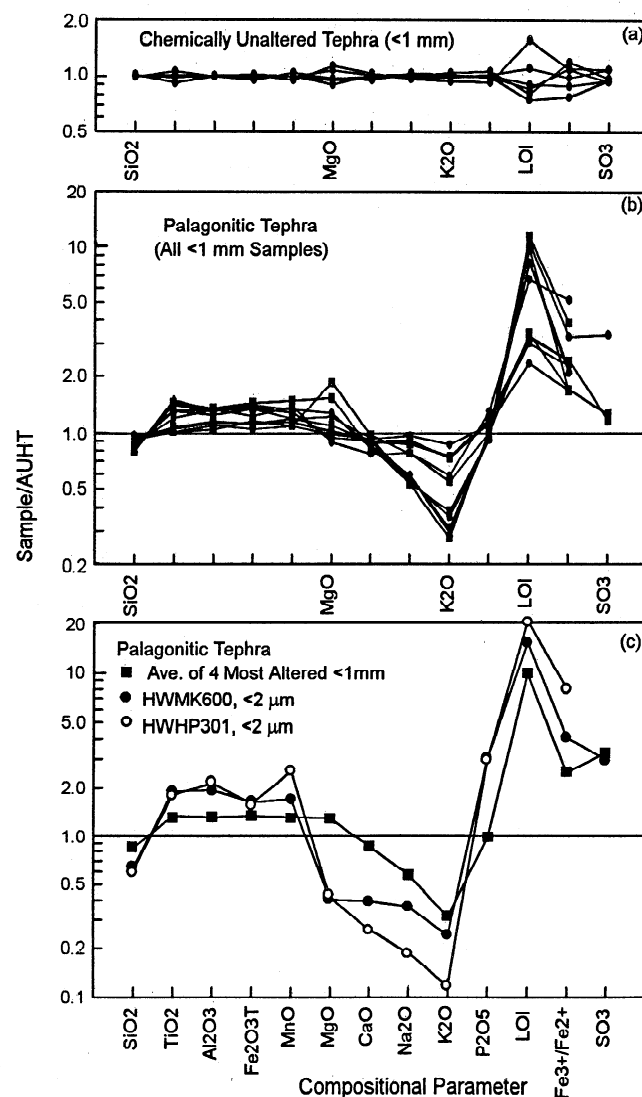


**Figure 6.** Variation in compositional parameters relative to average unaltered hawaiitic tephra (AUHT) for (a) samples of chemically unaltered tephra, (b) all samples of palagonitic tephra ( $<1\text{-mm}$  size fraction), and (c) the average of the four most altered  $<1\text{-mm}$  palagonitic tephra and the  $<2\text{-}\mu\text{m}$  size fractions of HWHP301 and HWMK600. All samples are from Mauna Kea Volcano. The strong depletion in  $\text{SiO}_2$  and alkalis results from leaching during hydrolytic alteration.

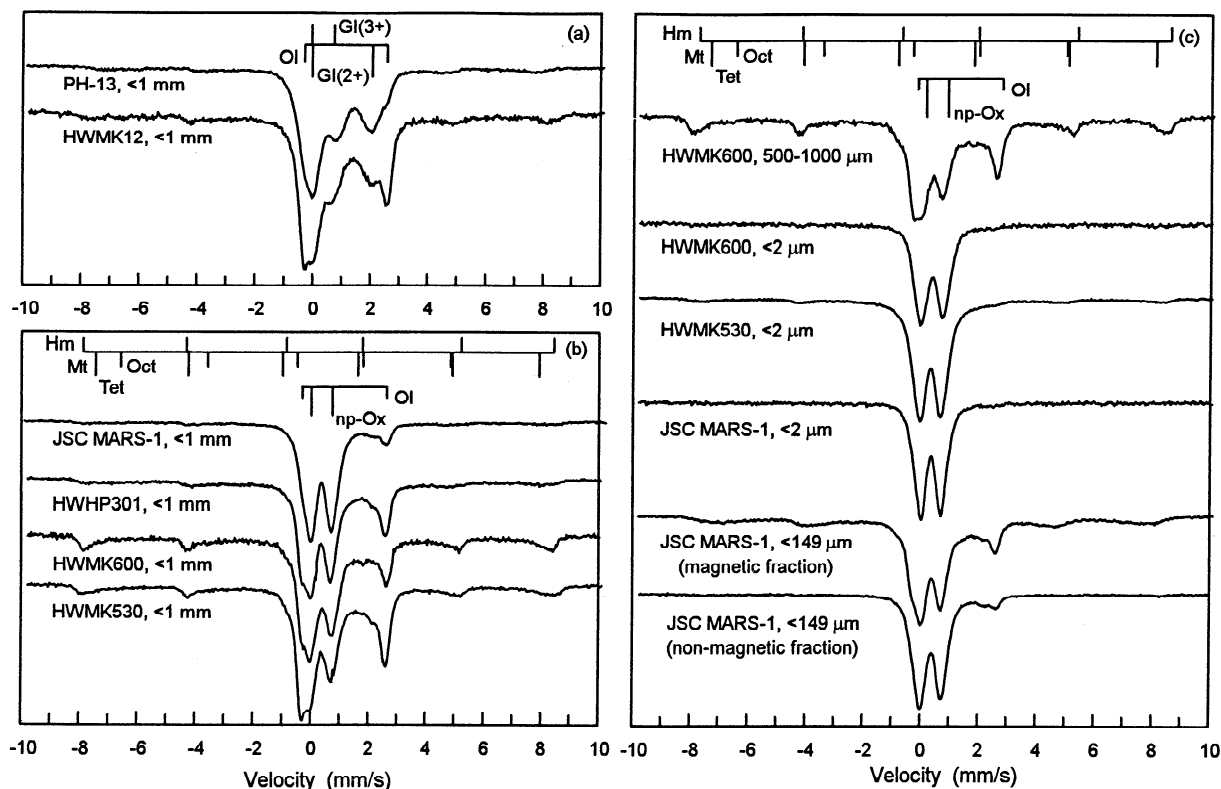


**Figure 7.** Mössbauer spectra (293 K) for unaltered and palagonitic tephra from Mauna Kea: (a) unaltered tephra (<1 mm); (b) palagonitic tephra (<1 mm); and (c) selected size and magnetic separates of HWMK600, HWMK530, and JSC Mars-1. Note that the doublet from nanophase ferric oxide (np-Ox) dominates spectra for the clay size fractions (<2  $\mu\text{m}$ ). (Ol, olivine; Gl, glass; Hm, hematite; Mt, magnetite; Oct, octahedral; Tet, tetrahedral.)

unknown amount of water, so their mineralogy could range from ferrihydrite to its anhydrous equivalent (nanophase hematite).

Mössbauer studies of size separates of palagonitic tephra [Morris *et al.*, 1990, 1993; Bell *et al.*, 1993] show that the proportion of iron associated with np-Ox increases with decreasing size fraction; it is the dominant iron-bearing phase in size fractions smaller than 20  $\mu\text{m}$ . The difference in relative proportions of np-Ox in coarse and fine size fractions is shown in Figure 7 for the 500- to 1000- $\mu\text{m}$  and the <2- $\mu\text{m}$  size fractions of HWMK600. The preferential enrichment of palagonite (i.e., the np-Ox particles and their hydrated matrix material) in the finest size fractions is also shown by chemical data for this tephra. The values of LOI and  $\text{Fe}^{3+}/\text{Fe}^{2+}$  for the relatively unaltered material in the 500- to 1000- $\mu\text{m}$  size fraction (3.27% and 1.85, respectively) are significantly lower than the corresponding values for the <2- $\mu\text{m}$  size fraction (22.7% and 3.05, respectively). Enrichment of palagonitic material in the finest size fractions is the expected result for a product of hydrolytic alteration. Allen *et al.* [1981] and Singer [1982] show scanning electron microscope (SEM) photomicrographs of friable rinds on individual particles of palagonitic tephra. The rinds flake off and become the fine-grained palagonitic material.

As discussed by Morris *et al.* [1990], the presence and near absence of disseminated Fe-Ti spinels in tachylite and palagonitized sideromelane particles, respectively, account for the dominance of relatively unaltered material in magnetic separates and highly weathered sideromelane (palagonite) in nonmagnetic separates of HWMK1. Mössbauer spectra for magnetic and nonmagnetic separates of JSC Mars-1 are consistent with this

result, as shown in Figure 7. By visual inspection, the Fe-Ti spinel sextet and olivine doublet are a larger proportion of the total spectral area for the magnetic separate. The higher values of LOI (24.89 versus 9.66%) and  $\text{Fe}^{3+}/\text{Fe}^{2+}$  (5.38 versus 1.62) for nonmagnetic versus magnetic separates of JSC Mars-1 (Table 7) are chemical evidence for enrichment of palagonitic material in the nonmagnetic fraction.

Like unaltered tephra, XRD data for palagonitic tephra (JSC Mars-1, HWMK530, HWMK600, and HWHP301) are dominated by diffraction lines for plagioclase feldspar (Figure 8b). Lines for titanomagnetite are present near  $33.2^\circ$  and  $62.5^\circ$   $2\theta$ . Very weak lines corresponding to the most intense olivine and pyroxene lines are present at  $29^\circ$  and  $32.4^\circ$   $2\theta$ , respectively. The broad structure near  $35.5^\circ$   $2\theta$  is an envelope of lines from Fe-Ti spinel, feldspar, olivine, and pyroxene; the peak maximum corresponds to the feldspar line, and the asymmetric broadening to lower angles is the unresolved titanomagnetite peak.

In contrast to many studies of palagonitic samples [e.g., Jakobsson, 1972; Ailin-Pyzik and Sommer, 1981; Staudigel and Hart, 1983; Eggleton *et al.*, 1987; Jercinovic *et al.*, 1990; Berggaut *et al.*, 1994], we did not observe (except for HWMK12) phyllosilicates (smectites) or zeolites as alteration products, as indicated by the absence of phyllosilicate diffraction lines in the region  $5^\circ$ - $10^\circ$   $2\theta$ . We also were not able to detect these lines in oriented mounts of clay size fractions (<2  $\mu\text{m}$ ) of seven palagonitic tephra (HWHP301, HWMK1, HWMK530, HWMK600, HWMK612, JSC Mars-1, and PN-9 [Golden *et al.*, 1998]); the crystalline phases were plagioclase and magnetite. Ugolini [1974], however, does report the presence of phyllo-

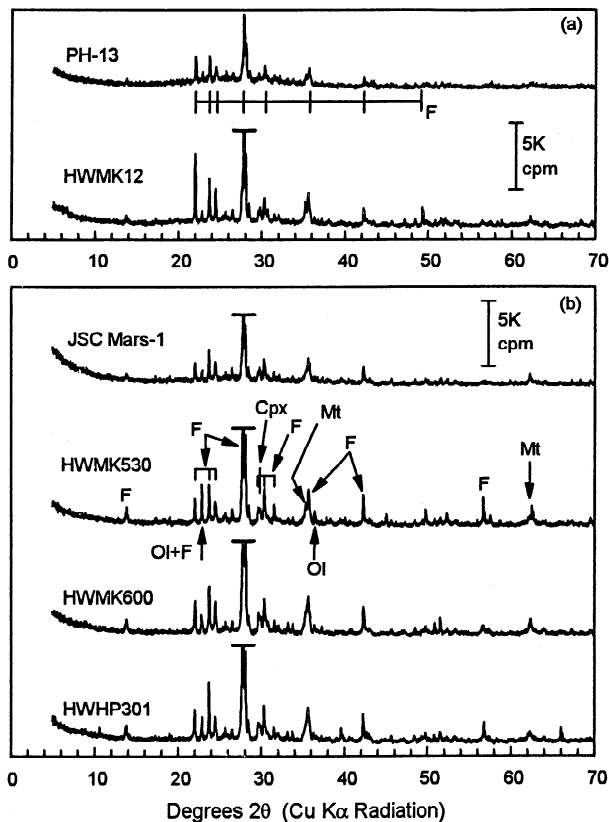


**Figure 8.** Representative XRD powder patterns (293 K) of (a) unaltered and (b) palagonitic tephra from Mauna Kea. Plagioclase feldspar (F) dominates the spectra, but olivine (Ol), Fe-Ti spinel (Mt), and trace clinopyroxene (Cpx) are also present. The horizontal bar on the feldspar peak at  $\sim 28^\circ$   $2\theta$  indicates the peak is truncated.

silicates as products of hydrothermal alteration of basaltic tephra on the upper slopes of Mauna Kea Volcano, possibly by hydrothermal solutions after tephra emplacement or by inter-action of hot tephra with ice during subglacial eruptions. Wolfe *et al.* [1997] discuss evidence that the alteration is subsequent to emplacement. Presumably, the absence of phyllosilicates in our palagonitic tephra implies subaerial alteration under ambient conditions. We also found no obvious manifestation in XRD data of the np-Ox that is readily apparent in Mössbauer spectra (Figure 7). Either XRD is blind to np-Ox particles (because their nanoscale dimension renders them amorphous to X-rays) or, as in the case of ferrihydrite, np-Ox XRD lines are weak and broad and consequently not detectable in the presence of abundant crystalline material, especially magnetites. The 0.25- and 0.15-nm lines of magnetites are at the same positions as the lines for 2-XRD-line ferrihydrite.

IMP-equivalent spectra for the <1-mm and <2- $\mu$ m size fractions of palagonitic tephra are shown in Figure 10. Like previously published spectra of Mauna Kea palagonitic tephra [e.g., Singer, 1982; Morris *et al.*, 1990, 1993; Bell *et al.*, 1993], they are characterized by shallow ferric absorption edges from 445 to  $\sim 750$ -800 nm which result from nanophase ferric oxides [Morris *et al.*, 1993]. Between  $\sim 750$ -800 and 1000 nm, the spectral slope ranges from positive (e.g., PN-9 and JSC Mars-1) to approximately zero (e.g., HWMK530 and HWMK600) to negative (e.g., HWP301 and HWMK612). Negative spectral slopes produce a reflectivity maximum at either 750 or 800 nm.

The reflectivity at 750 nm is highly variable and varies from sample to sample at constant size fraction and, for size fractions of the same sample, increases with decreasing particle diameter. The ranges in  $R_{750}$  for the <1-mm size fraction and for the <2-, 2- to 5-, and <5  $\mu$ m-size fractions of different tephra samples are 0.10-0.39 and 0.30-0.49, respectively. Figure 11a shows for JSC Mars-1 that  $R_{750}$  increases regularly from 0.21 to 0.49 as the size fraction decreases from 500-1000 through <2  $\mu$ m. Similar results are reported for size separates of HWMK1 [Morris *et al.*, 1990], PN-9 [Morris *et al.*, 1993], and six samples from Puu Huluhulu [Bell *et al.*, 1993]. Figure 10 shows that, although the general shape of tephra spectra is relatively constant and not strongly dependent on particle diameter, the natural variation in reflectivity between samples is significant even for the <1-mm size fraction.

Two factors, particle diameter and Fe-Ti spinel content, contribute to the within-sample and between-sample variations in  $R_{750}$ . For size separates of the same soil, the increasing reflectivity with decreasing size fraction is the variation expected from the well-known dependence of particle size on optical scattering coefficient [e.g., Wendlandt and Hecht, 1966]. Thus a suite of tephra samples having a range in mean particle diameters will have a range in  $R_{750}$ . The effect of Fe-Ti spinels on  $R_{750}$  can be shown by magnetic separates because the opaque, black, and strongly magnetic spinels are concentrated in the magnetic fraction. The magnetic fraction of the <149  $\mu$ m size fraction of JSC Mars-1 has a higher low-field susceptibility ( $19.1 \times 10^{-6}$  m<sup>3</sup>/kg versus  $1.46 \times 10^{-6}$  m<sup>3</sup>/kg) and lower  $R_{750}$  (0.14 versus 0.32) than the corresponding nonmagnetic fraction (Figure 11a and Table 7).

The variation of  $R_{750}$  with titanomagnetite concentration, as represented by  $\chi_{lf}$ , is shown in Figure 11b. The extreme values of  $\chi_{lf}$  are for nonmagnetic and magnetic separates derived from JSC Mars-1 and HWMK513. The finest size fractions (<2, 2-5, and <5  $\mu$ m) define a regular trend that, for any value of  $\chi_{lf}$ , is the observed upper limit  $R_{750}$ . Thus we expect that the natural range of  $R_{750}$  and  $\chi_{lf}$  for Mauna Kea palagonitic tephra is the region

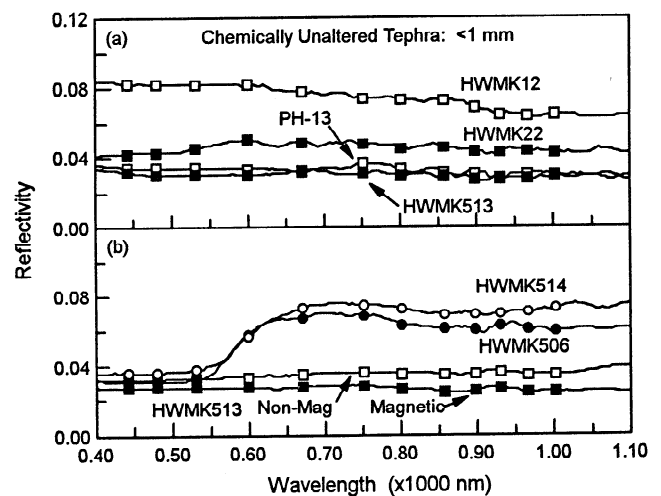


**Figure 9.** Representative high-resolution and IMP-equivalent spectral data (293 K) for unaltered tephra (<1 mm) from Mauna Kea. (a) Spectra for HWMK12, HWMK22, HWMK513, and PH-13 are nearly flat without significant indications of a ferric absorption edge. (b) Spectra for HWMK506 and HWMK514 show weak ferric absorption edges, indicating minor (surface?) oxidation. The magnetic and nonmagnetic separates of HWMK513 are both very dark with no apparent ferric absorption edge.

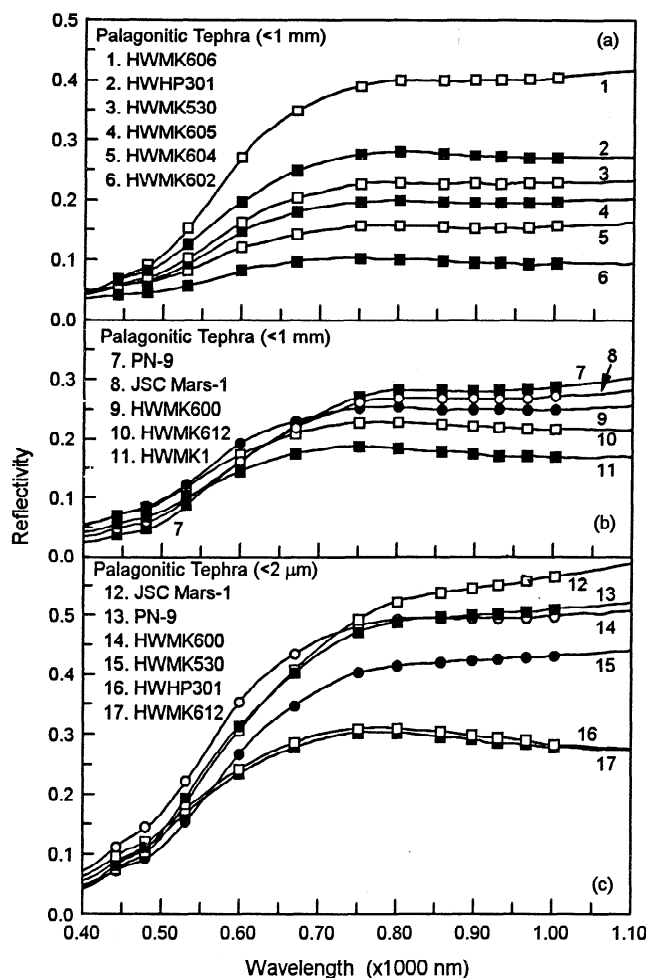


**Figure 10.** High-resolution and IMP-equivalent spectral data (293 K) for the <1-mm (Figures 10a and 10b) and the <2-μm (Figure 10c) size fractions of palagonitic tephra from Mauna Kea. Note the featureless ferric absorption edge extending from ~445 to ~750 nm. No minima from ferric or ferrous absorptions are apparent in the region between 750 and 1005 nm.

between the two dashed lines in Figure 11b. The actual values obtained for a particular palagonitic tephra depend on the value of  $\chi_{lf}$  for its unaltered precursor tephra (range from Figure 11b is  $\sim 1.5 \times 10^{-6}$  to  $70 \times 10^{-6} \text{ m}^3/\text{kg}$ ) and the extent of alteration of glass to palagonitic material, which decreases the mean particle size and increases  $R_{750}$ . Although we do not have such a sample, aeolian processes could entrain and form drifts from fine-grained materials like the <2-μm size fractions of palagonitic tephra.

**5.3.3. Sulfatetic tephra.** Compositional parameters for sulfatetic tephra are given in Table 8. Relative to unaltered tephra (Figure 12), they are oxidized, rich in volatiles ( $\text{H}_2\text{O}$  and  $\text{SO}_3$ ), and, on a volatile-free basis, strongly depleted in  $\text{MgO}$  and moderately depleted in  $\text{MnO}$  and  $\text{CaO}$ . Most sulfatetic tephra (Figure 12a) are moderately enriched in  $\text{Fe}_2\text{O}_3\text{T}$ ; the other major elements ( $\text{SiO}_2$ ,  $\text{TiO}_2$ ,  $\text{Al}_2\text{O}_3$ ,  $\text{Na}_2\text{O}$ ,  $\text{K}_2\text{O}$ , and  $\text{P}_2\text{O}_5$ ) are not systematically enriched or depleted. K-rich jarosite ( $(\text{K}, \text{Na}, \text{H}_3\text{O})\text{Fe}_3(\text{SO}_4)_2(\text{OH})_6$ ) is the sulfatetic alteration product for all 10 tephra samples shown in Figure 12a, as shown by the XRD line at  $17.7^\circ 2\theta$  for HWMK515 and HWMK620 in Figure 13. The presence of jarosite is confirmed by the ferric doublet ( $\text{IS}=0.36 \text{ mm/s}$  and  $\text{QS}=1.15 \text{ mm/s}$ ) in their Mössbauer spectra (Figure 14). Two of the 10 sulfatetic tephra (HWMK503 and

HWMK504) have both jarosite and hematite as alteration products, as shown by the Mössbauer spectrum of HWMK504 in Figure 14.

For clarity, the three sulfatetic tephra in Figure 12a with the most extreme fractionation patterns (HWMK511, HWMK515, and HWMK620) are replotted in Figure 12b. These patterns are consistent with alteration of the tephra by acid-sulfate (sulfuric acid) solutions. According to Lindsay [1979], the relative solubility of sulfate salts decreases in the order  $\text{MgSO}_4 \gg \text{FeSO}_4 \gg \text{KAl}_3(\text{SO}_4)_2(\text{OH})_6$  (alunite)  $\sim \text{CaSO}_4 \cdot \text{H}_2\text{O} > \text{KFe}_3(\text{SO}_4)_2(\text{OH})_6$  (K-jarosite). The elemental fractionation pattern in Figures 12a and 12b follows this solubility sequence. Precipitation of insoluble jarosites enables retention of  $\text{Fe}_2\text{O}_3$  and the alkalis and accounts for the large  $\text{SO}_3$  concentration.  $\text{MgO}$  and  $\text{MnO}$ , which form very soluble sulfate salts, are lost by leaching.

Four sulfatetic tephra (HWMK20, HWMK24, HWMK26 and HWMK508) have elemental fractionation patterns (Figure 12c) and/or alteration products (Figures 13 and 14) distinctly different from those discussed above. HWMK24, whose iron mineralogy is previously discussed by Morris *et al.* [1996], is a case where so

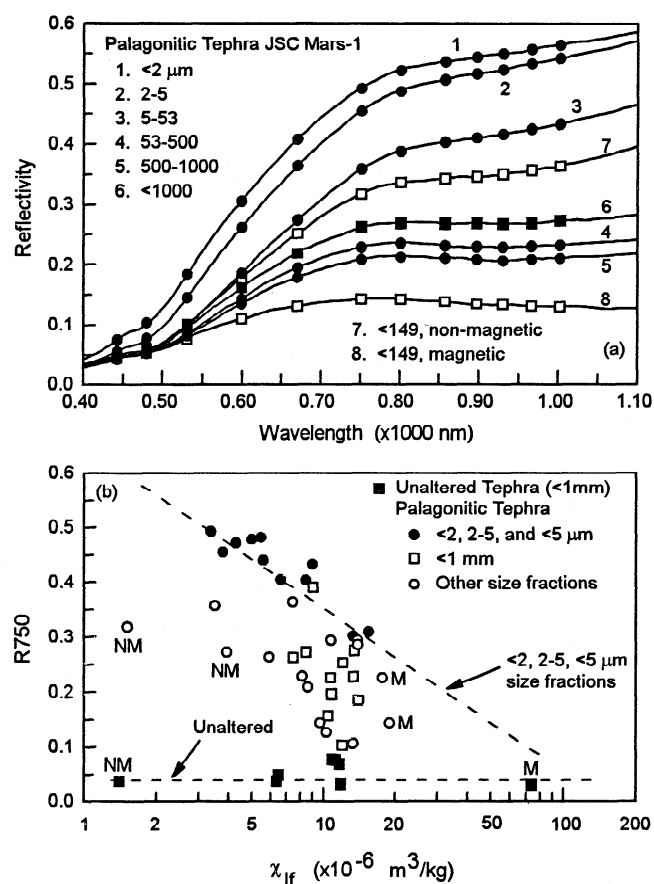


**Figure 11.** (a) Variation of high-resolution and IMP-equivalent spectral data for size and magnetic separates of JSC Mars-1. The magnetic fraction is darker than the nonmagnetic fraction. (b) Variation of the reflectivity at 750 nm as a function of low-field susceptibility for size and magnetic (M, magnetic; NM, nonmagnetic) separates of unaltered and palagonitic tephra. The horizontal dashed line at  $R_{750} \sim 0.04$  is the reflectivity defined by the <1-mm size fraction of unaltered tephra. As indicated by the diagonal dashed line, the finest size fractions become darker with increasing susceptibility, a result of increasing concentrations of opaque, black, and magnetic Fe-Ti oxides.

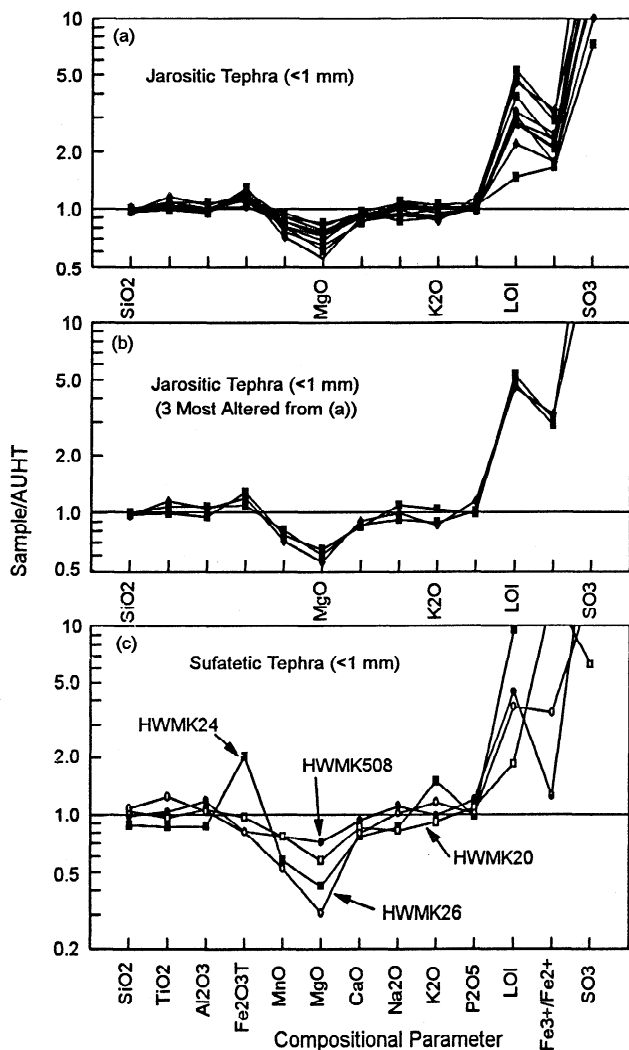


**Figure 12.** Variation in compositional parameters relative to average unaltered hawaiitic tephra (AUHT) for (a) samples of sulfatetic tephra that have jarosite as an alteration product, (b) the four most altered jarositic tephtras in Figure 12a, and (c) sulfatetic tephtras with alunite (HWMK508), hematite (HWMK20), and Ti-containing jarosite (HWMK26) as alteration products and a very extreme case of jarosite formation (HWMK24). For jarositic tephtra (excluding the extreme case of HWMK24), MnO and MgO are the only elements that are strongly leached during sulfuric (acid-sulfate) alteration.

much K-rich jarosite is present that only the major elements (volatile-free basis) associated with K-jarosite ( $K_2O$  and  $Fe_2O_3$ ) are enriched. Possibly, this tephtra came from a region where, in addition to leaching, there was accumulation of K-jarosite. Fractionation patterns for the other three tephtras are different because their alteration products are not K-rich jarosite. Alunite (generalized formula  $(K,Na,H_3O)Al_3(SO_4)_2(OH)_6$ ) is the alteration product identified in the XRD spectrum of HWMK508. Note that alunitic and jarositic tephtra are enriched and depleted, respectively, in  $Al_2O_3$  relative to  $Fe_2O_3T$  in response to the chemistry of their alteration products. XRD and especially Mössbauer data indicate the presence of hematite as an alteration product in HWMK20; no jarosite or alunite is indicated. The Mössbauer parameters for the prominent doublet ( $IS \sim 0.32$  mm/s and  $QS \sim 1.04$  mm/s) for HWMK20 are consistent with tetrahedrally

coordinated ferric iron, probably in association with glass. This sample and HWMK24 have the highest  $Fe^{3+}/Fe^{2+}$  ratio ( $\sim 12$ ) we observed for palagonitic and sulfatetic tephtra (<1-mm size fraction). In spite of the fact that no sulfate minerals were detected, the element fractionation pattern for HWMK20 is quite similar to that for jarositic tephtras.

The fractionation pattern for HWMK26 is unique. It has the most extreme depletion in MgO and MnO, which is consistent with extensive acid-sulfate alteration. The unusual aspect of the pattern is that both  $Al_2O_3$  and  $Fe_2O_3T$  are depleted relative to  $TiO_2$ . The XRD data indicate the presence of jarosite but in reduced amounts in comparison to other jarositic tephtras like HWMK515; the Mössbauer spectrum is also consistent with jarosite. At present we have no explanation for this fractionation pattern, except that *Golden et al.* [1996] report the possibility of Ti-bearing jarosite in this sample.

In the above discussion, we identified jarosite, alunite, and hematite as products of sulfuric alteration processes. As summarized in Table 9, K-rich jarosite is the most common sulfuric alteration product, with HWMK24 and HWMK515 having the highest proportions of this mineral. Multiple alteration products are often present in the same sample. For example, both K- and Na-jarosite are identified in the XRD pattern of HWMK515, and both jarosite and hematite are present in the Mössbauer spectra of HWMK503 and HWMK504. *Bishop et al.* [1998a] report both jarosite and hematite in an altered tephtra from Haleakula Volcano (island of Maui, Hawaii). HWMK20 and HWMK508 have the highest proportions of hematite and alunite, respectively. XRD data (Figure 13) show that Na-jarosite is the dominant sulfate in

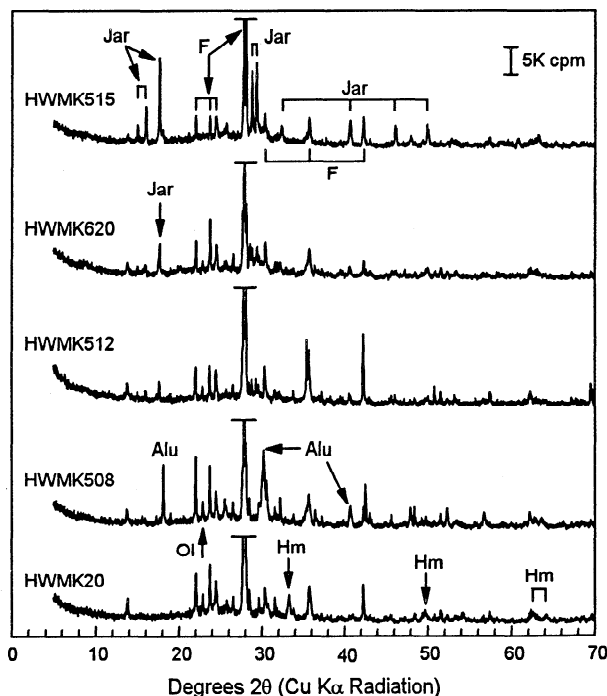


**Figure 13.** Representative XRD powder patterns (293 K) for sulfatetic tephtra (<1-mm size fraction). Plagioclase feldspar (F) is the dominant mineral phase (intense peak at  $\sim 28^\circ 2\theta$  is truncated). Diffraction peaks from jarosite (Jar) are present in HWMK515, HWMK620, and HWMK512. Diffraction lines from alunite (Alu) and hematite (Hm) are present in HWMK508 and HWMK20, respectively.

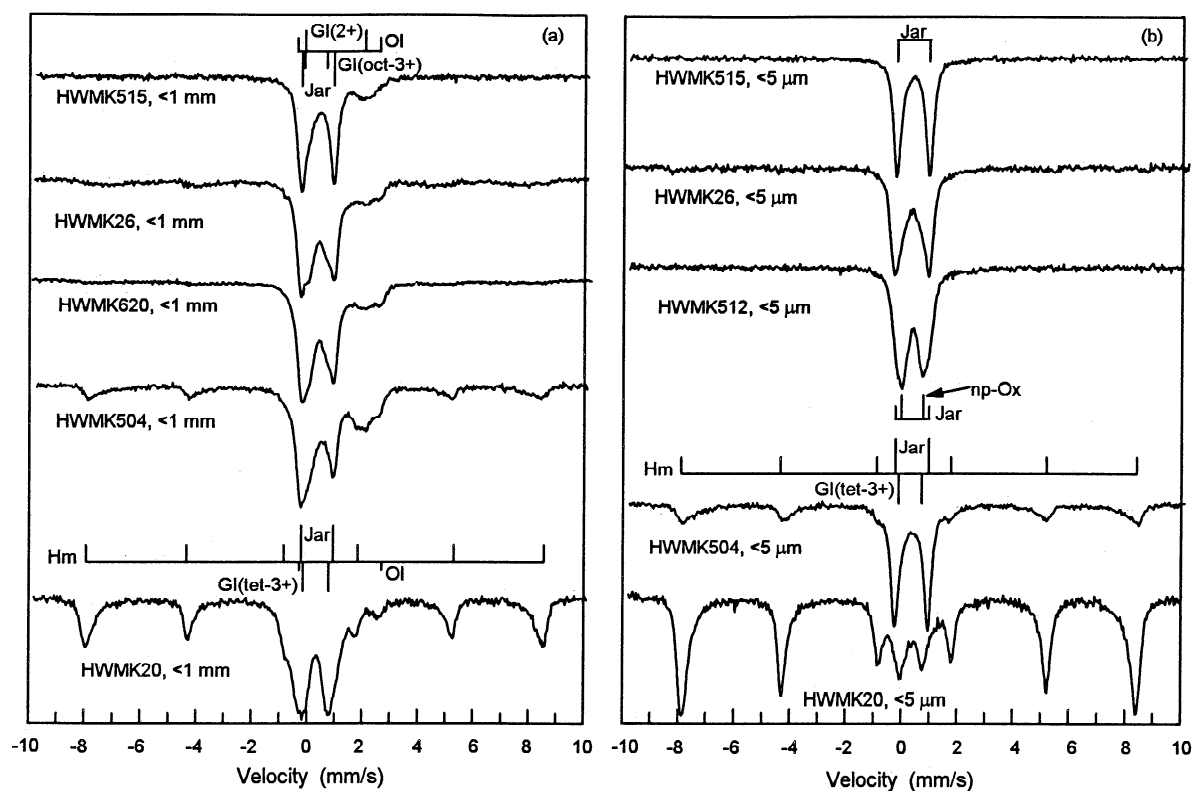


**Figure 14.** Mössbauer spectra (293 K) for representative sulfatetic tephros from Mauna Kea: (a) <1-mm size fractions and (b) <5- $\mu$ m size fractions. Jarosite is the dominant ferric alteration product for HWMK515, HWMK26, and HWMK620. An unidentified mineral with a smaller quadrupole splitting than jarosite dominates the HWMK512 spectrum. The ferric mineralogy of HWMK504 is dominated by hematite and jarosite. The ferric mineralogy of HWMK20 is dominated by hematite and  $\text{Fe}^{3+}$  in tetrahedral coordination (glass). (Gl, glass; Jar, jarosite; Hm, hematite; tet, tetrahedral.)

HWMK512; unfortunately, we did not have enough of this sample to do major element analyses.

Like np-Ox and palagonitic tephra, sulfatetic alteration products are preferentially concentrated in the finest size fractions, as shown by the Mössbauer data in Figure 14. The doublets associated with ferrous and ferric iron in glass and ferrous iron in olivine, which are clearly evident in the <1-mm size fractions, are absent or have reduced intensity in comparison to peaks from alteration products in <5- $\mu$ m size fractions. Presumably, this variety in sulfate minerals and the proportions of sulfates to hematite results from variations in local conditions of pH and temperature. Jarosite, for example, is generally considered to precipitate in acidic (pH <4), oxidizing environments [e.g., van Breemen, 1982]. We found no evidence in XRD data for gypsum ( $\text{CaSO}_4 \cdot 2\text{H}_2\text{O}$ ), which is a common sulfuric alteration product, or any ferric oxide alteration product other than hematite. As discussed by Morris *et al.* [1996] in connection with sample HWMK24, hydrothermal acid-sulfate alteration probably occurred during or after cinder cone formation when  $\text{SO}_2$ -rich volcanic gases percolated through the cone forming (in an oxidizing environment) the sulfuric acid that attacked the volcanic glass (sideromelane).

IMP-equivalent spectra for 17 sulfatetic tephros (<1-mm size fraction) can be categorized into four spectral groups (Figure 15). The reflectivity for the first group (Figure 15a) is relatively flat with a weak ferric absorption edge and no apparent evidence for a ferric reflectivity minimum. A very broad and ill-defined

reflectivity maximum occurs between 600 and 750 nm. The most reflective sample (HWMK508) is gray in color (black unaltered tephra plus white alunite). The remaining samples are olive green. The second group (Figure 15b) is similar to the first except that the ferric absorption edge is stronger, which results in a better defined reflectivity maximum between 670 and 750 nm. Their color is yellow from jarosite. The third spectral group (HWMK24 (yellow) and HWMK512 (orange)) is characterized by definable reflectivity maxima at 750 nm and minima near 915 nm (Figure 15c). The fourth group (HWMK20, HWMK503, and HWMK504 (all red)) has reflectivity maxima at 750 nm and minima at 860–875 nm. Comparison with reflectivity spectra for ferric minerals (Figure 3) confirms that the positions of the spectral features for the third and fourth groups are spectral manifestations of the jarosite and hematite, respectively, identified in these samples by XRD and Mössbauer. Spectral identification of hematite, but not jarosite, in HWMK503 and HWMK504 shows spectral masking of jarosite features by hematite.

IMP-equivalent spectra for the <5- $\mu$ m size fraction for 10 sulfatetic tephros are shown in Figure 16. With one exception (HWMK512), the reflectivity is higher and the M1-T1 spectral contrast is greater for the <5- $\mu$ m size fraction compared to the <1-mm size fraction of the same sample. For example, the maximum reflectivity for the <1-mm size fraction of HWMK511 is about 0.16, and no definable M1 feature is present (Figure 15). The maximum reflectivity for the <5- $\mu$ m size fraction is 0.47, and



**Table 9.** Hydrolytic, Sulfuric, and Hydrochloric Alteration Products Identified in Tephra, Steam Vent, and Impactite Samples by Mössbauer Spectroscopy, X-Ray Diffraction, and IMP Multispectral Data

Sample	Mössbauer Spectroscopy	X-ray Diffraction	IMP Multispectral Data	All Techniques
<i>Palagonitic Tephra (Hydrolytic Alteration)</i>				
HWHP301	np-Ox	none (no Sm)	np-Ox	np-Ox
IWMK1, IWMK11, IWMK12, HWMK530, and HWMK600 through HWMK612	np-Ox	none (no Sm, except HWMK12)	np-Ox	np-Ox
JSC Mars-1	np-Ox	none (no Sm)	np-Ox	np-Ox
PN-9	np-Ox	none (no Sm)	np-Ox	np-Ox
<i>Sulfatetic Tephra (Sulfuric Alteration)</i>				
HWMK20	Hm, Gl(tet-Fe <sup>3+</sup> )	Hm	Hm	Hm, Gl(tet-Fe <sup>3+</sup> )
HWMK24 and HWMK26	Jar	K-Jar	Jar	Jar
HWMK501, HWMK502, HWMK505, HWMK507, HWMK509 HWMK510, HWMK511, HWMK515, HWMK517, and HWMK620	Jar	Jar	Jar	Jar
HWMK503, HWMK504	Jar, Hm	K-Jar, Hm	Hm	Jar, Hm
HWMK508	None	Alu	none	Alu
HWMK512	np-Ox	Jar	pc-Gt/Sch/Akg	np-Gt/Sch/Akg
<i>Steam Vents (Hydrolytic Alteration)</i>				
IWSB501	Hm, np-Ox	Hm, pc-Gt, Cri	pc-Gt/Sch/Akg	Hm, np-Gt, Cri
HWSB531	Hm, np-Ox	Hm, pc-Gt, Cri, Hal	Hm	Hm, np-Gt, Cri, Hal
HWSB532	Hm, np-Ox	Hm, pc-Gt, Cri	pc-Gt/Sch/Akg	Hm, np-Gt, Cri
HWSB533	Hm, np-Gt/np-Ox	pc-Gt, pc-Hm, Hal, Sm	pc-Gt/Sch/Akg	Hm, np-Gt, Hal, Sm
HWSB534 and HWSB535	Hm, np-Ox	Hm, Cri	pc-Gt/Sch/Akg	Hm, Cri, np-Gt/Sch/Akg
HWSB536	Hm, np-Ox	Hm, pc-Gt, Cri	pc-Gt/Sch/Akg	Hm, np-Gt, Cri
<i>Steam Vents (Hydrochloric Alteration)</i>				
HWMU387	np-Ox	Akg	pc-Gt/Sch/Akg	Akg
<i>Impactites (Relithification)</i>				
H3A1	Mh, np-Ox	Mh	np-Ox	Mh, np-Ox
H3A2	Mh, Gt	Mh, Gt	pc-Gt/Sch/Akg	Mh, Gt
H11A	Mh, np-Ox	Mh	np-Ox	Mh, np-Ox

Minerals: Hm, hematite; Gt, goethite; Mh, maghemite; Sch, schwertmannite; Akg, akaganéite; Feh, ferrihydrite; np-Ox, nanophase ferric oxide; Cri, cristobalite; Jar, jarosite; Alu, alunite; Sm, smectite; Hal, halloysite; Gl, glass. Phases separated by slashes are all possible interpretations; only one need be present. Prefixes: np, nanophase; pc, poorly crystalline; tr, trace; tet, tetrahedral.

a M1 feature is present at 915 nm (Figure 16). The <5- $\mu$ m size fractions of sulfatetic tephra are systematically brighter (R750) and less magnetic than the finest size fractions of palagonitic tephra, presumably because the black, magnetic Ti-Fe spinels in unaltered tephra suffer partial dissolution by sulfuric acid and are not reconstituted (see section 10.2).

## 6. Kilauea Steam Vents

### 6.1. Samples and Alteration Process

Eight samples of altered volcanic material from active steam vents associated with Kilauea Volcano were studied (Table 5). One was collected in 1987 (J. B. Adams) at Mauna Ulu, and the remaining seven were collected at Sulfur Bank in 1995 and 1996 (R. V. Morris and J. F. Bell III). Major element, magnetic, and IMP-equivalent spectral data are given in Table 10. Spectral and magnetic data for the <2- $\mu$ m size fraction are also reported for

several samples. Chemical data for Kilauea basalt BHVO-1 [Govindaraju, 1994] are used as the composition for the precursor lava for the Sulfur Bank samples because we do not have an unaltered basalt from this location.

LOI and SO<sub>3</sub> data for Kilauea steam vent samples are included in Figure 5a along with data for palagonitic and sulphatetic tephra. Their LOI/SO<sub>3</sub> ratios (6<LOI/SO<sub>3</sub><40) are intermediate to those for palagonitic (LOI/SO<sub>3</sub>>40) and sulfatetic (1<LOI/SO<sub>3</sub><6) tephra. Are these samples subjected to hydrolytic or sulfuric alteration? We cannot use the K<sub>2</sub>O/MgO ratio to differentiate alteration type (as in Figure 5) because we do not have chemical analyses for samples that are demonstrably the precursor (unaltered) material of the steam vent samples. As discussed below, sulfate minerals are not observed as alteration products, so Sulfur Bank samples most likely experienced hydrothermal hydrolytic alteration. This is perhaps not surprising because the H<sub>2</sub>O/SO<sub>3</sub> ratio, on a mole basis, ranges between 40 and 180, assuming that the balance of LOI is H<sub>2</sub>O.

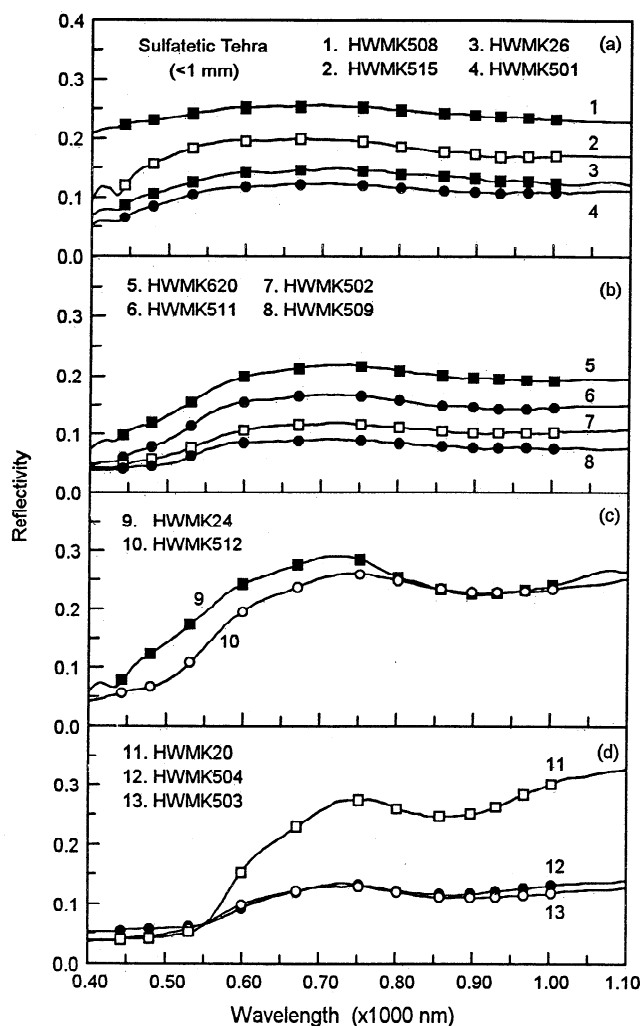


**Figure 15.** High-resolution and IMP-equivalent spectral data (293 K) for sulfatetic tephra (<1-mm size fraction). (a) Sulfatetic tephra with no apparent band minimum in the region 750–1000 nm. All samples contain jarosite, except HWMK508, which has alunite. (b) Jarositic tephra with no apparent band minimum and a steeper ferric absorption edge than the jarositic tephra in Figure 15a. (c) Sulfatetic tephra that have a band minimum near 920 nm. HWMK24 contains jarosite, and HWMK512 contains jarosite and another ferric phase. (d) Sulfatetic tephra whose spectral properties are dominated by hematite (band minimum near 860 nm, reflectivity maximum at 750 nm, and strong ferric absorption edge).

## 6.2. Sulfur Bank

The steam vent samples from Sulfur Bank are volatile rich (LOI = 11–18%) and oxidized ( $\text{Fe}^{3+}/\text{Fe}^{2+}=2.5\text{--}20$ ). The variation of compositional parameters (volatile-free basis) relative to BHVO-1 is shown in Figure 17. These samples are heavily altered, and the fractionation patterns are distinctly different from the ones discussed earlier for palagonitic and sulfatetic tephra.  $\text{Fe}_2\text{O}_3\text{T}$ ,  $\text{TiO}_2$ , and  $\text{P}_2\text{O}_5$  are enriched by factors of 2–4.  $\text{Al}_2\text{O}_3$  is slightly enriched in two samples and depleted in five samples;  $\text{MgO}$  and  $\text{MnO}$  are undepleted to slightly enriched in three samples and depleted in the other four. Variations in  $\text{MgO}$  and  $\text{MnO}$  are coupled by sample, but variations of  $\text{MgO}$  and  $\text{Al}_2\text{O}_3$  are not.  $\text{SiO}_2$  is generally depleted, and  $\text{CaO}$ ,  $\text{Na}_2\text{O}$ , and  $\text{K}_2\text{O}$  are

strongly depleted for all samples. In general, all elements except  $\text{Fe}_2\text{O}_3\text{T}$ ,  $\text{TiO}_2$ , and  $\text{P}_2\text{O}_5$  are being leached under oxidizing conditions, leaving highly oxidized residues with high proportions of  $\text{Fe}_2\text{O}_3$  and  $\text{TiO}_2$  (33–61%).

Differences in the compositional fractionation patterns of Sulfur Bank samples correlate with the amount of residual pyroxene. The three samples in Figure 17a (HWSB501, HWSB534, and HWSB535) are unfractionated or slightly enriched in  $\text{MgO}$ , and the four samples in Figure 17b (HWSB531, HWSB532, HWSB533, and HWSB536) are strongly depleted in  $\text{MgO}$ . As shown by comparison of the pyroxene-dominated Mössbauer spectrum of unaltered basalt BHVO-1 to representative Mössbauer spectra for the steam vent samples (Figure 18), pyroxene is present in the high- $\text{MgO}$  group and absent in the low- $\text{MgO}$  group. The same result follows from XRD data (Figure 19). Diffraction lines from pyroxene are strong for the first group (e.g., HWSB535) and absent (HWSB531) to very weak (HWSB536) for the second group. Presumably, differences in local conditions resulted in more severe leaching of  $\text{MgO}$  (and covarying  $\text{MnO}$ ?) from the samples in the second group relative to the first. Depletion of  $\text{Al}_2\text{O}_3$  relative to  $\text{Fe}_2\text{O}_3\text{T}$

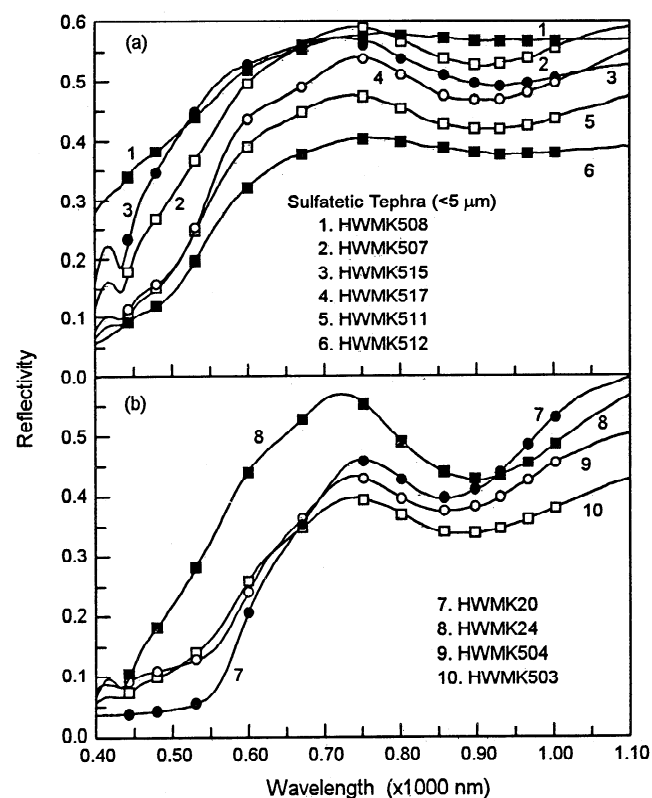


**Figure 16.** High-resolution and IMP-equivalent spectral data (293 K) for sulfatetic tephra (<5- $\mu\text{m}$  size fraction) for selected samples from Figure 15. Compared to the <1-mm size fraction, IMP-equivalent multispectral data of the <5- $\mu\text{m}$  size fraction show enhanced spectral characteristics of ferric alteration products. (a) Jarositic tephra without a definable jarosite band minimum in the <1-mm size fraction have a definable minimum (~920 nm) in the <5- $\mu\text{m}$  fraction. HWMK508 does not have a minimum, in keeping with the presence of alunite. (b) The jarosite (HWMK24) and hematite (HWMK20, HWMK503, and HWMK504) bands are present with increased spectral contrast in the <5- $\mu\text{m}$  compared to the <1-mm fractions.

**Table 10.** Multispectral, Magnetic, and Chemical data for Steam Vent Samples from Sulfur Bank and Mauna Ulu, Kilauea Volcano

	HWSB501		HWSB-531	HWSB532		HWSB-533	HWSB534		HWSB535		HWSB-536	HWMU-387
	<1 mm	<5 $\mu$ m	<1 mm	<1 mm	<2 $\mu$ m	<1 mm	<1 mm	<2 $\mu$ m	<1 mm	<2 $\mu$ m	<1 mm	<1 mm
Wavelength <sup>a</sup> , nm												
445	0.058	0.057	0.044	0.039	0.044	0.071	0.055	0.053	0.050	0.049	0.070	0.062
480	0.068	0.069	0.046	0.042	0.053	0.081	0.062	0.066	0.056	0.060	0.080	0.070
530	0.112	0.116	0.058	0.058	0.085	0.135	0.084	0.105	0.074	0.094	0.124	0.100
600	0.202	0.222	0.135	0.128	0.220	0.267	0.134	0.192	0.126	0.184	0.245	0.192
670	0.252	0.285	0.207	0.177	0.314	0.321	0.167	0.243	0.159	0.239	0.293	0.241
750	0.282	0.326	0.246	0.207	0.364	0.384	0.194	0.283	0.182	0.277	0.337	0.261
800	0.278	0.322	0.233	0.197	0.353	0.362	0.190	0.286	0.180	0.276	0.321	0.246
860	0.266	0.311	0.223	0.186	0.340	0.333	0.185	0.281	0.173	0.269	0.298	0.230
900	0.259	0.308	0.226	0.182	0.338	0.327	0.178	0.278	0.167	0.266	0.289	0.226
930	0.256	0.307	0.232	0.182	0.340	0.330	0.173	0.277	0.164	0.265	0.289	0.226
970	0.255	0.309	0.244	0.185	0.345	0.344	0.173	0.279	0.165	0.267	0.293	0.230
1005	0.258	0.311	0.252	0.190	0.351	0.363	0.174	0.280	0.165	0.270	0.300	0.236
Magnetic Properties												
$J_s$ , Am <sup>2</sup> /kg	0.91	0.69	1.09	1.55	1.10	0.108	1.00	1.19	1.36	1.55	1.09	0.00
$\chi_{lf}$ , 10 <sup>-6</sup> m <sup>3</sup> /kg	8.1	7.9	12.1	16.6	15.6	1.00	9.3	12.3	11.8	14.9	9.6	0.24
Chemical Composition, %												
SiO <sub>2</sub>	35.89	--	30.42	23.49	--	47.65	40.67	--	37.98	--	49.25	--
TiO <sub>2</sub>	5.13	--	8.41	10.08	--	4.63	5.43	--	6.46	--	6.05	--
Al <sub>2</sub> O <sub>3</sub>	18.42	--	16.68	7.43	--	8.11	5.45	--	4.24	--	3.46	--
Fe <sub>2</sub> O <sub>3</sub> T	27.74	--	40.92	50.66	--	35.03	27.82	--	32.55	--	33.71	--
MnO	0.16	--	0.06	0.09	--	0.03	0.17	--	0.16	--	0.07	--
MgO	7.68	--	1.17	3.85	--	1.73	10.68	--	9.74	--	3.09	--
CaO	3.85	--	0.41	2.16	--	1.42	7.47	--	6.58	--	2.04	--
Na <sub>2</sub> O	0.30	--	0.09	0.22	--	0.27	0.72	--	0.57	--	0.37	--
K <sub>2</sub> O	0.16	--	0.07	0.13	--	0.14	0.36	--	0.35	--	0.38	--
P <sub>2</sub> O <sub>5</sub>	0.44	--	0.57	0.86	--	0.58	0.44	--	0.50	--	0.77	--
V, $\mu$ g/g	416	--	893	1076	--	410	671	--	775	--	911	--
Cr, $\mu$ g/g	1504	--	1812	2232	--	1516	1388	--	1595	--	1001	--
Total	99.77	--	98.80	98.97	--	99.59	99.21	--	99.13	--	99.19	--
LOI	18.35	--	14.40	14.11	--	15.96	14.12	--	12.64	--	10.65	--
SO <sub>3</sub>	1.68	--	1.45	1.83	--	1.20	--	--	0.74	--	1.317	--
FeO	3.91	--	1.95	4.11	--	1.50	7.11	--	6.61	--	3.95	--
Fe <sub>2</sub> O <sub>3</sub>	23.39	--	38.75	46.09	--	33.36	19.92	--	25.20	--	29.32	--
Fe <sup>3+</sup> /Fe <sup>2+</sup>	5.38	--	17.9	10.1	--	20.0	2.52	--	3.43	--	6.68	--

<sup>a</sup>Values given for each wavelength are the reflectivity (equivalent IMP multispectral data).

and TiO<sub>2</sub> implies dissolution and removal of the elements associated with feldspar. The diffraction line from cristobalite in all the samples except one (HWSB533) shows that some of the dissolved SiO<sub>2</sub> precipitates as that phase. Diffraction lines from poorly crystalline halloysite (Al<sub>2</sub>Si<sub>2</sub>O<sub>5</sub>(OH)<sub>4</sub>) are clearly present in HWSB531 and just visible in HWSB532 and HWSB533. This mineral is a plausible explanation for the relatively high Al<sub>2</sub>O<sub>3</sub> concentration for these three samples.

The Mössbauer and XRD data show that the liberated ferrous iron is oxidized and precipitated primarily as poorly-crystalline to nanophase hematite and goethite. Poor crystallinity is indicated by the broad and low-intensity XRD lines. On the basis of XRD line intensities, the ratio of hematite to goethite is highest in HWSB531 and lowest in HWSB533. The Mössbauer data are consistent with the XRD data: the relative intensity of the hematite sextet (IS~0.38 mm/s, QS~0.16 mm/s, and  $B_{hf}$ =50.2 T at 293 K) is greater in HWSB531 than HWSB533. The asymmetric shape of the hematite peaks and reduced value of  $B_{hf}$  compared to well-crystalline hematite ( $B_{hf}$ ~51.4 T) are consistent with impurities/defects in the hematite structure, possibly Al<sup>3+</sup> and/or H<sub>2</sub>O and OH<sup>-</sup> [e.g., *De Grave et al.*, 1982; *Dang et al.*, 1998]. Al<sup>3+</sup> is a common substitutional impurity for Fe<sup>3+</sup> in oxides in terrestrial environments [e.g., *Cornell and Schwertmann*, 1996]. Goethite

sextets are not present, implying the phase is probably superparamagnetic (nanophase) and contributes to the ferric doublet.

The IMP-equivalent spectral data (Figure 20) are all characterized by a ferric absorption edge extending from 445 nm to a reflectivity maximum at 750 nm. The three pyroxene-bearing samples (Figure 20a) have either no definable ferric minimum (HWSB534 and HWSB535) or a poorly defined minimum (HWSB501) near 945 nm. Presumably, this behavior is a result of the high-energy wing of a more intense ferrous pyroxene band centered near 1000 nm. The four essentially pyroxene-free samples have definable minima associated with ferric iron. The spectral presence of hematite in HWSB531 is clearly indicated by the minimum at 860 nm and relatively strong absorption at 530 nm. The 900- to 930-nm T1 values for HWSB532, HWSB533, and HWSB536 are consistent with the goethite observed in the XRD data.

### 6.3. Mauna Ulu

We did not have sufficient quantities of the Mauna Ulu sample (HWMU387) to obtain major element analysis. The Mössbauer spectrum (293 K) of the <1-mm size fraction (Figure 18) is consistent with doublets from glass (Fe<sup>2+</sup> and Fe<sup>3+</sup>) and np-Ox

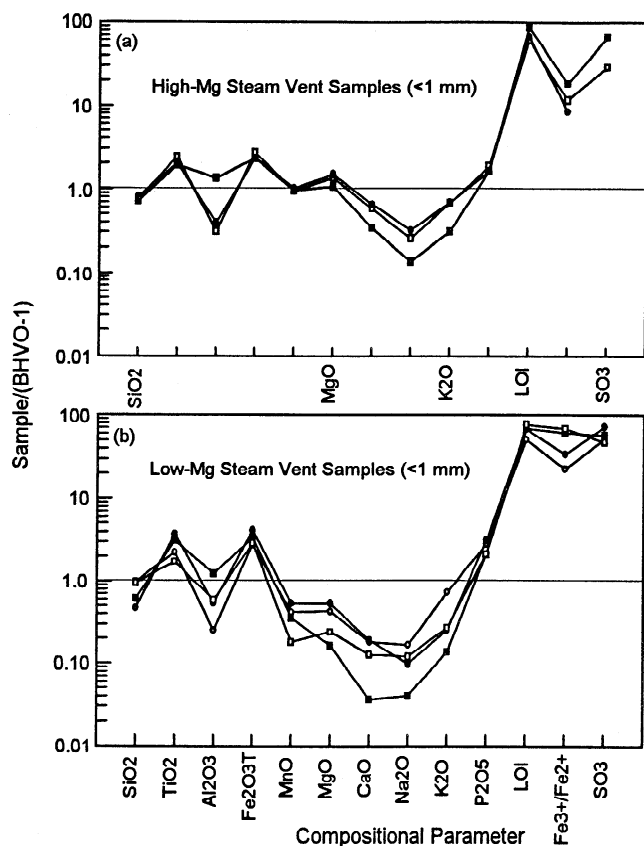


**Figure 17.** Variation in compositional parameters relative to BHVO-1 for Sulfur Bank steam vent samples. (a) Samples (HWSB501, HWSB534 and HWSB535) which have no MgO depletion and (b) samples (HWSB531, HWSB532, HWSB533, and HWSB536) which have a MgO depletion. For all samples,  $\text{SiO}_2$ ,  $\text{Fe}_2\text{O}_3\text{T}$ , and  $\text{P}_2\text{O}_5$  are the only major elements that are always enriched.

and a minor hematite sextet. The XRD pattern of the  $<5\text{-}\mu\text{m}$  size fraction (Figure 19) has lines characteristic of akaganéite, implying that the np-Ox is at least in part this oxide. HWMU387 is the only sample for which we observed this mineral. Akaganéite usually forms in the presence of chloride ion [Cornell and Schwertmann, 1996], presumably in association with HCl-rich volcanic gasses at the steam vent (hydrothermal, hydrochloric alteration). The IMP-equivalent spectrum (Figure 20) has M1 (750 nm), T1 (931 nm), and spectral shape that are consistent with akaganéite (Figure 3a).

## 7. Meteor Crater Impactites

Samples of irregularly shaped beads of impact melt (impactites) produced during the formation of Meteor Crater (Arizona) at  $49 \pm 3$  ka [Sutton, 1985] were obtained from C. B. Moore. The impactor was the Canyon Diablo octahedrite whose main mass is reported by Moore *et al.* [1967] to be 89.7% Fe, 7-10% Ni, and 0.40% Co. Impactite beads are brown in color and sorted into two groups by size (1-5 mm and 5-10 mm). About 20% of the 1- to 5-mm beads (sample H3A) were strongly attracted to magnetized tweezers. The magnetic beads were removed to constitute sample H3A2; the remaining, relatively nonmagnetic beads are sample H3A1. The group of 5- to 10-mm particles (sample H11A) did not contain strongly magnetic

members. Aliquots of H3A1 and H11A were ground and sieved into  $<150\text{-}\mu\text{m}$  and 150- to  $1000\text{-}\mu\text{m}$  size fractions. All of H3A2 was ground and sieved to  $<150\text{-}\mu\text{m}$ . Because sample quantities were limited, we were able to obtain major element data for only a bulk sample of H11A (Table 11). We also obtained a rectangular piece ( $\sim 0.5 \times 1.5 \times 5$  cm) of iron shale (oxidized iron meteorite; sample MCIS1) that was collected by J. H. Jones on an alluvial fan south of the south rim of Meteor Crater (circa 1978). We ground a portion of the slab to a  $<150\text{-}\mu\text{m}$  powder.

XRD spectra for the  $<150\text{-}\mu\text{m}$  size fractions of MCIS1, H3A1, H3A2, and H11A are shown in Figure 21. The iron shale (MCIS1) is predominantly maghemite, although very weak lines from quartz and goethite are present. The absence of the tetragonal superlattice lines implies that cation vacancies are not ordered. Because the iron meteorite contains Ni, MCIS1 may actually be a maghemite-rich solid solution of maghemite and trevorite ( $\text{NiFe}_2\text{O}_4$ ). The XRD patterns of maghemite and trevorite are very similar. The Mössbauer spectrum of MCIS1 (Figure 22) shows a single-sextet pattern whose Mössbauer parameters are characteristic of maghemite (Table 2). Asymmetric broadening toward zero velocity is indicative of vacancy disorder and/or impurity-ion substitution. This piece of

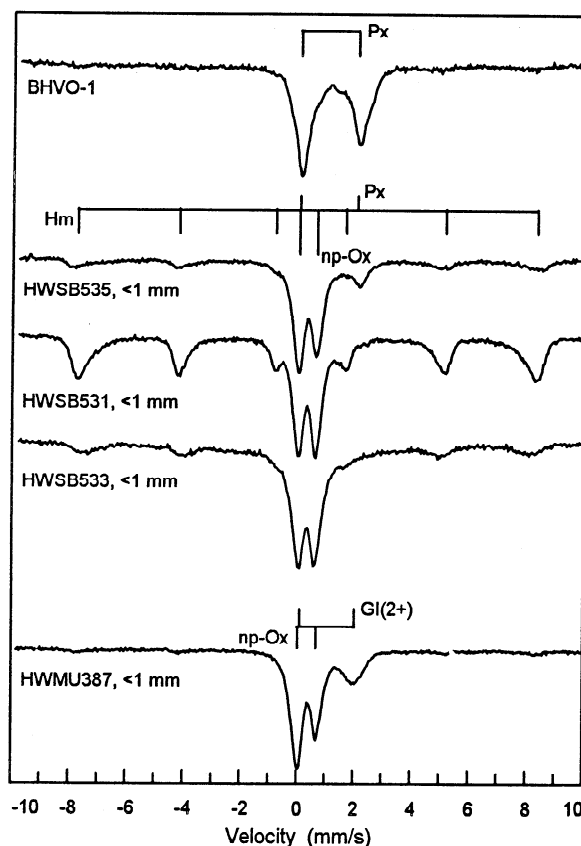


**Figure 18.** Mössbauer spectra (293 K) for Hawaiian basalt BHVO-1, representative Kilauea steam vent samples (HWSB535, HWSB531, and HWSB533), and Mauna Ulu steam vent sample HWMU387. The basalt spectrum is dominated by  $\text{Fe}^{2+}$  in pyroxene. HWSB535 is characterized by a pyroxene doublet, a hematite sextet, and a ferric doublet resulting from np-Ox. HWSB531 and HWSB532 are characterized by different proportions of the hematite sextet and the np-Ox ferric doublet. The spectrum of HWMU387 has a ferrous doublet associated with glass and a ferric doublet resulting from np-Ox.

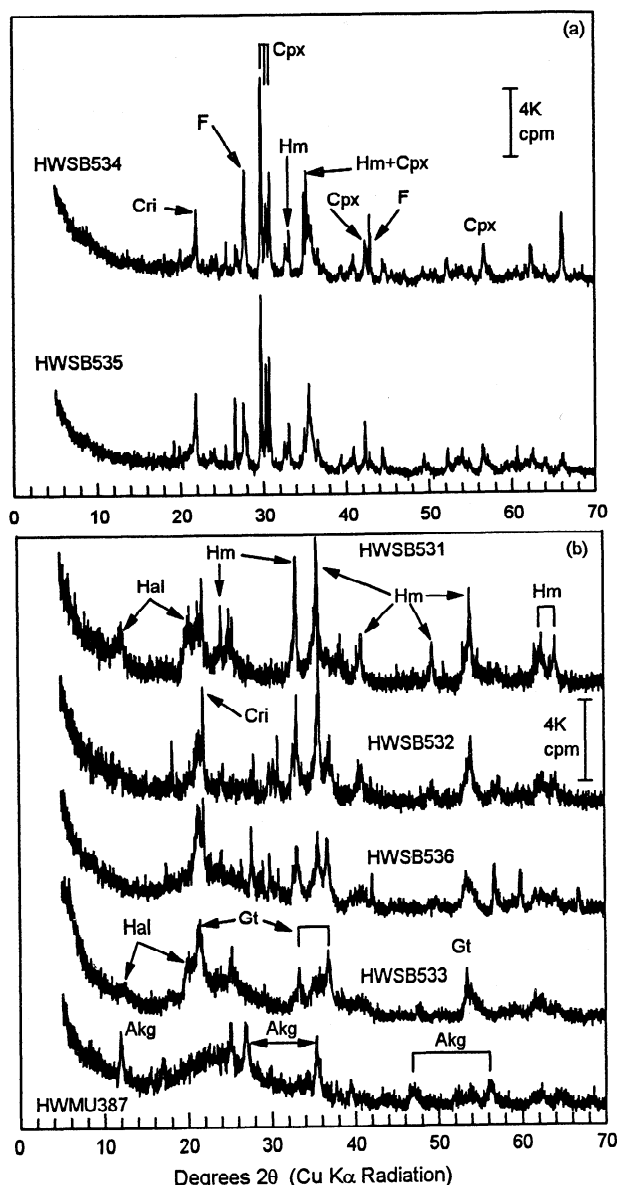


**Figure 19.** Representative XRD powder patterns (293 K) for Sulfur Bank and Mauna Ulu and steam vent samples. (a) Samples HWSB534 and HWSB535 are rich in clinopyroxene (Cpx) and also contain plagioclase feldspar (F), hematite (Hm), and cristobalite (Cri). (b) Steam vent samples that contain little or no pyroxene and feldspar. The Sulfur Bank samples have variable proportions of hematite and goethite (Gt) with HWSB531 mostly hematite and HWSB533 mostly goethite. Cristobalite and halloysite (Hal) are present in some samples. Akaganéite (Akg) is present in the Mauna Ulu sample.

the impacting iron meteorite (a class IIIA) thus appears to be completely oxidized to maghemite.

XRD patterns of H3A1 and H11A have diffraction lines from pyroxene and quartz but not maghemite. Their Mössbauer spectra (Figure 22) are consistent with pyroxene ( $IS=1.15\pm0.01$  mm/s;  $QS=1.99\pm0.01$  mm/s), olivine ( $IS=1.16\pm0.01$  mm/s;  $QS=2.79\pm0.01$  mm/s), and np-Ox ( $IS=0.36\pm0.01$  mm/s and  $QS=0.69\pm0.01$  mm/s) and also have weak sextets from maghemite. The presence of pyroxene and olivine is perhaps unexpected because the target lithology consists of Moenkopi

Sandstone, dolomitic limestones (Kaibab and Toroweap), and Coconino Sandstone [Shoemaker and Kiefer, 1974; Roddy, 1978]. See *et al.* [1998], who are studying samples from the same suite as ours, found that Meteor Crater impactites contain optically and compositionally homogeneous glass whose composition [Mittlefehldt *et al.*, 1992] requires that meteorite (source of Fe), sandstone (source of Si), and dolomitic limestone (source of Ca and Mg) lithologies participated in its formation. The composition of H11A also requires all three lithologies. Presumably, pyroxene and olivine formed either from glass divitrification or crystallization directly from the impact melt shortly after impact. See *et al.* [1998] note that the near-surface materials of glass impactites are substantially crystallized and contain clastic quartz.

Impactite H3A2 has XRD lines from goethite, maghemite, and quartz but not from pyroxene. Like maghemite, goethite may be an oxidation product of the iron meteorite, or it may result from alteration of ferrous-bearing glass. Evidence for maghemite (sextet) and goethite (relaxed sextet) is also present in the Mössbauer spectrum. Feldspar was not detected in the XRD data for any impactite, presumably because the low concentration of  $Al_2O_3$  (2.94%, Table 11) precluded its formation.

As expected, the low-field susceptibilities of the maghemite-rich samples (MCIS1 and H3A2) are very high ( $380\times10^{-6}$  and  $160\times10^{-6}$  m<sup>3</sup>/kg, respectively). The other two impactites (H3A1 and H11A), with minor amounts of maghemite as indicated by Mössbauer data, have values of  $\chi_{lf}$  ( $16\times10^{-6}$  and  $11\times10^{-6}$  m<sup>3</sup>/kg, respectively) that are more than a factor of 10 less than the maghemite-rich samples.

IMP-equivalent spectral data for Meteor Crater iron shale and impactites are shown in Figure 23. High-resolution 350- to 2100-

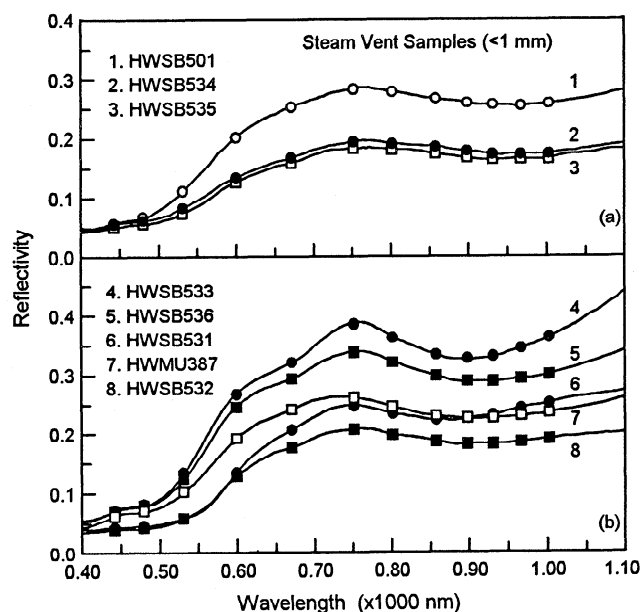


**Figure 20.** High-resolution and IMP-equivalent spectral data (293 K) for steam vent samples (<1-mm size fraction). (a) Clinopyroxene-rich samples have a ferric absorption edge between 445 and 750 nm and a poorly defined minimum between 930 and 965 nm from pyroxene. (b) In agreement with XRD data, pyroxene-poor samples (Sulfur Bank) are characterized by hematite-like spectra (HWSB531) with a minimum near 860 nm to goethite-like spectra (HWSB533) with a minimum near 900 nm. The spectrum of HWMU387 is consistent with the akaganéite observed in XRD data (minimum near 915 nm).

**Table 11.** Multispectral, Magnetic, and Chemical Data for Meteor Crater Impactites and Rocks with Alteration Rinds

	H3A1 Meteor Crater			H3A2 Met. Crater	H11A Meteor Crater			MCIS1 Met. Crater	WD232 Meridan, CN Powder	M1497 Munro, CD Powder
	1-4 mm	1000 $\mu\text{m}$	<150 $\mu\text{m}$		5-10 mm	1000 $\mu\text{m}$	<150 $\mu\text{m}$			
Wavelength <sup>a</sup> , nm										
445	0.063	0.049	0.058	0.040	0.068	0.060	0.076	0.038	0.270	0.453
480	0.070	0.056	0.071	0.045	0.074	0.067	0.092	0.039	0.294	0.481
530	0.088	0.077	0.110	0.066	0.089	0.085	0.130	0.046	0.317	0.508
600	0.125	0.123	0.200	0.123	0.119	0.114	0.199	0.068	0.324	0.499
670	0.140	0.147	0.253	0.161	0.131	0.124	0.229	0.100	0.320	0.475
750	0.147	0.163	0.288	0.192	0.136	0.129	0.247	0.129	0.325	0.467
800	0.146	0.162	0.293	0.193	0.132	0.129	0.252	0.138	0.332	0.460
860	0.141	0.153	0.287	0.182	0.129	0.126	0.251	0.133	0.314	0.439
900	0.135	0.147	0.278	0.175	0.122	0.121	0.244	0.131	0.297	0.421
930	0.130	0.142	0.271	0.173	0.115	0.115	0.234	0.127	0.287	0.407
970	0.125	0.138	0.264	0.172	0.109	0.109	0.222	0.123	0.285	0.395
1005	0.123	0.137	0.263	0.174	0.106	0.105	0.216	0.122	0.289	0.390
Magnetic Properties										
$J_s$ , Am <sup>2</sup> /kg	--	2.42	2.27	25.5	--	1.68	1.84	50.1	--	--
$\chi_{lf}$ , 10 <sup>-6</sup> m <sup>3</sup> /kg	16.0	18.4	13.5	160	11.0	10.5	11.6	306	9.27	0.26
Chemical Composition, %										
SiO <sub>2</sub>	--	--	--	--	48.97	--	--	0.60	52.04	51.02
TiO <sub>2</sub>	--	--	--	--	0.20	--	--	0.05	1.06	0.72
Al <sub>2</sub> O <sub>3</sub>	--	--	--	--	2.94	--	--	0.22	13.87	13.57
Fe <sub>2</sub> O <sub>3</sub> T	--	--	--	--	25.73	--	--	97.89	14.16	12.69
MnO	--	--	--	--	0.08	--	--	0.00	0.23	0.21
MgO	--	--	--	--	8.36	--	--	0.11	5.67	8.84
CaO	--	--	--	--	12.17	--	--	0.70	9.89	10.31
Na <sub>2</sub> O	--	--	--	--	0.09	--	--	0.05	2.31	1.74
K <sub>2</sub> O	--	--	--	--	0.32	--	--	0.03	0.57	0.58
P <sub>2</sub> O <sub>5</sub>	--	--	--	--	0.45	--	--	0.32	0.13	0.05
V, $\mu\text{g/g}$	--	--	--	--	<3	--	--	21	333	264
Cr, $\mu\text{g/g}$	--	--	--	--	107	--	--	21	43	363
Total	--	--	--	--	99.31	--	--	99.98	99.93	99.73
LOI	--	--	--	--	1.40	--	--	3.97	1.93	3.50
SO <sub>3</sub>	--	--	--	--	--	--	--	--	--	--
FeO	--	--	--	--	16.72	--	--	2.09	10.06	9.90
Fe <sub>2</sub> O <sub>3</sub>	--	--	--	--	7.15	--	--	95.57	2.98	1.69
Fe <sup>3+</sup> /Fe <sup>2+</sup>	--	--	--	--	0.385	--	--	41.2	0.267	0.154

<sup>a</sup>Values given for each wavelength are the reflectivity (equivalent IMP multispectral data).

nm spectra show that the ferrous minimum for the pyroxene-bearing impactites is near 1000 nm, which is expected for high-Ca pyroxene [Cloutis and Gaffey, 1991]. The negative spectral slope near 1000 nm in IMP-equivalent spectra of H3A1 and H11A results from the high-energy wing of this band. Although the general increase in reflectivity between 400 and 750-800 nm implies the presence of ferric iron, its mineralogy is not clearly indicated in the reflectivity spectra. The only sample where a particular ferric mineral is indicated in reflectivity data is H3A2 (<150  $\mu\text{m}$ ), where the T1 near 930 nm and M1 near 800 nm are consistent with the maghemite observed in XRD and Mössbauer data (see Figure 3).

## 8. Alteration Rinds on Rocks

Rocks exposed on the Martian surface will tend to have dust coatings and will interact with their chemical and physical environment and potentially develop alteration rinds on their exterior. If rinds and/or coatings are present, data obtained from analyses at rock surfaces (i.e., IMP spectral and APXS elemental data) will preferentially report rind/coating properties and not interior rock properties [e.g., Crisp, 1998]. The magnitude of the

influence of a rind and/or coating depends on their combined thickness and the sampling depth of the analysis technique. We investigated the effect of rinds on the optical and Mössbauer properties of two rocks (a basalt and a basaltic komatiite) which have both fresh and altered surfaces to determine if a strong ferric signature in optical spectra necessarily corresponds to a completely oxidized surface. Dark, fresh surfaces were obtained by breaking the rocks. Altered surfaces, which were brown to reddish brown in color, were produced by unknown natural processes at some unknown time in the past. Reflectivity spectra were obtained for both altered and unaltered surfaces and for powders obtained from interior chips with no visibly altered material. Thickness of alteration rinds were estimated using a binocular microscope and calibrated micrometer disk with 50- $\mu\text{m}$  divisions. Transmission Mössbauer spectra were obtained for the powder, and backscatter Mössbauer spectra were obtained for the same exterior surfaces as reflectivity data. Major element compositions for the bulk rocks are given in Table 11.

### 8.1. Rock WD232 (Basalt)

WD232 is a hand specimen of basalt from Meridan, Connecticut (Ward's Scientific). One side is a brown-colored

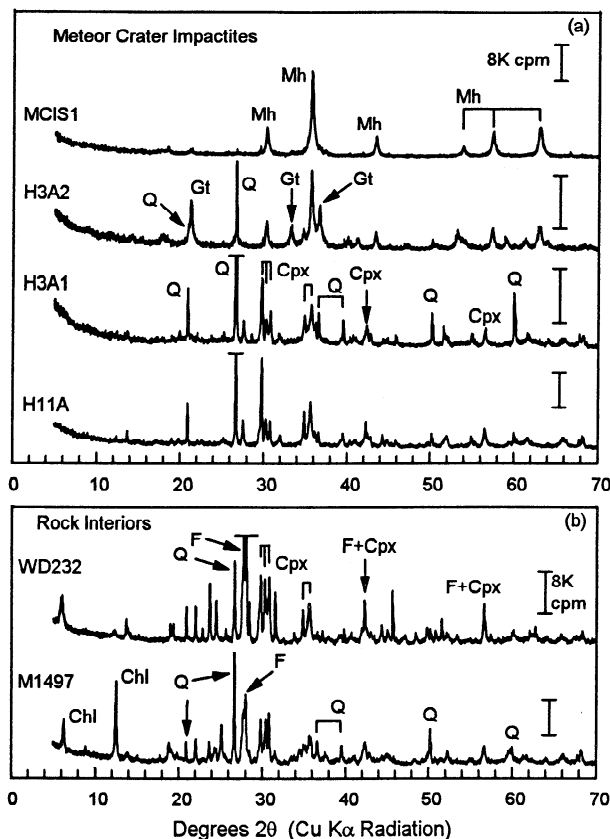


**Figure 21.** (a) XRD powder patterns (293 K) of iron shale and impactites from Meteor Crater. Iron shale (MCIS1) is essentially pure maghemite (Mh). Impactite H3A2 is a mixture of goethite (Gt), quartz (Q), and maghemite. Impactites H3A1 and H11A contain pyroxene (Cpx) and quartz. (b) XRD powder patterns of samples from the interior portions of rocks WD232 (basalt) and M1497 (basaltic komatiite). The WD232 spectrum shows the presence of plagioclase feldspar (F), pyroxene, quartz, and chlorite (Chl). For M1497, different proportions of the same minerals are present.

altered surface whose thickness was estimated to be  $200 \pm 20 \mu\text{m}$ . XRD (Figure 21) and transmission Mössbauer (Figure 24a) data of a powder obtained from interior rock chips show that the interior mineralogy is primarily plagioclase, quartz, pyroxene, and magnetite. The backscatter Mössbauer spectrum of the freshly broken surface is essentially equivalent to the transmission spectrum; both are dominated by  $\text{Fe}^{2+}$  in pyroxene. The backscatter spectrum of the altered surface shows the pyroxene lines and a doublet from octahedrally coordinated  $\text{Fe}^{3+}$ . The ferric doublet is equivalent to the ones we observe in palagonitic tephra and probably results from nanophase ferric oxide particles associated with an unknown amount of water. It is also possible that some of the  $\text{Fe}^{2+}$  in the pyroxene oxidized and is present at lattice sites as paramagnetic  $\text{Fe}^{3+}$ . In either case, the ferric doublet is a product of hydrolytic alteration of exterior rock surfaces.

The high-resolution reflectivity spectrum (350–2100 nm) of unaltered powder of WD232 has a well-defined minimum at 970 nm, which is indicative of high-Ca pyroxene [e.g., Cloutis and Gaffey, 1991]. The high-energy wing of this band is apparent in the IMP-equivalent spectra in Figure 24b. There is also a shallow minimum near 670 nm, which probably results from a

$\text{Fe}^{2+} \rightarrow \text{Fe}^{3+}$  charge transfer band. The same features are present in the spectrum of the fresh rock surface, but the spectral contrast is lower. Spectral evidence for pyroxene is not present in the IMP-equivalent spectrum for the altered surface. The shallow minimum near 900 nm, reflectivity maximum near 800 nm, and absorption edge from 400 to 800 nm are characteristics of  $\text{Fe}^{3+}$ , not  $\text{Fe}^{2+}$ ; ferrihydrite, for example, is a possible interpretation of this spectrum (Figure 24b) that is consistent with the Mössbauer data.

## 8.2. Rock M1497 (Basaltic Komatiite)

M1497 is a hand specimen of basaltic komatiite collected in Munro Township (Canada) in 1978 (G. E. Lofgren). It has three different altered surfaces and a broken surface dating from 1978 when the rock was collected. The thicknesses of the three rinds are  $<50 \mu\text{m}$ ,  $200 \pm 50 \mu\text{m}$ , and  $5.5 \pm 0.8 \text{ mm}$ . Lichens on the surface of the thickest rind were removed with a soft nylon brush without destroying the surface. The two thicker rinds appeared to have a redder-colored layer  $<50 \mu\text{m}$  thick at the top surface. XRD (Figure 21) and transmission Mössbauer (Figure 25a) data of a powder obtained from interior rock chips show that the interior mineralogy is primarily quartz, plagioclase, chlorite, and pyroxene.

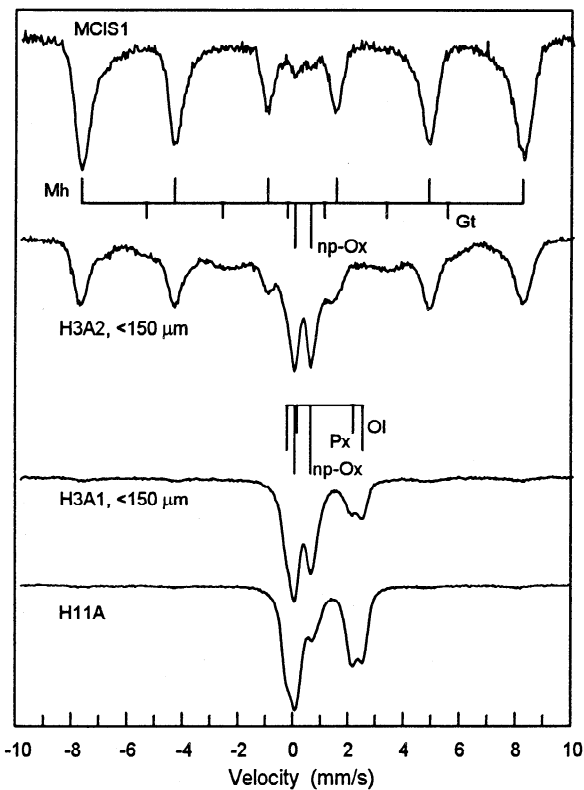


**Figure 22.** Mössbauer spectra (293 K) for samples from Meteor Crater. The maghemite sextet is the dominant feature present in the spectrum of iron shale (MCIS1). The maghemite and a partially relaxed sextet from goethite are present for impactite H3A2; the goethite assignment is based on XRD data and the Mössbauer spectrum for disordered goethite 6D-2 (Figure 2a). Impactites H3A1 and H11A are characterized by ferrous doublets from pyroxene and olivine and a ferric doublet resulting from np-Ox.



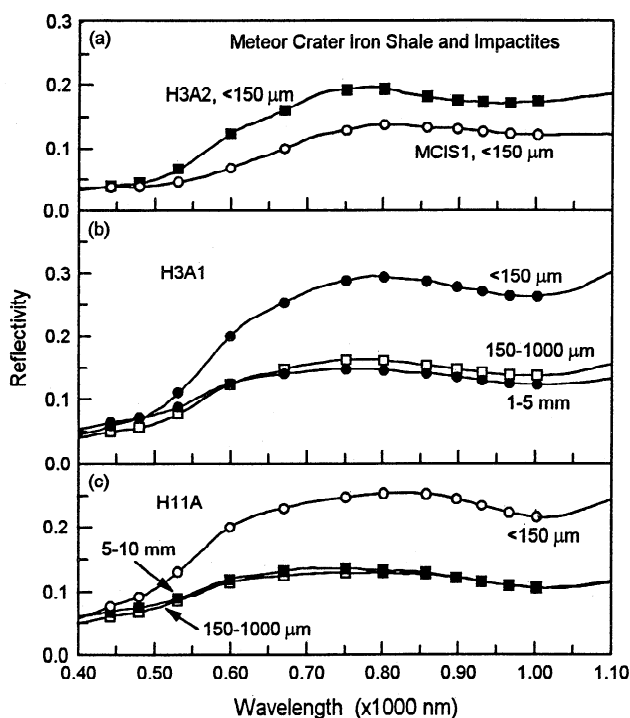


**Figure 23.** High-resolution and IMP-equivalent reflectivity spectra (273 K) for samples from Meteor Crater. (a) Iron shale MCIS1 is essentially monomineralic maghemite and impactite H3A2 is maghemite, goethite, and quartz, on the basis of XRD and Mössbauer data. (b) Impactite H3A1 is pyroxene, quartz, and goethite. The 1- to 5-mm spectrum corresponds to the original impactite beads. The other two spectra are for size separates made by grinding and sieving. (c) Impactite H11A is mostly clinopyroxene and quartz. The 5- to 10-mm spectrum corresponds to the original impactite beads. All impactite spectra are characterized by a ferric absorption edge (445 to ~800 nm). The minimum for ferrous iron in pyroxene occurs at ~1000 nm and is not observed for H3A1 and H11A in IMP-equivalent spectra. The weak minimum near 930 nm in H3A2 results from goethite and/or maghemite. MCIS1 has no minimum even though it is essentially monomineralic maghemite, suggesting the minimum in H3A2 results from goethite.

Backscatter Mössbauer spectra for the unaltered surface and the 200-μm and 5.5-mm rinds are shown in Figure 25a. The backscatter spectrum of the 1997 surface is equivalent to the transmission spectrum of a powder of unaltered interior chips. Two overlapping doublets are present and correspond to ferrous iron in the pyroxene and chlorite observed in the XRD data. The spectrum for the 200-μm rind is the same except that, analogous to WD232, a doublet from octahedrally coordinated ferric iron in an alteration product is also present. Similarly, the spectrum for the 5.5-mm rind contains a doublet from a ferric alteration product. Note, however, that the outer ferrous doublet is relatively less intense than the inner one in comparison to spectra for other rinds and interior rock. Without more detailed analyses of the rind, we cannot explain the difference. Possibly, alteration preferentially removed the ferrous-bearing material associated with the outer doublet (chlorite), or the rind initially had a distinctly different ferrous mineral composition in comparison to interior rock. The latter could happen if the surface represented by thick rind was the original surface of the flow when it was

extruded and consequently evolved differently than interior material.

IMP-equivalent reflectivity spectra are shown for powdered interior chips and five exterior surfaces of M1497 in Figure 25b. Similar to WD232, the spectrum for the powder has a minimum at 1000 nm, so that only the high-energy wing of the band is observed in IMP-equivalent spectra, and a shallow minimum presumably associated with a  $\text{Fe}^{2+} \rightarrow \text{Fe}^{3+}$  charge transfer transition. The 1997 surface and the darker 1978 surface show evidence for both features with reduced spectral contrast. The strength of the ferric absorption edge increases with the thickness of the rind, in qualitative agreement with Mössbauer data. It is difficult to argue convincingly for manifestations of ferrous iron in IMP-equivalent spectra for any of the rinds with the possible exception of the thinnest one (<50 μm). The overall low reflectivity and negative spectral slope longward of 750 nm parallels the spectra of the 1978 and 1997 surfaces and is suggestive of the high-energy wing of a high-Ca pyroxene band. The spectra of the 200-μm and 5.5-mm rinds have positive spectral slopes over the same region, so the suggestion of ferrous iron is not present. The suggestion of a feature near 670 nm in the spectrum of the 5.5-mm rind, which probably results from a  $\text{Fe}^{2+} \rightarrow \text{Fe}^{3+}$  charge transfer transition [e.g., Burns, 1993] based on the spectrum of the powder, could be interpreted (incorrectly) as evidence for a ferric  ${}^6\text{A}_1 \rightarrow {}^4\text{T}_{2g}$  transition.

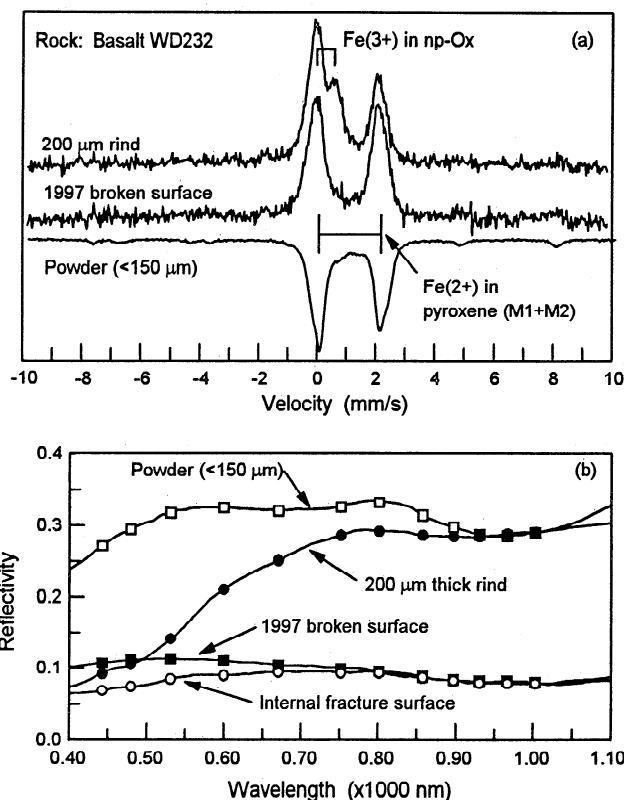


**Figure 24.** (a) Mössbauer and (b) reflectivity spectra (293 K) for a powder (made from internal chips) and fresh and altered surfaces of basalt WD232. Mössbauer spectra of rock surfaces and powder were obtained using backscatter and transmission geometry, respectively. There is no apparent influence of ferrous minerals in the optical spectra of the surface with a 200-μm-thick rind. Mössbauer spectra show, however, that the rind is mostly ferrous iron.

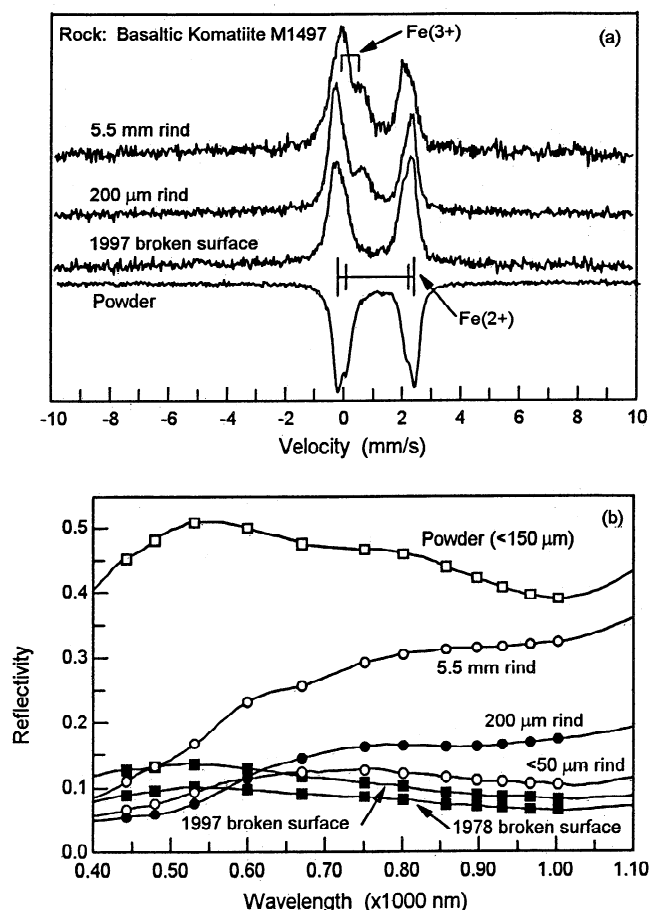


**Figure 25.** (a) Mössbauer and (b) reflectivity spectra (293 K) for a powder (made from internal chips) and fresh and altered surfaces of basaltic komatiite M1497. Mössbauer spectra of rock surfaces and powder were obtained using backscatter and transmission geometry, respectively. The regular increase in reflectivity and strength of the ferric absorption edge with rind thickness (<50 μm to 5.5 mm) implies decreasing influence of ferrous iron with increasing rind thickness. Mössbauer spectra show that, even for the thickest rind, most of the iron within the rind is ferrous.

### 8.3. Reconciliation of Mössbauer and Reflectivity Data

Why do reflectivity spectra of the rinds of both WD232 and M1497 imply predominantly, if not exclusively, ferric mineralogies while Mössbauer spectra indicate predominantly ferrous iron? A simple explanation is that the sampling volume for optical radiation is confined primarily to the ferric-rich rind and that the more energetic 14.4-keV  $\gamma$  rays used in the Mössbauer experiment penetrate the rinds into the ferrous-rich material beneath. We show next that this model is too simplistic.

Buckingham and Sommer [1983] experimentally investigated the penetration depths of optical radiation in fine powders at the centers of the hematite and goethite  $^6A_1 \rightarrow ^4T_{1g}$  transitions near 860 and 900 nm, respectively. The experiments were done by varying the thickness of oxide-phylosilicate powders for different oxide-phylosilicate ratios. They found that 50-μm-thick coatings will block spectral signatures of the substrate. This coating depth is less than the thickness of all of our rinds, except for the <50-μm rind on M1497. The observation implies that our ferric-like reflectivity spectra of rinds were derived entirely from

ferric-rich material within the rind. This is consistent with the observation that the <50-μm rind is the only one for which possible evidence for ferrous iron is indicated.

We calculated penetration depths in the Mössbauer experiment using mass absorption coefficients compiled by McMaster *et al.* [1969] for an energy of 15.0 keV (approximately the energy of the Mössbauer 14.4-keV  $\gamma$  ray), the bulk composition for WD232 (Table 11), and rind/coating densities of 0.4, 1.2, 2.4, and 4.0 g/cm<sup>3</sup>. The results are shown in Figure 26 as a plot of rind/coating thickness versus the percentage of radiation absorbed within the rind. At constant density the calculated lines are insensitive to bulk composition for basaltic materials. Densities between 2.4 and 4.0 g/cm<sup>3</sup> span the range for the dry bulk density of most types of rocks. For example, terrestrial andesites and basalts have dry bulk densities of  $2.65 \pm 0.13$  and  $2.74 \pm 0.47$  g/cm<sup>3</sup>, respectively [Johnson and Olhoeft, 1984]. The value of 0.4 g/cm<sup>3</sup> corresponds to the dry bulk density of our <2-μm powder of palagonitic tephra HWMK600.

The theoretical calculations predict that the 200-μm rinds on WD232 and M1497 will absorb 80-90% of the incident Mössbauer radiation. This is a lower limit because the calculation assumes no penetration into the substrate (which is required to return a substrate spectrum) and it assumes 100% efficiency for backscattering the Mössbauer  $\gamma$  rays. Thus it seems unlikely that the high proportion of ferrous iron in the backscatter spectra of the 200-μm rinds is entirely derived from ferrous iron beneath a rind that contains no ferrous iron. More likely, a better physical model is a rind that contains ferrous minerals that are individually stained by np-Ox along grain boundaries.

Irrespective of the actual internal constitution of the alteration rinds, the observation is that they are more effective in masking the mineralogy of interior rock in the IMP spectral region (445-1005 nm) than in backscatter Mössbauer measurements. Thus rocks on the surface of Mars that have well-developed alteration rinds on the basis of IMP multispectral data may be amenable for analysis of their ferrous minerals by Mössbauer spectroscopy. This is an important consideration for the Athena Precursor

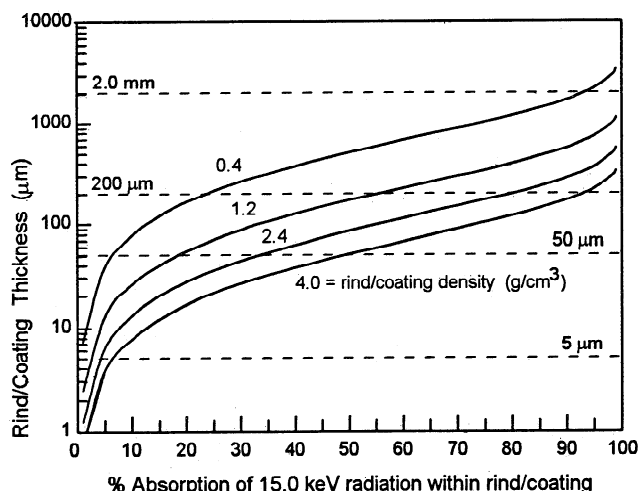


**Figure 26.** Calculated relationship between rind/coating thickness and percent absorption of 15.0-keV  $\gamma$ -rays within the rind/coating for four rind/coating densities. The energy approximates the energy of the  $\gamma$ -rays (14.4 keV) used in the Mössbauer experiment. A rind with a density of 2.4 g/cm<sup>3</sup> and 200 μm thick will absorb ~80% of the  $\gamma$  rays incident from the Mössbauer spectrometer.

**Table 12.** Listing of SNC Meteorite Samples, Their Classifications, and Physical Forms

Sample	Classification and Physical Form
ALH77005	Lherzolite; coarse powder
ALH84001	Orthopyroxenite; fine powder
EETA79001, Lithology. A	Basalt; <45 $\mu$ m
EETA79001	Basalt; <45, 45-90, 90-150 $\mu$ m and 1-10 mm saw fines
Governador Valadares	Clinopyroxenite; 75-150 $\mu$ m
Lafayette	Clinopyroxenite; coarse powder
Nakhla	Clinopyroxenite; coarse powder
Shergotty	Basalt; 45-75 $\mu$ m
Zagami	Basalt; coarse powder and <45 $\mu$ m

Experiment (APEX) and Athena payloads for the Mars Surveyor 2001 and 2003 missions [Squyres *et al.*, 1998, 1999; Morris *et al.*, 1998c], respectively, which are scheduled to carry optical (400-1000 nm) and Mössbauer instrumentation.

## 9. SNC Meteorites

The SNC (Martian) meteorites can be classified into five petrographic groups [McSween, 1994]: dunite (Chassigny), lherzolites (ALH77005 and LEW88516), basalts (Shergotty, Zagami, EET79001, and QUE94201), clinopyroxenites (Nakhla, Lafayette, and Governor Valadares), and orthopyroxenite (ALH84001). As summarized by McSween [1994], the absence of an irradiation history prior to their ejection from Mars implies that the meteorites were not exposed near the surface for any significant length of time. This consideration applies only to the meteorites, and does not exclude the presence of similar rocks on the surface of contemporary Mars. Several studies [McSween, 1994; Mustard and Sunshine, 1995; Mustard *et al.*, 1997] have linked the two-pyroxene mineralogy (low-Ca and high-Ca pyroxene) inferred for relatively unaltered surfaces on Mars from spectral data returned by the Phobos-2 mission (Imaging Spectrometer for Mars (ISM)) with the two-pyroxene mineralogy of the basaltic SNC meteorites. According to Singer and McSween [1993], basaltic Martian meteorites are likely common lava types on the surface of Mars. McSween [1994] notes that spectra resembling nakhlites have apparently not been observed for the Martian surface.

IMP-equivalent spectra for our 12 samples of eight SNC meteorites (Table 12), representing every petrographic class except dunite, are shown in Figure 27. Except for differences in reflectivity resulting from samples with different mean particle diameters, the spectra are consistent with previously published spectra [e.g., Salisbury *et al.*, 1975; Feierberg and Drake, 1980; McFadden, 1987; Morris, 1989; Sunshine *et al.*, 1993; Bishop *et al.*, 1998b, c]. The spectra are typical of those expected for pyroxene, and the position of the so-called 1- $\mu$ m band, which results from the  $^5T_{2g} \rightarrow ^5E_g$  transition of ferrous iron [Burns, 1993], varies in accordance with the Ca content of the pyroxene [e.g., Cloutis and Gaffey, 1991]. The minima (IMP spectra) for ALH84001 and EET79001 (930 nm) and for Zagami and Shergotty (950-965 nm) result from low-Ca pyroxene. The minimum for the nakhlites, which results from high-Ca pyroxene, is beyond the 1000-nm limit of IMP spectra, so that only the low-wavelength wing of the band is observed. There is a strong resemblance between the spectra of the nakhlites and the lepid-

crocites, particularly LPS3 (Figure 3b), even though the former is dominated by ferrous iron and the latter is dominated exclusively by ferric iron. The apparent absorption edge in the nakhlites between 445 and 600 nm, which is not apparent in other SNC meteorites, probably results from ferric-bearing phases observed in these meteorites [e.g., Bunch and Reid, 1975; Treiman *et al.*, 1993].

## 10. Synthesis of Analogue and Meteorite Studies

### 10.1. Mineralogy of Alteration Products

The alteration products we identified in our analogue samples are summarized by sample and by technique in Table 9. With a few exceptions (discussed above), all identifications are based on

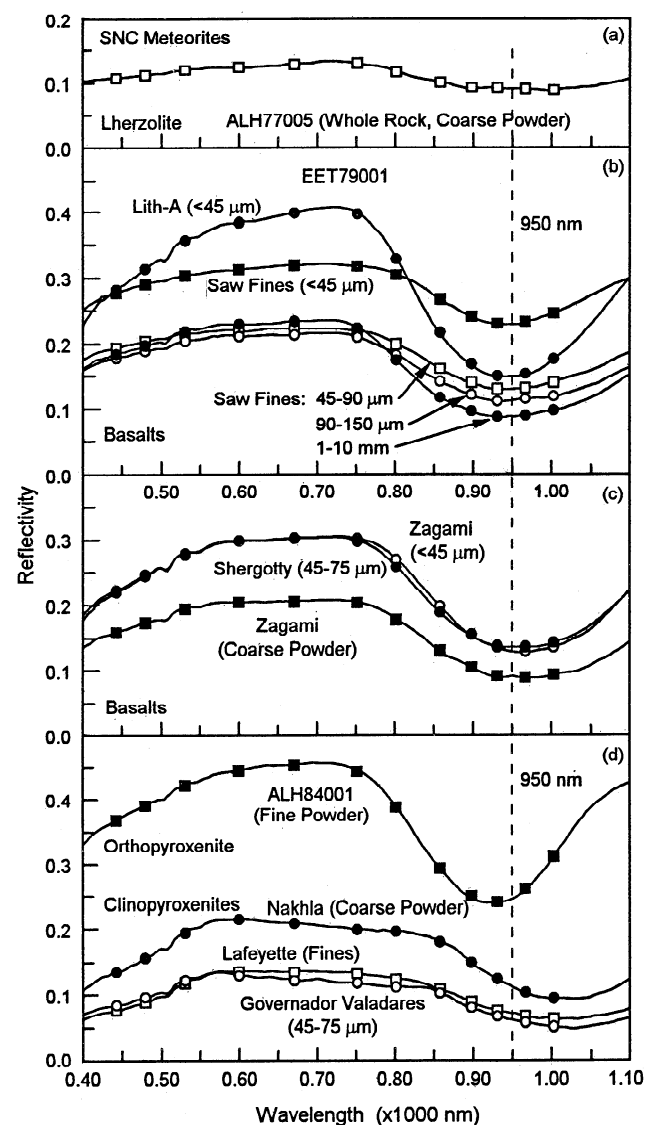


**Figure 27.** High-resolution and IMP-equivalent reflectivity spectra (293 K) for SNC meteorites: (a) ALH77005; (b) EET79001; (c) Shergotty and Zagami; and (d) ALH84001, Nakhla, Lafayette, and Governor Valadares. The spectra are dominated by ferrous minerals having reflectivity minima near 930-945 nm (low-Ca pyroxene in basalts and orthopyroxenite) and at wavelengths near 1000 nm (high-Ca pyroxene/olivine in clinopyroxenites).

analyses of <1 mm samples. The listed minerals were inferred from data obtained by the respective techniques. "Np-Ox" is the general term used for nanoscale ferric oxide particles whose specific mineralogy we cannot identify. For example, an entry of "np-Ox" in Mössbauer spectroscopy implies the observation of a ferric doublet at 293 K with IS~0.33–0.36 mm/s and QS~0.6–0.8 mm/s. In general, the doublet could result from any combination of lepidocrocite, akaganéite, ferrihydrite and schwertmannite (which are inherently small-particle minerals), and nanophase (superparamagnetic) particles of Fe<sub>2</sub>O<sub>3</sub> and FeOOH polymorphs. Slashes mean that the technique cannot distinguish among them. For example, "np-Gt/Sch/Akg" under reflectance spectroscopy means the spectral reflectance data are consistent with any combination of those three minerals. The final column lists the minerals identified when all three techniques are considered. An entry of "np-Ox" in this column results when neither XRD nor spectral reflectance data permitted a more specific assignment (e.g., np-Gt or np-Hm), as is the case for palagonitic tephra. For steam vent and impactite samples, XRD and spectral data sufficiently identified the np-Ox particles. Strictly speaking, however, we cannot tell if all the np-Ox detected in Mössbauer data can actually be assigned to the ferric minerals observed in XRD and/or IMP-style reflectivity data. A doublet-to-sextet transition in Mössbauer spectra at low temperatures would provide more specific mineralogical information about the np-Ox phase. Table 9 is a good example of the need for multiple techniques (both in the laboratory and on a planetary surface) to identify the mineralogy of alteration products in complex natural samples.

Hydrolytic alteration products were identified in palagonitic tephra and in steam vent samples from Sulfur Bank. Np-Ox is the dominant product derived from the alteration of basaltic glass (sideromelane) in palagonitic tephra. The alteration product is easily detected in Mössbauer and reflectivity data, but its manifestation in XRD spectra is not apparent. We looked for, but did not find, evidence of phyllosilicates. We did not see evidence in XRD or Mössbauer data that crystalline phases (e.g., feldspar, olivine, and titanomagnetites) are significantly altered. Apparently, alteration of basaltic glass under subaerial, ambient conditions on the upper slopes of Mauna Kea did not favor formation of iron oxide particles more evolved than np-Ox (e.g., nanophase hematite and/or goethite). In contrast, the steam vent samples from Sulfur Bank are extensively altered. XRD lines for feldspar and pyroxene are very weak or not even present in five of seven samples. Cristobalite is present in five samples. Phyllosilicates (halloysite and smectite) were detected in two samples. Highly disordered goethite and/or hematite, which are evident in the XRD data, are reasonably the source of the superparamagnetic doublets in the corresponding Mössbauer spectra. That is, the doublets are from superparamagnetic particles of hematite and goethite that are crystalline enough to be detected by XRD and not from primitive, XRD-amorphous np-Ox particles like those in palagonitic tephra. The extent of alteration and formation of more crystalline iron oxides and silicates as alteration products is consistent with the hydro-thermal environment in the Sulfur Bank steam vents.

The most common sulfuric alteration product for the 17 sulphatetic tephra was jarosite. Jarosite alone was present in 12 samples, and jarosite plus hematite was identified in two samples. Only two samples did not contain jarosite; alunite and hematite are the alteration products for HWMK508 and HWMK20, respectively. We are uncertain of the ferric alteration product in

the final sulfatetic tephra (HWMK512). Although jarosite is identified in XRD data, the reflectivity spectrum is most consistent with either nanophase goethite, schwertmannite, or akaganéite; the Mössbauer parameter QS is intermediate to jarosite and the other three phases. We did not observe phyllosilicates as an alteration product in any of the sulfatetic tephra samples.

The steam vent sample from Mauna Ulu (HWMU387) was the only sample we encountered with a hydrochloric alteration product (akaganéite). As this FeOOH polymorph is known to form only in environments enriched in chloride ions [e.g., *Cornell and Schwertmann, 1996*], ambient vent gases must have been rich in HCl.

Meteor Crater impactites are distinctly different from the samples just discussed because the precursor silicate lithologies (clinopyroxene and glass) originate in impact, rather than vol-

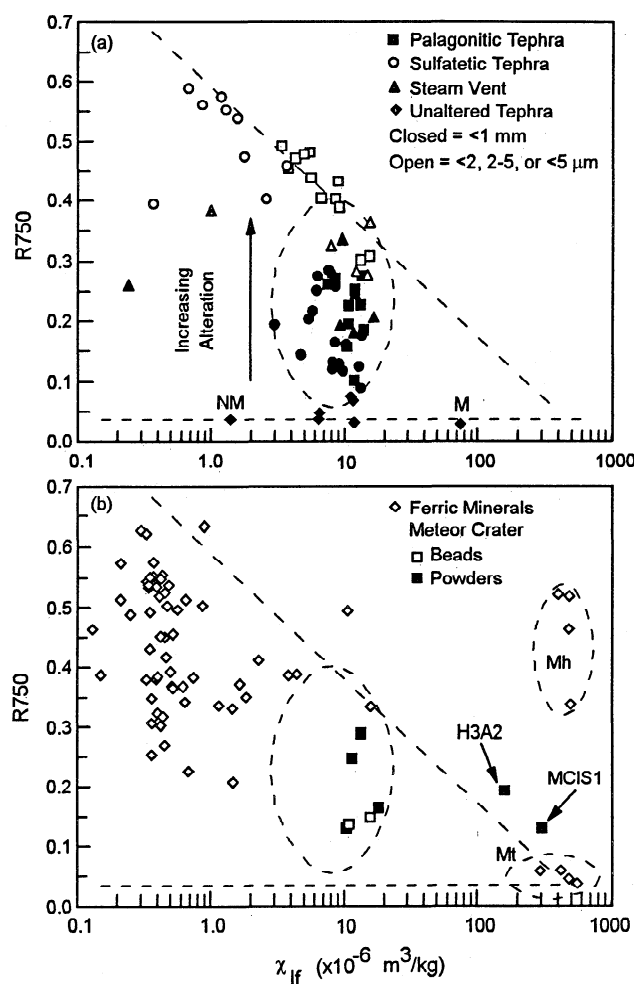


**Figure 28.** R750 versus low-field susceptibility (293 K) for (a) palagonitic, sulfatetic, and unaltered tephra from Mauna Kea and steam vent samples from Kilauea and (b) ferric minerals and samples from Meteor Crater. In Figure 28a the horizontal dashed line is drawn through the unaltered tephra samples (M, magnetic separate; NM, nonmagnetic separate), the diagonal dashed line is drawn through the <2-, 2- to 5-, and <5- $\mu\text{m}$  size fractions, and the dashed ellipse encloses the <1-mm data for palagonitic and sulfatetic tephra. The lines and ellipse are reproduced in Figure 28b for reference. Except for the maghemite-containing analogue samples from Meteor Crater (MCIS1 and H3A2) and magnetite and maghemite minerals, all samples have  $\chi_{lf} \leq 20 \times 10^{-6} \text{ m}^3/\text{kg}$ .

canic, environments. No feldspar is present, reflecting the low  $\text{Al}_2\text{O}_3$  content of the target materials. The low iron content of the target materials implies that virtually all of the iron incorporated into iron-bearing silicate phases and oxide alteration products is derived from the impacting iron meteorite. We identified alteration products as maghemite, goethite, and np-Ox. Maghemite is generally considered to be an alteration product of the iron meteorite. At present we are uncertain whether goethite forms (like maghemite) directly from oxidation and hydroxylation of meteoritic metal or, differently, from alteration of iron-bearing glassy or crystalline silicate phases or both.

## 10.2. Magnetic Properties and Reflectivity

In section 5.3.2 we discussed the relationship between low-field magnetic susceptibility  $\chi_{\text{lf}}$  and R750 for palagonitic tephra. Figure 28a is a version of Figure 11b expanded to include data for sulfatetic tephra and steam vent samples. Data largely overlap for <1-mm size fractions of all three types of altered samples, with ranges for R750 and  $\chi_{\text{lf}}$  equal to 0.1–0.3 and  $3 \times 10^{-6}$  to  $20 \times 10^{-6} \text{ m}^3/\text{kg}$ , respectively, except for two steam vent samples. Unaltered tephra, the precursors of palagonitic and sulfatetic tephra, have lower reflectivities (<0.075) and comparable values of  $\chi_{\text{lf}}$  (average and standard deviation:  $(10 \pm 2) \times 10^{-6} \text{ m}^3/\text{kg}$ ). The extreme values of  $\chi_{\text{lf}}$  for unaltered tephra ( $1.40 \times 10^{-6}$  and  $74.5 \times 10^{-6} \text{ m}^3/\text{kg}$ ) were obtained from nonmagnetic and magnetic fractions (<1 mm) of HWMK513. The wide range in  $\chi_{\text{lf}}$  results from different proportions of strongly magnetic Fe-Ti spinels.

The data plotted in Figure 28a imply an evolutionary sequence: Black, unaltered tephra ( $R750 < 0.075$ ) undergoes oxidative alteration to brighter, finer-grained ferric-rich material. The diagonal dashed line drawn through the data for the <2-, 2- to 5-, and <5- $\mu\text{m}$  size fractions represents the upper limit of R750 for completely altered material for any given value of  $\chi_{\text{lf}}$ . Individual tephra (<1 mm), being mixtures of this fine-grained material and larger particles of partially altered material, plot in the region between the two dashed lines. All our palagonitic and sulfatetic tephra seem to be derived from unaltered tephra that has  $\chi_{\text{lf}} \sim 10 \times 10^{-6} \text{ m}^3/\text{kg}$ , which is also the average value for our <1-mm unaltered tephra. Also, the diagonal line intersects at high susceptibilities the data for black magnetite (Figure 28b), and not the data for relatively bright maghemite, which is consistent with other data showing the strongly magnetic phase is (titano)magnetite.

The average values for  $\chi_{\text{lf}}$  for the <1-mm size fraction and the <2-, 2- to 5-, and <5- $\mu\text{m}$  size fractions of palagonitic tephra are  $(11 \pm 2) \times 10^{-6} \text{ m}^3/\text{kg}$  and  $(8 \pm 5) \times 10^{-6} \text{ m}^3/\text{kg}$ , respectively. Because the two averages are not significantly different, hydrolytic alteration proceeds without significant modification of magnetic properties. In contrast, the corresponding average values for  $\chi_{\text{lf}}$  for sulfatetic tephra are  $(8 \pm 3) \times 10^{-6} \text{ m}^3/\text{kg}$  and  $(1.6 \pm 1.0) \times 10^{-6} \text{ m}^3/\text{kg}$ , respectively. This difference is statistically significant and implies that, under conditions of acid-sulfate alteration, Fe-Ti spinels are soluble and magnetic phases are not precipitated. Thus the strongly magnetic component of palagonitic and sulfatetic tephra (Fe-Ti spinel) originates during crystallization of lava (lithogenic origin) and not as a product of hydrolytic or sulfatetic alteration processes. Presumably, the same conclusion holds for samples from Kilauea steam vents, but we have insufficient samples to test this assumption.

The relationship between R750 nm and  $\chi_{\text{lf}}$  for ferric minerals is shown in Figure 28b. The dashed lines from Figure 28a are reproduced to indicate the relationship of analogue sample and

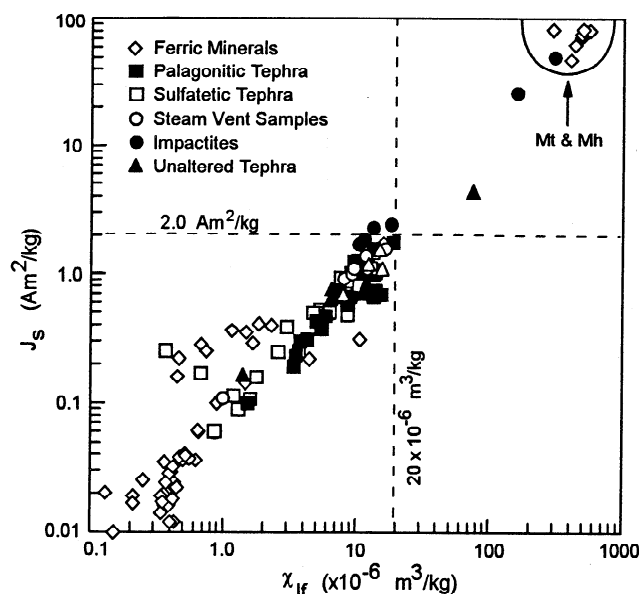


**Figure 29.** Saturation magnetization  $J_s$  versus low-field magnetic susceptibility  $\chi_{\text{lf}}$  (293 K) for ferric minerals and analogue samples.

ferric mineral data. Except for the strongly magnetic magnetites and maghemites, only three ferric mineral samples (hematite HMN3, lepidocrocite LPS2, and ferrihydrite FE152) have susceptibilities comparable to those of <1-mm tephra samples. We suspect that these samples have a magnetic impurity and that their susceptibilities are anomalously high and not representative of their phase. The trend line for the finest size fractions of tephra samples extrapolates at low susceptibility to higher reflectivity than observed for the ferric minerals. Presumably, this is a manifestation of feldspar (a nonmagnetic, high-reflectivity mineral in pure, fine-particle form) in tephra samples and lower  $\text{Fe}_2\text{O}_3$  concentrations in tephra as compared to the ferric minerals.

Data for Meteor Crater samples are also plotted in Figure 28b. The open squares correspond to data for the naturally occurring 1- to 5- and 5- to 10-mm-diameter impactite beads corresponding to samples H3A1 and H11A, respectively. All other data are for size fractions (<150 and 150–1000  $\mu\text{m}$ ) obtained by sieving powders derived by grinding the beads; reflectivity data for the size separates are thus not derived from naturally formed surfaces. The data for the beads and size fractions of H3A1 and H11A plot within the region for the <1-mm tephra samples. According to the Mössbauer and XRD data, these samples contain pyroxene, olivine, and minor maghemite. The other two samples (<150- $\mu\text{m}$  powders of impactite H3A2 and iron shale MCIS1) are strongly magnetic because they contain maghemite (and possibly trevorite). The Meteor Crater samples show that one impact event involving a metallic iron impactor can produce mineralogically diverse particles whose magnetic properties range from weakly to strongly magnetic.

Magnetic parameters inferred for aeolian dust adhering to the permanent magnets on the Viking and Mars Pathfinder landers are the low-field susceptibility and saturation magnetization [Hargraves *et al.*, 1979, 1999; Hviid *et al.*, 1997; Madsen *et al.*, 1999]. As shown by the log-log plot in Figure 29, there is an approximately linear correlation between  $J_s$  and  $\chi_{\text{lf}}$  for our ferric mineral and analogue samples.

### 10.3. Oxidation State and Reflectivity

The inverse relationship between  $R_{750}$  and  $\chi_{\text{lf}}$  for <2-, 2- to 5- and <5- $\mu\text{m}$  size fractions of palagonitic and sulfatetic tephra (Figure 28) and the formation of ferric-bearing phases during alteration of dark ferrous-bearing phases both suggest a positive correlation exists between  $R_{750}$  and  $\text{Fe}^{3+}/\text{Fe}^{2+}$ . Figure 30a is the correlation of  $R_{750}$  and  $\text{Fe}^{3+}/\text{Fe}^{2+}$  for all analogue samples and ferric minerals. Unfortunately, sample availability limited  $\text{Fe}^{3+}/\text{Fe}^{2+}$  chemical analyses for the bright <5- $\mu\text{m}$  size fractions to two samples (HWHP301 and HWMK600). All ferric minerals are arbitrarily plotted at  $\text{Fe}^{3+}/\text{Fe}^{2+}=500$ , except for the samples whose values of  $\text{Fe}^{3+}/\text{Fe}^{2+}$  are known from this study and Morris *et al.* [1985]. For analogue samples, there is a general correlation that can be used to set limits on  $\text{Fe}^{3+}/\text{Fe}^{2+}$  from  $R_{750}$ , but it is too poor to have good predictive capability. A similar relationship holds between  $R_{750}/R_{445}$  and  $\text{Fe}^{3+}/\text{Fe}^{2+}$  (Figure 30b).

There are several reasons for the poor correlation of  $R_{750}/R_{445}$  and  $\text{Fe}^{3+}/\text{Fe}^{2+}$  for analogue samples: (1) The first is mineralogical diversity. Ranges of  $R_{750}$  and  $R_{750}/R_{445}$  for individual ferric minerals are different and very wide. For example, ranges of  $R_{750}$  for jarosites, maghemites, and hema-

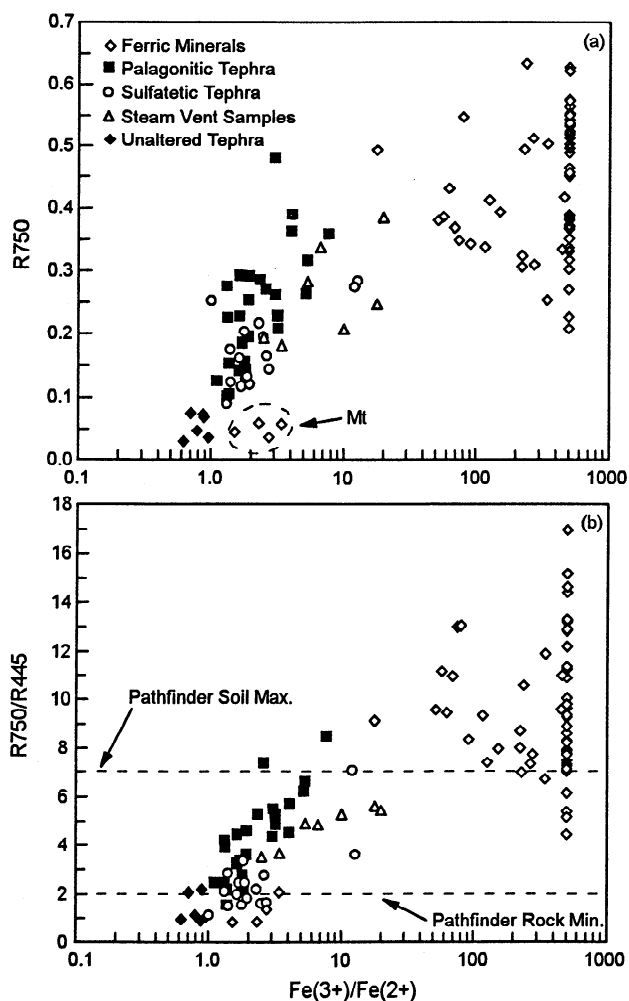


**Figure 30.** Correlation of (a)  $R_{750}$  and (b)  $R_{750}/R_{445}$  with  $\text{Fe}^{3+}/\text{Fe}^{2+}$ . Both  $R_{750}$  and  $R_{750}/R_{445}$  positively correlate with  $\text{Fe}^{3+}/\text{Fe}^{2+}$  because ferrous iron in dark unaltered materials (e.g., Ti-magnetite and glass) is oxidized to bright (at 750 nm) ferric-bearing materials (e.g., np-Ox, goethite, hematite, and jarosite).

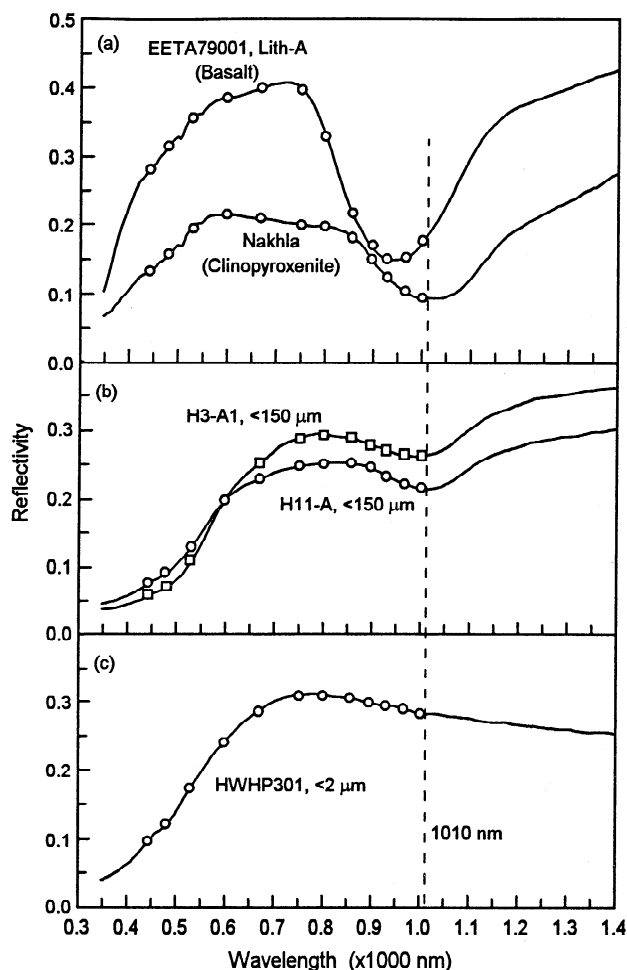


**Figure 31.** Two possible explanations for negative spectral slopes at wavelengths between ~750–800 nm and 1005 nm. One is the low-wavelength (high-energy) wing of a high-Ca pyroxene/olivine band centered at 1000 nm or longer wavelengths as observed for (a) the SNC meteorite Nakhla and (b) impactites from Meteor Crater. The other is a mixture of fine-grained dark (Ti-magnetite) and light (np-Ox) materials as for (c) the <2- $\mu\text{m}$  size fraction of HWHP301.

titic are 0.45–0.62, 0.34–0.52, and 0.21–0.46, respectively. For  $R_{750}/R_{445}$ , the ranges are 4.4–6.4, 9.3–14.4, and 5.3–13.3, respectively. (2) The second is bulk versus surface property. Our values of  $\text{Fe}^{3+}/\text{Fe}^{2+}$  are derived from measurements of bulk sample, but reflectivity measurements are a surface property. Particles with oxidized rinds or thin dust coatings and reduced interiors would appear oxidized to reflectivity measurements and reduced to bulk measurements of  $\text{Fe}^{3+}/\text{Fe}^{2+}$ . (3) And the third is particle size effects. A bulk sample with one magnetite particle 1 mm in diameter has the same  $\text{Fe}^{3+}/\text{Fe}^{2+}$  ratio as the same sample with  $10^{15}$  magnetite particles 10 nm in diameter. Because of the higher number density of particles, the second sample would be darker than the first. In general, we expect a good correlation between either  $R_{750}$  or  $R_{750}/R_{445}$  and  $\text{Fe}^{3+}/\text{Fe}^{2+}$  only for a group of closely related samples.

### 10.4. Ferrous Silicates and Negative Spectral Slopes

The crystalline ferrous silicates identified in our analogue samples are olivine and high-Ca pyroxene. As shown by

Mössbauer and XRD analyses, olivine is more abundant than pyroxene in the palagonitic and sulfatetic tephra from Mauna Kea, high-Ca pyroxene alone is present in some of the Kilauea steam vent samples, and both high-Ca pyroxene and olivine are present in the Meteor Crater impactites. Low-Ca pyroxene was not identified in any analogue sample but is present in SNC meteorites.

High-Ca pyroxene and olivine both have minima from ferrous iron near or somewhat beyond 1000 nm [Cloutis and Gaffey, 1991; Burns, 1993]. Because the spectral range of IMP multi-spectral data is 445–1005 nm, the minima from these minerals cannot be detected. As shown in Figure 31a, the manifestation of such a band is a negative slope in reflectivity spectra that is imparted by the high-energy wing of the band. Figure 31a shows high-resolution spectral data from 350 to 1400 nm (solid lines) and derived IMP-equivalent spectra (open symbols) for two SNC meteorites, EETA79001 (basalt) and Nakhla (clinopyroxenite). Ferrous band minima are well defined at 940 (low-Ca pyroxene) and 1010 nm (high-Ca pyroxene and olivine) in the high-resolution spectra. Figure 31b shows the same behavior for two high-Ca pyroxene samples from Meteor Crater (<150- $\mu$ m size fractions of H3A1 and H11A). The ferrous pyroxene band minimum is just outside the IMP spectral range, resulting in a negative spectral slope extending from 1000 nm to shorter wavelengths.

There are two other possible explanations for negative spectral slopes. Figure 31c shows that the 350- to 1400-nm spectrum of palagonitic tephra HWHP301 (<2  $\mu$ m) has a negative slope from 800 nm to beyond 1400 nm without any evidence for a ferrous band. In this case the negative slope probably results from the presence of fine-grained bright (np-Ox) and dark (titanomagnetite) particles. Similar negative slopes are reported by Morris and Neely [1982] for mechanical mixtures of sub-micron powders of hematite and magnetite. The second possibility is thin coatings of fine ferric-bearing particles (e.g., acolian dust) on dark substrates (e.g., dark rocks) [e.g., Singer, 1982; Singer and Roush, 1983; Fischer and Pieters, 1993]. The negative slope results from a monotonic increase in transparency of the ferric coating with wavelength.

### 10.5. Major Element Fractionation

The fractionation patterns for compositional parameters associated with hydrolytic alteration in the formation of palagonitic tephra and steam vent samples and sulfuric alteration in the formation of jarositic tephra are summarized in Figure 32. Palagonite-A is the average of the four most altered <1-mm palagonitic tephra samples in Figure 6c (HWHP301, HWMK1, HWMK612, and PN-9). It is enriched in TiO<sub>2</sub>, Al<sub>2</sub>O<sub>3</sub>, Fe<sub>2</sub>O<sub>3</sub>T, MnO, and MgO, depleted in SiO<sub>2</sub>, Na<sub>2</sub>O, and K<sub>2</sub>O, and relatively unfractionated in CaO and P<sub>2</sub>O<sub>5</sub>. Palagonite-B is the average for the <2- $\mu$ m size fractions of HWHP301 and HWMK600. Because this size fraction is enriched in the residues of leaching, the fractionation is more extreme than for Palagonite-A. Palagonite-B is strongly enriched in TiO<sub>2</sub>, Al<sub>2</sub>O<sub>3</sub>, Fe<sub>2</sub>O<sub>3</sub>T, MnO, and P<sub>2</sub>O<sub>5</sub> and strongly depleted in SiO<sub>2</sub>, MgO, CaO, Na<sub>2</sub>O, and K<sub>2</sub>O. The apparently anomalous behavior of MgO (enriched in Palagonite-A, depleted in Palagonite-B) can be explained if MgO is leached more slowly than the other depleted elements in Palagonite-A and insoluble MgO-bearing phases are not formed as fine particles in Palagonite-B.

Goulet et al. [1998] report major element data for tholeiitic basalt altered under tropical conditions. The fractionation pattern is similar to what we observed for Palagonite-B. TiO<sub>2</sub>,

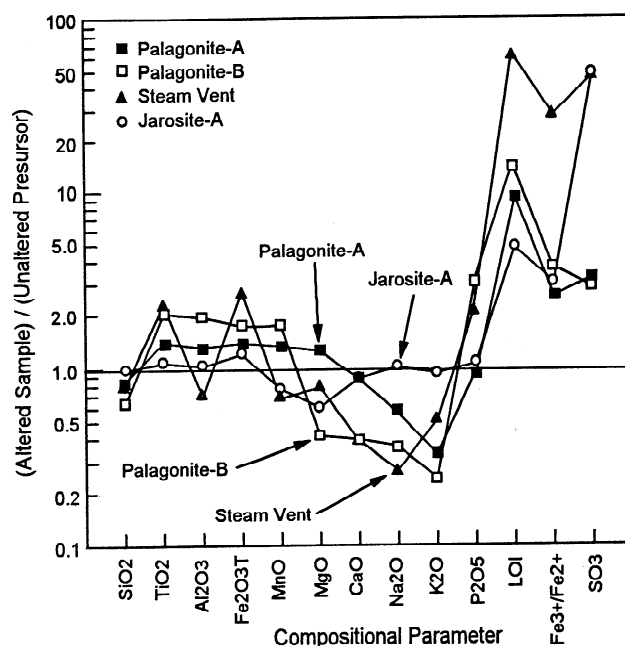


**Figure 32.** Summary of major element fractionation patterns associated with formation of palagonitic tephra, jarositic tephra, and steam vent samples by leaching. Palagonite-A is the average of the fractionation patterns for the <1-mm size fractions of HWHP301, HWMK1, HWMK612, and PN-9. Palagonite-B is the average of the <2- $\mu$ m size fractions for HWHP301 and HWMK600. Jarosite-A is the average of the <1-mm size fractions for HWMK511, HWMK515, and HWMK620.

Al<sub>2</sub>O<sub>3</sub>, Fe<sub>2</sub>O<sub>3</sub>, and MnO are enriched and SiO<sub>2</sub>, MgO, and CaO are depleted in soil relative to unaltered basalt; Na<sub>2</sub>O, K<sub>2</sub>O, and P<sub>2</sub>O<sub>5</sub> analyses were not reported for the soils.

For the steam vent fractionation pattern in Figure 32, all seven samples from Figure 17 were averaged. TiO<sub>2</sub>, Fe<sub>2</sub>O<sub>3</sub>T, and P<sub>2</sub>O<sub>5</sub> are strongly enriched, and all other major elements are moderately to strongly depleted. The magnitude of fractionation for steam vent samples and for Palagonite-B and steam vent samples is comparable for Fe<sub>2</sub>O<sub>3</sub>T and TiO<sub>2</sub>, even though the former were altered at higher temperatures by steam.

Generalizing, removal of soluble species by hydrolytic leaching of basaltic materials under nonmarine conditions typically leaves a residue enriched in TiO<sub>2</sub> and Fe<sub>2</sub>O<sub>3</sub>T and depleted in SiO<sub>2</sub>, Na<sub>2</sub>O, and K<sub>2</sub>O relative to unaltered materials. P<sub>2</sub>O<sub>5</sub> is unfractionated to enriched, and CaO is unfractionated to depleted. Al<sub>2</sub>O<sub>3</sub>, MnO, and MgO are either enriched or depleted, implying their behavior is more sensitive to local conditions. The higher Fe<sup>3+</sup>/Fe<sup>2+</sup> ratios (<1-mm size fraction) for altered samples (1.32–3.08) compared to unaltered samples (0.60–0.96) is evidence that the hydrolytic alteration occurred under oxidizing conditions. The maximum time our palagonitic tephra have undergone hydrolytic alteration is the 4-ka to 66-ka age of Mauna Kea hawaiitic lavas [Porter, 1979; Wolfe et al., 1997].

Jarosite-A in Figure 32 is the average of the three most altered <1-mm jarositic tephra in Figure 12b (HWMK511, HWMK515, and HWMK620). This fractionation pattern is significantly different from the ones for hydrolytic alteration. MgO and MnO are depleted, and all other major elements are either essentially unfractionated or slightly to moderately enriched relative to unaltered tephra. This behavior results because of the relatively

high solubility of Mg and Mn sulfates and the precipitation of Na and K as insoluble jarosites. The high  $\text{Fe}^{3+}/\text{Fe}^{2+}$  ratios for altered relative to unaltered samples (larger by factors of 2.5-30) and the presence of sulfur in high oxidation states (sulfates) imply alteration under oxidizing conditions. Sulfuric alteration probably occurred only during or shortly after deposition of unaltered tephra when Mauna Kea Volcano was active and emitting  $\text{SO}_2$ -rich gases. Since the time of sulfatetic alteration, the sulfatetic tephra experienced environmental conditions similar to palagonitic tephra.

Ponding of leachate solutions from hydrolytic and sulfatetic alteration and subsequent evaporation of volatiles would produce evaporites enriched in the elements that are depleted in palagonitic, steam vent, and sulfatetic tephra. Evaporites rich in  $\text{SiO}_2$ , alkalis, and possibly MgO are the complement of hydrolytic alteration, and evaporites rich in MgO and MnO (as sulfates) are the complement of sulfatetic alteration where jarosites are formed.

## 11. Application to Post-Pathfinder Mars

Data from analogue and meteorite samples can be applied to the multispectral, magnetic, and elemental data returned by Mars Pathfinder in two general ways. (1) The first is phase identification. What silicate and oxide phases can be inferred for the Ares Vallis landing site and what are their distributions? Can primary igneous minerals be identified, or do products of alteration dominate the scene? Are variations in spectral parameters a consequence of many minerals having a range of spectral manifestations? Or do spectral variations result simply from different proportions of a binary mixture whose packing density (from dust to rock) and/or particle diameter are also variable? Are minerals inferred from multispectral data consistent with minerals inferred from the magnetic properties experiment and elemental abundances? (2) The second way is process identification. Do hydrolytic or sulfuric processes dominate? Do specific alteration products imply specific formation pathways? We develop below the implications of our results for Mars Pathfinder. Papers by *McSween et al.* [1999], *Bell et al.* [this issue], and *Madsen et al.* [1999] also address the mineralogy and evolution of rocks, soils, and aeolian dust at the Pathfinder landing site.

### 11.1. IMP Multispectral Data

**11.1.1. Representative Ares Vallis spectra.** The IMP multispectral data used in this study are the multispectral spot (MSS) spectra for 58 surface regions. The MSS number, targeted geologic feature, time of data acquisition, and calibration are discussed by *Bell et al.* [this issue]. Representative spectra for the seven spectral classes of soil at the Mars Pathfinder site according to *Bell et al.* [this issue] are shown in Figure 33a. For comparison, composite spectra for Martian bright and dark regions published by *Mustard and Bell* [1994] are shown in Figure 33b after convolving to IMP band passes.

Like all Martian spectra published to date [e.g., *McCord et al.*, 1977, 1982; *Singer et al.*, 1979; *Bell et al.*, 1990; *Mustard and Bell*, 1994; *Erard and Calvin*, 1997], Pathfinder spectra are characterized by a ferric absorption edge between (IMP wavelengths) 445 and 750-800 nm. Except for Surface Dust, IMP spectra are more like typical Martian dark region spectra because they have negative spectral slopes at wavelengths longer than the reflectivity maximum at 750-800 nm. None of the IMP spectra closely resembles the composite Martian bright region

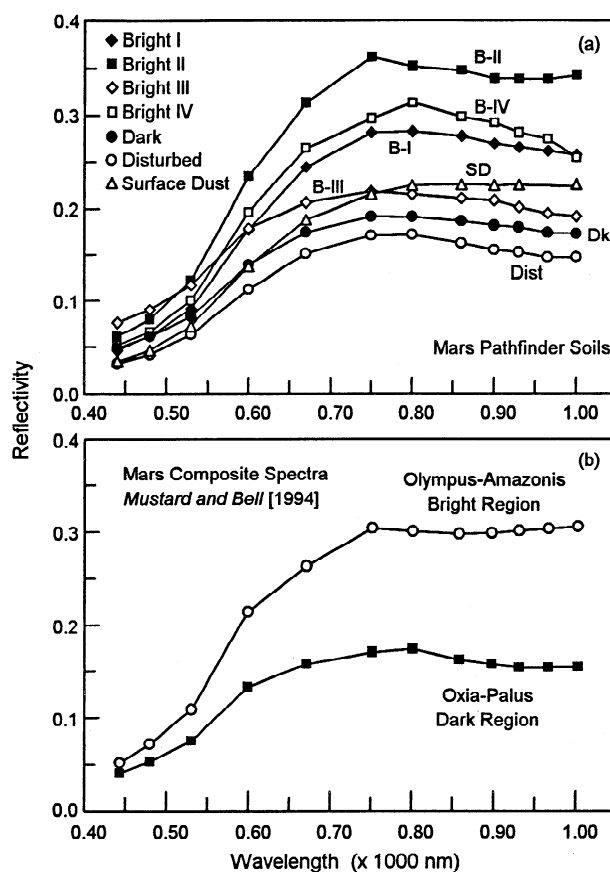


**Figure 33.** (a) IMP multispectral data for seven spectral classes of Mars Pathfinder soils [Bell et al., this issue]. (b) IMP-equivalent multispectral data derived from telescopic and Phobos-2 spectral data [Mustard and Bell, 1994] for Olympus-Amazonsis (bright) and Oxia-Palus (dark) regions of Mars.

spectrum, which has a shallow but well-defined minimum near 860 nm that has been attributed to minor well-crystalline hematite [e.g., *Morris et al.*, 1997]. Bright II soils exhibit evidence for an absorption band in the region between 800 and 1005 nm [Bell et al., this issue].

Comparison of the IMP Martian spectra to equivalent spectra for individual ferric minerals (Figure 3) shows that there is no one-to-one correspondence between IMP spectra and any ferric mineral spectrum. Correspondence is particularly poor for phases with significant spectral contrast of the M1 and T1 spectral features. This includes well-crystalline ferric phases like hematite HMS3, goethite GTS5, lepidocrocite LPS3, akaganéite AKS1, and jarosite JSRKS1 and also nanophase oxide samples like schwertmannite BT-4 and nanophase goethite 4FG-10. Ferric mineral spectra with little M1-T1 spectral contrast, like many of the ferrihydrites, maghemite LPS2-3-265, and schwertmannite 6PM-0, are more similar, but still have significant differences. This may seem like a trivial result because Martian soils are formed in a complex natural environment, and the ferric minerals are either synthetics formed under controlled laboratory or industrial conditions or are naturals present in relatively pure form with respect to their ferric phase. However, it is not unreasonable to anticipate, on a planet where orbital and telescopic spectral observations indicate the presence of hematite [e.g., *Morris et al.*, 1989, 1997; *Bell et al.*, 1990], that there are



local areas where hematite and possibly other ferric minerals might be optically dominant when observations are made at high spatial resolution on the surface. For example, spectra that clearly reflect their hematite (HWMK20) and jarosite (HWMK24) minerals (see Figure 15) are present within meters of each other on Mauna Kea Volcano.

The presence of a band in the 800- to 1005-nm region and structure in the ferric absorption edge (e.g., the bend at 530 nm) imply that well-crystalline iron-bearing minerals are present (potentially identifiable) but at a low level compared with the optically dominant phases that are responsible for the generally featureless ferric absorption edge. Evidence for this includes the mixing experiments of Morris *et al.* [1997] and Morris and Golden [1998], who showed that palagonitic tephra (optically dominated by spectrally featureless np-Ox) plus minor hematite or hematite plus goethite (<5% by weight of sample) can account for the essential features of the Olympus-Amazons spectrum, including the shallow 860-nm minimum, 750-nm reflectivity maximum, and bends near 530 and 620 nm. In sections 11.1.2 through 11.1.6 we use the spectral data for our analogue samples and their relatively well-characterized ferric mineralogy (from Mössbauer and XRD data) to infer mineralogical and other properties (e.g.,  $\text{Fe}^{3+}/\text{Fe}^{2+}$ ) of Pathfinder rocks, soils, and dust from IMP multispectral data.

**11.1.2. Spectral parameters.** On the basis of our studies of analogue and SNC meteorite samples, the seven parameters that we used to quantify spectral variations of Pathfinder soils, rocks, and dust are (1) the reflectivity ( $R_{445}$ ) at a blue wavelength (445 nm); (2) the reflectivity ( $R_{750}$ ) at a red wavelength (750 nm); (3) the red/blue reflectance ratio ( $R_{750}/R_{445}$ ); (4) the IMP wavelength where maximum reflectivity occurs (either 750 or 800 nm); (5) the magnitude of band depth (BD530b) at 530 nm defined as  $1 - (R_{530}/(0.575 \times R_{480} + 0.425 \times R_{600}))$ ; (6) the magnitude of band depth (BD600) at 600 nm defined as  $1 - (R_{600}/(0.507 \times R_{530} + 0.493 \times R_{670}))$ ; and (7) the IMP wavelength for a band minimum occurring between the IMP reflectivity maximum and 1005 nm, the maximum IMP wavelength. See Bell *et al.* [this issue] for a complete listing of IMP multispectral parameters.

The reflectivity at a red wavelength ( $R_{750}$ ) is representative of the intrinsic brightness of rock and soil materials, plus photometric effects. Reflectance at a blue wavelength ( $R_{445}$ ) is, in general, much less variable between Martian rocks and soils [Soderblom, 1992], and it is the IMP wavelength where ferric-bearing phases are the least reflective (Figure 3). The red/blue reflectance ratio ( $R_{750}/R_{445}$ ) indicates the magnitude of the red slope (i.e., the ferric absorption edge) in the region of strong ferric electronic absorptions by ferric-bearing phases (Figure 3). Its magnitude is a complex function of many parameters, including sample mineralogy (both ferrous and ferric minerals), the mineral relative abundance, the physical setting of minerals (e.g., as discrete particles or as components in composite particles), and the size distribution of discrete and composite particles in a particulate material. In this context a rock is a very large particle. The band depth parameters (BD530b and BD600) and wavelengths for reflectivity maxima and band minima are sensitive to the mineralogy of iron-bearing phases. See Bell *et al.* [this issue] for a more detailed discussion of these and other IMP spectral parameters.

**11.1.3. Red/blue ratios, red reflectivity, and oxidation states.** Figure 34 shows that the  $R_{670}/R_{445}$  and  $R_{750}/R_{445}$  red/blue ratios are highly correlated and that either can be used as

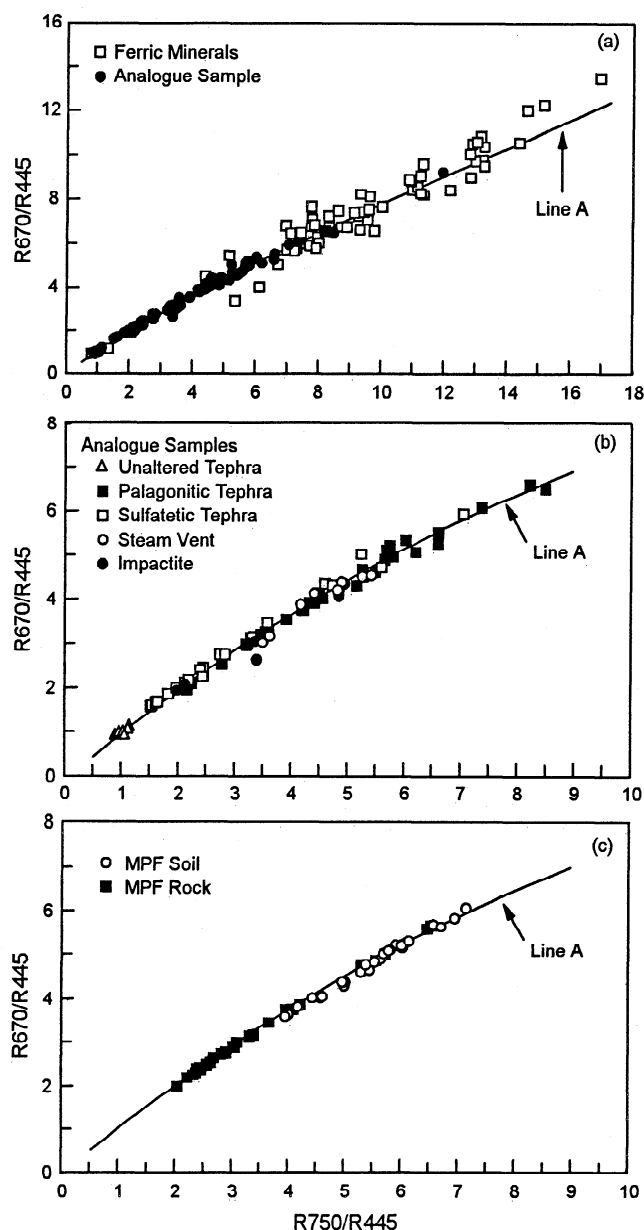


**Figure 34.** Correlation of  $R_{670}/R_{445}$  and  $R_{750}/R_{445}$  reflectance ratios (also known as red/blue ratio or red slope) for (a) ferric minerals and analogue samples, (b) analogue samples by type, and (c) comparison of Pathfinder soils and rocks with analogue samples. Line A in Figure 34a is reproduced in Figures 34b and 34c for reference. The ratios are highly correlated (independent of kind of sample), and either ratio can be used as a measure of the strength of the ferric absorption edge.

a measure of red slope. Figure 34a shows that deviations from the trend line are greater for ferric minerals than for analogue samples. Figure 34b shows data for only analogue samples with the symbols coded for sample origin. The lowest values of both ratios are represented by magnetite powders and unaltered tephra samples. The observation that all samples, independent of mineral composition, plot along the same trend line shows that the trend is insensitive to specific ferric mineralogy. Because of the diverse nature of our samples, we expect that any natural material that is characterized by a ferric absorption edge will fall

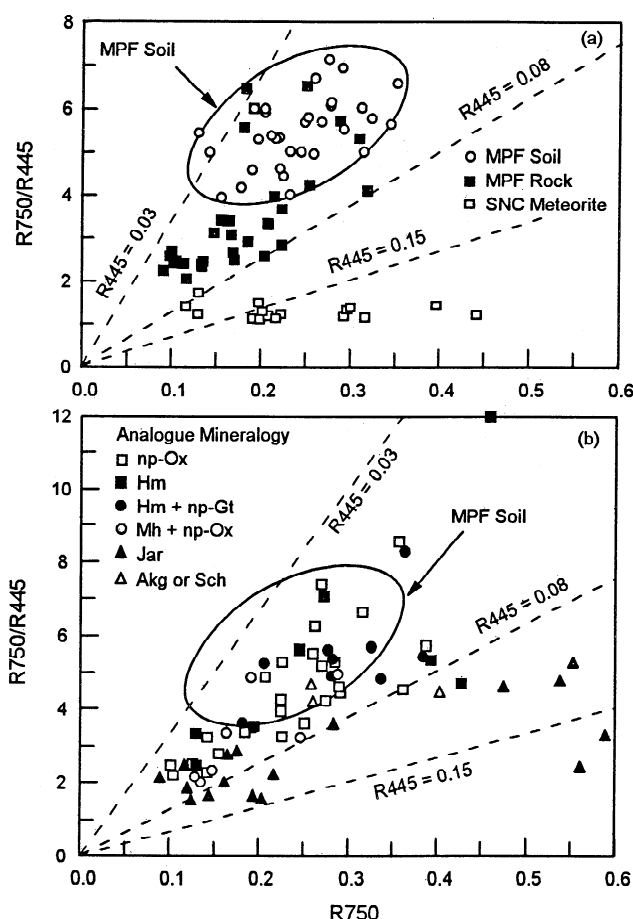


**Figure 35.** Correlation of red slope ( $R750/R445$ ) with  $R750$  (visible brightness) for (a) Pathfinder soils and rocks and SNC meteorites and (b) all size fractions of analogue samples. The solid ellipse enclosing Pathfinder soils in Figure 35a is reproduced in Figure 35b for reference.

along this line. As shown in Figure 34c, the red/blue ratios for Pathfinder soils and rocks are coincident with the same trend line as our analogue samples.

As a group, rocks have systematically lower red/blue ratios than soils; ratios for rocks that plot in the region with soils are actually for rock surfaces with thick soil/dust coatings. In Figure 35a,  $R750/R445$  is correlated with  $R750$  for Pathfinder soils and rocks. A mathematical property of such a plot is that for any value of  $R445$ , the locus of points for all values of  $R750$  is a straight line. The three diagonal dashed lines in Figure 35a correspond to values of  $R445$  equal to 0.03, 0.08, and 0.15. Pathfinder rocks and soils generally have values of  $R445$  between 0.03 and 0.08; the average and standard deviation values for soils ( $0.044 \pm 0.010$ ) are indistinguishable from corresponding values for rocks ( $0.057 \pm 0.013$ ). Soils have  $R750/R445 > \sim 4.0$  with an average value of  $5.7 \pm 1.2$ . Rocks have  $R750/R445 < \sim 4.0$  with an average value of  $2.9 \pm 0.6$ . The factor of  $\sim 2$  difference in the red/blue ratio of Martian soils and rocks has long been attributed on a global scale to the difference between oxidized (ferric rich), fine-grained soil and relatively unoxidized (mafic rich) soils and rocks [e.g., Adams and McCord, 1969; Bell et al., 1990; Soderblom, 1992; Bell, 1996]. For comparison, SNC meteorites, whose spectra are not characterized by a significant ferric absorption edge, have an even lower  $R750/R445$  ratio ( $1.3 \pm 0.2$ ).

The wide and narrow ranges for  $R750$  and  $R750/R445$  for SNC meteorites (Figure 35a) imply that  $R750/R445$  is the better of the two parameters to use for qualitative estimates of the  $Fe^{3+}/Fe^{2+}$  ratio for Pathfinder rocks and soils.

If we assume that all Pathfinder rocks are spectrally contaminated by ferric-rich dust and that all soils are spectrally contaminated by ferrous-rich rock particles, we can estimate the upper and lower limits of  $Fe^{3+}/Fe^{2+}$  for rock and soil, respectively, from values of  $R750/R445$  (see section 11.1.4). The upper limit for rocks is the minimum  $R750/R445$  value observed for all Pathfinder rocks ( $R750/R445 = 2.0$  for Shark rock). The lower limit for soil is the maximum value observed for all Pathfinder soils ( $R750/R445 = 7.0$ ). On the basis of analogue samples in Figure 30b, the estimated ranges of  $Fe^{3+}/Fe^{2+}$  for uncontaminated rock and soil are within the ranges 0.7–3 and 3–20, respectively. Analogue samples, and not individual ferric minerals, were used for the estimate because they, like Pathfinder rocks and soils, are compositionally and mineralogically complex samples. Although the estimates of iron oxidation states are broad, they are still observational evidence that the Pathfinder rocks contain reduced iron (e.g., ferrous silicates and Fe-Ti magnetites) and that the soils, by comparison, are oxidized.

Figure 35b shows the correlation of  $R750/R445$  and  $R750$  for analogue samples. The symbols are coded for mineralogy, not type of sample, using data from Table 9. Although not apparent in Figure 35b, the finest size fractions ( $<5$ , 2–5, and  $<2 \mu m$ ) generally have larger values of both  $R750$  and  $R750/R445$  compared to  $<1$ -mm size fractions. Except for jarositic samples, values of  $R445$  for ferric minerals generally plot between 0.03 and 0.08. Excluding jarositic tephra and jarosites, the average and standard deviation values of  $R445$  for analogues (58 samples) and ferric minerals (63 samples) are  $0.061 \pm 0.018$  and  $0.044 \pm 0.014$ , respectively. The corresponding values for jarositic tephra (17 samples) and jarosite minerals (3 samples) are  $0.099 \pm 0.048$  and  $0.111 \pm 0.030$ . Thus the only meaningful mineralogical distinction that can be made on the basis of  $R750/R445$  and  $R750$  correlations is between jarosites and all the other ferric-bearing analogue samples we studied.

The region occupied by the Pathfinder soils in Figure 35a is indicated by the ellipse in Figure 35b. The average value of  $R445$  for analogue samples excluding jarositic tephra ( $0.061 \pm 0.018$ ) is, within the standard deviation, the same as the average for Pathfinder soils ( $0.044 \pm 0.010$ ). The implication is that only jarosite seems an unlikely interpretation for Pathfinder multispectral data.

**11.1.4. Structure of the ferric absorption edge.** Band depths BD530b and BD600 provide information about the structure of the ferric absorption edge. Both parameters can be positive or negative depending on the deviation from reference lines. As shown in Figure 36a, hematites, ferrihydrites, goethites and lepidocrocites (both well-crystalline), and jarosites fall into nonoverlapping regions on the basis of their values of BD600 and BD530b. Another region encloses data for nanophase goethite, akaganéite, schwertmannite, and maghemite. Additional data may justify separating these minerals into different regions, but for the present we consider them together. This region and that for ferrihydrite partially overlap, with the maghemites generally plotting in the intersection of the two regions. Although we do not have data, disordered lepidocrocite may also plot in the np-Gt/Akg/Sch/Mh region (by analogy with goethite). The regions for other phases, like jarosite and maghemite, might expand if more samples were analyzed.

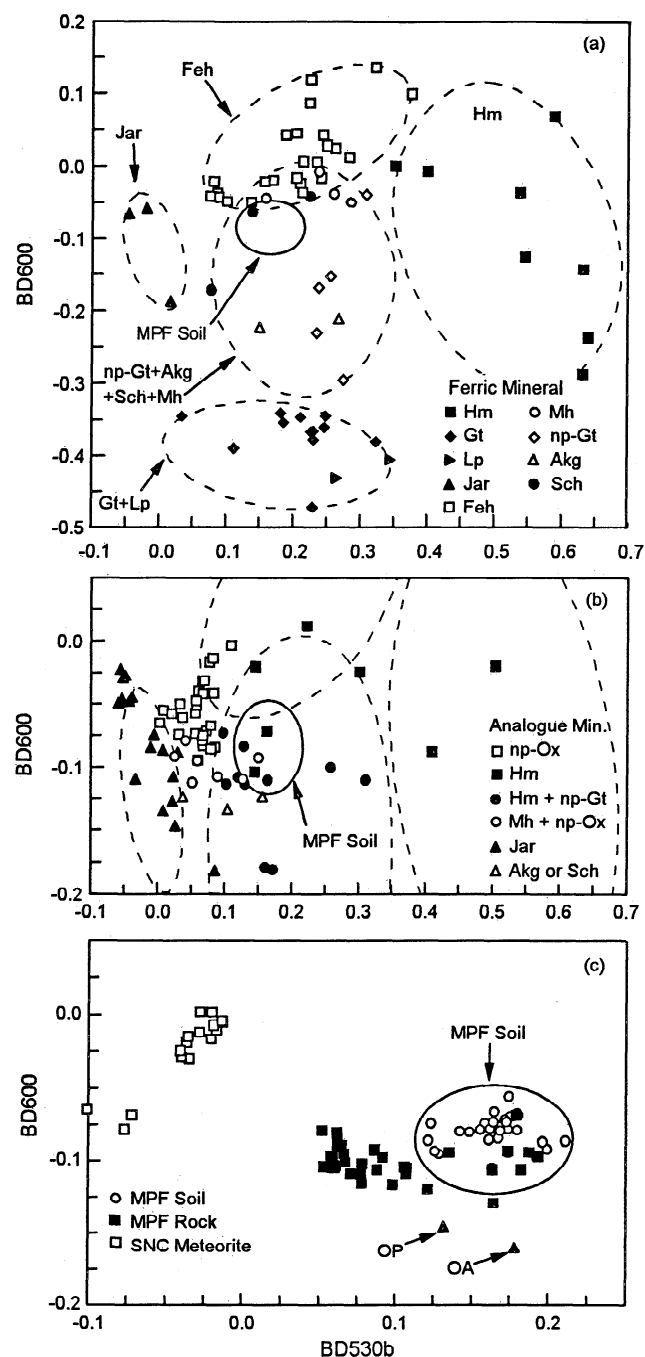


**Figure 36.** Correlation BD600 and BD530b for (a) ferric minerals, (b) analogue samples, and (c) Pathfinder soils and rocks and SNC meteorites. The regions occupied by the ferric minerals in Figure 36a are indicated in Figure 36b by the dashed ellipses, and the region occupied by Pathfinder soils in Figure 36c is indicated by the solid ellipses in Figures 36a and 36b. OP (Oxia-Palus) and OA (Olympus-Amazons) reference data are from telescopic spectra.

The band depth plot for <1-mm analogue samples is shown in Figure 36b along with the regions for ferric minerals. Conspicuously absent in analogue samples is spectral evidence for well-crystalline goethite and lepidocrocite, an observation consistent with previously discussed Mössbauer and XRD data. Np-Ox in palagonitic tephra plots in a region largely distinct from ferri-

hydrite. Because of the presence of sulfur in jarositic tephra, it is not possible to represent the np-Ox data as jarosite-ferrihydrite mixtures, suggesting that palagonitic np-Ox is itself a distinct ferric phase. If so, it is possible to represent the ferrihydrite data as mixtures between np-Ox at one extreme (BD530b ~0.05, BD600 ~-0.06) and the two synthetic (pure?) ferrihydrites at the other (BD530b ~0.35, BD600 ~0.12).

In some cases (e.g., jarosite and jarositic tephra), there is partial overlap of the regions where a ferric mineral and the tephra with the same mineral as a constituent plot. In other cases (e.g., hematite and hematitic tephra), the analogue data seem to plot between np-Ox and the ferric mineral, implying different proportions of the two mineralogies. The region where Pathfinder soils and rocks occur is indicated by the solid ellipse in Figure 36b. This region is consistent with ferric mineral assemblages containing np-Ox and lesser proportions of any combination of hematite, nanophase goethite, akaganéite, magnetite, and schwertmannite. Only jarosite and well-crystalline goethite and lepidocrocite are excluded on the basis of Figure 36b as spectrally dominant phases.

As shown in Figure 36c, values of BD530b increase in the order SNC meteorites >Pathfinder rocks >Pathfinder soils. The same order is seen in Figure 35c for R750/R445. Because increasing R750/R445 and BD530b are measures of increasing strength of ferric absorption edges and increasing contribution of crystalline ferric oxides (except jarosites), respectively, both trends can be interpreted as unaltered rock to unaltered rock dusted with or coated by soil to soil. Spectra of newly broken surfaces of rocks that we analyzed (see Figures 24 and 25) have values of BD530b and R750/R445 that are consistent with this interpretation. Although we cannot exclude the possibility that values of BD530b and R750/R445 for Pathfinder rocks are intrinsic properties of their solid surfaces, the data are consistent with the presence of unaltered rocks surfaces whose ferric character is not intrinsic and results from some combination of illumination by "orange" light and thin coatings of the ferric-rich aeolian dust. Evidence for orange light is provided by Thomas *et al.* [1999], who showed that the reflectance spectrum of Martian sky (diffuse part) has a ferric absorption edge resulting from dust particles in the atmosphere. The presence of thin, possibly discontinuous dust coatings on all solid rock surfaces is implied by the collection of aeolian dust by the Pathfinder Magnet Array [Hviid *et al.*, 1997; Madsen *et al.*, 1999], by the slow decrease in efficiency of solar power generation, which was attributed to deposition of aeolian dust on the solar power arrays [Landis and Jenkins, 1997], and by the positive correlation of R750/R445 and SO<sub>3</sub> for Pathfinder rocks [McSweeney *et al.*, 1999].

**11.1.5. Reflectivity maxima and band minima.** IMP wavelengths for the positions of maximum reflectivity (M1) and band minima (T1) that occur between 750 and 1000 nm are diagnostic indicators for mineral identification. The relevant data for pure ferric-bearing phases are the M1 and T1 values plotted in Figure 4. We must also consider the position of ferrous bands from pyroxene which also occur in this region, as observed for SNC meteorites (see Figures 27 and 31). Minima for low-Ca pyroxene are present at 930 nm (EET79001 and ALH79001) and 930-970 nm (Shergotty and Zagami). Note that the high-energy wing of the band extends to 750 nm (Figure 27). Minima for high-Ca pyroxene are just beyond the limit of the IMP spectral range (Figure 31); its manifestation in IMP data is a negative spectral slope extending from ~750 to 1000 nm. It is possible to have an M1 in the 750- to 800-nm region that is defined by the

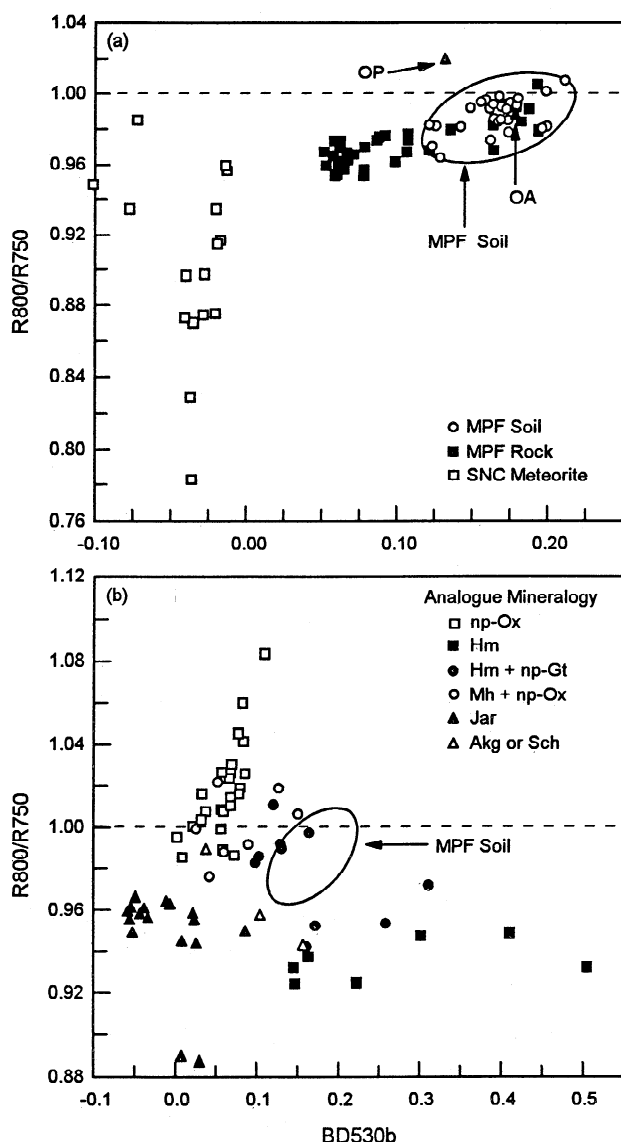


**Figure 37.**  $R800/R750$  correlated with  $BD530b$  for (a) Pathfinder soils and rocks and SNC meteorites and (b) analogue samples. The region occupied by Pathfinder soils in Figure 37a is indicated by the solid ellipses in Figure 37b. OP (Oxia-Palus) and OA (Olympus-Amazons) reference data are from telescopic spectra.

np-Ox ferric absorption edge on its high-energy side and the wing of a ferrous band on its low-energy side.

Figure 37a is a correlation of the ratio  $R800/R750$  and  $BD530b$  for Pathfinder rocks and soils and SNC meteorites. Because M1 for Pathfinder spectra is always either 750 or 800 nm (except for Surface Dust),  $R800/R750 > 1$  corresponds to  $M1 = 800$  nm and  $R800/R750 < 1$  corresponds to  $M1 = 750$  nm. Most Pathfinder spectra have  $M1 = 750$  nm, and there is a general trend for  $R800/R750$ , like  $R750/R445$  and  $BD530b$ , to increase from SNCs to Pathfinder rocks to Pathfinder soils. As discussed in section 11.1.4, the trends are a measure of increasing spectral contributions of soil and dust that have relatively high values of  $R750/R445$ ,  $BD530b$ , and  $R800/R750$ . Because we cannot distinguish whether the M1 of 750 nm for Pathfinder soils results from two ferric bands or a ferric absorption edge and a ferrous band, we do not use M1 values to constrain mineralogy.

Figure 37b compares analogue data to Pathfinder soils. The value  $R800/R750$  does not necessarily imply the value of M1 for analogue spectra. For example, palagonitic tephra (np-Ox) are generally characterized by a smooth ferric absorption edge (no M1) for which  $R800 > R750$  (Figures 10 and 11). Pathfinder soils plot in the region between analogue samples containing np-Ox at low values of  $BD530b$  and samples containing Hm and Hm+np-Gt at high values of  $BD530b$ . A few analogue samples with Hm+np-Gt plot in the same region as Pathfinder soils. Note that the maghemite-bearing samples plot between Pathfinder soils and palagonitic tephra, suggesting maghemite is not as spectrally compatible as hematite-bearing assemblages. However, the only

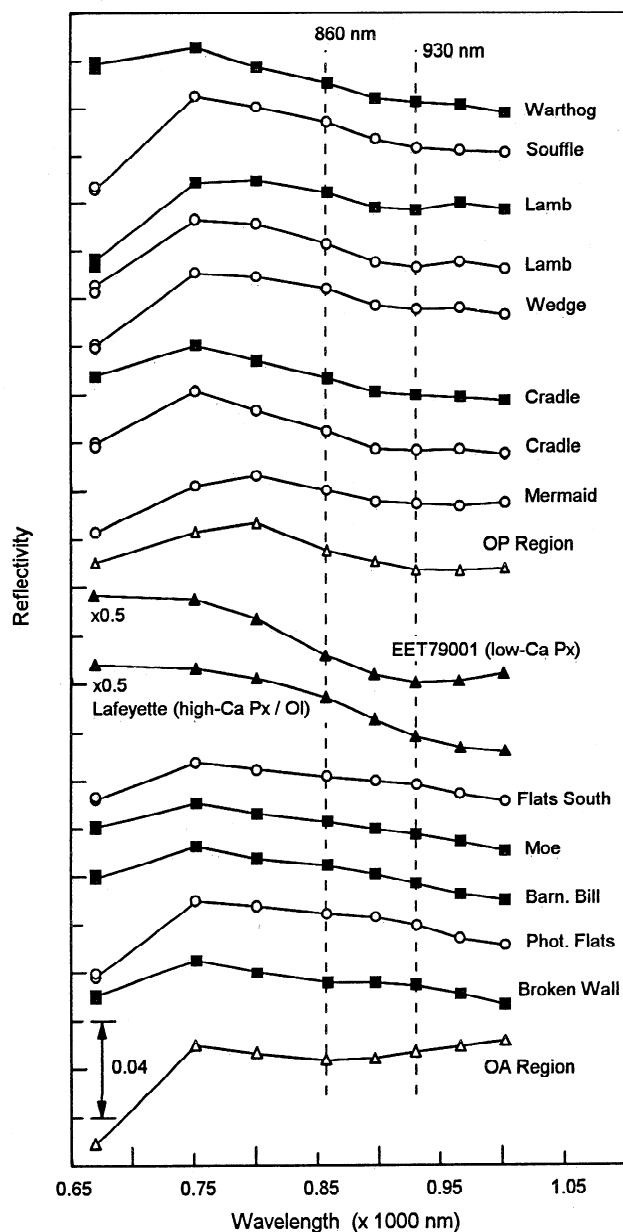


**Figure 38.** IMP reflectivity versus wavelength for Pathfinder soils (open circles) and rocks (solid squares), SNC meteorites EET79001 and Lafayette (solid triangles), and composite spectra of the Olympus-Amazons and Oxia Palus regions (open triangles). The dashed vertical lines at 860 and 930 nm indicate positions for the band minima of red hematite and low-Ca pyroxene, respectively.

ferric mineral that is not a reasonable interpretation on the basis of Figure 37b is jarosite.

In Figure 38 we plot several IMP spectra that have indications of a band minimum between 750 and 1000 nm. Also shown are convolved spectra for Olympus-Amazons (bright region spectrum) and Oxia Palus (dark region spectrum) published by *Mustard and Bell* [1994] and spectra for low-Ca pyroxene and high-Ca pyroxene/olivine as represented by two SNC meteorites. As discussed by *Mustard et al.* [1997] from their analysis of Phobos-2 ISM data, pyroxenes with these spectral characteristics commonly occur in Martian dark regions. The Olympus-Amazons spectrum is representative of Martian surface material that contains spectral evidence for minor red (well-crystalline) hematite [e.g., *Morris et al.*, 1997], as indicated by M1 and T1 values at 750 and 860 nm, respectively (see Figure 3).

The eight Pathfinder spectra at the top of Figure 38 (Warthog through Mermaid) all have evidence for a minimum whose position (~930 nm) corresponds to the one for low-Ca pyroxene in EET79001 (Figures 27 and 31) and to the one for the Oxia Palus spectrum. Note the striking similarity between Mermaid and Oxia Palus spectra. In their analysis of the Phobos-2 Oxia Palus spectrum, *Mustard et al.* [1997] concluded it represented a mixture of low-Ca and high-Ca pyroxenes, with the former being more spectrally important. Thus a reasonable assignment for the Pathfinder minimum near 930 nm is low-Ca pyroxene. As discussed above, BD530b data imply spectral contributions from a well-crystalline ferric oxide like hematite with a strong positive BD530b. Apparently, the M1 and T1 features associated with the ferric oxide are too weak to be detected in the presence of the more spectrally dominant low-Ca pyroxene. This view is consistent with the analysis of *Mustard et al.* [1997], who used a band with an 850 nm minimum (approximately the position for hematite) in their fitting procedure for the Oxia Palus spectrum. A reasonable interpretation of these spectra is thus an assemblage containing np-Ox (for the generally featureless absorption edge), low-Ca pyroxene, and an unidentified crystal-line ferric oxide (possibly Hm or Hm + np-Gt) to account for the features in the absorption edge.

Alternatively, the 930-nm minimum could be assigned to a ferric oxide, in which case a single component accounts for both the minimum and the structure in the ferric absorption edge. Nanophase goethite, maghemite, akaganéite, and schwertmannite all have T1 values near 930 nm (Figure 4) and are not excluded on the basis of other spectral parameters as discussed in previous sections. Jarosites and also well-crystalline goethite and lepidocrocite, which also have T1 values near 930 nm, are not reasonable assignments because their values of BD530b and BD600 are too positive. Although we do not exclude ferric oxides as an interpretation of the 930-nm T1 feature, we consider it less likely because the spectrally similar Oxia Palus spectrum (over IMP wavelengths) shows evidence for the second pyroxene band near 2000 nm [*Mustard et al.*, 1997].

The five Pathfinder spectra at the bottom of Figure 38 (Flats South through Broken Wall) are distinctly different from those we just discussed. There is no evidence for a 930-nm minimum, and, overall, the spectra approximate those of the Nakhilites, which have a band minimum just beyond the IMP spectral range near 1010 nm from high-Ca pyroxene/olivine (Figures 27 and 31). For comparison, the spectrum of Lafayette is shown in Figure 38. There is also a hint, particularly for Broken Wall, for a band minimum near 860 nm. The spectrum for Olympus-Amazons clearly shows this band, which is assigned to hematite [e.g.,

*Morris et al.*, 1997; *Morris and Golden*, 1998]. However, we hesitate to make an assignment of hematite on the basis of one spectrum. Thus a possible, but not well-constrained, interpretation of these five spectra is an assemblage consisting of np-Ox, high-Ca pyroxene, and an unidentified crystalline ferric oxide to account for the structure in the ferric absorption edge. An equally viable interpretation is that negative spectral slope near 1000 nm results from an np-Ox and (titano)magnetite assemblage as in Figure 31c and not high-Ca pyroxene.

**11.1.6. Ferric and ferrous minerals at Ares Vallis.** IMP multispectral data provide reasonable evidence for two ferric minerals (np-Ox and a second ferric oxide that is possibly well crystalline) and one ferrous mineral (low-Ca pyroxene) and weak evidence for two more iron-bearing minerals (high-Ca pyroxene and/or titanomagnetite). Np-Ox accounts for the general position and shape of the ferric absorption edge in all spectra (rocks and soils). The ferric edge is strongest ( $R_{750}/R_{445} > 4$ ; Figure 35b) for soils and for soil-coated rocks. The lower value of  $R_{750}/R_{445}$  for rocks ( $< 4$ ) may be intrinsic, but it more likely results from very thin, probably discontinuous coatings of dust that are rich in np-Ox with possible contributions from residual diffuse sky illumination effects. Np-Ox does not have a characteristic ferric band (T1 feature) at wavelengths longward of the absorption edge (~750 nm). By analogy with terrestrial samples, some H<sub>2</sub>O is likely associated with the np-Ox, but we cannot specify how much. We cannot firmly identify the second ferric oxide whose presence is responsible for high values of BD530b for Pathfinder spectra relative to np-Ox (palagonitic) analogue spectra. Because of its large value of BD530b, hematite is particularly effective in accounting for Pathfinder BD530b values, and this mineral has been firmly identified in Olympus-Amazons spectra [*Morris et al.*, 1997; *Morris and Golden*, 1998]. If present, red hematite (as opposed to gray, spectrally neutral hematite) is spectrally less important at the Pathfinder site than in the Olympus-Amazons region because the 860-nm hematite band is not present in the spectrum of the former. Equally viable alternatives for the second ferric oxide are nanophase goethite (and probably nanophase lepidocrocite, for which we have no spectra), akaganéite, maghemite, and schwertmannite.

The ferric minerals that we studied that are consistently not favored for interpretation of Pathfinder spectra are jarosites, well-crystalline goethite, and well-crystalline lepidocrocite. These phases can still be present if spectrally masked. For example, *Morris and Golden* [1998] were able to match the Olympus-Amazons spectrum with laboratory mixtures of palagonitic tephra and minor red hematite plus well-crystalline goethite.

The 930-nm band in Bright II soils and certain rocks is evidence for ferrous iron in low-Ca pyroxene. This assignment is based largely on the strong correspondence of the Mermaid spectrum to that for Oxia Palus, which is optically dominated by low-Ca pyroxene according to *Mustard et al.* [1997] and the low-Ca pyroxene spectral feature present in the spectra of basaltic (EET79001, Zagami, and Shergotty) and orthopyroxenite (ALH84001) SNC meteorites (Figure 31).

Instead of a 930-nm band, other rocks and soils have generally decreasing reflectivity between ~800 nm and 1005 nm which can be construed as evidence for the low-wavelength wing of a ferrous iron band centered near 1000 nm (high-Ca pyroxene and/or olivine). It could also result (for rocks) from the presence of thin coatings of ferric-rich dust over a dark ferrous-bearing rock substrate or from (for soils) an assemblage containing np-Ox and (titano)magnetite (see section 10.4).

An alternative to ferrous iron in low-Ca pyroxene for the 930-nm band is the oxides discussed above (akaganéite, maghemite, and schwertmannite) that satisfy the constraints of the ferric absorption edge and have T1 values near 930 nm (Figure 4). Even goethite and possibly hematite are permitted on the basis of studies of aluminum-substituted ferric oxides.  $\text{Al}^{3+}$  for  $\text{Fe}^{3+}$  substitution in ferric oxides is a well-documented and well-studied phenomenon in synthetic and naturally occurring samples because of its importance in the terrestrial alteration environment [e.g., *Fyfe and Clark*, 1982a, b; *Buckingham and Sommer*, 1983; *De Grave et al.*, 1982; *Kosmas et al.*, 1986; *Murad and Johnston*, 1987; *Cornell and Schwertmann*, 1996]. The effect of Al substitution on hematite and goethite is to shift the T1 values to longer wavelengths [*Buckingham and Sommer*, 1983; *Morris et al.*, 1992]. For example, *Morris et al.* [1992] show that T1 for hematite ranges from ~850 to ~900 nm with increasing Al substitution. *Scheinost et al.* [1998] report T1 ranges of 848-906 nm and 929-1022 nm for suites of hematite and goethite samples, respectively, that contain Al-substituted members. Although we have no good basis for discriminating between the ferric and ferrous interpretations for the 930-nm band, our preferred interpretation is that it results from ferrous iron in low-Ca pyroxene because the band is often associated with rocks and soils near rocks as for Lamb and Cradle in Figure 38 and because of its correspondence to the Oxia Palus spectrum. A ferric interpretation is advocated by *Bell et al.* [this issue], who point out that soils that have a 930-nm feature also tend to have higher values of BD530b.

## 11.2. Major Element Systematics of Pathfinder Soils

**11.2.1. Soil-free rock and rock-free soil compositions.** In their treatment of Pathfinder APXS data, *Rieder et al.* [1997] calculated the major element composition of a "soil-free" rock (sf-rock) from the y intercept of individual plots of major element versus  $\text{SO}_3$  concentrations under the assumption that the values of  $\text{SO}_3$  for the rocks (0.7-3.9%) are entirely derived from variable proportions of  $\text{SO}_3$ -rich soil on rock surfaces. Low sulfur abundances for igneous rocks are expected from the limited solubility of  $\text{SO}_3$  in silicate liquids (0.5-1.0% [*Danckwerth et al.*, 1979]) and low  $\text{SO}_3$  concentrations in Archean basalts (~0.2-0.5% [*BVSP*, 1981]) and Martian meteorites (0.03-0.48% [*Lodders*, 1998]). Figure 39 shows plots similar to those of *Rieder et al.* [1997] for  $\text{SiO}_2$ ,  $\text{TiO}_2$ ,  $\text{Al}_2\text{O}_3$ ,  $\text{Fe}_2\text{O}_3\text{T}$ ,  $\text{MgO}$ , and  $\text{CaO}$  in which major element data were calculated to a "fully oxidized" (i.e., all Fe as  $\text{Fe}_2\text{O}_3$ ) and "volatile-free" (i.e., no  $\text{SO}_3$ ) basis (Table 13). This calculation expresses Pathfinder analyses in the same format as major element data for our analogue samples. Both rock and soil analyses were used for calculating the regression lines that are shown in Figure 39 (method of *York* [1969] with uncorrelated errors). *Rieder et al.* [1997] used only the rock analyses, but they noted that the soils fell along the regression line. The sf-rock composition obtained from our regressions is, within uncertainty, the same as that reported by *Rieder et al.* [1997] (Table 13).

The correlations in Figure 39 imply a two-component mixture. One component is the sf-rock discussed above. Because Pathfinder rocks were not preselected to have the same major element composition, we infer that all rocks in the vicinity of the Pathfinder lander likely have the sf-rock composition. The other component is a soil, and we can calculate the composition of a "rock-free" soil (rf-soil) if we can infer its  $\text{SO}_3$  concentration. The rf-soil composition compiled in Table 14 was obtained assuming  $\text{SO}_3=7.0\%$ . This value is approximately the upper limit

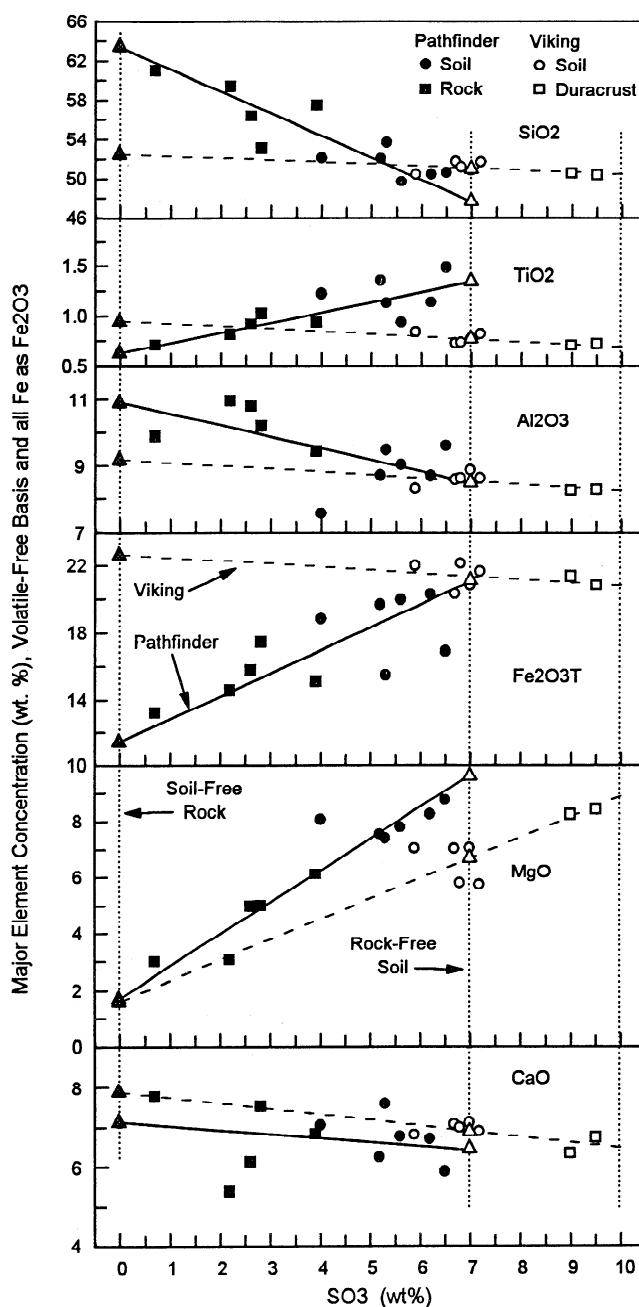


**Figure 39.** Correlation of major element concentrations (on volatile-free and all Fe as  $\text{Fe}_2\text{O}_3$  basis) with  $\text{SO}_3$  concentration for Pathfinder and Viking samples. The solid and dashed diagonal lines are regression fits using the method of *York* [1969] with uncorrelated errors. The dashed vertical lines at  $\text{SO}_3=0.0\%$  and  $7.0\%$  represent the compositions of soil-free rocks and rock-free soils, respectively. Note that both the Pathfinder and Viking soil-free rocks have low  $\text{MgO}$  concentrations (~2.0%).

of observed  $\text{SO}_3$  concentrations (taking analytical uncertainty into account) and does not give unrealistically low  $\text{SiO}_2$  or high  $\text{Fe}_2\text{O}_3\text{T}$  concentrations.

The Viking major element analyses, which we recalculated from *Clark et al.* [1982] to a  $\text{SO}_3$ -free basis and major element total of 94% (Table 13), are also plotted in Figure 39. We used only the data for the more complete analyses from the Viking 2 (Chryse) landing site. The range in  $\text{SO}_3$  abundances (~6-10%) is

Table 13. Volatile-Free Major Element Compositions for Pathfinder and Martian Meteorite Samples

Sample	SiO <sub>2</sub>	TiO <sub>2</sub>	Al <sub>2</sub> O <sub>3</sub>	Fe <sub>2</sub> O <sub>3</sub> T	MnO	MgO	CaO	Na <sub>2</sub> O	K <sub>2</sub> O	P <sub>2</sub> O <sub>5</sub>	Cr <sub>2</sub> O <sub>3</sub>	Cl	Total	SO <sub>3</sub>
<i>Pathfinder Compositions<sup>a</sup></i>														
A-2, After deploy	52.1±2.5	1.2±0.2	7.6±0.7	18.9±1.9	-	8.1±1.2	7.1±1.0	2.4±0.9	0.2±0.1	-	-	0.5±0.1	98.0	4.0±0.8
A-4, Next to Yogie	50.6±2.4	1.5±0.2	9.6±0.9	16.9±1.5	-	8.7±1.2	5.9±0.8	4.0±1.5	0.2±0.1	-	-	0.6±0.2	98.0	6.5±1.3
A-5, Dark next to Yogie	49.7±2.4	0.9±0.1	9.0±0.9	19.9±1.9	-	7.8±1.1	6.7±1.0	2.9±1.1	0.3±0.1	-	-	0.6±0.2	98.0	5.6±1.1
A-8, Scooby Doo	53.6±2.6	1.1±0.2	9.5±0.9	15.5±1.4	-	7.4±1.1	7.6±1.1	2.1±0.8	0.5±0.1	-	-	0.7±0.2	98.0	5.3±1.1
A-10, Next to Lamb	50.4±2.4	1.2±0.2	8.7±0.8	20.2±1.9	-	8.3±1.2	6.7±1.0	1.6±0.6	0.2±0.1	-	-	0.7±0.2	98.0	6.2±1.2
A-15, Mermaid Dune	52.0±2.5	1.3±0.2	8.7±0.8	19.7±1.9	-	7.6±1.1	6.2±0.9	1.3±0.7	0.5±0.1	-	-	0.6±0.2	98.0	5.2±1.0
<i>Viking (Chryse) Compositions<sup>b</sup></i>														
C-1, Fines	51	0.77	8.9	20.8	-	7.1	7.1	-	-	-	-	0.7	-	7.0
C-5, Crust	50	0.72	8.3	20.9	-	8.4	6.7	-	-	-	-	0.9	-	9.5
C-6, Fines	52	0.72	8.6	20.3	-	7.0	7.0	-	-	-	-	0.8	-	6.7
C-7, Fines	51	0.73	8.6	22.1	-	5.8	7.0	-	-	-	-	0.6	-	6.8
C-8, Fines	50	0.83	8.3	22.0	-	7.0	6.8	-	-	-	-	0.65	-	5.9
C-9, Fines	52	0.81	8.6	21.7	-	5.7	6.9	-	-	-	-	0.8	-	7.2
C-13, Crust	51	0.69	8.2	21.4	-	8.2	6.3	-	-	-	-	0.9	-	9.0
Precision	±2	±0.10	±0.4	±0.5	-	±1	±1	-	-	-	-	±0.25	-	-
Total Uncertainty	±6	±0.25	±4	-2 to +5	-	-3 to +5	±2	-	-	-	-	-0.5 to +1.5	-	-
<i>Martian Meteorite Compositions<sup>c</sup></i>														
Lafayette	46.1	0.4	2.4	23.6	0.5	12.7	13.2	0.4	0.1	0.4	0.2	-	100.0	0.10
Nakhla	47.8	0.3	1.7	22.5	0.5	11.9	14.4	0.5	0.1	0.1	0.3	-	100.0	0.06
G. Valadares	49.9	0.4	1.8	22.0	0.7	11.0	13.0	0.8	0.3	0.0	0.2	-	100.0	-
ALH77005	41.7	0.4	2.8	22.0	0.4	27.8	3.1	0.5	0.0	0.4	1.0	-	100.0	0.13
LEW88516	44.9	0.4	3.2	20.6	0.5	24.4	4.1	0.5	0.0	0.4	0.8	-	100.0	0.24
Y793605	44.5	0.3	2.3	21.4	0.5	25.7	4.0	0.4	0.0	0.0	1.0	-	100.0	-
Chassigny	36.5	0.1	0.7	29.6	0.5	31.0	0.6	0.1	0.0	0.1	0.7	-	100.0	0.07
ALH84001	51.6	0.2	1.3	19.0	0.4	24.4	1.8	0.1	0.0	0.0	1.1	-	100.0	0.03
QUE94201	47.4	1.8	10.9	20.3	0.4	6.2	11.3	1.6	0.0	0.0	0.1	-	100.0	-
EET79001-B	48.3	1.2	11.0	18.9	0.4	6.4	10.6	1.7	0.1	1.3	0.2	-	100.0	0.48
EET79001-A	48.5	0.7	5.7	19.9	0.5	15.6	7.1	0.8	0.0	0.6	0.6	-	100.0	0.53
Shergotty	50.1	0.8	6.7	21.0	0.5	9.1	9.4	1.4	0.2	0.7	0.2	-	100.0	0.32
Zagami	49.6	0.8	5.9	19.8	0.5	11.1	10.3	1.2	0.1	0.5	0.2	-	100.0	0.48
<i>Type-I Carbonaceous Chondrites<sup>d</sup></i>														
	32.0	0.10	2.3	37.3	0.3	22.4	1.7	1.0	0.1	0.4	-	-	97.7	-

Total iron concentration is expressed as Fe<sub>2</sub>O<sub>3</sub>T, and all concentrations except SO<sub>3</sub> are normalized to the "Total" column. Concentrations are in wt %.<sup>a</sup>After Rieder *et al.* [1997].<sup>b</sup>After Clark *et al.* [1982].<sup>c</sup>After Lodders [1998].<sup>d</sup>After Mason [1979].

**Table 14.** Volatile-Free Major Element Compositions for Soil-Free Rock, Rock-Free Soil, Duricrust, and Component A at Pathfinder and Viking (Chryse) Landing Sites

Sample	SiO <sub>2</sub>	TiO <sub>2</sub>	Al <sub>2</sub> O <sub>3</sub>	Fe <sub>2</sub> O <sub>3</sub> T	MgO	CaO	Na <sub>2</sub> O	K <sub>2</sub> O	Cl	Total	SO <sub>3</sub>
<i>Soil-Free Rock</i>											
Pathfinder <sup>a</sup>	61.2±2.7	0.69±0.10	10.5±0.7	13.2±1.3	2.0±0.7	7.2±1.1	2.6±1.5	0.7±0.2	0.2±0.2	98.1	0.0
Pathfinder <sup>b</sup>	61.5±3.4	0.63±0.27	10.6±1.5	13.3±3.1	2.1±1.4	7.1±1.3	2.4±1.5	0.8±0.3	0.2±0.2	98.6	0.0
Viking <sup>c</sup>	52±3.5	0.94±0.26	9.2±0.14	22.3±1.5	2.8±4.9	7.9±1.3	(2.5)	(0.8)	(0.2)	98.8	0.0
<i>Rock-Free Soil</i>											
Pathfinder <sup>b</sup>	48.9±2.6	1.34±0.20	8.7±1.1	19.7±2.4	9.4±1.0	6.5±1.0	2.5±1.1	0.2±0.2	0.2±0.2	97.4	7.0
Viking <sup>c</sup>	51±0.6	0.76±0.04	8.5±0.2	21.4±0.7	6.8±0.8	6.9±0.2	(2.5)	(0.2)	(0.2)	98.2	7.0
<i>Duricrust</i>											
Viking <sup>c</sup>	50.5±1.3	0.69±0.10	8.3±0.5	21.0±1.6	8.5±1.8	6.5±0.5	(2.5)	(0.2)	(0.2)	98.6	10.0
<i>Component A</i>											
Viking <sup>d</sup>	55.4	0.89	9.3	22.0	0.0	7.2	--	--	0.0	94.8	0.0

Total iron concentrations are expressed as Fe<sub>2</sub>O<sub>3</sub>T and all compositions except SO<sub>3</sub> are normalized to the "Total" column. Concentrations are in wt %.

Viking concentrations in parenthesis are Pathfinder results.

<sup>a</sup>After Rieder *et al* [1997].

<sup>b</sup>This study.

<sup>c</sup>This study using elemental data from Clark *et al.* [1982].

<sup>d</sup>Silicate component of Clark [1993]; calculated from his major element correlations and preferred model where all elements except MgO, Cl, and SO<sub>3</sub> are associated with the silicate component.

not as great as at the Pathfinder site (~1-7%), presumably because rocks were not analyzed. Regression lines (York fit) for the Viking data are shown by the dashed lines in Figure 39. Note that the positions of these lines are primarily determined by compositional differences between the two duricrust samples (highest SO<sub>3</sub> samples) and the soils. If these differences result, as presumed at Pathfinder, from mixing of different proportions of rock, soil, and duricrust, the major element compositions at SO<sub>3</sub>=0.0% represent the sf-rock composition at the Chryse landing site. We also calculate a rf-soil composition at SO<sub>3</sub>=7.0% and a duricrust composition at SO<sub>3</sub>=10% (Table 14). The 7.0% SO<sub>3</sub> concentration is consistent with the Pathfinder value and falls within the grouping of SO<sub>3</sub> values for Viking soils (Figure 39).

Both Pathfinder and Viking sf-rock compositions have low MgO concentrations (~1.6%) compared to both rf-soil concentrations (6-10%). The sf-rock compositions at Pathfinder and Viking differ principally in their SiO<sub>2</sub> and Fe<sub>2</sub>O<sub>3</sub>T concentrations. Pathfinder has higher SiO<sub>2</sub> concentrations (63 versus 53%), and Viking has higher Fe<sub>2</sub>O<sub>3</sub>T concentrations (23 versus 12%). The rf-soil compositions at the Pathfinder and Viking sites are comparable; the only significant difference is for TiO<sub>2</sub>, which is 0.76±0.04% for Viking and 1.34±0.20% for Pathfinder. The difference may not be real, however, because Dreibus *et al.* [1999] report that the average value of TiO<sub>2</sub> for three soils (A-4, A-5, A-10, and A-15) is lower by 0.30% (absolute) than the values reported by Rieder *et al.* [1997]. In the next two sections we consider possible explanations to account for differences between sf-rock and rf-soil compositions at each landing site and for differences in sf-rock compositions and similarities in rf-soil compositions between the two landing sites.

**11.2.2. Evidence for chemical alteration processes.** If we assume that Viking [Anderson and Tice, 1979] and remote sensing [Yen *et al.*, 1998] value of ~2% H<sub>2</sub>O in Martian soil is applicable to Pathfinder soil, its LOI/SO<sub>3</sub> ratio is 1.3-1.5 (LOI=SO<sub>3</sub>+H<sub>2</sub>O=6.0-8.0%). According to Figure 5a, this ratio is permissive for acid-sulfate alteration processes. Pathfinder K<sub>2</sub>O concentrations are not known with sufficient precision to use

values of K<sub>2</sub>O/MgO to discriminate hydrolytic and sulfidic styles of alteration (see Figure 5b). As summarized in section 10.5, leaching of basaltic materials during hydrolytic and sulfidic processes results in depletion and enrichment of major elements relative to unaltered materials. Each process has a distinctive fingerprint pattern of enrichment and depletion (see Figures 5 and 32). If the Pathfinder and Viking sf-rocks represent the initial composition for the rf-soils, major element ratios of Pathfinder and Viking rf-soil to sf-rock would be fingerprints of leaching processes at two places on Mars.

The major-element ratio patterns of Pathfinder and Viking rf-soil relative to corresponding sf-rock are shown in Figure 40. For Pathfinder, rf-soil is enriched in TiO<sub>2</sub>, Fe<sub>2</sub>O<sub>3</sub>T, and (especially) MgO and depleted in SiO<sub>2</sub> and Al<sub>2</sub>O<sub>3</sub>. The CaO and

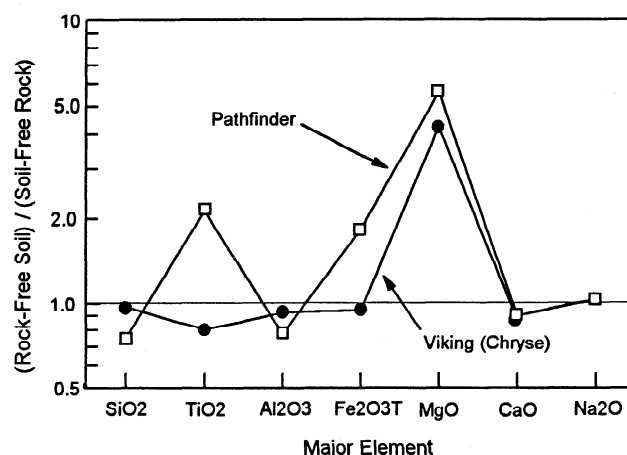


**Figure 40.** Ratio of rock-free soil to soil-free rock for major elements. The fractionation pattern is not consistent with any of the fractionation patterns observed for hydrolytic and sulfidic alteration of basaltic materials (see Figure 32), suggesting the pattern is not a fingerprint for a chemical alteration process. Particularly discrepant is MgO.



Na<sub>2</sub>O concentrations are the same to within 10%. For Viking, only MgO is enriched. SiO<sub>2</sub>, Al<sub>2</sub>O<sub>3</sub>, Fe<sub>2</sub>O<sub>3</sub>T, and CaO are slightly depleted, and TiO<sub>2</sub> is moderately depleted. The major element ratio patterns for Pathfinder and Viking rf-soils are distinct from each other and do not correspond to chemical fractionation patterns we observed for hydrolytic and sulfuric alteration (Figure 32). Particularly discrepant is MgO, which is the element most enriched for Martian rf-soils but is generally depleted for analogue samples. Although we cannot exclude the possibility that Figure 40 represents fingerprints for styles of alteration not represented by our analogue samples, we believe that the figure carries little or no information about chemical alteration. The similarity in elemental compositions of soil at the Pathfinder and two Viking sites argues that soil compositions are a product of global mixing processes and not a product of local leaching processes. In this view, Figure 40 is simply the element-by-element ratio of global-average-soil to local-rock compositions. This result does not imply that element fractionation by chemical alteration processes is not significant on Mars. It means only that the fractionation is not observed in elemental data because the residue of leaching is efficiently recombined (by global mixing processes) with evaporites formed from the leachate, resulting in no net change in chemical composition.

If chemical alteration is active, the Pathfinder sf-rock analyses might represent the composition of a leached surface and not the composition of bulk rock. Assuming the Pathfinder analyses correspond to the composition of an alteration rind, possible bulk rock compositions can be calculated using the chemical fractionation factors (Figure 32) corresponding to palagonitic (hydrolytic) and sulfatetic alteration processes. The results are compared with the sf-rock composition (the "rind" in this model) in Table 15. Interior-P1, Interior-P2, and Interior-P3 refer to light (as in HWMK600, <1 mm), moderate (as in Palagonite-A), and heavy (as in Palagonite-B) degrees of palagonitic alteration, respectively. Interior-P2 and Interior-P3 are physically unreasonable compositions (totals >> 100%), implying only minor palagonitic alteration (Interior-1 composition) can be present. The Interior-S1 and Interior-S2 compositions have physically reasonable sums, but they are physically unreasonable because they require that the rinds contain sulfur in the form of jarosite and alunite, respectively. As discussed above, the sulfur is interpreted to be associated with the dust coating and not the rock.

**Table 15.** Calculated Interior Composition of Pathfinder Rock

Element	Rock Rind Composition, %	Calculated Rock Interior Composition, %				
		P1	P2	P3	S1	S2
SiO <sub>2</sub>	61.5	64.9	73.0	98.2	62.1	61.8
TiO <sub>2</sub>	0.63	0.60	0.47	0.34	0.62	0.64
Al <sub>2</sub> O <sub>3</sub>	10.6	9.1	8.0	5.2	10.2	8.8
Fe <sub>2</sub> O <sub>3</sub> T	13.3	12.3	10.0	8.3	11.6	17.0
MgO	2.1	1.9	1.6	5.1	3.6	3.0
CaO	7.1	7.8	8.2	21.7	8.1	7.5
Na <sub>2</sub> O	2.4	2.6	4.2	8.7	2.3	2.1
K <sub>2</sub> O	0.8	1.1	2.5	4.5	0.8	0.8
Total	98.4	100.4	108.1	152.0	99.3	101.6

Calculations assume that the soil-free rock composition is an alteration rind whose composition is the residue of hydrolytic or sulfuric alteration. Major element fractionation patterns used for calculations are as follows: HWMK600 (<1 mm) for Interior-P1; Palagonite-A for Interior-P2; Palagonite-B for Interior-P3; Jarosite-A for Interior-S1; and HWMK508 (<1 mm) for Interior-S2.

If it could be established that the sulfur in rock analyses is associated with rock surfaces, and not adhering dust, then compositions like Interior-S1 and Interior-S2 are physically valid.

An important observation from the model in Table 15 is that all calculated interior rock compositions have comparable or larger SiO<sub>2</sub> concentrations than the rind. This means that, within the constraints of our chemical data, the conclusions of *Rieder et al.* [1997] and *McSween et al.* [1999] that SiO<sub>2</sub>-rich (andesitic or icelandic?) rocks are present at the Pathfinder site is valid even if the APXS analyses were done on rinds formed from rock by chemical leaching processes. That is, the rock interior will have at least as much SiO<sub>2</sub> as the rind. Our work does not address the issue of SiO<sub>2</sub>-rich coatings (i.e., SiO<sub>2</sub>-rich material adhering to but not derived from the rock), which could give high SiO<sub>2</sub> measurements by APXS relative to interior rock.

**11.2.3. Rock-based chemical mixing models for global Martian soil.** It is reasonable to base chemical mixing model calculations of the global Martian soil on igneous rocks if the rock to soil/dust process is a closed system with respect to bulk chemical composition (on a volatile-free basis). This is equivalent to placing an assemblage of igneous rocks into a box where only volatiles can be added and removed. Adding aqueous acids (volatiles) to the box and allowing H<sub>2</sub>O to slowly evaporate will chemically alter the rocks and form secondary minerals. Perhaps an evaporite deposit will form in one corner of the box. Although the alteration is not isomineralogical, it is isochemical (on a volatile-free basis) with respect to the whole box because none of the nonvolatile elements can get out. Thus, if we forgot the proportions of igneous rocks we put into the box, we could use chemical mixing models and individual rock compositions to calculate the proportions initially in the box. The issue is, can global Martian soil (i.e., Pathfinder rf-soil) be considered a closed system with respect to the rocks from which it was derived?

The direct observation of global-scale Martian dust storms [e.g., *Martin and Zurek*, 1993; *Zurek and Martin*, 1993] implies planetary-wide mixing and thus chemical and mineralogical homogenization of aeolian dust. Estimates for the mean particle diameter of aeolian dust (and surface deposits thereof) range from 0.2 to 10  $\mu$ m [e.g., *Murphy et al.*, 1993; *Pollack et al.*, 1995; *Markiewicz et al.*, 1999]. The similar elemental composition of soil at three different and widely separated places on the Martian surface (Chryse, Utopia, and Ares Vallis) is also cited [*Clark et al.*, 1982; *Rieder et al.*, 1997; rf-soil compositions in Table 14] as observational evidence for global homogenization of dust and soil. Mixing associated with individual impact events integrated over Martian history and large-scale fluvial processes when Mars was wet presumably promoted homogenization of soil material coarser than aeolian dust. Thus, although we cannot conclusively demonstrate that global Martian soil is a closed system with respect to the rocks from which it formed, the idea is at least a reasonable working hypothesis.

For chemical mixing models to provide physically reasonable and unique solutions, the number of chemical components (i.e., rocks) must be less than the number of chemical elements. Unfortunately, for Martian soils there are at least 10 known components (eight SNC meteorites, the Pathfinder sf-rock, and Type-1 carbonaceous chondrites) and only seven chemical elements (volatile-free basis). The situation is actually not quite this unfavorable because, on the basis of seven elements, the SNC meteorites fall into four geochemical groups (Table 13 and Figure 41): High-Ca (Lafayette, Nakhla, and Governador Valadares), high-Mg (ALH77005, LEW88516, Y93605, ALH84001, and Chassigny), high-Al basalt (QUE94201 and EET79001-B), and

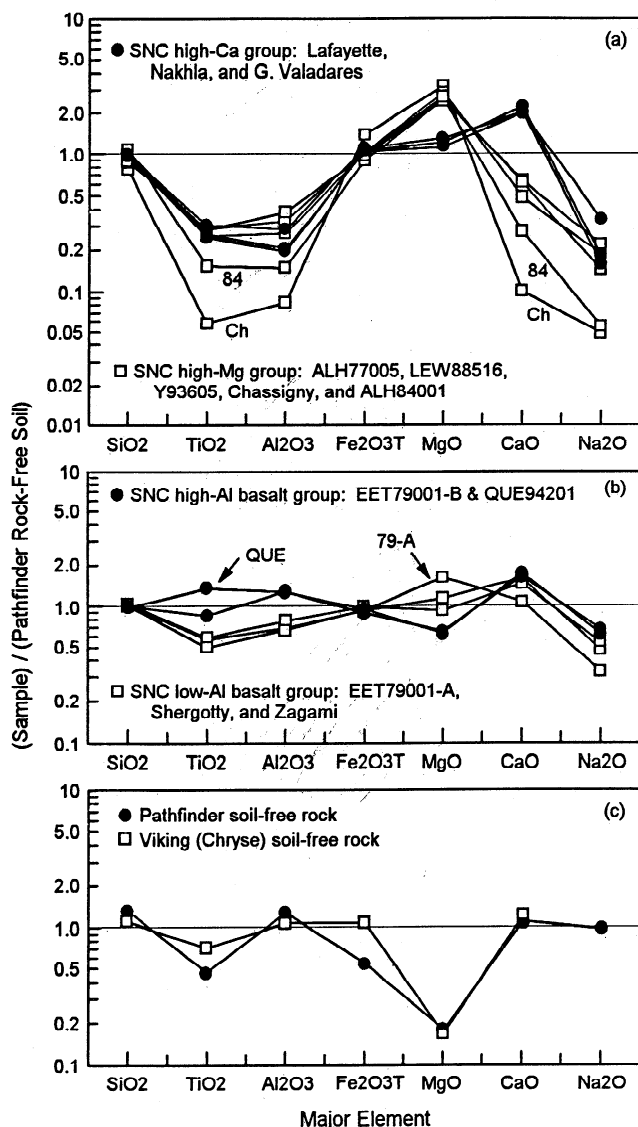


**Figure 41.** Major element ratio of SNC meteorites (Figures 41a and 41b) and soil-free rocks (Figure 41c) to Pathfinder rock-free soil. QUE94201 is the only rock composition that has more  $\text{TiO}_2$  than the Pathfinder rock-free soil, which makes it a major component in chemical mixing models.

low-Al basalt (Shergotty, Zagami, and EET79001-A). This grouping gives six components and seven elements. To search for chemical trends, we performed mixing calculations (method of Korotev *et al.* [1995]) under the constraint of three or fewer components. It is obvious from Figure 41 that QUE94201 is a required component because it is the only rock that has higher  $\text{TiO}_2$  contents than the Pathfinder rf-soil. Requiring QUE94201 to be a component excludes EET79001-B as a component because it is, except for  $\text{TiO}_2$ , compositionally equivalent to QUE94201 (for the seven elements).

The results of the chemical mixing calculations are given in Table 16. The top, middle, and bottom parts of the table give the difference between calculated and observed concentrations, the calculated concentrations of the components, and the statistical parameters for goodness of fit, respectively. The mixes are ordered with increasingly poorer fits from left to right. Several observations can be made from these results. (1) The proportion of QUE94201 is high (40–72%). (2) A component high in MgO

is required. All mixes, except 6 and 8, which use the most Mg-rich member of the high-Al basalt group, use a member of the high-Mg group. (3) The Pathfinder sf-rock is a viable mixing component (mixes 1 through 6). Mixtures without it (7 through 9) tend to be depleted in  $\text{SiO}_2$ . (4) Mixtures using members of the high-Ca group (Nakhlites) are not present in Table 16 because calculations using them as components did not yield physically possible solutions (i.e., positive concentrations and component totals  $\sim 100\%$ ). (5) Volatile-free carbonaceous chondrites, which have high MgO concentrations, are nearly equivalent in mixing-model calculations to the high-Mg SNC group. Thus, in contrast to the inferences of Clark *et al.* [1982] that Martian soil could have 40% chondritic component, current knowledge of Martian soil chemistry does not require a meteoritic component. Concentrations of siderophile elements (e.g., Ni) are necessary in order to meaningfully constrain the magnitude of the meteoritic component.

The chemical composition of Martian globally mixed soil (i.e., the Pathfinder rf-soil) can thus be adequately explained as a mixture of high-Al basalt (like QUE94201), andesite (like the Pathfinder sf-rock), and Mg-rich cumulate (like ALH84001, LEW88516, ALH77005, or Chassigny). Andesitic compositions are not required, but the statistical fits are better with it present. High-Ca compositions like the Nakhlites are not important chemical components with relatively high-Ca QUE94201 as a required component. A meteoritic component could be present at significant levels (up to 22%), but the calculations are equally consistent with no meteoritic component.

The mixing calculations deal strictly with elemental abundances and do not constrain mineralogy. That is, within (volatile-free) chemical constraints, the mineralogy of Pathfinder rf-soil could be anywhere between primary silicates and oxides associated with the SNC and Pathfinder rock components at one extreme (e.g., Table 16) and an assemblage of alteration products at the other extreme. Chemical mixing models describing Viking and Pathfinder soils predominantly as mixtures of alteration products (e.g., phyllosilicates and soluble salts) have been developed by Baird *et al.* [1976], Toulmin *et al.* [1977], Gooding [1992], and Bell *et al.* [this issue].

**11.2.4. Summary of major element systematics.** Major element data are consistent with a two-component model in which the endmembers for local Pathfinder and Viking soils are a global-average soil (Pathfinder rf-soil) that has high  $\text{SO}_3$  concentrations ( $\sim 7\%$ ) and particulate material derived from local rocks that has low  $\text{SO}_3$  concentrations ( $\sim 0\%$ ). On the basis of  $\text{SO}_3$  contents, the chemical contribution of local rocks to Pathfinder soils is  $\sim 7\text{--}42\%$ . The model accounts for the correlation of major element concentrations with  $\text{SO}_3$  (Figure 39), including the strong positive correlation of MgO and  $\text{SO}_3$ . Clark [1993] developed a different two-component mixing model for Viking soils where component A is a silicate component that contains all the Si and most or all the Al, Ca, Ti, and Fe. Its composition is very similar to that for the Viking soil-free rock (see Table 14). Component B ( $16\pm 3\%$ ) is a nonsilicate component that contains all of the S and most or all of the Cl and Mg. The basic rationale for the Clark [1993] model can be seen in Figure 39; MgO is the only major element for Viking samples that correlates positively with  $\text{SO}_3$ . Because  $\text{Fe}_2\text{O}_3\text{T}$  and  $\text{TiO}_2$  also correlate with  $\text{SO}_3$  at Pathfinder, the Clark [1993] model would not explain Pathfinder chemical data without modification. In any event, the two models differ in how they account for the correlation of MgO and  $\text{SO}_3$ . For Clark [1993], the correlation results from mixtures of MgO- and  $\text{SO}_3$ -rich salts (magnesium sulfates?) and MgO- and  $\text{SO}_3$ -poor silicate material. In our model

**Table 16.** Rock-Based Seven-Element Mixing-Model Calculations for Pathfinder Rock-Free Soil

	Rock-free Soil Observed, %	Mix 1	Mix 2	Mix 3	Mix 4	Mix 5	Mix 6	Mix 7	Mix 8	Mix 9
<i>Calculated-Observed, %</i>										
SiO <sub>2</sub>	48.9±2.5	-0.3	-0.1	0.4	0.0	-0.9	0.0	-2.2	-2.5	-3.0
TiO <sub>2</sub>	1.34±0.2	-0.2	-0.2	-0.1	-0.2	-0.3	-0.2	0.0	-0.1	-0.1
Al <sub>2</sub> O <sub>3</sub>	8.7±0.9	0.0	0.1	-0.4	-0.1	0.1	-0.3	-0.5	-0.4	-0.5
Fe <sub>2</sub> O <sub>3</sub> T	19.7±1.8	-0.1	-1.4	-1.4	-1.4	1.8	-1.2	-0.4	-0.2	0.4
MgO	9.4±1.2	0.1	0.4	0.2	0.3	-1.1	-0.1	1.0	0.8	0.6
CaO	6.5±1.0	1.3	1.6	1.6	1.7	1.2	2.1	2.1	2.6	2.7
Na <sub>2</sub> O	2.5±1.0	-1.0	-1.0	-1.2	-1.0	-0.8	-1.1	-1.3	-1.3	-1.2
<i>Equivalent Chemical Abundance wt %</i>										
QUE94201		50±8	49±9	58±8	49±9	45±10	40±12	72±5	53±10	54±20
Shergotty		---	---	---	---	---	---	---	---	28±26
EET79001-A		---	---	---	---	---	42±9	---	44±11	---
ALH84001		---	---	23±4	---	---	---	25±5	---	---
LEW88516		---	---	---	25±5	---	---	---	---	---
ALH77005		---	22±4	---	---	---	---	---	---	15±9
Chassigny		19±3	---	---	---	---	---	---	---	---
VF-CChon-1		---	---	---	---	22±4	---	---	---	---
Path. sf-Rock		30±7	27±8	16±8	23±9	32±9	16±10	---	---	---
Total Component		98±11	98±13	97±13	98±14	99±14	98±18	96±7	97±15	97±34
χ <sup>2</sup>		4.1	5.2	5.2	5.8	6.3	7.6	8.0	10.2	11.0
χ <sup>2</sup> /v		0.59	0.74	0.75	0.83	0.90	1.08	1.14	1.46	1.57

Components are SNC meteorites, volatile-free Type-1 carbonaceous chondrites, and the Pathfinder soil-free rock. Weighting factors used for calculated fits are the element uncertainties for the rock-free soil. Component compositions are in Table 13. The mixes are ordered with increasingly poorer fits from left to right.

the correlation results from mixtures of a global MgO- and SO<sub>3</sub>-rich soil and MgO- and SO<sub>3</sub>-poor particles of local rocks.

Our global-soil, local-rock model for Pathfinder soils, which was developed using chemical data, is also consistent with mineralogical results derived from IMP multispectral data (section 11.2.1). The ferric absorption edge is associated predominantly with global soil. The apparent absence of ferrous silicate bands in aeolian dust sampled by Pathfinder Magnet Arrays (see section 11.3) and the higher R750/R445 of soil relative to rock (Figures 34 and 35) are evidence for a high oxidation state of aeolian dust. This result is supported by Mars-like ferric absorption edges and high Fe<sup>3+</sup>/Fe<sup>2+</sup> ratios of palagonitic tephra relative to unaltered tephra. We associate the 930-nm band (low-Ca pyroxene) and possibly the negative IR slope (if from high-Ca pyroxene) with ferrous silicates from unoxidized fragments of local rock in Pathfinder soils. If the negative spectral slope is associated with Fe-Ti oxides, they could be directly formed in soil particles by analogy with palagonitic tephra or inherited from the rocks. Soil particles that contain ferrous silicates are likely to be larger than 10 μm, or they would be susceptible to aeolian transport [e.g., Murphy *et al.*, 1993; Pollack *et al.*, 1995] and deposited and detected on the Magnet Arrays. The presence of particles of local rock in Pathfinder soil has implications for the timing of Martian alteration processes (see section 11.4). Similar element-spectral comparisons are not possible with Viking data because IMP-like multispectral data were not obtained during that mission [e.g., Guinness *et al.*, 1987; Arvidson *et al.*, 1989].

### 11.3. Magnetic Properties

The results of the Mars Pathfinder magnetic properties experiments indicate that Martian aeolian dust is magnetic with a

saturation magnetization of 4±2 Am<sup>2</sup>/kg [Hviid *et al.*, 1997; Madsen *et al.*, 1999], a value that is a refinement of the 1-7 Am<sup>2</sup>/kg range estimated from the Viking magnetic properties experiment [e.g., Hargraves *et al.*, 1979]. Hargraves *et al.* [1999] report that *J<sub>s</sub>* value is equivalent to a low-field susceptibility of at least 18×10<sup>-6</sup> m<sup>3</sup>/kg. The Pathfinder experiment team concluded that the magnetic properties result from the presence of a strongly magnetic phase dispersed within composite particles and that the concentration of the strongly magnetic phase varies from particle to particle. These considerations are independent of the crystalline structure of the strongly magnetic phase. The phase preferred by both the Viking and Pathfinder experiment teams is maghemite (*J<sub>s</sub>* ~50-80 Am<sup>2</sup>/kg), which they consider to form as the endproduct of a two-step process involving oxidative alteration of ferrous silicates to nonmagnetic lepidocrocite followed by dehydroxylation to maghemite [Hargraves *et al.*, 1979; Hviid *et al.*, 1997]. The value of *J<sub>s</sub>* for Martian dust is the equivalent of 2-12% maghemite using *J<sub>s</sub>* ~50-80 Am<sup>2</sup>/kg for pure maghemite. Assuming that the chemical analyses of Pathfinder soils are applicable to the magnetic dust (average Fe<sub>2</sub>O<sub>3</sub>T ~ 19% [Rieder *et al.*, 1997]), 10-60% of the total iron in the dust is present as maghemite. The suggested maghemite formation process is in keeping with general observations from terrestrial environments that its formation proceeds via a precursor phase and apparently does not precipitate directly from aqueous solutions [e.g., Cornell and Schwertmann, 1996]. Dehydroxylation of lepidocrocite to maghemite is well established [e.g., de Bakker, 1990; Morris *et al.*, 1998a], and Banin *et al.* [1993] have argued that the oxyhydroxide should form on Mars. Hviid *et al.* [1997] and Madsen *et al.* [1999] do allow, however, that strongly magnetic titanomagnetite and/or titanomaghemite (Fe-Ti spinels) are also possible interpretations.

What insights do our analogue studies provide into the nature

of the strongly magnetic phase on Mars and its formation processes? As shown in Figure 29, our analogue samples, with the exception of the maghemite-bearing samples from Meteor Crater and a titanomagnetite-bearing magnetic separate of unaltered tephra, have values of  $J_s$  and  $\chi_{lf}$  that are at or less than the values inferred for Martian aeolian dust ( $J_s = 4 \pm 2 \text{ Am}^2/\text{kg}$  and  $\chi_{lf} > 18 \times 10^{-6} \text{ m}^3/\text{kg}$ ). Does this result imply that lithogenic titanomagnetite (i.e., formed during cooling of molten silicates), the strongly magnetic mineral in our palagonitic, sulfatetic, and steam vent samples, is not a reasonable interpretation for the strongly magnetic phase in Martian aeolian dust? As discussed next, we believe that lithogenic titanomagnetite is a viable interpretation of the Pathfinder magnetic properties experiment.

As considered previously by Morris *et al.* [1990] and Coey *et al.* [1990], lithogenic titanomagnetite ( $\text{Fe}_{3-x}\text{Ti}_x\text{O}_4$ ,  $0 \leq x \leq 1$ ) or its oxidative alteration product titanomaghemite ( $\text{Fe}_{(8-4y)}\text{Ti}_y\text{O}_4$ ,  $0 \leq y \leq 2$ ) are candidate phases provided that the Ti content is not too high. For both minerals the compositional range that can be considered strongly magnetic ( $J_s \geq 10\text{--}30 \text{ Am}^2/\text{kg}$  at room temperature) extends at least to  $0 \leq x \leq 0.5$  and  $0 \leq y \leq 0.5$ , respectively, on the basis of magnetic studies of titanomagnetites [e.g., Nagata, 1961] and magnetic measurements for a titanomaghemite with  $y=0.5$  [Allan *et al.*, 1989]. The issue, which is difficult to address because rocks from the uppermost Martian surface have not been collected as meteorites, is whether lithogenic processes on Mars produced sufficient quantities of these minerals in composite particles to account for the observed magnetic properties. As mentioned above, the values of  $J_s$  and  $\chi_{lf}$  for our Hawaiian volcanic samples with lithogenic titanomagnetites are at the low end of the range inferred for Martian aeolian dust. It might be that the style of volcanism on Mars, because of differences in bulk composition and/or oxygen fugacities, produces materials with higher titanomagnetite concentrations. In support of this view, the style of volcanism in Brazil (southern Goias State) produces basalt with  $\sim 23\%$  Fe as  $\text{Fe}_2\text{O}_3$ , which subsequently alters to soil with a Mars-like susceptibility of  $40 \times 10^{-6} \text{ m}^3/\text{kg}$  (soil G6 [Curi and Franzmeier, 1987]). The strongly magnetic phases are lithogenic titanomagnetites inherited from the parent basalt and titanomaghemites formed from oxidation of titanomagnetites. Other instances of Fe-Ti spinels in Brazilian soils developed from basalts are described in the literature [e.g., Allan *et al.*, 1988, 1989; Fontes and Weed, 1991; Cornell and Schwertmann, 1996].

Another line of evidence suggests that Mauna Kea palagonitic tephra does, in fact, satisfy the constraints of the Pathfinder Magnet Array experiment and that the values of  $J_s$  and  $\chi_{lf}$  determined for Martian aeolian dust by the experiment are too high. Morris *et al.* [1999] conducted simulation experiments on Mauna Kea Volcano with a copy of the Pathfinder Magnet Array. Palagonitic aeolian dust, produced by mechanical agitation of palagonitic tephra, was collected by the four strongest MA magnets, the same result as obtained on Mars [Hviid *et al.*, 1997; Madsen *et al.*, 1999]. The values of  $\chi_{lf}$  for palagonitic dust adhering to the magnets were  $\sim 20 \times 10^{-6} \text{ m}^3/\text{kg}$  [Morris *et al.*, 1999]. Palagonite particles are composites of strongly magnetic (Fe-Ti spinel) and weakly magnetic or nonmagnetic (e.g., feldspar, glass, and hydrated aluminosilicate material containing np-Ox particles) phases and are thus in compliance with the constraint of Mars Pathfinder [e.g., Madsen *et al.*, 1999] that aeolian dust particles be composite particles of strongly magnetic and weakly magnetic or nonmagnetic phases.

By analogy with impactites from Meteor Crater, the strongly magnetic mineral in Martian soil could be maghemite formed by

dissemination and oxidation of metallic iron into target materials. Estimates of the meteoritic contribution to Martian soil range from 2 to 40% by mass [Clark and Baird, 1979; Flynn and McKay, 1990]. The upper limit, which is based on chemical mixing models [Clark and Baird, 1979], is probably unrealistically high (see section 11.2.3). As discussed earlier in this section, the amount of maghemite required to account for the magnetic properties of aeolian dust is 2–12%. This range is also a lower limit for the meteoritic contribution, because it assumes that all impacting meteorites are metallic iron and that all the iron is oxidized to maghemite. If average meteoritic material is 10% metallic iron, a more realistic value based on the mineralogy of meteorites and their frequency of fall, the meteoritic component is an unrealistic 20–100%. Thus we conclude that it is unlikely that the strongly magnetic nature of Martian dust is traceable entirely to meteoritic maghemite.

IMP multispectral data of aeolian dust collected by the Magnet Arrays [Madsen *et al.*, 1999] are an important source of information about the mineralogy of the strongly magnetic phase and its potential precursors. Unfortunately, the dust coatings may not be optically thick, so that consideration must be given to the optical properties of the MA surface. The magnetic dust spectrum shown by Madsen *et al.* [1999] is similar to a small set of Pathfinder soil spectra (Surface Dust) that have positive spectral slopes between 750 and 1000 nm [Bell *et al.*, this issue]. A potentially mitigating factor for the magnetic dust spectrum is that the MA surface also has a slight positive spectral slope through the IMP spectral region (P. Gunnlaugsson, personal communication, 1998). However, the magnetic dust has lower reflectivity than the MA surface at all IMP wavelengths, and the positive spectral slope is more positive for the dust than the MA surface. Both factors imply that the positive slope is an intrinsic feature of the magnetic dust. Thus the MA surface may contribute to the positive slope but cannot be solely responsible for it.

The magnetic dust spectrum published by Madsen *et al.* [1999] does not have definable M1 and T1 spectral features. If the magnetic phase is maghemite, then 2–12% is present on the basis of observed magnetic properties. Is this level of maghemite above or below its spectral detection limit? The detection limits for mixtures of palagonitic tephra and submicron powders of hematite and goethite are  $\sim 2\%$  [Morris *et al.*, 1997; Morris and Golden, 1998]. The detection limit for maghemite has not been similarly determined, but it will be  $>2\%$  because, in comparison to hematite and well-crystalline goethite, the contrasts of maghemite spectral features are reduced (i.e., shallower absorption edge and less M1-T1 spectral contrast; Figure 3), so that the general shape of the spectrum more closely resembles the palagonite spectrum. Because we do not know if the maghemite detection limit is more or less than the 2–12%, we cannot infer the presence or absence of maghemite on the basis of the magnetic dust spectrum.

We note, however, that IMP-equivalent multispectral data for the  $<2\text{-}\mu\text{m}$  size fraction of palagonitic tephra (Figure 10c), which is comparable to the size range for Martian aeolian dust [e.g., Markiewicz *et al.*, 1999], are similar in shape to the magnetic dust spectrum. Because Fe-Ti spinel is the magnetic phase in the size separates, the magnetic dust spectrum is not inconsistent with the presence of Fe-Ti spinels.

The Olympus-Amazons region of Mars is considered to be covered with deposits of Martian global dust. Comparison of the IMP-style spectrum for this region and the Surface Dust spectrum (Figure 33) shows important differences that are unexpected if both are representative of global dust. The former has spectral

features (e.g., M1 ~ 750 nm and T1 ~ 860 nm) that are indicative of hematite [e.g., *Morris et al.*, 1997; *Morris and Golden*, 1998], and the latter, as discussed above, does not have M1 and T1 spectral features. The different nature of the spectra can be reconciled if either the hematite in the Olympus-Amazons region is not associated with aeolian dust or aeolian dust has a hematitic and weakly magnetic component that is not collected by the Magnet Array. We favor the latter alternative because *Madsen et al.* [1999] conclude that not all aeolian dust is necessarily collected by the Magnet Array.

A strongly magnetic phase that is spectrally neutral or below optical detection limits is consistent with the spectral diversity for Martian soils from Pathfinder and telescopic data (e.g., Figure 38). If the ubiquitous strongly magnetic phase were also an optically dominant phase with sharp ferric absorption edges and large M1-T1 spectral contrast (e.g., like hematite or well-crystalline goethite or lepidocrocite), we would expect to see less diversity in spectral data for soils. It is clear from the above discussion that more work on detection limits of phases like maghemite is needed and that obtaining spectral data for magnetic dust collected by MAs should have a high priority.

In summary, we agree with *Hviid et al.* [1997] and *Madsen et al.* [1999] that magnetic aeolian dust contains composite particles of a strongly magnetic phase and one or more weakly magnetic phases. Their preferred interpretation is that the magnetic phase is maghemite, possibly derived by dissolution of ferrous silicates, precipitation of lepidocrocite, and dehydration to maghemite, possibly as a cementing agent. Our studies of Meteor Crater impactites show that oxidation of iron metal from impacting iron meteorites could also contribute maghemite to Martian soil and dust. Our preferred interpretation, which *Hviid et al.* [1997] and *Madsen et al.* [1999] give as an alternative to their preferred interpretation, is that the strongly magnetic phase is lithogenic titanomagnetites and/or their titanomaghemite oxidation products. Composite materials containing titanomagnetites (and/or titanomaghemites) are consistent with the magnetic properties of Pathfinder and Viking soil and dust, the Pathfinder magnetic dust spectrum, and optical requirements for an opaque mineral phase [e.g., *Pollack et al.*, 1995].

#### 11.4. Alteration Processes on Mars

Collectively, the chemical, multispectral, and magnetic data from Mars Pathfinder are consistent with a two-component model where local soils are mixtures of a globally distributed soil (the Pathfinder rock-free soil) that is rich in ferric iron, MgO, and SO<sub>3</sub> and fragments of local andesitic rock that are rich in ferrous silicates and depleted in MgO and SO<sub>3</sub>. The global soil cannot be derived solely from either Pathfinder rocks or any Martian meteorite by direct chemical alteration based on major element fractionation patterns for palagonitic and sulfatetic tephra, basaltic rocks altered in steam vents, and tholeiitic basalt altered under tropical conditions (section 10.5). A possible explanation is that our analogue samples are not representative of alteration styles on the planet. More likely, however, the global soil is a mixture of alteration products of a variety of rocks having a wide range in chemical compositions. Chemical fractionation during alteration undoubtedly took place on Mars, but its signatures have been erased by mixing processes. Possible combinations of rocks that could yield the global soil (assuming a closed system except for volatiles) are the results of the chemical mixing model described in section 11.2.3.

Another approach to understanding the styles of alteration on Mars is to focus on the mineralogy of Martian soil. Despite the highly successful nature of both Viking and Pathfinder missions, there is still a paucity of mineralogical information about alteration products. Arguably, only hematite and np-Ox (poorly crystalline, nanometer-sized particles of ferric iron dispersed in a matrix material) have been identified with a high degree of certainty as alteration products [e.g., *Morris et al.*, 1990, 1993, 1997; *Lane et al.*, 1999; *Christensen et al.*, 1999], although there are clues that other crystalline ferric oxides are present [e.g., *Murchie et al.*, 1993]. On Earth, np-Ox is abundant in palagonite, the hydrous alteration product of basaltic glass (section 5.3.2). The clear implication is that high production rates of basaltic glass on Mars (by any mechanism) could account for the seemingly large amounts of np-Ox in Martian bright regions (i.e., in soil and dust).

As on the Earth and the Moon, basaltic volcanism and meteoritic impact are sources for basaltic glass on Mars [e.g., *Gooding and Keil*, 1978; *Allen et al.*, 1981; *Bouska and Bell*, 1993]. On the Earth, the current or past presence of glass can be inferred anywhere palagonitic material is present. Many occurrences associated with volcanism are known, including Hawaii (see section 5.3.2), the continental United States [e.g., *Allen et al.*, 1981; *Farrand and Singer*, 1991, 1992], Canada [e.g., *Jercinovic et al.*, 1990], Iceland [e.g., *Jakobsson*, 1972; *Allen et al.*, 1981; *Jakobsson and Moore*, 1986; *Thorseth et al.*, 1991], Italy [*Buemi et al.*, 1998], Antarctica [e.g., *Soderblom and Wenner*, 1978; *Allen et al.*, 1981], and submarine deposits [e.g., *Frey et al.*, 1974; *Ailin-Pyzik and Sommer*, 1981; *Staudigel and Hart*, 1983; *Heidner et al.*, 1993; *Zhou and Fyfe*, 1989; *Schiffman and Southard*, 1996]. On the Moon, *Weitz et al.* [1998] report that there are seven locales with areas ranging between 4000 km<sup>2</sup> and 37,400 km<sup>2</sup> that are covered with pyroclastic deposits from episodes of lunar fire fountaining. We know of no way to estimate the amount of glassy volcanic ash that can be produced on Mars, but the possibility exists that it is substantial and enhanced on Mars relative to the Earth as discussed by *Wilson and Head* [1994], *Head and Wilson* [1998], and *Hargraves* [1999]. As in our samples of palagonitic tephra, the glassy volcanic ash particles might be composite particles that contain sufficient titanomagnetite (or titanomaghemite if oxidized) to satisfy the results of the Pathfinder magnetic properties experiment [e.g., *Madsen et al.*, 1999].

An occurrence of palagonite (referred to as "devitrified palagonite") associated with meteoritic impact into basalt is documented by *Kieffer et al.* [1976] for Lonar Impact Crater (India). Although basaltic materials were not impacted, impact glass is associated with many other terrestrial impact structures, including Meteor Crater and Monturaqui, Ries, and Wabar craters [e.g., *Bunch and Cassidy*, 1972; *Stahle*, 1972; *Newsom et al.*, 1986; *See et al.*, 1998]. Titanomagnetites, formed by crystallization during rapid cooling of impact melt, are found in impact palagonite at Lonar Impact Crater [*Kieffer et al.*, 1976]. Impact processes, like volcanic processes, can thus provide the strongly magnetic phase observed in Martian dust [e.g., *Madsen et al.*, 1999] through either crystallization or incorporation of magnetic minerals (or their oxidation products) from projectile material (see section 7).

We expect that the production of basaltic glass from impact events will be considerably enhanced on Mars relative to the Earth and Moon because of higher cratering rates (possibly factors of 2-4 relative to the Moon [*BVSP*, 1981; *Nyquist et al.*,

1998]) and higher glass to crystalline ratios per impact [Kieffer and Simonds, 1980]. Glass abundances for the lunar regolith can thus be used to provide an estimate for the amount of glass that might be produced on Mars by impact processes. Mössbauer studies of lunar samples [Morris *et al.*, 1998b] show that immature clastic regoliths [Morris, 1978] have  $26 \pm 9$  atom % of all iron atoms associated with glass. Immature clastic regoliths are used as the reference point because they have the lowest contribution of glass derived from impacting micrometeorites, which on Mars are prevented from making hypervelocity impact by the current Martian atmosphere. Vasavada *et al.* [1993] calculate that only meteors with initial masses  $>10$  kg survive transit through the present Martian atmosphere and have hypervelocity impacts. However, during periods of low obliquity the Martian atmosphere is less dense, and meteoroids with initial masses between  $2 \times 10^{-6}$  and  $2 \times 10^{-4}$  kg have hypervelocity impacts [Vasavada *et al.*, 1993]. If Mars had no atmosphere through time (the upper limit case for glass production by meteoritic impact), the amount of iron associated with glass on the Martian surfaces would be on the order of 50 atom % on the basis of mature lunar soils [Morris *et al.*, 1998b]. If, as discussed by Nyquist *et al.* [1998], the Martian cratering rate is 4 times the lunar cratering rate, both estimates are too low.

The calculations of Kieffer and Simonds [1980] predict that impacts into volatile-rich targets (like Mars) and volatile-poor targets (like the Moon) will produce comparable volumes of impact melt and that the melt will distribute in different ways. In volatile-poor targets, impact melts form melt sheets which subsequently crystallize as they cool. In volatile-rich targets the melt is finely dispersed by the great expansion of shocked volatiles. Fine dispersal (high surface to volume ratios relative to melt sheets) provides the opportunity for rapid cooling and formation of glass. This consideration also implies that our estimates of the amount of glass formed on Mars are too low.

The above considerations are at least consistent with the idea that considerable glass was produced on the Martian surface through time by volcanic and impact processes and that the surface underwent oxidative alteration to the palagonite-like material that is the spectrally dominant ferric-bearing phase (np-Ox) in Martian bright regions. A conservative lower limit for the percentage of iron atoms in Martian that went through or are in a glassy state is  $\sim 30\%$ , the value for immature clastic lunar regoliths. This limit does not include contributions from volcanic processes and upward corrections for higher impact rates into the volatile-rich Martian surface.

Possible sources of the high levels of  $\text{SO}_3$  in Martian soils (4–9% [Clark *et al.*, 1982; Rieder *et al.*, 1997]) include volcanic exhalations in association with fire fountaining or other volcanic activity and mobilization during oxidative alteration of sulfides in association with impacts into volatile- and sulfide-rich surface materials. Settle [1979] concluded that volcanic  $\text{SO}_2$  and  $\text{H}_2\text{S}$  gases released at the surface formed sulfate aerosols that were circulated around the planet and ultimately deposited and incorporated into surface materials. Burns and coworkers have argued for the presence of basaltic komatiites basalts hosting iron sulfides [Burns, 1988; Burns and Fischer, 1990a, b].

The presence of ferrous silicates in Pathfinder soils is readily explained if addition of rock fragments is an ongoing process. The presence of possible spall zones and sharp, irregularly shaped areas on otherwise relatively smooth rocks are both evidence for ongoing impact comminution of rocks at the Pathfinder site [Horz and Cintala, 1999] (and presumably the entire Martian surface) and a mechanism for introducing rock fragments into the soil.

Even if Pathfinder rocks have thin oxidation rinds, the size of the features on the rocks implies removal of rock to depths below rinds. Failure of the Viking robotic arm to produce visible scratches on rock surfaces at Viking [e.g., Moore *et al.*, 1977, 1979] and similar failure of the Pathfinder Sojourner Rover to produce visible scratches on the flat-lying and possibly duricrusted rock called Scooby Doo imply that rinds, if present on contemporary Mars, are thin and hard. No or thin rinds are also suggested by remote-sensing observation of pyroxene at visible and near-IR wavelengths in Martian dark regions [e.g., Mustard *et al.*, 1997] because, if present, they must be thinner than optical penetration depths. Although more data are needed to understand the relationship between physico-chemical properties of rinds and optical penetration depths, a 200- $\mu\text{m}$  rind on basalt WD232 was enough to block observation of a 930-nm ferrous band (Figure 24b).

As discussed above, alteration of basaltic glass and comminution of rocks provide a way to account for the dominant large-scale mineralogical observations of Mars: oxidized global soil with np-Ox as the spectrally dominant ferric-bearing material and ferrous-bearing rocks (pyroxene). If Mars was wetter and warmer in earlier epochs as has been advocated [Pollack, 1979; Pollack *et al.*, 1987], we would expect, on the basis of terrestrial experience, observational evidence for phyllosilicates,  $\text{SiO}_2$  (as quartz, chert, and/or opal), salts, and a variety of ferric oxides as final endproducts of chemical and solution alteration. Phyllosilicates, in particular, should form. According to Goulet *et al.* [1998], the alteration products of a tholeiitic basalt in tropical Brazil include kaolinite, gibbsite, aluminous hematite, and (strongly magnetic) titanaluminous maghemite. The mag-hemites are thought to be oxidation products of lithogenic magnetites in parent rocks [Resende *et al.*, 1986; Allan *et al.*, 1989]. Other reports of phyllosilicates as alteration products of ultramafic, basaltic, and andesitic rocks are common in the literature [e.g., Glassmann, 1982; Nahon and Colin, 1982; Eggleton *et al.*, 1987; Berggaut *et al.*, 1994]. Phyllosilicates have also been reported as the product of hydrothermal alteration of basaltic tephra on the upper slopes of Mauna Kea Volcano, possibly by hydrothermal solutions or interaction of hot tephra with ice during subglacial eruptions [Ugolini, 1974]. Hydro-thermal alteration of basaltic tephra (originally 88–92% glass by volume) to phyllosilicate-bearing materials has been observed in modern times at Surtsey Volcano (Iceland) [Jakobsson and Moore, 1986]. By analogy with terrestrial impact events [Floran *et al.*, 1978; Newsom, 1980; Allen *et al.*, 1982; Newsom *et al.*, 1986; Morris *et al.*, 1995], phyllosilicate formation can occur sporadically throughout Martian history by hydrothermal alteration of impact melt sheets. Thermodynamic calculations by Gooding [1978] show that kaolinite is probably the only thermodynamically stable phyllosilicate gas-solid alteration product under current Martian surface conditions. He concludes it is doubtful that significant amounts of phyllosilicates can be forming on contemporary Mars from solid mineral phases. Subsequently, Gooding and Keil [1978] show that phyllosilicates are favorable gas-solid alteration products of feldspar and mafic silicate glasses under present Martian surface conditions. They suggest a global phyllosilicate layer  $\sim 0.1$ – $1.0$  m thick is possible.

Despite the expectations for crystalline phyllosilicates on a phenomenological basis, there is little compelling evidence for their presence as a major constituent on contemporary Mars. Phyllosilicates have characteristic M-OH (M = Al, Mg, or Fe) lattice modes in the 2200- to 2500-nm spectral region [e.g., Clark *et al.*, 1990]. These features are very weak, if present at all, in

Martian spectral data (see summaries by *Soderblom* [1992] and *Bell et al.* [1994]). Preliminary results [*Christensen et al.* 1998] from the Mars Global Surveyor – Thermal Emission Spectrometer (MGS-TES) instrument also do not indicate the presence of crystalline phyllosilicates, at a level of ~5%. A way around this dilemma is to consider that phyllosilicates were destroyed after formation, which we presume was mostly when Mars was wetter and warmer. A possible mechanism for this exists during times of enhanced numbers of hypervelocity impacts into the Martian surface when its atmosphere is less massive at low obliquity [*Vasavada et al.*, 1993]. Phyllosilicate-bearing target materials are melted and form basaltic glass which is subsequently palagonitized under dryer and cooler conditions to form np-Ox phases. A precedence for recycling of “sedimentary” materials to “lithogenic” materials is the impactites from Meteor Crater (see section 7.0). Pyroxene, olivine, and basaltic glasses were formed from the projectile and sandstone and dolomite target materials; the glass subsequently palagonitized.

## 12. Summary and Conclusions

Our combined multispectral (445-1005 nm), compositional, and magnetic studies of analogue samples and SNC meteorites, together with corresponding data from the Mars Pathfinder mission, provide constraints on the mineralogy of rocks and soils, the chemical relationship between global Martian soil and local Pathfinder rocks and soils, and soil-forming processes and their timing. The salient results and interpretations are as follows:

1. Ferric minerals (67 samples), both well-crystalline and nanophase, have strong ferric absorption edges through the visible spectral region that are responsible for their color and diagnostic minima (T1) and maxima (M1) that can be used for phase identification. Unfortunately, only the T1 feature of hematites and the M1 of jarosites are unique and permit relatively firm phase identification in complex natural samples where more than one phase may be present. Magnetite and maghemite are strongly magnetic.

2. Palagonitic tephtras (11 samples), mostly from the upper slopes of Mauna Kea Volcano, are natural powders of composite particles containing mainly hydrated glass, np-Ox, titanomagnetites, plagioclase, and olivine. Palagonitization (hydrolytic alteration) most likely occurred subaerially under ambient conditions; phyllosilicates are virtually absent. The featureless absorption edge results from np-Ox and, its magnitude (R750/R445) varies from sample to sample and between size fractions of the same sample. The saturation magnetization and low-field magnetic susceptibility (293 K) for the <1-mm size fraction range from 0.65 to 1.24 Am<sup>2</sup>/kg and 8x10<sup>-6</sup> to 14x10<sup>-6</sup> m<sup>3</sup>/kg, respectively. Titanomagnetite is the strongly magnetic phase and, as an opaque mineral, also influences albedo. Depending on sample, the susceptibility either increases or decreases with decreasing size fraction of palagonitic tephtra. Relative to unaltered tephtra, palagonitic tephtra is enriched in TiO<sub>2</sub>, Al<sub>2</sub>O<sub>3</sub>, Fe<sub>2</sub>O<sub>3</sub>T, and MnO and depleted in SiO<sub>2</sub>, CaO, K<sub>2</sub>O, and Na<sub>2</sub>O for both <1-mm and <2-μm size fractions. MgO is enriched in the <1-mm size fraction and depleted in the <2-μm size fraction; P<sub>2</sub>O<sub>5</sub> is unfractionated in the <1-mm size fraction and enriched in the <2-μm size fraction.

3. Sulfatetic tephtras (17 samples), from the summit region of Mauna Kea, are powders of composite particles containing mostly sulfate minerals, glass, plagioclase, olivine, and titanomagnetite; phyllosilicates were not detected. Sulfatetic (acid sulfate) alteration most likely occurred hydrothermally while the tephtra

was still hot and H<sub>2</sub>SO<sub>4</sub> (from volcanic SO<sub>2</sub> gases) circulated in the cinder cone. The sulfate usually present was jarosite, but one sample each was dominated by alunite, hematite, and an unknown phase. Jarositic tephtras have lower R750/R445 values than palagonitic tephtras because R445 is larger in the former. Some jarositic tephtras have a band minimum near 900 nm that is a characteristic of the mineral. The saturation magnetization and low-field magnetic susceptibility (293 K) for the <1-mm size fraction range from 0.38 to 1.45 Am<sup>2</sup>/kg and 3x10<sup>-6</sup> to 14x10<sup>-6</sup> m<sup>3</sup>/kg, respectively; titanomagnetite is the strongly magnetic phase. Relative to unaltered tephtra, jarositic tephtra is slightly enriched in TiO<sub>2</sub> and Fe<sub>2</sub>O<sub>3</sub>T, depleted in MnO and especially MgO, and unfractionated in SiO<sub>2</sub>, Al<sub>2</sub>O<sub>3</sub>, CaO, K<sub>2</sub>O, Na<sub>2</sub>O, and P<sub>2</sub>O<sub>5</sub>. SO<sub>3</sub> contents of sulfatetic tephtras range from 0.6 to 9.3% (<1-mm size fraction).

4. Basaltic materials hydrothermally altered at steam vents were obtained from Sulfur Bank (eight samples) and Mauna Ulu (one sample) on Kilauea Volcano. For Sulfur Bank samples most to all of lithogenic minerals were altered; residual feldspar and clinopyroxene are present in a few of the samples. Poorly crystalline hematite and goethite, cristobalite, and in some cases halloysite were the alteration products. For the Mauna Ulu sample, akaganéite, glass, and possibly other amorphous products are present; akaganéite implies that the alteration took place in the presence of chloride ion. The steam vent samples have ferric absorption edges and, except for Sulfur Bank samples that have clinopyroxene, shallow band minima associated with the ferric oxide. The clinopyroxene-bearing samples have a ferrous pyroxene band centered just outside the IMP range at ~1000 nm. The saturation magnetization and low-field magnetic susceptibility (293 K) for the <1-mm size fraction range from 0.91 to 1.55 Am<sup>2</sup>/kg and 1x10<sup>-6</sup> to 16x10<sup>-6</sup> m<sup>3</sup>/kg, respectively, for Sulfur Bank samples. We do not have firm evidence, but the magnetic phase is probably titanomagnetite or titanomaghemite. For the Mauna Ulu sample the saturation magnetization and susceptibility are 0.00 Am<sup>2</sup>/kg and 0.24x10<sup>-6</sup> m<sup>3</sup>/kg, respectively, indicating that only weakly magnetic or nonmagnetic phases are present. Relative to unaltered materials, all Sulfur Bank samples are enriched in TiO<sub>2</sub>, Fe<sub>2</sub>O<sub>3</sub>T, and P<sub>2</sub>O<sub>5</sub> and depleted in SiO<sub>2</sub>, CaO, Na<sub>2</sub>O, and K<sub>2</sub>O. Al<sub>2</sub>O<sub>3</sub> is usually depleted, and MnO and MgO are depleted only in the samples that do not have residual ferrous silicates.

5. Impactites from Meteor Crater (Arizona) contain quartz, pyroxene, olivine, goethite, and maghemite. Quartz is residual target material, and maghemite and possibly goethite are oxidation products of the impacting iron meteorite. Pyroxene and olivine are not target lithologies but are formed from the projectile (FeO source) and target sandstone (SiO<sub>2</sub> source) and dolomite (CaO and MgO source). Maghemite-bearing impactites are strongly magnetic.

6. Alteration rinds ~200 μm thick on two basaltic rocks are sufficient to block multispectral detection of ferrous silicate bands that are present in freshly broken surfaces. However, the rinds were only moderately enriched in ferric iron relative to rock interiors, as shown by backscatter Mössbauer spectroscopy.

7. Multispectral data were obtained on eight SNC meteorites. The basalts (EET79001, Shergotty, and Zagami) and orthopyroxenite (ALH84001) have a minimum near 930 nm corresponding to ferrous iron in low-Ca pyroxene. The ilmenite (ALH77005) and clinopyroxenites (Nakhla, Lafayette, and Governador Valadares) have negative spectral slopes shortward of 1000 nm from the high-energy wing of ferrous olivine and/or



high-Ca pyroxene bands centered at wavelengths longer than 1000 nm.

8. Because ferric-bearing phases (excluding Fe-Ti spinels) have strong ferric absorption edges at visible wavelengths (high values of R750/R445), there is a positive correlation of R750/R445 (red/blue slope) and  $\text{Fe}^{3+}/\text{Fe}^{2+}$  for analogue samples. To some extent, the correlation results from mixing fine-grained material with high values of R750/R445 and  $\text{Fe}^{3+}/\text{Fe}^{2+}$  (the products of oxidative alteration) with relatively coarse-grained material with low values of R750/R445 and  $\text{Fe}^{3+}/\text{Fe}^{2+}$  (relatively unaltered material).

9. On a plot of R670/R445 versus R750/R445, ferric minerals, analogue samples, and Pathfinder rocks and soils all fall along the same trend line. On the basis of analogue samples, the minimum value of R750/R445 for Pathfinder rocks (~2.0) implies values of  $\text{Fe}^{3+}/\text{Fe}^{2+}$  in the range 0.7-3.0. The maximum value of R750/R445 for Pathfinder soils (~7.0) implies values of  $\text{Fe}^{3+}/\text{Fe}^{2+}$  in the range 3-20.

10. Plots of BD600 and R800/R750 versus BD530b, which are measures of the strength of spectral features in the ferric absorption edge and the position of the reflectivity maximum (M1), are consistent with the dominant ferric-bearing material being np-Ox occurring in composite particles plus a well-crystalline ferric mineral. For the crystalline ferric mineral, hematite and/or hematite plus nanophase goethite are most consistent with the data, but nanophase goethite by itself, maghemite, akagenéite, schwertmannite, and nanophase lepidocrocite are also possible interpretations. The ferric oxides that are consistently not favored by the data as sole alteration products are jarosites and well-crystalline goethite and lepidocrocite.

11. The spectral region between 750 and 1000 nm provides evidence for ferrous iron. A subset of rocks and soils has a weak minimum near 930 nm (Bright II soils), which corresponds to the ferrous band from low-Ca pyroxene in basaltic and orthopyroxenite SNC meteorites. A similar band (assigned to low-Ca pyroxene) is also observed in the composite spectrum of the Oxia-Palpus dark region, which is derived from telescopic and Phobos-2 data. A second subset of spectra is characterized by a negative spectral slope from ~800 to 1000 nm. It could result from the high-energy wing of a ferrous high-Ca pyroxene/olivine band as in the clinopyroxenite SNC meteorites or Meteor Crater impactites, a mixture of bright and dark materials like some palagonitic tephra, and/or thin coatings of bright dust on dark rocks. In any case, there is spectral evidence for ferrous silicates in both Pathfinder rocks and soils. The spectrum of the Surface Dust (and magnetic dust), however, does not show evidence for ferrous silicates.

12. Instead of ferrous iron, the 930-nm band can be assigned to the ferric oxides that have T1 values near 930 nm and satisfy the constraints discussed above for the ferric absorption edge (nanophase goethite, maghemite, akagenéite, and schwertmannite). It is possible that these ferric minerals and low-Ca pyroxene are both present.

13. Chemical data for Pathfinder rocks and soils are consistent with two-component mixtures between an "andesitic" rock with low MgO and  $\text{SO}_3$  concentrations (the Pathfinder soil-free rock) and a global, more basaltic soil with high MgO and  $\text{SO}_3$  concentrations (the Pathfinder rock-free soil). The Pathfinder rock-free soil can be modeled as a chemical (but not mineralogical) mixture of SNC meteorites and the Pathfinder soil-free rock.

14. Chemically, Pathfinder soil cannot be derived from Pathfinder rocks by any of the hydrolytic and sulfuric alteration

processes we studied for analogue samples. Chemical fractionation during alteration undoubtedly took place, but its signatures have been erased by mixing processes that produced a global-average soil (the Pathfinder rock-free soil), so that local soils are not derived solely from local rocks.

15. The strongly magnetic phase in palagonitic and sulfatetic tephra is titanomagnetite and/or possibly its oxidation product titanomaghemite (collectively Fe-Ti spinel) and is thus lithogenic in origin or has a lithogenic precursor. The saturation magnetization of tephra samples (~1.0  $\text{Am}^2/\text{kg}$  for the <1-mm size fraction) is too low to satisfy the value ( $4 \pm 2 \text{ Am}^2/\text{kg}$ ) inferred for Martian dust. Despite this, Fe-Ti spinels cannot be excluded as the strongly magnetic minerals because they may be present in higher concentrations in Martian dust and because simulation experiments using palagonitic tephra with a Pathfinder Magnet Array on Mauna Kea Volcano reproduce Pathfinder results. The latter consideration implies that the saturation magnetization may not be the appropriate parameter to infer whether or not a material will satisfy the constraints of the Pathfinder Magnetic Array experiment.

16. The predominantly palagonitic spectral signature and magnetic nature of Martian soil and dust are consistent with glassy precursors with imbedded Fe-Ti spinel particles. Comparison with lunar glass production rates suggests that production of sufficient quantities of glassy materials on Mars by volcanic (e.g., fire fountaining) and impact processes is sufficient to account for these observations.

**Acknowledgements.** This work was supported by NASA's Cosmochemistry Program under RTOP 344-31-20-24 (R.V.M.) and by NSF (award EAR-9217945) and Franklin & Marshall College for funds to purchase the Philips 2404 XRF vacuum spectrometer (S.A.M.). R.V.M. thanks C. Pamplin for  $\text{SO}_3$  analyses done as part of an LPI Summer Intern Project. S.A.M. thanks Karen R. Mertzman for her invaluable work in the sample preparation laboratory. We thank the following individuals for making samples available for this study: U. Schwertmann (natural ferrihydrites), C. B. Moore (Meteor Crater impactites), E. Murad (akagenéite SAK1 and schwertmannite BT-4), D. Blaney (palagonitic tephra HWP301), J. H. Jones (Meteor Crater iron shale MCIS1), and G. E. Lofgren (basaltic komatiite M1497). D. Blaney and J. Mustard provided thoughtful reviews of the manuscript.

## References

- Adams, J. B., and T. B. McCord, Mars: Interpretation of spectral reflectivity of light and dark regions, *J. Geophys. Res.*, **74**, 4851-4856, 1969.
- Adams, J. B., M. O. Smith, and P. E. Johnson, Spectral mixture modeling: A new analysis of rock and soil types at the Viking lander site, *J. Geophys. Res.*, **91**, 8089-8112, 1986.
- Ailin-Pyzik, I. B., and S. E. Sommer, Microscale chemical effects of low temperature alteration of DSDP basaltic glasses, *J. Geophys. Res.*, **86**, 9503-9510, 1981.
- Allan, J. E. M., J. M. D. Coey, M. Resende, and J. D. Fabris, Magnetic properties of iron-rich oxisols, *Phys. Chem. Miner.*, **15**, 470-475, 1988.
- Allan, J. E. M., J. M. D. Coey, I. S. Sanders, U. Schwertmann, G. Friedrich, and A. Wiechowski, An occurrence of a fully-oxidized natural titanomaghemite in basalt, *Mineral. Mag.*, **53**, 299-304, 1989.
- Allen, C. C., J. L. Gooding, M. Jercinovic, and K. Keil, Altered basaltic glass: A terrestrial analog to the soil of Mars, *Icarus*, **45**, 347-369, 1981.
- Allen, C. C., J. L. Gooding, and K. Keil, Hydrothermally altered impact melt rock and breccia: Contributions to the soil of Mars, *J. Geophys. Res.*, **87**, 10,083-10,101, 1982.
- Allen, C. C., K. M. Jager, R. V. Morris, D. J. Lindstrom, M. M. Lindstrom, and J. P. Lockwood, JSC Mars-1: A Martian soil simulant, in *Space 98*, edited by R. G. Galloway and S. Lokaj, pp. 469-476, Am. Soc. Civil Engin., Reston, Va., 1998a.
- Allen, C. C., K. M. Jager, R. V. Morris, D. J. Lindstrom, M. M. Lindstrom, and J. P. Lockwood, Martian soil simulant available for



- scientific, educational study, *Eos, Trans. AGU*, 79(34), 405, 408-409, 1998b.
- Anderson, D. M., and A. R. Tice, The analysis of water in the Martian regolith, *J. Mol. Evol.*, 14, 33-38, 1979.
- Arvidson, R. E., J. L. Gooding, and H. J. Moore, The Martian surface as imaged, sampled, and analyzed by the Viking landers, *Rev. Geophys.*, 27, 39-60, 1989.
- Baird, A. K., P. Toulmin, B. C. Clark, H. J. Rose, K. Keil, R. P. Christian, and J. L. Gooding, Mineralogic and petrologic implications of Viking geochemical results from Mars, *Science*, 194, 1288-1293, 1976.
- Banin, A., T. Ben-Shlomo, L. Margulies, D. F. Blake, R. L. Mancinelli, and A. U. Gehring, The nanophase iron mineral(s) in Mars soil, *J. Geophys. Res.*, 98, 20,831-20,853, 1993.
- Banin, A., F. X. Han, I. Kan, and A. Cicelsky, Acidic volatiles and the Mars soil, *J. Geophys. Res.*, 102, 13,341-13,356, 1997.
- Basaltic Volcanism Study Project, *Basaltic Volcanism on the Terrestrial Planets*, 1286 pp., Pergamon, Tarrytown, NY, 1981.
- Bell, J. F., III, Iron, sulfate, carbonate, and hydrated minerals on Mars, in *Mineral Spectroscopy: A Tribute to Roger G. Burns*, edited by M. D. Dyar, C. McCammon, and M. W. Schaefer, *Spec. Publ. Geochem. Soc.*, 5, 359-380, 1996.
- Bell, J. F., III, T. B. McCord, and P. D. Owensby, Observational evidence of crystalline iron oxides on Mars, *J. Geophys. Res.*, 95, 14,447-14,461, 1990.
- Bell, J. F., III, R. V. Morris, and J. B. Adams, Thermally altered palagonitic tephra: A spectral and process analog to the soil and dust of Mars, *J. Geophys. Res.*, 98, 3373-3385, 1993.
- Bell, J. F., III, J. B. Pollack, T. R. Gaballe, D. P. Cruikshank, and R. Freedman, Spectroscopy of Mars from 2.04 to 2.44  $\mu\text{m}$  during the 1993 opposition: Absolute calibration and atmospheric vs. mineralogic origin of narrow absorption features, *Icarus*, 111, 106-123, 1994.
- Bell, J. F., III, et al., Mineralogic and compositional properties of Martian soil and dust: Results from Mars Pathfinder, *J. Geophys. Res.*, this issue.
- Berggaut, V., A. Singer, and K. Stahr, Palagonite reconsidered: Paracrystalline illite-smectites from regoliths on basic pyroclastics, *Clays Clay Miner.*, 42, 582-592, 1994.
- Bigham, J. M., U. Schwertmann, L. Carlson, and E. Murad, A poorly crystallized oxyhydroxysulfate of iron formed by bacterial oxidation of Fe(II) in acid mine waters, *Geochem. Cosmochim. Acta*, 54, 2743-2758, 1990.
- Bishop, J. L., and E. Murad, Schwertmannite on Mars? Spectroscopic analyses of schwertmannite, its relationship to other ferric minerals, and its possible presence in the surface material on Mars, in *Mineral Spectroscopy: A Tribute to Roger G. Burns*, edited by M. D. Dyar, C. McCammon, and M. W. Schaefer, *Spec. Publ. Geochem. Soc.*, 5, 337-358, 1996.
- Bishop, J. L., C. M. Pieters, and R. G. Burns, Reflectance and Mössbauer spectroscopy of ferrihydrite-montmorillonite assemblages as Mars soil analog materials, *Geochim. Cosmochim. Acta*, 57, 4583-4595, 1993.
- Bishop, J. L., H. Froschl, and R. L. Mancinelli, Alteration processes in volcanic soils and identification of exobiologically important weathering products on Mars using remote sensing, *J. Geophys. Res.*, 103, 31,457-31,476, 1998a.
- Bishop, J. L., C. M. Pieters, T. Hiroi, and J. F. Mustard, Spectroscopic analysis of Martian meteorite Allan Hills 84001 powder and applications for spectral identification of minerals and other soil components on Mars, *Meteorit. Planet. Sci.*, 33, 699-707, 1998b.
- Bishop, J., J. F. Mustard, C. M. Pieters, and T. Hiroi, Recognition of minor constituents in reflectance spectra of Allan Hills 84001 chips and the importance for remote sensing of Mars, *Meteorit. Planet. Sci.*, 33, 693-698, 1998c.
- Borggaard, O. K., Effect of surface area on mineralogy of iron oxides on their surface charge and anion-adsorption properties, *Clays Clay Minerals*, 31, 230-232, 1983.
- Bouska, V., and J. F. Bell III, Assumptions about the presence of natural glasses on Mars, *J. Geophys. Res.*, 98, 18,719-18,725, 1993.
- Boyd, F. R., and S. A. Mertzman, Composition and structure of the Kaapvaal lithosphere, southern Africa, in *Magmatic Processes: Physicochemical Principles*, edited by B. O. Mysen, *Spec. Publ. Geochem. Soc.*, 1, 13-24, 1987.
- Brophy, G. P., and M. F. Sheridan, Sulfate studies, IV, The jarosite-nartojarosite-hydroxium jarosite solid solution series, *Am. Mineral.*, 50, 1595-1607, 1965.
- Buckingham, W. F., and S. E. Sommer, Mineralogical characterization of rock surfaces formed by hydrothermal alteration and weathering: Application to remote sensing, *Econ. Geol.*, 78, 664-674, 1983.
- Buemi, A., G. Cimino, and G. Strazzula, Characterization of Etean soils and application to Mars, *J. Geophys. Res.*, 103, 13,667-13,674, 1998.
- Bunch, T. E., and W. A. Cassidy, Petrographic and electron microprobe study of the Monturaqui impactite, *Contrib. Mineral. Petrol.*, 36, 95-112, 1972.
- Bunch, T. E., and A. M. Reid, The nakhlites, part I, Petrography and mineral chemistry, *Meteoritics*, 10, 303-315, 1975.
- Burns, R. G., Terrestrial analogues of the surface rocks of Mars?, *Nature*, 320, 55-56, 1986.
- Burns, R. G., Gossans on Mars, *Proc. Lunar Planet. Sci. Conf. 18th*, 713-721, 1988.
- Burns, R. G., *Mineralogical Applications of Crystal Field Theory*, 551 pp., Cambridge Univ. Press, New York, 1993.
- Burns, R. G., and D. S. Fisher, Evolution of sulfide mineralization on Mars, *J. Geophys. Res.*, 95, 14,169-14,173, 1990a.
- Burns, R. G., and D. S. Fisher, Iron-sulfur mineralogy of Mars: Magmatic evolution and chemical weathering products, *J. Geophys. Res.*, 95, 14,415-14,421, 1990b.
- Burns, R. G., and T. C. Solberg,  $^{57}\text{Fe}$ -bearing oxide, silicate, and aluminosilicate minerals: Crystal structure trends in Mössbauer spectra, in *Spectroscopic Characterization of Minerals and Their Surfaces*, edited by L. M. Coyne, S. W. S. McKeever, and D. F. Blake, *ACS Symp. Ser.*, 415, 262-283, 1990.
- Carlson, L., and U. Schwertmann, Natural ferrihydrites in surface deposits from Finland and their association with silica, *Geochim. Cosmochim. Acta*, 45, 421-429, 1981.
- Carlson, L., and U. Schwertmann, Iron and manganese oxides in Finnish ground water treatment plants, *Water Res.*, 21, 165-170, 1987.
- Carmichael, R. S., Magnetic properties of minerals and rocks, in *CRC Handbook of Physical Properties of Rocks*, vol. II, edited by R. S. Carmichael, pp. 229-287, CRC Press, Boca Raton, Fla., 1982.
- Christensen, P. R., et al., Results from the Mars Global Surveyor Thermal Emission Spectrometer, *Science*, 279, 1692-1697, 1998.
- Christensen, P. R., et al., The composition of Martian surface materials: Mars Global Surveyor Thermal Emission Spectrometer observations, in *Lunar Planet. Sci. XXX*, abstract 1461 [CD-ROM], 1999.
- Clark, B. C., Geochemical components in Martian soil, *Geochim. Cosmochim. Acta*, 57, 4574-4581, 1993.
- Clark, B. C., and A. K. Baird, Is the Martian lithosphere sulfur rich?, *J. Geophys. Res.*, 84, 8395-8403, 1979.
- Clark, B. C., A. K. Baird, R. J. Weldon, D. M. Tsusaki, L. Schnabel, and M. P. Candelaria, Chemical composition of Martian fines, *J. Geophys. Res.*, 87, 10,059-10,067, 1982.
- Clark, R. C., T. V. V. King, M. Klejwa, G. A. Swayze, and N. Vergo, High spectral resolution reflectance spectroscopy of minerals, *J. Geophys. Res.*, 95, 12,653-12,680, 1990.
- Cloutis, E. A., and M. J. Gaffey, Pyroxene spectroscopy revisited: Spectral-compositional correlations and relationship to geothermometry, *J. Geophys. Res.*, 96, 22,809-22,826, 1991.
- Coey, J. M. D., S. Morup, M. B. Madsen, and J. M. Knudsen, Titanomaghemite in magnetic soils on Earth and Mars, *J. Geophys. Res.*, 95, 14,423-14,425, 1990.
- Cornell, R., and U. Schwertmann, *The Iron Oxides: Structure, Properties, Reactions, Occurrences, and Uses*, 573 pp., VHC, New York, 1996.
- Crisp, J., The effect of thin coatings of dust or soil on the bulk APXS composition of the underlying rocks at the Pathfinder landing site, in *Lunar Planet. Sci. XXIX*, abstract 1962 [CD-ROM], 1998.
- Curi, N., and D. P. Franzmeier, Effect of parent rocks on chemical and mineralogical properties of some oxisols in Brazil, *Soil Sci. Soc. Am. J.*, 51, 153-158, 1987.
- Danckwerth, P. A., P. C. Hess, and M. J. Rutherford, The solubility of sulfur in high-TiO<sub>2</sub> basalts, *Proc. Lunar Planet. Sci. Conf. 10th*, 517-530, 1979.
- Dang, M.-Z., D. G. Rancourt, J. E. Dutrizac, G. Lamarche, and R. Provencher, Interplay of surface conditions, particle size, stoichiometry, cell parameters, and magnetism in synthetic hematite-like minerals, *Hyperfine Interact.*, 117, 271-319, 1998.
- de Bakker, P. M. A., E. De Grave, R. E. Vandenberghe, and L. H. Bowen, Mössbauer study of small-particle maghemite, *Hyperfine Interact.*, 54, 493-498, 1990.
- De Grave, E., L. H. Bowen, and S. B. Weed, Mössbauer study of aluminum-substituted hematites, *J. Magn. Magn. Mater.*, 27, 98-108, 1982.
- Dreibus, G., J. Bruechner, R. Reider, and H. Wanke, Implications of in situ measurements of chemical compositions of rocks and soils at the Mars Pathfinder landing site, *Proc. Internat. Symp. Mars Explor. Prog. Samp. Ret. Missions (Paris)*, P15/S2(9), 1999.

- Eggleton, R. A., and R. W. Fitzpatrick, New data and a revised structural model for ferrihydrite, *Clays Clay Miner.*, 36, 111-124, 1988.
- Eggleton, R. A., C. Foudoulis, and D. Varkevissar, Weathering of basalt: Changes in rock chemistry and mineralogy, *Clays Clay Miner.*, 35, 161-169, 1987.
- Erard, S., and W. Calvin, New composite spectra of Mars, 0.4-5.7  $\mu$ m, *Icarus*, 130, 449-460, 1997.
- Evans, D. L., and J. B. Adams, Comparison of Viking Lander multispectral images and laboratory reflectance spectra of terrestrial samples, *Proc. Lunar Planet. Sci. Conf. 10th*, 1829-1834, 1979.
- Farrand, W. H., and R. B. Singer, Spectral analysis and mapping of palagonitic tuffs of Pavant Butte, Millard County, Utah, *Geophys. Res. Lett.*, 18, 2237-2240, 1991.
- Farrand, W. H., and R. B. Singer, Alteration of hydrovolcanic basaltic ash: Observations with visible and near-infrared spectrometry, *J. Geophys. Res.*, 97, 17,393-17,408, 1992.
- Feierberg, M. A., and M. J. Drake, The meteorite-asteroid connection: The infrared spectra of Eucrites, Shergottites, and Vesta, *Science*, 209, 805-807, 1980.
- Fischer, E. M., and C. M. Pieters, The continuum slope of Mars: Bidirectional reflectance investigations and applications to Olympus Mons, *Icarus*, 102, 185-202, 1993.
- Fleischer, M., G. Y. Chao, and A. Kato, New mineral names, *Am. Mineral.*, 485-486, 1975.
- Floran, R. J., R. A. F. Grieve, W. C. Phinney, J. L. Warner, C. H. Simonds, D. P. Blanchard, and M. R. Dence, Manicouagan impact melt, Quebec, 1, Stratigraphy, petrology, and chemistry, *J. Geophys. Res.*, 83, 2737-2759, 1978.
- Flynn, G. J., and D. S. McKay, An assessment of the meteoritic contribution to the Martian soil, *J. Geophys. Res.*, 95, 14,497-14,509, 1990.
- Fontes, M. P. F., and S. B. Weed, Iron oxides in selected Brazilian oxisols, I, Mineralogy, *Soil Sci. Soc. Am. J.*, 55, 1143-1149, 1991.
- Frey, F. A., W. B. Bryan, and G. Thompson, Atlantic Ocean floor: Geochemistry and petrology of basalts from legs 2 and 3 of the Deep-Sea Drilling Project, *J. Geophys. Res.*, 79, 5507-5527, 1974.
- Furniss, G., N. W. Hinman, G. A. Doyle, and D. D. Runnells, Radiocarbon-dated ferricrete provides a record of natural acid rock drainage and paleoclimatic changes, *Environ. Geol.*, 37, 102-106, 1999.
- Fysh, S. A., and P. E. Clark, Aluminous goethite: A Mössbauer study, *Phys. Chem. Miner.*, 65, 1044-1049, 1982a.
- Fysh, S. A., and P. E. Clark, Aluminous hematite: A Mössbauer study, *Phys. Chem. Miner.*, 8, 257-267, 1982b.
- Geissler, P. E., R. B. Singer, G. Komatsu, S. Murchie, and J. Mustard, An unusual spectral unit in West Candor Chasma: Evidence for aqueous or hydrothermal alteration in the Martian canyons, *Icarus*, 106, 380-391, 1993.
- Gibson, E. K., Jr., A comparison of the spectral reflectivity of Mars with oxidized meteoritic material, *Icarus*, 13, 96-99, 1970.
- Glasmann, J. R., Alteration of andesite in wet, unstable soils of Oregon's Western Cascades, *Clays Clay Miner.*, 30, 253-263, 1982.
- Golden, D. C., R. V. Morris, H. V. Lauer Jr., and S. R. Yang, Mineralogy of three slightly palagonitized tephra samples from the summit of Mauna Kea, Hawaii, *J. Geophys. Res.*, 98, 3401-3411, 1993.
- Golden, D. C., R. V. Morris, D. W. Ming, J. F. Bell III, S. V. Yang, and D. R. Thompson, Occurrence of a titanium-bearing jarosite from Hawaii, in *Lunar Planet. Sci. XXVII*, 427-428, 1996.
- Golden, D. C., R. V. Morris, and D. W. Ming, Mineralogy of the clay size fraction (<2  $\mu$ m) of palagonitic tephra from the upper slopes of Mauna Kea Volcano, Hawaii, *Lunar Planet. Sci. XXIX*, abstract 1720 [CD-ROM], 1998.
- Gooding, J. L., Chemical weathering on Mars, *Icarus*, 33, 483-513, 1978.
- Gooding, J. L., Soil mineralogy and chemistry on Mars: Possible clues from salts and clays in SNC meteorites, *Icarus*, 99, 28-41, 1992.
- Gooding, J. L., and K. Keil, Alteration of glass as a possible source of clay minerals on Mars, *Geophys. Res. Lett.*, 5, 727-730, 1978.
- Goulart, A. T., J. D. Fabris, M. F. de Jesus Filho, J. M. D. Coey, G. M. da Costa, and E. De Grave, Iron oxides in a soil developed from basalt, *Clays Clay Miner.*, 46, 369-378, 1998.
- Govindaraju, K., 1994 Compilation of working values and sample description for 383 geostandards, *Geostand. Newsl.*, 18, 1-158, 1994.
- Guinness, E. A., R. E. Arvidson, M. A. Dale-Bannister, R. B. Singer, and E. A. Bruckenthal, On the spectral reflectance properties of materials exposed at the Viking landing sites, *J. Geophys. Res.*, 92, E575-E587, 1987.
- Hargraves, R. B., Could Mars soil be a volcanic aerosol deposit?, in *Lunar Planet. Sci. XXX*, abstract 1364 [CD-ROM], 1999.
- Hargraves, R. B., D. W. Collinson, R. V. Arvidson, and C. R. Spitzer, The Viking magnetic properties experiment: Primary mission results, *J. Geophys. Res.*, 82, 4547-4558, 1977.
- Hargraves, R. B., D. W. Collinson, R. E. Arvidson, and P. M. Cates, Viking magnetic properties experiment: Extended mission results, *J. Geophys. Res.*, 84, 8379-8384, 1979.
- Hargraves, R. B., J. M. Knudsen, and N. B. Madsen, Caution advised on suitability of a Mars soil simulant, *Eos Trans. AGU*, 80(15), 168-169, 1999.
- Head, J. W., III, and L. Wilson, Interpretation of Mars Pathfinder and Viking soil and rock geochemical results: A physical volcanology perspective, in *Lunar Planet. Sci. XXX*, abstract 1328 [CD-ROM], 1998.
- Heidner, F., U. Korner, and P. Bitschene, Volcanic ash particles as carriers of remanent magnetization in deep-sea sediments from the Kerguelen Plateau, *Earth Planet. Sci. Lett.*, 118, 121-134, 1993.
- Herbert, R. B., Jr., Properties of goethite and jarosite precipitated from acidic groundwater, Dalarna, Sweden, *Clays Clay Miner.*, 45, 261-273, 1997.
- Horz, F., and M. Cintala, Collisionally processed rocks on Mars, in *Lunar Planet. Sci. XXX*, abstract 1641 [CD-ROM], 1999.
- Hviid, S. F., et al., Magnetic properties experiments on the Mars Pathfinder Lander: Preliminary results, *Science*, 278, 1768-1770, 1997.
- Jakobsson, S. P., On the consolidation and palagonitization of the tephra of the Surtsey volcanic island, Iceland, *Surtsey Res. Progr. Rep. VI*, 121-128, 1972.
- Jakobsson, S. P., and J. G. Moore, Hydrothermal minerals and alteration rates at Surtsey volcano, Iceland, *Geol. Soc. Am. Bull.*, 97, 648-659, 1986.
- Jercinovic, M. J., K. Keil, M. R. Smith, and R. A. Schmitt, Alteration of basaltic glasses from north-central British Columbia, Canada, *Geochim. Cosmochim. Acta*, 54, 2679-2696, 1990.
- Johnson, G. R., and G. R. Olhoeft, Densities of rocks and minerals, in *CRC Handbook of Physical Properties of Rocks*, vol. III, edited by R. S. Carmichael, pp. 1-38, CRC Press, Boca Raton, Fla., 1984.
- Johnston, J. H., and K. Norrish, A  $^{57}\text{Fe}$  Mössbauer spectroscopic study of a selection of Australian and other goethites, *Aust. J. Soil Res.*, 19, 231-237, 1981.
- Kieffer, S. W., and C. H. Simonds, The role of volatiles and lithology in the impact cratering process, *Rev. Geophys. Space Phys.*, 18, 143-181, 1980.
- Kieffer, S. W., R. B. Schaal, R. Gibbons, F. Horz, D. J. Milton, and A. Dube, Shocked basalt from Lunar Impact Crater, India, and experimental analogues, *Proc. Lunar Sci. Conf. 7th*, 1391-1412, 1976.
- Korotev, R. L., L. A. Haskin, and B. L. Jolliffe, A simulated geochemical rover mission to the Tarus-Littrow valley of the Moon, *J. Geophys. Res.*, 100, 14,403-14,420, 1995.
- Kosmas, C. S., D. P. Franzmeier, and D. G. Schulze, Relationship among derivative spectroscopy, color, crystallite dimensions, and Al substitution of synthetic goethites and hematites, *Clays Clay Miner.*, 34, 625-634, 1986.
- Landis, G. A., and P. P. Jenkins, Dust on Mars: Materials adherence experiment results from Mars Pathfinder, *Proc. 26th IEEE Photovoltaic Specialists Conf.*, pp. 865-869, Anaheim Ca., Sept. 29-Oct. 3, 1997.
- Lane, M. D., R. V. Morris, and P. R. Christensen, An extensive deposit of crystalline hematite in Terra Meridiani, Mars, in *Lunar Planet. Sci. XXX*, abstract 1469 [CD-ROM], 1999.
- Lindsay, W. L., *Chemical Equilibria in Soils*, 449 pp., Wiley-Interscience, New York, 1979.
- Lodders, K., A survey of shergottite, nakhlite, and chassigny meteorites whole-rock compositions, *Meteorit. Planet. Sci.*, 33, A183-A190, 1998.
- Madsen, M. B., S. F. Hviid, H. P. Gunnlaugsson, J. M. Knudsen, W. Goetz, C. T. Pedersen, A. R. Dinesen, C. T. Morgensen, M. Olsen, and R. B. Hargraves, The magnetic properties experiments on Mars Pathfinder, *J. Geophys. Res.*, 104, 8761-8779, 1999.
- Markiewicz, W. J., R. M. Sablotny, H. U. Keller, N. Thomas, D. Titov, and P. Smith, Optical properties of the Martian aerosols derived from Imager for Mars Pathfinder midday sky brightness data, *J. Geophys. Res.*, 104, 9009-9017, 1999.
- Martin, L. J., and R. W. Zurek, An analysis of the history of dust activity on Mars, *J. Geophys. Res.*, 98, 3221-3246, 1993.

- Mason, B., Cosmochemistry, part I, Meteorites, in *Data of Geochemistry*, 6th ed., edited by M. Fleischer, *U. S. Geol. Surv. Prof. Pap., Chap. B, 440-B-1*, 1979.
- McCammon, C., Mössbauer spectroscopy of minerals, in *Mineral Physics and Crystallography: A Handbook of Physical Constants*, edited by T. J. Ahrens, pp. 332-347, AGU, Washington D. C., 1995.
- McCord, T. B., R. L. Huguenin, D. Mink, and C. Pieters, Spectral reflectance of martian areas during the 1973 opposition: Photoelectric filter photometry 0.33-1.10  $\mu\text{m}$ , *Icarus*, **31**, 25-39, 1977.
- McCord, T. B., R. N. Clark, and R. B. Singer, Mars: Near-infrared spectral reflectance of surface regions and compositional implications, *J. Geophys. Res.*, **87**, 3021-3032, 1982.
- McFadden, L. A., Spectral reflectance of SNC meteorites: Relationships to Martian surface compositions, *Tech. Rep. 88-05*, pp. 88-90, Lunar and Planet. Inst., Houston, Tex., 1987.
- McMaster, W. II., N. K. Del Grande, J. H. Mallett, and J. H. Hubbell, Compilation of X-ray cross sections, *UCRL-50174 Sec. II Rev. 1*, 350 pp., Lawrence Radiat. Lab., Univ. of Calif., Livermore, 1969.
- McSween, H. Y., Jr., SNC meteorites: Clues to martian petrologic evolution?, *Rev. Geophys.*, **23**, 391-416, 1985.
- McSween, H. Y., Jr., What we have learned about Mars from SNC meteorites, *Meteoritics*, **29**, 757-779, 1994.
- McSween, H. Y., Jr., et al., Chemical, multispectral, and textural constraints on the composition and origin of rocks at the Mars Pathfinder landing site, *J. Geophys. Res.*, **104**, 8679-8715, 1999.
- Merenyi, E., R. B. Singer, and J. S. Miller, Mapping of spectral variations on the surface of Mars from high spectral resolution telescopic images, *Icarus*, **124**, 280-295, 1996.
- Mittlefehldt, D. W., T. H. See, and F. Horz, Projectile dissemination in impact melts from Meteor Crater, AZ, *Lunar Planet. Sci. XXIII*, 919-920, 1992.
- Moore, C. B., P. J. Birrell, and C. F. Lewis, Variations in the chemical and mineralogical composition of rim and plains specimens of the Canyon Diablo meteorite, *Geochim. Cosmochim. Acta*, **31**, 1885-1892, 1967.
- Moore, H. J., R. E. Hutton, R. F. Scott, C. R. Spitzer, and R. W. Shorthill, Surface materials at the Viking landing sites, *J. Geophys. Res.*, **82**, 4497-4523, 1977.
- Moore, H. J., C. R. Spitzer, K. Z. Bradford, P. M. Cates, R. E. Hutton, and R. W. Shorthill, Sample fields of the Viking landers, physical properties, and aeolian processes, *J. Geophys. Res.*, **84**, 8365-8377, 1979.
- Morris, R. V., The surface exposure (maturity) of lunar soils: Some concepts and  $\text{I}_0/\text{FeO}$  compilation, *Proc. Lunar Planet. Sci. Conf. 9th*, 1827-1860, 1978.
- Morris, R. V., Reflectivity spectra (350-2200 nm) of SNC meteorites, *Lunar Planet. Sci. XX*, 719-720, 1989.
- Morris, R. V., and D. C. Golden, Goldenrod pigments and the occurrence of hematite and possibly goethite in the Olympus-Amazons region of Mars, *Icarus*, **134**, 1-10, 1998.
- Morris, R. V., and H. V. Lauer Jr., Stability of goethite ( $\alpha\text{-FeOOH}$ ) and lepidocrocite ( $\gamma\text{-FeOOH}$ ) to dehydration by UV radiation: Implications for their occurrence on the Martian surface, *J. Geophys. Res.*, **86**, 10,893-10,899, 1981.
- Morris, R. V., and H. V. Lauer Jr., Matrix effects for reflectivity spectra of dispersed nanophase (superparamagnetic) hematite with application to Martian spectral data, *J. Geophys. Res.*, **95**, 5101-5109, 1990.
- Morris, R. V., and S. C. Neeley, Optical properties of hematite-magnetite mixtures: Implications for Mars, *Lunar Planet. Sci. XIII*, 548-549, 1982.
- Morris, R. V., H. V. Lauer Jr., C. A. Lawson, E. K. Gibson Jr., G. A. Nace, and C. Stewart, Spectral and other physicochemical properties of submicron powders of hematite ( $\alpha\text{-Fe}_2\text{O}_3$ ), maghemite ( $\gamma\text{-Fe}_2\text{O}_3$ ), magnetite ( $\text{Fe}_3\text{O}_4$ ), goethite ( $\alpha\text{-FeOOH}$ ), and lepidocrocite ( $\gamma\text{-FeOOH}$ ), *J. Geophys. Res.*, **90**, 3126-3144, 1985.
- Morris, R. V., D. G. Agresti, H. V. Lauer Jr., J. A. Newcomb, T. D. Shelfer, and A. V. Murali, Evidence for pigmentary hematite on Mars based on optical, magnetic, and Mössbauer studies of superparamagnetic (nanocrystalline) hematite, *J. Geophys. Res.*, **94**, 2760-2778, 1989.
- Morris, R. V., J. J. Gooding, H. V. Lauer Jr., and R. B. Singer, Origins of Marslike spectral and magnetic properties of a Hawaiian palagonitic soil, *J. Geophys. Res.*, **95**, 14,427-14,434, 1990.
- Morris, R. V., H. V. Lauer Jr., D. G. Schulze, and R. G. Burns, Preparation and characterization of a nanophase hematite powder, *Lunar Planet. Sci. XXII*, 927-928, 1991.
- Morris, R. V., D. G. Schulze, H. V. Lauer Jr., D. G. Agresti, and D. D. Shelfer, Reflectivity (visible and near-IR), Mössbauer, static magnetic, and X-ray diffraction properties of aluminum-substituted hematites, *J. Geophys. Res.*, **97**, 10,257-10,266, 1992.
- Morris, R. V., D. C. Golden, J. F. Bell III, H. V. Lauer Jr., and J. B. Adams, Pigmenting agents in Martian soils: Inferences from spectral, Mössbauer, and magnetic properties of nanophase and other iron oxides in Hawaiian palagonitic soil PN-9, *Geochim. Cosmochim. Acta*, **57**, 4597-4609, 1993.
- Morris, R. V., D. C. Golden, J. F. Bell III, and H. V. Lauer Jr., Hematite, pyroxene, and phyllosilicates on Mars: Implications from oxidized impact melt rocks from Manicouagan Crater, Quebec, Canada, *J. Geophys. Res.*, **100**, 5319-5328, 1995.
- Morris, R. V., D. W. Ming, D. C. Golden, and J. F. Bell III, An occurrence of jarositic tephra on Mauna Kea, Hawaii: Implications for the ferric mineralogy of the Martian surface, in *Mineral Spectroscopy: A Tribute to Roger G. Burns*, edited by M. D. Dyar, C. McCammon, and M. W. Schaefer, *Spec. Publ. Geochem. Soc.*, **5**, 327-336, 1996.
- Morris, R. V., D. C. Golden, and J. F. Bell III, Low-temperature reflectivity spectra of red hematite and the color of Mars, *J. Geophys. Res.*, **102**, 9125-9133, 1997.
- Morris, R. V., S. W. Squyres, J. F. Bell III, T. Economou, G. Klingelhoefer, P. Held, L. A. Haskin, A. Wang, B. L. Jolliffe, and R. Rieder, Analysis of Martian surface materials during the Mars Surveyor 2001 mission by the Athena instrument payload, in *Lunar Planet. Sci. XXX*, abstract 1326 [CD-ROM], 1998a.
- Morris, R. V., D. C. Golden, T. D. Shelfer, and H. V. Lauer Jr., Lepidocrocite to maghemite to hematite: A pathway to magnetic and hematitic Martian soil, *Meteorit. Planet. Sci.*, **33**, 743-751, 1998b.
- Morris, R. V., G. Klingelhoefer, R. L. Korotev, and T. D. Shelfer, Mössbauer mineralogy on the Moon: The lunar regolith, *Hyperfine Interact.*, **117**, 405-432, 1998c.
- Morris, R. V., T. D. Shelfer, D. W. Ming, and D. C. Golden, Magnetic properties experiments with a Pathfinder Magnet Array on Mauna Kea volcano: Evidence the Martian magnetic mineralogy is Fe-Ti spinel, *Lunar Planet. Sci. XXX*, abstract 1802, [CD-ROM], 1999.
- Moskowitz, B. M., and R. B. Hargraves, Magnetic changes accompanying the thermal decomposition of nontronite (in air) and its relevance to Martian mineralogy, *J. Geophys. Res.*, **87**, 10,115-10,128, 1982.
- Murad, E., Mössbauer and X-ray data on  $\beta\text{-FeOOH}$  (akaganéite), *Clay Miner.*, **14**, 273-283, 1979.
- Murad, E., Iron oxide mineralogy of a hydrothermal assemblage on Santorini Island, Aegean Sea, *Mineral. Mag.*, **46**, 89-93, 1982.
- Murad, E., Application of  $^{57}\text{Fe}$  Mössbauer spectroscopy to problems in clay mineralogy and soil science: Possibilities and limitations, in *Advances in Soil Science*, edited by A. B. Stewart, pp. 125-157, Springer-Verlag, New York, 1990.
- Murad, E., Magnetic properties of microcrystalline iron (III) oxides and related materials as reflected in their Mössbauer spectra, *Phys. Chem. Miner.*, **23**, 248-262, 1996.
- Murad, E., and J. H. Johnston, Iron oxides and oxyhydroxides, in *Mössbauer Spectroscopy Applied to Inorganic Chemistry*, vol. 2, edited by G. J. Long, pp. 507-582, Plenum, New York, 1987.
- Murchie, S., J. Mustard, J. Bishop, J. Head, and C. Pieters, Spatial variations in the spectral properties of bright regions on Mars, *Icarus*, **105**, 454-468, 1993.
- Murphy, J. R., R. M. Haberle, O. B. Toon, and J. B. Pollack, Martian global dust storms: Zonally symmetric numerical simulations including size-dependent particle transport, *J. Geophys. Res.*, **98**, 3197-3220, 1993.
- Mustard, J. F., and J. F. Bell III, New composite reflectance spectra of Mars from 0.4 to 3.14  $\mu\text{m}$ , *Geophys. Res. Lett.*, **21**, 353-356, 1994.
- Mustard, J. F., and J. M. Sunshine, Seeing through the dust: Martian crustal heterogeneity and links to the SNC meteorites, *Science*, **267**, 1623-1626, 1995.
- Mustard, J. F., S. Murchie, S. Erard, and J. Sunshine, In situ compositions of Martian volcanics: Implications for the mantle, *J. Geophys. Res.*, **102**, 25,605-25,615, 1997.
- Nagano, T., S. Nakashima, S. Nakayama, K. Osada, and M. Senoo, Color variations associated with rapid formation of goethite from protoferrihydrite at pH 13 and 40°C, *Clays Clay Miner.*, **40**, 600-607, 1992.
- Nagata, T., *Rock Magnetism*, 350 pp., Maruzen, Tokyo, 1961.
- Nahon, D. B., and F. Colin, Chemical weathering of orthopyroxenes under lateritic conditions, *Am. J. Sci.*, **282**, 1232-1234, 1982.
- Newsom, H. E., Hydrothermal alteration of impact melt sheets with implications for Mars, *Icarus*, **44**, 207-216, 1980.

- Newsom, H. E., G. S. T. Graup, and K. Keil, Fluidization and hydrothermal alteration of the suevite deposit at the Ries Crater, West Germany, and implications for Mars, *Proc. Lunar Planet. Sci. Conf. 17th, Part 1, J. Geophys. Res.*, 91, suppl., E239-E251, 1986.
- Nyquist, L. E., L. E. Borg, and C.-Y. Shih, The Shergottite age paradox and the relative probabilities of Martian meteorites of differing ages, *J. Geophys. Res.*, 103, 31,445-31,455, 1998.
- Parfitt, R. L., Anion adsorption by soil and soil materials, *Adv. Agron.*, 30, 1-50, 1978.
- Pena, F., and J. Torrent, Relationships between phosphate sorption and iron oxides in alfisols from a river terrace sequence of Mediterranean Spain, *Geoderma*, 33, 283-296, 1984.
- Pick, T., and L. Tauxe, Characteristics of magnetite in submarine basaltic glass, *Geophys. J. Int.*, 119, 116-128, 1994.
- Pollack, J. B., Climatic change on the terrestrial planets, *Icarus*, 37, 479-553, 1979.
- Pollack, J. B., J. F. Kasting, S. M. Richardson, and K. Poliakov, The case for a wet, warm climate on early Mars, *Icarus*, 71, 203-244, 1987.
- Pollack, J. B., M. E. Ockert-Bell, and M. K. Shepard, Viking lander image analysis of Martian atmospheric dust, *J. Geophys. Res.*, 100, 5235-5250, 1995.
- Porter, S. C., Quaternary stratigraphy and chronology of Mauna Kea, Hawaii, *Geol. Soc. Am. Bull.*, Part 2, 90, 980-1093, 1979.
- Posy-Dowty, J., B. Moskowitz, D. Crerar, R. Hargraves, L. Tanenbaum, and E. Dowty, Iron oxide and hydroxide precipitation from ferrous solutions and its relevance to Martian surface mineralogy, *Icarus*, 66, 105-116, 1986.
- Reichen, L. E., and J. J. Fahey, An improved method for the determination of FeO in rocks and minerals including garnet, *U. S. Geol. Surv. Bull.*, 1144B, 1-5, 1962.
- Resende, M., J. Allan, and J. M. D. Coey, The magnetic soils of Brazil, *Earth Planet. Sci. Lett.*, 78, 322-326, 1986.
- Rieder, R., T. Economou, H. Wanke, A. Turkevich, J. Crisp, J. Bruckner, G. Drebus, and H. Y. McSweeney Jr., The chemical composition of Martian soil and rocks returned by the mobile alpha proton X-ray spectrometer: Preliminary results from the X-ray mode, *Science*, 278, 1771-1774, 1997.
- Roddy, D. J., Pre-impact geologic conditions, physical properties, energy calculations, meteorite, and initial dimensions and orientations of joins, faults, and walls at Meteor Crater, Arizona, *Proc. Lunar Planet. Sci. Conf. 8th*, 1697-1729, 1978.
- Salisbury, J. W., G. R. Hunt, and C. J. Lenhoff, Visible and near-infrared spectra, X, Stony meteorites, *Mod. Geol.*, 5, 115-126, 1975.
- Scheinost, A. C., A. Chavernas, V. Barron, and J. Torrent, Use and limitations of second-derivative diffuse reflectance spectroscopy in the visible to near-infrared range to identify and quantify Fe Oxide minerals in soils, *Clays Clay Miner.*, 5, 528-536, 1998.
- Schiffman, P., and R. J. Southard, Cation exchange capacity of layer silicates and palagonitized glass in mafic volcanic rocks: A comparative study of bulk extraction and in situ techniques, *Clays Clay Miner.*, 44, 624-634, 1996.
- Schwertmann, U., and R. M. Cornell, *Iron Oxides in the Laboratory: Preparation and Characterization*, 137 pp., VCH, New York, 1991.
- Schwertmann, U., and W. R. Fischer, Natural 'amorphous' ferric hydroxide, *Geoderma*, 10, 237-247, 1973.
- Schwertmann, U., and R. M. Taylor, Iron oxides, in *Minerals in Soil Environments*, 2nd ed., edited by J. B. Dixon and S. B. Weed, pp. 379-438, Soil Sci. Soc. of Am., Madison, Wis., 1989.
- Schwertmann, U., P. Cambier, and E. Murad, Properties of goethites of varying crystallinity, *Clays Clay Miner.*, 33, 369-378, 1985.
- See, T. H., J. Wagstaff, V. Yang, F. Horz, and G. A. McKay, Compositional variation and mixing of impact melts on microscopic scales, *Meteorit. Planet. Sci.*, 33, 937-948, 1998.
- Settle, M., Formation and deposition of volcanic sulfate aerosols on Mars, *J. Geophys. Res.*, 84, 8343-8354, 1979.
- Sherman, D. M., and T. D. Waite, Electronic spectra of Fe<sup>3+</sup> oxides and oxide hydroxides in the near IR and near UV, *Am. Mineral.*, 70, 1262-1269, 1985.
- Sherman, D. M., R. G. Burns, and V. M. Burns, Spectral characterization of the iron oxides with application to the Martian bright region mineralogy, *J. Geophys. Res.*, 87, 10,169-10,180, 1982.
- Shoemaker, E. M., and S. W. Kieffer, *Guidebook to the Geology of Meteor Crater*, Meteoritical Society, 66 pp., 1974.
- Singer, R. B., Spectral evidence for the mineralogy of high-albedo soils and dust on Mars, *J. Geophys. Res.*, 87, 10,159-10,168, 1982.
- Singer, R. B., and H. Y. McSweeney Jr., The igneous crust of Mars: Compositional evidence from remote sensing and the SNC meteorites, in *Resources of Near-Earth Space*, edited by J. S. Lewis, M. S. Matthews, and M. M. L. Guerrieri, pp. 709-736, Univ. of Arizona Press, Tucson, 1993.
- Singer, R. B., and T. L. Roush, Spectral reflectance properties of particulate weathered coatings on rocks: Laboratory modeling and applicability to Mars, in *Lunar Planet. Sci. XIV*, 708-709, 1983.
- Singer, R. B., T. B. McCord, R. N. Clark, J. B. Adams, and R. L. Huguenin, Mars surface composition from reflectance spectroscopy: A summary, *J. Geophys. Res.*, 84, 8415-8425, 1979.
- Smith, P. H., et al., Results from the Mars Pathfinder camera, *Science*, 278, 1558-1765, 1997a.
- Smith, P. H., et al., The imager for Mars Pathfinder experiment, *J. Geophys. Res.*, 102, 4003-4025, 1997b.
- Soderblom, L. A., The composition and mineralogy of the Martian surface from spectroscopic observations: 0.3 to 50  $\mu$ m, in *Mars* edited by H. Kiefer et al., pp. 557-593, Univ. of Ariz. Press, Tucson, 1992.
- Soderblom, L. A., and D. B. Wenner, Possible fossil H<sub>2</sub>O liquid-ice interfaces in the Martian crust, *Icarus*, 34, 622-637, 1978.
- Squyres, S. W., et al., The Athena Mars Rover science payload, in *Lunar Planet. Sci. XXIX*, abstract 1101 [CD-ROM], 1998.
- Squyres, S. W., et al., The Mars 2001 Athena Precursor Experiment (APEX), in *Lunar and Planetary Science XXX*, abstract 1672 [CD-ROM], 1999.
- Stahl, V., Impact glasses from the suevite of the Nordlinger Ries, *Earth Planet. Sci. Lett.*, 17, 275-293, 1972.
- Stanjek, H., and P. G. Weidler, The effect of dry heating on the chemistry, surface area, and oxalate solubility of synthetic 2-line and 6-line ferrihydrites, *Clay Miner.*, 27, 397-412, 1992.
- Staudigel, H., and S. R. Hart, Alteration of basaltic glass: Mechanisms and significance for the oceanic crust-seawater budget, *Geochim. Cosmochim. Acta*, 47, 337-350, 1983.
- Stevens, J. G., A. M. Khasanov, J. W. Miller, H. Pollak, and Z. Li (Eds.), *Mössbauer Mineral Handbook*, 527 pp., Biltmore, Ashville, N. C., 1998.
- Sunshine, J. M., L. A. McFadden, and C. M. Pieters, Reflectance spectra of the Elephant Moraine A79001 meteorite: Implications for remote sensing of planetary bodies, *Icarus*, 105, 79-91, 1993.
- Sutton, S. R., Thermoluminescence measurements on shock-metamorphosed sandstone and dolomite from Meteor Crater, Arizona, 2, Thermoluminescence age of Meteor Crater, *J. Geophys. Res.*, 90, 3690-3700, 1985.
- Thomas, N., W. J. Markiewicz, R. M. Sablotny, M. W. Wuttke, H. U. Keller, J. R. Johnson, R. J. Reid, and P. H. Smith, The color of the Martian sky and its influence on the illumination of the Martian surface, *J. Geophys. Res.*, 104, 8795-8808, 1999.
- Thorseth, I. H., H. Furnes, and O. Tumyr, A textural and chemical study of Icelandic palagonite of varied composition and its bearing on the mechanism of the glass-palagonite transformation, *Geochim. Cosmochim. Acta*, 55, 731-749, 1991.
- Toulmin III, P., A. K. Baird, B. C. Clark, K. Keil, H. J. Rose Jr., R. P. Christian, P. H. Evans, and W. C. Kelliher, Geochemical and mineralogical interpretation of the Viking inorganic chemical results, *J. Geophys. Res.*, 82, 4625-4634, 1977.
- Tricman, A. H., R. A. Barrett, and J. L. Gooding, Preterrestrial aqueous alteration of the Lafayette (SNC) meteorite, *Meteoritics*, 28, 86-97, 1993.
- Ugolini, F. C., Hydrothermal origin of the clays from the upper slopes of Mauna Kea, Hawaii, *Clays Clay Miner.*, 22, 189-194, 1974.
- van Breemen, N., Genesis, morphology, and classification of acid sulfate soils in coastal plains, in *Acid Sulfate Weathering, SSA Spec. Publ. vol. 10*, edited by J. A. Kittrick et al., pp. 95-108, Madison, Wis., Soil Sci. Soc. of Am., 1982.
- Vasavada, A. R., T. J. Milavec, and D. A. Paige, Microcraters on Mars: Evidence for past climate variations, *J. Geophys. Res.*, 98, 3469-3476, 1993.
- Weidner, V. R., and J. J. Hsia, Reflection properties of pressed polytetrafluoroethylene powder, *J. Opt. Soc. Am.*, 71, 856-861, 1981.
- Weitz, C. M., J. W. Head III, and C. M. Pieters, Lunar regional dark mantle deposits: Geologic, multispectral, and modeling studies, *J. Geophys. Res.*, 103, 22,725-22,759, 1998.
- Wendlandt, W. W., and H. G. Hecht, *Reflectance Spectroscopy*, 298 pp., Wiley-Interscience, New York, 1966.
- West, H. B., M. O. Garcia, F. A. Frey, and A. Kennedy, Nature and cause of compositional variation among the alkalic cap lavas of Mauna Kea Volcano, Hawaii, *Contrib. Mineral. Petrol.*, 100, 383-397, 1988.
- Wilson, L., and J. W. Head III, Mars: Review and analysis of volcanic

- eruption theory and relationships to observed landforms, *Rev. Geophys.*, 32, 221-263, 1994.
- Wolfe, E. W., W. S. Wise, and G. B. Dalrymple, *The Geology and Petrology of Mauna Kea Volcano, Hawaii: A Study of Postshield Volcanism*, U.S. Geol. Surv. Prof. Pap. 1557, 129 pp., 1997.
- Yen, A. S., B. C. Murray, and G. R. Rossmann, Water content of the Martian soil: Laboratory simulations of reflectance spectra, *J. Geophys. Res.*, 103, 11125-11133, 1998.
- York, D., Least squares fitting of a straight line with correlated errors, *Earth Planet. Sci. Lett.*, 5, 320-324, 1969.
- Zhou, Z., and W. S. Fyfe, Palagonitization of basaltic glass from DSDP Site 335, Leg 37: Textures, chemical composition, and mechanism of formation, *Am. Mineral.*, 74, 1045-1053, 1989.
- Zurek, R. W., and L. J. Martin, Interannual variability of planet-encircling dust storms on Mars, *J. Geophys. Res.*, 98, 3247-3259, 1993.
- J. F. Bell III, Department of Astronomy, Cornell University, Ithaca, NY 14853.
- J. L. Bishop, NASA Ames Research Center, Moffett Field, CA 94035.
- D. T. Britt, Lunar and Planetary Laboratory, University of Arizona, Tucson, AZ 85721.
- G. Furniss and N. W. Hinman, Department of Geology, University of Montana, Missoula, MT 59812.
- S. A. Mertzman, Department of Geosciences, Franklin and Marshall College, Lancaster, PA 17604.
- D. W. Ming and R. V. Morris, NASA Johnson Space Center, Mail Code SN3, Houston, TX 77058. (richard.v.morris1@jsc.nasa.gov)
- A. C. Scheinost, Department of Plant and Soil Science, University of Delaware, Newark, DE 19717.

C. C. Allen, D. C. Golden, and T. D. Shelfer, Lockheed Martin Space Operations Co., Houston, TX 77058.

(Received April 2, 1999; revised September 15, 1999; accepted September 27, 1999.)